*Dissertation zur Erlangung des Doktorgrades der*
*Fakultät für Chemie und Pharmazie der*
Ludwig-Maximilians-Universität München

# Advanced Confocal Microscopy: From Setups To Applications

**Nikolaus Naredi-Rainer**

aus Graz, Österreich

2014

# Erklärung

Diese Dissertation wurde im Sinne von § 7 der Promotionsordnung vom 28. November 2011 von Herrn Professor Don C. Lamb, PhD betreut.

# Eidesstattliche Versicherung

Diese Dissertation wurde selbständig, ohne unerlaubte Hilfe erarbeitet.

München, den 14. Januar 2014

Nikolaus Naredi-Rainer

Dissertation eingereicht am: 16.01.2014

1. Gutachter: Prof Don C. Lamb, PhD

2. Gutachter: Prof Dr. Christoph Bräuchle

Mündliche Prüfung am: 12.02.2014

Alle Rechte, bereits veröffentlichte Texte oder Darstellungen wiederzuverwenden, wurden via *Rightslink* erworben.

“Science is like sex: sometimes something useful comes out, but that is not the reason we are doing it. ”

— Richard Feynman

# Abstract

Confocal microscopy is known for its capability to produce exceptional 3D images, even in living tissue. At the same time, it is a powerful spectroscopic tool, facilitating fluorescence methods such as Fluorescence Correlation Spectroscopy (FCS) or single-molecule Förster Resonance Energy Transfer (FRET). It is heavily used to investigate a wide range of biological problems. This holds true especially for protein properties such as ligand binding, complex formation, conformational changes, or the intracellular distribution of the species in question.

In this work, I will describe the assembly of two instruments: The first is a multi-parameter fluorescence detection (MFD) setup. It is a purely spectroscopic tool that offers the capability to characterize a fluorescent molecule, delivering information like fluorescence lifetime, anisotropy or the speed of its diffusion in free solution. When the molecule of interest is labelled with two fluorophores, additional information, like the energy transfer in-between them, becomes accessible and the correct distance between these two fluorophores can be calculated. If the two fluorophores are attached to different molecules, the MFD setup can detect interactions of these molecules in the range from pM up to µM with the help of Fluorescence Cross-Correlation Spectroscopy (FCCS).

The second instrument, a stimulated emission depletion setup, combines some of the mentioned techniques, like FCS, with the superior image capability of a confocal microscope. One particular problem of fluorescent microscopes, though, is that image resolution is always restricted to the diffraction limit of the wavelength of the laser light. The STED setup utilizes the effect of stimulated emission in order to circumvent the diffraction barrier and allows images with a three-fold resolution increase, down to $75nm$.

These two setups will be used for several applications: The first will be centered around the molecular conformation of proteins, which are sensitive to the nature of the aqueous environment. In particular, the presence of ions can stabilize or destabilize (denature) protein secondary structure. The underlying mechanisms of these actions are still not fully understood. I will apply single-pair FRET to a small 29 amino acid long model peptide to investigate unfolding mechanisms of different unfolding reagents from the Hofmeister series, like sodium perchlorate or guanidinium chloride. The results show that certain salts, which are commonly summarized as denaturing agents, achieve the unfolding by either collapsing the molecule to a compressed state or swelling it to a denatured state.

The second application of the MFD setup is the investigation of the enhanced green fluorescent protein (EGFP). Although highly used in biochemistry and biophysics, for example to read out the expression level of genes, it is still not fully known what percentage of EGFP is fluorescent. This lack of knowledge makes it nearly impossible to make quantitative statements. With the help of FCCS, it is shown that the folding efficiencies range from $40 - 90\%$, depending on the environment of the fluorescent protein and which particular mutant is used.

In the third application, the focus will be shifted to nucleation- and polymerization-behavior of actin. The actin cytoskeleton is a central mediator of cellular morphogenesis, and rapid actin reorganization drives essential processes such as cell migration and cell division. In order to compare results of confocal spectroscopy methods with well-established bulk essays, we successfully ported the standard bulk essay to the confocal microscope, allowing for the first time to follow the decrease of monomer concentration and appearance of small filaments. Also, the formation of dimers or other small oligomers below the critical concentration is proven for the first time, using FCCS.

The last application will utilize the STED setup in order to carry out the first steps towards the investigation of the nucleation and branching behavior of actin in cooperation with the actin related protein 2/3 (ARP2/3). This protein complex preferentially attaches to actin filaments that are located at the leading edge of a cell and forms branched filamentous structures. The exact conditions under which this process occurs are not well characterized. This part of the work will deal with the steps that are necessary to follow the polymerization process on the STED setup.

# Contents

# Chapter 1

# Introduction

Life, seen as an entity, is not comprehensible for any scientist, may it be from the perception of a chemist, biologist or physicist. Also on the cellular level, science is far from understanding the connections of the uncountable interactions that take place between biomolecules. Even the interaction pathway of one single molecule within one cell is too complex to study at once, mostly for the reason that no suitable technique is available to follow such a process. Hence, it is necessary to break down these instances into smaller problems that can be solved one piece at a time and afterwards be put together again and brought into context.

Over the course of the last few decades, techniques have emerged that offer the possibility to gain insight into biological processes at the desired resolution of down to the atom scale. With their help, the investigation of biomolecules can be approached from two directions: one set of technologies focusses on the bottom-up approach, like X-ray crystallography, nuclear magnetic resonance spectroscopy (NMR), or atomic force microscopy (AFM). These techniques isolate the molecule of interest and gain invaluable amounts of information. However, at the same time, the biomolecules are no longer in their native environment. Additionally, information regarding dynamics in the specimen is often lost during sample preparation. On the other hand, there are techniques that use a top-down approach: wide-field microscopy or single-particle tracking show images on a larger scale, but highlight molecules of interest with fluorescence labels. The problem here is apparent: while the molecule of interest is visible, most of the interaction partners stay unobserved and their influence is seldom known.

A few techniques are able to bridge the gap between these two approaches. One is in principle electron microscopy with a field of view that can cover the length of a single cell and offers at the same time a spacial resolution that can be as precise as a single atom. The disadvantage is that the sample is only rarely imaged under *in vivo* conditions so that dynamic processes are lost entirely.

A variety of techniques that in cooperation fulfill all mentioned requirements are avail-

able on a confocal microscope [1]. The confocal microscope, in contrast to wide-field microscopy, also allows the spectroscopic investigation of molecules. A subset of these available techniques is known as 'fluorescence fluctuation spectroscopy' (FFS) [2].

In general, the molecule of interest has to be equipped with a fluorescent label, either after biosynthesis with an organic dye, or genetically encoded with a fluorescent protein [3]. Valuable information about the molecule and its specific environment can be extracted by the fluorescence intensity, lifetime and the spectrum of the fluorophore. But FFS possesses the ability to extract detailed information about the sample by analyzing the fluctuations that are intrinsic in every measurement, thereby gaining for example insight e.g. into the diffusion coefficient of a specimen or its interaction with binding partners. Since the optical devices used in confocal microscopy have evolved significantly over the last two decades, it is now possible to measure the fluorescence intensity of single fluorophores at room temperatures [4]. This makes it possible to measure Förster resonance energy transfer (FRET) on the single-molecule level, avoiding any averaging or artifacts introduced by bulk measurements. This technique is ideally suited for the investigation of biomolecules, since FRET measurements are most sensitive in the range of $2 - 9nm$, which corresponds in many cases the size of e.g. proteins or small protein complexes.

Microscopes, including the confocal variant, were designed in the first place not as spectroscopic tools but to capture images on a scale that accessible for the human eye. Fluorescence imaging has been restricted to a resolution of approximately $200nm$. This was already shown by Ernst Abbe in 1873 [5] and has become a physical law during the last two centuries. In recent years, the thought appeared to circumvent this barrier instead of trying find means to break it. This resulted in a the new field of 'super-resolution microscopy'[1] [6]. Techniques that offer superior resolution than the Abbe limit can be divided into three groups (chapter 5.2), but the method of 'STimulated Emission Depletion' (STED) has draw special attention. This is based on the fact that STED still offers all spectroscopic tools of a confocal microscope, while at the same time providing images with a resolution on the single-digit nanometer scale.

In summary, it is not an exaggeration to state that the confocal microscope can reveal insights into questions that range from the Ångstrom- (FRET) over the nanometer- (STED) up to the hundreds of micrometer-range (imaging).

These technological advances would be a pure proof of principal if not applied to biological questions. But the field of biophysics has already been awarded with several nobel prices for discoveries that answered elemental biological questions with the help of the equipment mentioned above. Not only Gerd Binning and Ernst Ruska for the electron microscope and Watson and Crick for the X-ray structure of the DNA, but also Shimomura, Chalfie and Tsien for the discovery of the green fluorescent protein are among the best known of at least ten biophysicists nobel laureates. All of the methods

[1] Microscopy in the $nm$ range is often termed 'nanoscopy'.

mentioned above have added up considerable knowledge to describe the native structure of biomolecules. However, many particular problems are not fully answered yet: while the native structure of biomolecules, especially proteins, is often known, it is unclear how the transition of a newly synthesized, unfolded amino acid chain reaches its functioning three dimensional structure on a biological relevant time scale. Already 50 years ago, Cyrus Levinthal calculated that a random search throughout all possible combinations of conformations would take longer than the age of the universe (Levinnthal's paradox [7]). Together with Anfinsen's dogma, which states that the three-dimensional structure is already predetermined by the amino acid sequence [8], it becomes clear that protein folding must occur in a direct way and not random. This is especially true when misfolding of proteins leads to diseases like Creutzfeldt-Jakob, Alzheimer or Parkinson. Chapters 6.1, 6 and 7 will discuss the current opinion on protein folding, the importance of folding efficiency and the unfolding mechanism of proteins.

The scope of this work was to assemble and to successfully apply individual aspects of confocal microscopy to the mentioned biological problems. The underlying concepts and properties of the interaction of light with matter are covered in chapter 2 and chapter 3 describes the evolution of the confocal microscope with the a detailed view on the variety of its capabilities. The singe-molecule methods that are used in this work and needed for the comprehension of the applications are explained in chapter 4. The 'multi-parameter fluorescence' (MFD) and the 'stimulated emission depletion' (STED) setups that were assembled during the course of this work are introduced and characterized in chapter 5. The background of the applications, in particular the theory for protein folding and a general overview of the importance of actin in cells, is given in the chapters 6.1 and 8.1. Utilizing the MFD setup and combining it with single-molecule FRET, the effect of salts and their unfolding mechanism is investigated in Chapter 6. It is shown that salts, which are known to destabilize the structure of proteins, achieve this influence by very different means. Additionally, with the help of these single-molecule measurements, contradictions that appeared from CD spectroscopy could be resolved. In chapter 7, the folding efficiency of fluorescent proteins is explored using quantitative fluorescence cross-correlation spectroscopy (FCCS). The simple practicability of FCCS is shown alongside with the corrections that have to be applied for different modalities of this technique. How nature controls the nucleation and elongation of actin filaments is discussed in chapter 8. Here, the influence of the internal pH is shown and a theoretic model for the elongation of filaments is proposed. With the help of the STED setup and the superior resolution that it offers, the branching and elongation behavior of actin is probed in chapter 9.

# Chapter 2

# Fluorescence Spectroscopy

## 2.1 The Interaction of Light with Matter

Einstein described three possible types of interaction of light with matter in 1916 [9]: absorption of a photon from an electromagnetic field by e.g. an atom or molecule, resulting in an excited state for the atom; the spontaneous emission of a photon by an atom that currently is in an excited state; and as last possible interaction the stimulated emission of a photon by an incoming normal mode, i.e. the stimulated photon will have the same direction, frequency, and phase as the stimulating photon. To described the increase of the number of molecules $N_0$ in the ground state $S_0$, and at the same time the decrease of the number of molecules $N_1$ in the excited state $S_1$, he proposed the following equation:

$$\frac{dN_0}{dt} = -\frac{dN_1}{dt} = -N_0 \cdot B_{01} \cdot u + N_1 \cdot B_{10} \cdot u + N_{10} \cdot A_{10} \tag{2.1}$$

where $A_{10}$ , $B_{10}$, and $B_{01}$ are proportionality constants, better known as *Einstein Coefficients*, and $u$ is the spectral radiance density. $N_0 \cdot B_{01} \cdot u$ describes the probability of stimulated absorption, $N_1 \cdot B_{10} \cdot u$ of stimulated emission and $N_{10} \cdot A_{10}$ the probability of spontaneous emission. All three processes will be described in detail in the next paragraphs.

### 2.1.1 General Principle of Fluorescence

Fluorescence - the emission of light after absorption of a photon - is an often occurring form of luminescence, more precisely of photoluminescence. The general process is depicted in a Jablonski [10] scheme (see figure 2.1).

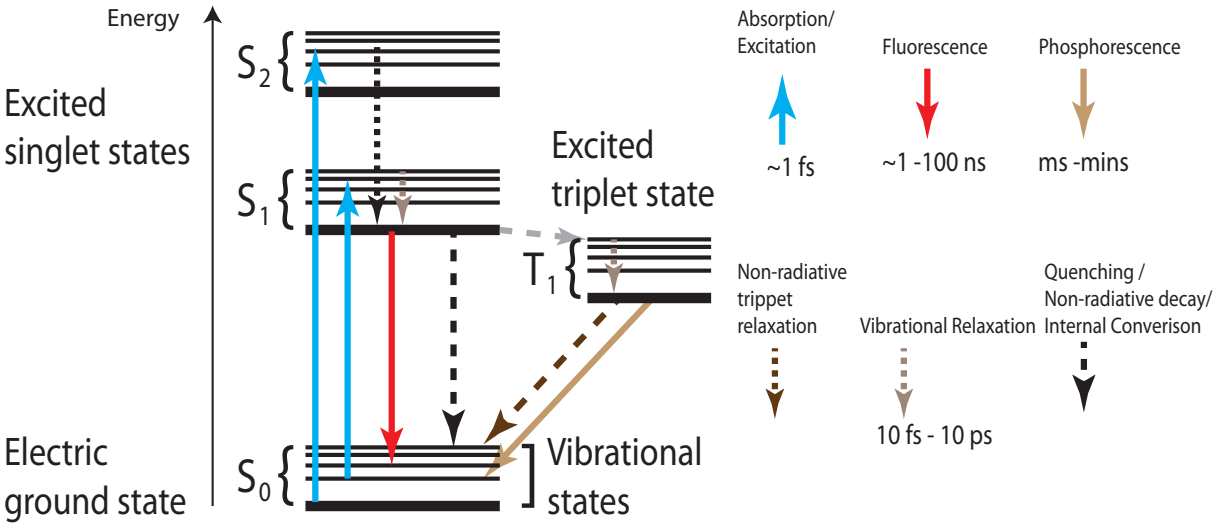


Figure 2.1: Jablonski diagram showing processes involved in fluorescence and the time scales on which they occur. Dashed lines are non-radiative decays.

Usually, a molecule can be found in the electric ground state, $S_0$ and also in the vibrational ground state $\nu_0$, since it takes approx. $1000 - 3000\ cm^{-1}$ to reach the next vibrational state $\nu_1$, a magnitude more than is available via the thermal energy at room temperature $kT$, which is roughly $200\ cm^{-1}$ [11]. Upon absorption of a photon that has a matching wavelength for the transition, one electron is excited into a higher electric state, $S_n$. The time scale for this process is in the femto-second range. Compared to this short time range, the nuclear motion of the absorbing molecule is negligible (Born-Oppenheimer approximation [12]). This means that when an electron undergoes an electric transition (for absorption as well as fluorescence), the new vibrational level has to be agreeable with nuclear positions and momentum of the original vibrational level.

For this reason, an electron is very rarely found in the vibrational ground state after a transition, but in a higher vibrational level (Frank-Condon-principle [13, 14], end of blue arrows in figure 2.1). The process of radiative de-excitation, or fluorescence (red arrow), is three orders of magnitude slower than the excitation. This means that processes that occur on shorter timescales than fluorescence will take place in the meantime. Hence, the system has time to undergo vibrational relaxation (light brown dashed arrows) to the vibrational ground state of the $S_1$ state (Kasha's rule [15]). Several other processes compete with the desired process of fluorescence: internal conversion to the ground state, together with other quenching processes, and intersystem crossing (ISC). When a molecule undergoes ISC, the spin of the excited electron flips and hence this is a singlet to triplet conversion. This transition is normally forbidden but can still occur when the spin-orbit interaction is strong enough. This is usually the case when heavy atoms are close by. ISC, however, is kinetically not favorable and thus afflicts directly its decay rates that stretches from milliseconds to several minutes.

### 2.1.2 Absorption and Emission Spectra

Fluorescent molecules - referred to as fluorophores or dyes - have distinct absorption, excitation and emission spectra [16–19]. Absorption spectra measure the amount of absorption of incoming light as a function of wavelength while emission spectra show the intensity of the fluorescence as a function of wavelength for a constant excitation wavelength. The last, and most seldom shown spectrum, is the excitation spectrum: here, the fluorescence detection wavelength or range is held constant and the excitation light is scanned over a range of wavelengths. Figure 2.2 shows the absorption and emission spectra of the fluorophore Atto647N, along with the optical properties of the filters used in the stimulated emission depletion (STED) setup (chapter 5.2).

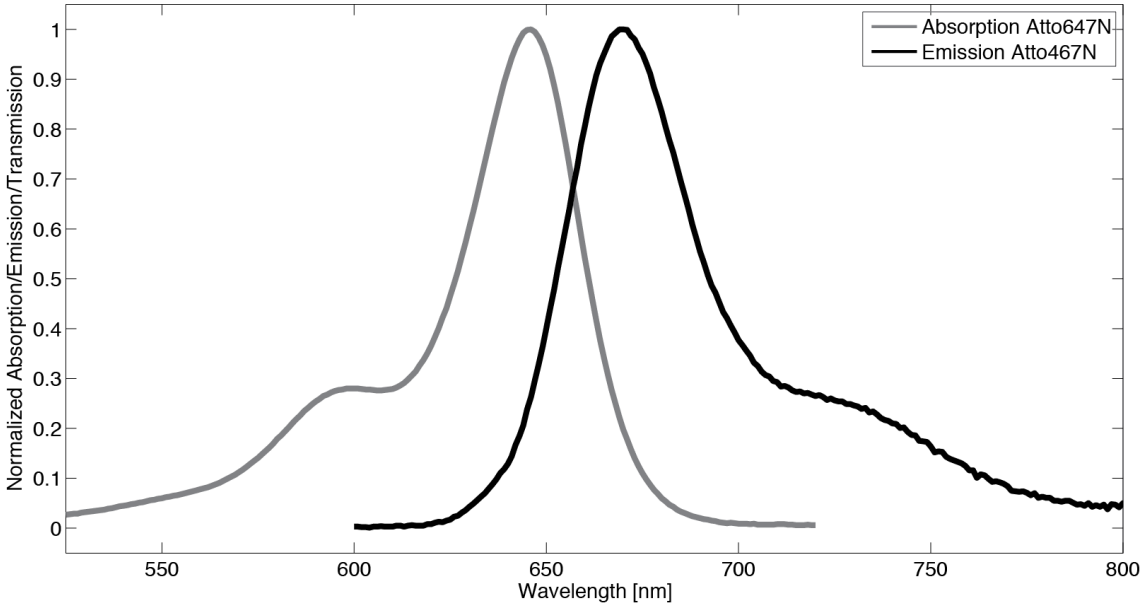


Figure 2.2: Spectral properties of the 647N dye: The absorption (light red) and emission spectra (dark red) of the dye Atto647N. Clearly visible is the red shifted emission peak in comparison to the excitation for each fluorophore, due to the loss of energy during internal conversion (Stokes Shift).

As Kasha's rule states and as already displayed in figure 2.1, fluorescence usually occurs from the lowest energy level of the $S_1$-state. The Franck-Condon principle is valid for absorption, as well as for fluorescence. Along with the fact that electric states are normally equidistant, this leads to the observation that absorption and emission spectra are approximately mirrored. The loss of energy during vibrational relaxation (the so called Stokes-Shift [20]) makes fluorescence techniques unique, compared to other spectroscopy methods: as figure5.9 shows, the excitation light can be effectively suppressed by correct filters without significantly interfering with the desired signal.

### 2.1.3 Stimulated Emission

Stimulated emission, or induced emission, is the occurrence of a photon, which happens not spontaneously, like described in chapter 2.1.1, but rather induced by another photon. This process is the last of three possible interactions of light with matter, after absorption and emission. It was in 1928, when Rudolf Ladenburg performed the first experiment with stimulated emission [21]. In the years 1954 and 1960, stimulated emission was used to produce the first fully coherent light sources, the *maser*[22] and the *laser*[23], respectively.

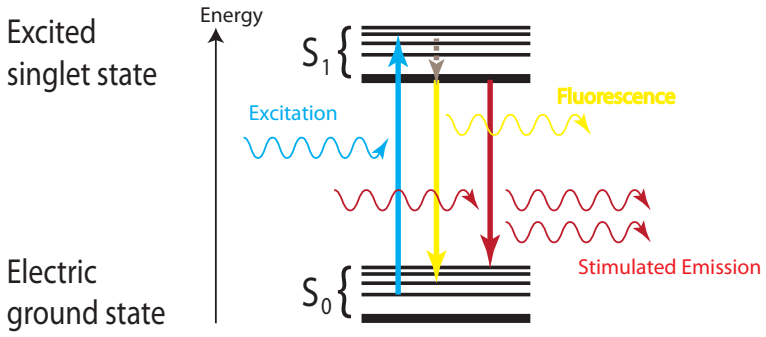


Figure 2.3: Jablonski scheme for fluorescence (yellow arrow) with additional process of stimulated emission (red arrow). A second light source (red) is used to introduce stimulated emission. The stimulated photon is in phase with the stimulating photon and, hence, has the same energy, direction, and phase.

Figure 2.3 shows the general principle: necessary for stimulated emission is an excited electron in the $S_1$ -state. If an incoming photon has the correct properties - its energy has to match the exact transition energy between higher and lower state and the transition has to fulfill the selection rules - it can trigger the de-excitation of the electron and at the same time the emission of photon corresponding to that energy. This second photon inherits all properties of the stimulating photons: they have the same wavelength, direction of movement, polarization and phase.

This effect of stimulated emission is not only used to create powerful light sources, the lasers used in the optical setups described later on, but also in the stimulated emission depletion setup (STED), used in order to circumvent Abbey's diffraction limit [5].

## 2.2 Fluorescence Lifetime

As already mentioned, the process of spontaneous emittion is a statistical process, meaning that for every excited molecule the probability to emit a photon is the same no matter how long the molecule already spend in the excited state. It is simply not possible to predict when a certain molecule will return into the ground state. Only the probability can be calculated that this event occurs within a certain interval $\Delta t$. Hence, the number of fluorescing molecules within a certain time frame $\Delta t$, with a given number of excited fluorophors $N_{S_1}(t = 0)$ can be calculated as:

$$dN_{S_1}(t) = -k_f \cdot N_{S_1}(t = 0) \cdot dt \tag{2.2}$$

where $k_f$ is the rate of fluorescence. As depicted in figure 2.1, not only the fluorescent pathway for de-excitation exists, but also non-fluorescent, leading to non-fluorescent decay rates, summarized as $\sum k_{nf}$:

$$\frac{dN_{S_1}(t)}{dt} = -(k_f + \sum k_{nf}) \cdot N_{S_1} \tag{2.3}$$

When integrating over $t$, equation 2.3 yields to a mono-exponential function:

$$N_{S_1}(t) = N_{S_1}(0) \cdot e^{-k_f \cdot t} \tag{2.4}$$

From an experimental point-of-view, the lifetime $\tau$ of a fluorophore can simply be measured as the time it takes till the fluorescence intensity of a dye solution has decayed to $1/e$ of its original value after a short excitation pulse. But as illustrated in the chapter 2.1.1, there are more decay paths available than simply fluorescence. Each decay path has a characteristic rate. Hence, the lifetime $\tau$ additionally consists of decay rates that are non-fluorescent, $k_{nf}$:

$$\tau = \frac{1}{k_f + \sum k_{nf}} \tag{2.5}$$

The quantum yield describes the ratio of emitted fluorescence photons to absorbed photons and can be determined from $k_f$ and $\sum k_{nf}$:

$$\Phi = \frac{k_f}{k_f + \sum k_{nf}} \tag{2.6}$$

An ideal dye possesses a mono-exponential decay and a quantum yield close to 1. However, several fluorophores, like the green-fluorescent protein (GFP), are known to have multi-exponential lifetime decays.

Figure 2.4 shows a histogram of fluorescence events after an excitation pulse for a solution of the dye Atto532. The excitation laser pulse arrives at the beginning of the

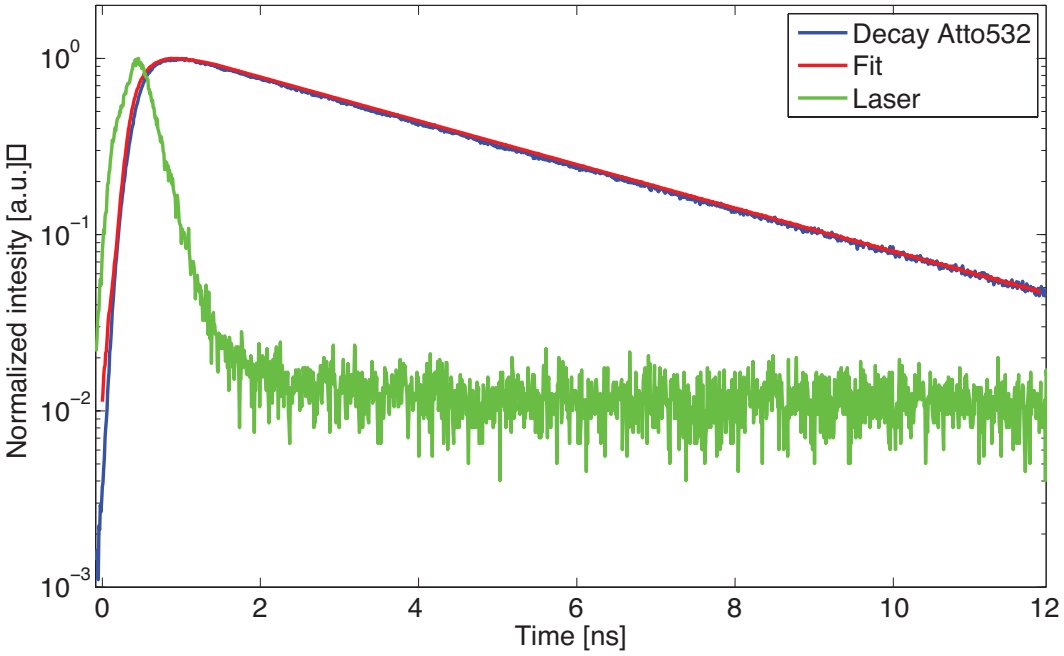


Figure 2.4: Distribution of detected fluorescence photons for Atto532 shown in blue. The convolution of excitation and detection response function of the system (the IRF) is shown in green. This IRF is needed to calculate the correct lifetime fit (red) out of a fluroescence decay curve, yielding here $3.75ns$.

measurement and starts to excite the fluorophore. The stochasitical nature of fluorescence leads to an exponential decay. The fit to the data yields a lifetime of $3.75ns$[1].

The lifetime information has evolved into a very important parameter in microscopy and can be utilized to detect quenching in the sample or, for example, to form images that are not intensity based, but rather show a map of the lifetimes, therefore making for example auto-fluorescence and desired signal easier to distinguish [24].

## 2.3 Fluorescence Energy Transfer

Förster Resonance Energy Transfer (FRET) [25–32] is the transfer of energy from an excited donor fluorophore to an acceptor molecule. There are some basic requirements for FRET to occur: the overlap of the acceptor's absorption spectrum with the donor's fluorescence emission spectrum, the correct orientation of the dipol moments, and the spacial proximity of $20-100\ nm$ in between these two. The mechanism of energy transfer is based on a long-range dipole-dipole coupling [33]. Since fluorescence is not necessary

[1]The temporal response of the microscope system to a detected photon has to be considered when dealing with fluorescence lifetime in the time domain. Since especialy detector and electronics have a certain amount of jitter, the timing gets imprecise compared to the very small excitation pulse. For example the excitation lasers used in this work feature a pulse duration of $150-250ps$, whereas the laser excitation in figure 2.4 has a length of $\sim 900ps$. To extract therefore a correct lifetime, this broadening has to be taken into account and the histogram has to be deconvoluted with the instrument response function (IRF), which describes the reaction of the optical detection system to the arriving photon.

for FRET, the term “fluorescence resonance energy transfer” may be misleading and the name "Förster resonance energy transfer" is preferred. It is named after the German scientist Theodor Förster [25, 34]. His contibution to science is remarkable, considering that nearly all papers, which deal with FRET nowandays, still cite his publications from the 1940s. But these papers are written in German, leading to the fact that he “may hold the record of citations that have never been read” [35]. Förster became aware of and interested in the problem of FRET through the process of photosynthesis: experimantal data [36, 37] had shown that the process of conversion of $CO_2$ was too efficient for normal absorption of light in leafs. Or, the other way around, there are too few reaction centers within a plant cell for the amount of captured energy.

Förster was by far not the first to develop a theoretical model for FRET, but he was rather aware of the work that preceded his own: *Kallmann and London* [38] dealt with energy transfer of vapors of atoms and showed the correct $1/R^6$ dependence, but due to wrong reasoning and therefore with false corrections. Hence, their theory could not explain the theory behind energy transfer in condensed matter. *J. Perrin* [39] tried to explain experiments from *Weigert* [40] and *Gaviola* [41] with the help of energy transfer. In these experiments it was observed that the polarization of fluorescence decreased strongly when the concentration was raised above a certain threshold of $\sim 3mM$. But he and later on his son, *F. Perrin* [42], failed to deduce the correct distance dependency due to wrong assumptions for their model. An interesting point is that *Oppenheimer and Arnold* might have been very close to explaining the theoretical background of FRET, but the work on the atomic bomb lead to a publication only in 1950 [43].

Although much effort was already dedicated to explaining the phenomenon of FRET, it was Förster who was able to derive a full explanation of energy transfer [44]. For this he conducted three important steps:

i) He was aware of the fact that the emission and absorption spectra of molecules are considerably broadened in condensed matter. Hence, he took correctly into account the overlapping frequencies of the excited state of the donor and the ground state of the acceptor, making their resonance one of the requirements of FRET.

ii) He derived the correct theory for the overlap integral, based on the treatment of the two fluorophores as oscillating dipoles. Also he took the angular dependence of energy transfer into account, creating the infamous $\kappa^2$.

iii) With the help of Fermi’s golden rule [45], he deduced the correct distance dependency of $1/R^6$.

This lead him to a transfer rate, which is given by:

$$k_T = \tau_D^{-1} \cdot (R_0/R)^6 \tag{2.7}$$

where $\tau_D$ is the lifetime of the donor fluorophore without an acceptor, $R$ is the actual

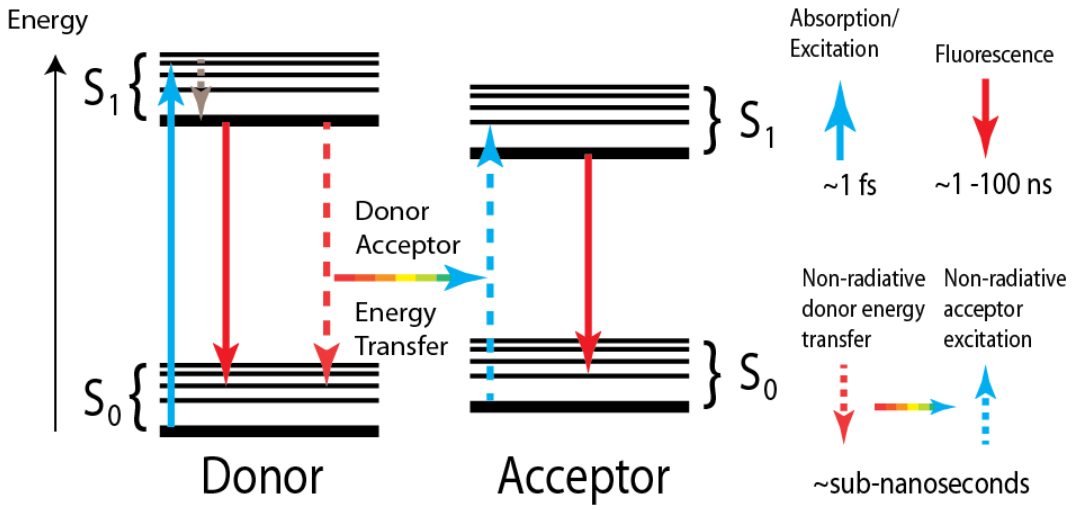


Figure 2.5: A simplified Jablonski diagram for FRET: another decay pathway becomes available for the excited donor, when a second dye is in the vicinity. The energy is transferred to the lower-energetic acceptor and can be detected e.g. by measuring the emission of acceptor fluorescence or the decreased lifetime of the donor dye.

distance between the dyes and $R_0$ is the Förster radius. The Förster radius describes the distance between the two dyes at which, on average, 50% transfer efficiency takes place:

$$R_0^6 = 8.8 \cdot 10^{-28} \cdot \kappa^2 \cdot n^{-4} \phi_D \cdot J \tag{2.8}$$

where $\kappa^2$ is the orientation factor, $n$ the index of refraction of the solvent, $\phi_D$ the quantum yield of the donor without acceptor and $J$ the spectral overlap integral. The Förster radius in this formula is given in Å. Figure 2.5 shows the Jablonski scheme of a fluorophore expanded with the possibility of transferring the energy of the excited donor molecule to the acceptor.

The FRET efficiency is defined as the ratio of transferred photons to photons absorbed by the donor:

$$f_E = \frac{k_T}{t_D^{-1} + k_T} = \frac{1}{1 + \left(\frac{R}{R_0}\right)^6} \tag{2.9}$$

Figure 2.6 shows the behavior of the FRET efficiency of Atto488 as donor with various acceptors. It becomes obvious here that the dye-pair should be chosen according to the experiment.

The precise FRET calculation, including correction factors, and its conversion to accurate distances is discussed in more detail in sections 4.5 and 4.6.

As already mentioned and shown in figure 2.6, the most sensitive region for FRET is between 20 and 80Å, which makes it immediately applicable for biomolecules, which often have the appropriate size. Since fluorescence microscopy is a non-invasive technique, molecules of interest can be labelled with synthetic dyes or immunofluorescent molecules

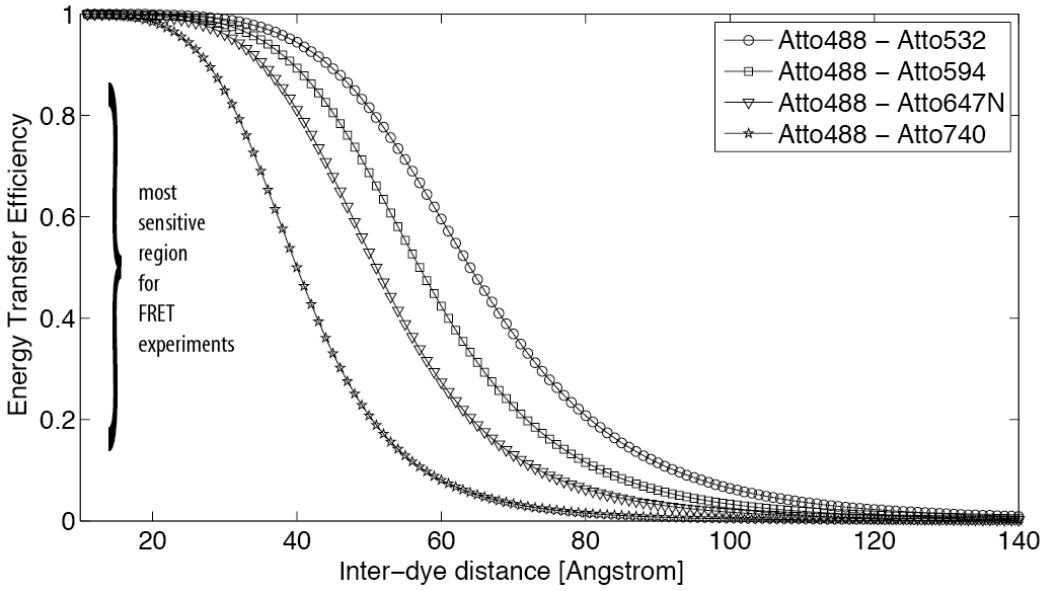


Figure 2.6: The calculated FRET efficiencies for several dye-pairs. The sensitive region stretches from $\approx 30\dot{A}$ to $\approx 80\dot{A}$, depending on the dye-pair used in the experiment.

and biological specimen can be studied *in vivo*. In general, there are two ways of approaching a FRET measurement: via the fluorescence intensity (amount of transferred photons) or via the change in fluorescent lifetime of the donor. Both approaches have advantages and disadvantages, but oftentimes compliment each other. In general, FRET is ideally suited to observe distances and distance changes in various biological samples, both *in vitro* and *in vivo*.

## 2.4 Fluorescence Anisotropy

Fluorescence anisotropy, in general, describes the discrepancy or the polarization of the incoming laser beam and the accordingly occurring fluorescence. This makes it possible to investigate the orientation of a molecule and therby gain information regarding e.g. its rotational diffusion [46].

The steady-state anisotropy of fluorescence photons in general is given by

$$r = \frac{\int_0^\infty r(t)F(t)dt}{\int_0^\infty F(t)dt} \tag{2.10}$$

where $r(t)$ is the time-dependent anisotropy:

$$r(t) = \frac{F_\parallel(t) - F_\perp(t)}{F_\parallel(t) + 2 \cdot F_\perp(t)} \tag{2.11}$$

$F_\parallel(t)$ and $F_\perp(t)$ are the fluorescence signals detected parallel and perpendicular with respect to the laser light. Figure 2.7 shows that the amount of light which arrives at detectos $x$ is composed of only light that is perpendicular to the exciting laser beam (orange double arrows). Each of the other detector's signal consists of a light polarized equally perpendicular and parallel to the incident laser beam. This means that the total intensity consists of two times the perpendicular intensity and one time the parallel intensity[47]:

$$F(t) = F_\parallel(t) + 2 \cdot F_\perp(t) \tag{2.12}$$

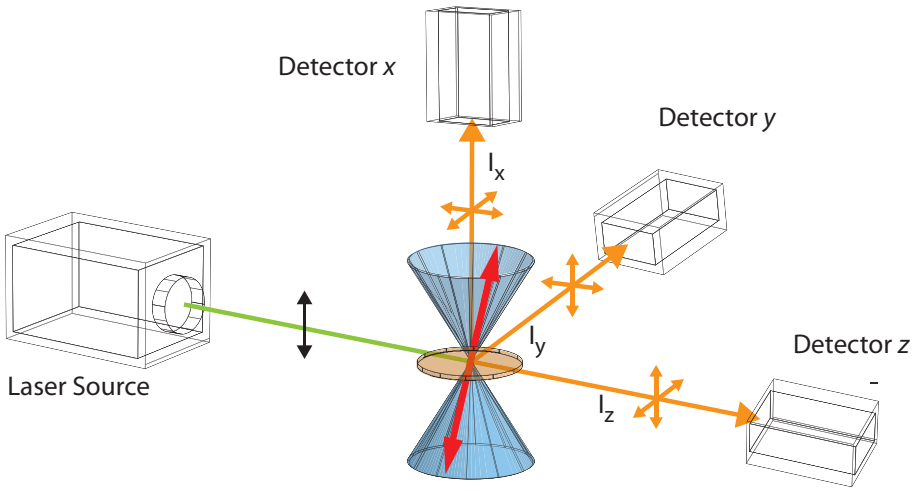


Figure 2.7: Detecting the polarization of photons. The transition dipole (red double arrow), of a fluorophore excited by a linearly polarized laser light source is shown. The electric field vector of the light source is shown as a black double arrow. The fluorescence is detected for each polarization with a detector, shown in black. Figure adapted from [47]

# Chapter 3

# Confocal Microscopy

Excerpts of this chapter have been published in the book 'Fluorescence Microscopy: From Principals to Biological Applications' [48].

## 3.1 Evolution of the Confocal Microscope

### 3.1.1 Reaching the Limits of Wide-field Microscopy...

Conventional wide-field microscopy intrigues with its simplicity: only basic equipment is needed to achieve amazing results in a broad variety of applications. Hence, scientists have tried to evolve this microscope since more than 350 years in order to push its limits even further. The first scientist to use more than a single lens, going away from a simple magnifying glass and constructing the first compound microscope, was Robert Hooke in 1667 [49]. Unfortunately, his microscope was mainly limited by the implemented lenses that were of rather poor quality at that time. Around that time, Antoni van Leeuwenhoek was able to manufacture glass lenses of such prominent quality that the resolving power of his microscopes could be increased significantly. His findings are still considered to be exceptional. From his detailed drawings and descriptions, it is possible to recognize the specimen of bacteria and algae that he investigated [50].

The following milestone in the evolution of microscopy was roughly 200 years later, in 1846, when the exceptionally gifted lens maker Carl Zeiss tried to build a microscope whose resolving power was no longer limited by the available technology. Together with Ernst Abbe, who provided the theoretical description of the diffraction of light, they worked on an already published theory by George Biddell Airy [51]: They showed that the diffraction of light at the objective lens is the most prominent reason for a limited resolution [5]. In the same publication it was shown that this diffraction depended on the angular aperture $\alpha$ of the incident beam after the lens and the index of refraction $n$ of the medium between lens and sample. Here, the term of numerical aperture $NA$ was

formulated for the first time:

$$NA = sin\alpha \cdot n \tag{3.1}$$

In cooperation with Hermann von Helmholtz, Abbe described the smallest distance $\Delta r$ by which objects could still be resolved as:

$$\Delta r = \frac{\lambda}{2 \cdot NA} \tag{3.2}$$

where $\lambda$ is the wavelength of light used for the observation. Lord Rayleigh later expanded this idea by taking into consideration how an ideal point-shaped object would be imaged in 2D space, where its signal (due to the diffraction) gives an intensity pattern described by the point spread function or the so called Airy disk. According to Rayleigh's criterion [52], the minimum distance $\Delta r$ at which two points can still be resolved corresponds to the distance from the centre of the Airy disk to its first minimum:

$$\Delta r = \frac{0.61 \cdot \lambda}{NA} \tag{3.3}$$

A mathematical description of the Rayleigh criterion is given in chapter 3.2.2. An element that wasn't considered at all at that time, due to the lack of recording devices besides the human eye, was the influence of image contrast and photon statistics, i.e. signal-to-noise ratio, onto the resolving power of a microscope. Hence, the signal of two individual point-sources may still be resolvable, although they are closer together than the the diffraction limit, if the dip in-between the two resulting PSFs is still visible. This approach was first presented by the astrophysicist C.M. Sparrow in 1916 [53].

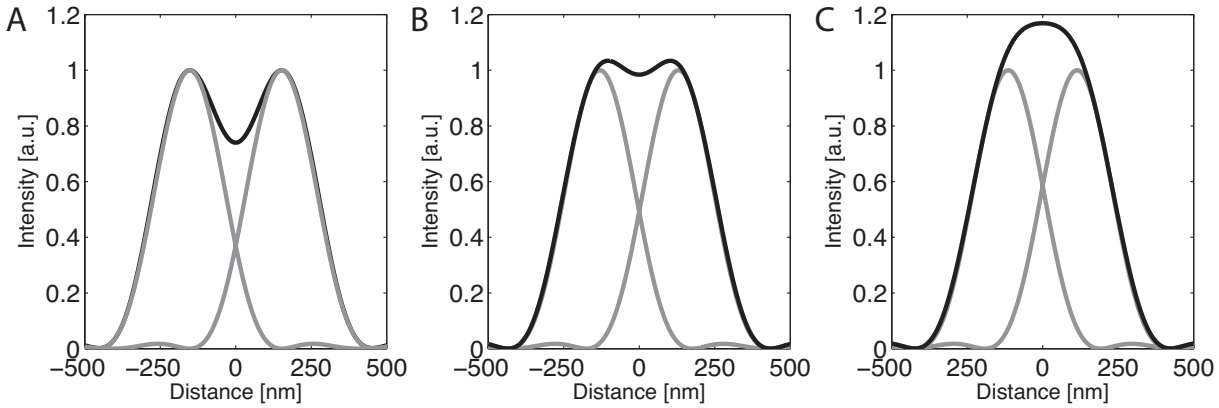


Figure 3.1: Comparison of Rayleigh and Sparrow criterion. Two individual PSFs (grey) sum up, resulting in a total intensity distribution (black) A) Rayleigh criterion: two objects are still resolvable if the two maxima are placed at least 0.5 Airy Units apart. B) Sparrow criterion: two objects can be resolved as long as a dip between the two maximum of the PSFs is detectable. C) the two individual PSFs sum up to a single, but broader maximum, making detection of the two underlying maxima impossible.

Figure 3.1 compares the criteria mentioned above. While the two objects on panel

A) fulfill the Rayleigh criterium, and the maximum of one Airy pattern is placed in the minimum of the second, the panel in the middle shows that although the Airy patterns move closer to each other, the dip in between is still distinguishable. Panel C) shows the case where the distance is so small that the resulting function only shows one maximum and the structure is not resolvable anymore.

As seen by this example, contrast plays a crucial role in wide-field microscopy. There are several reasons why the resolving power is diminished: excitation in wide-field microscopy occurs throughout the whole sample, if the sample is transparent. The recorded image on the detector will therefore not be restricted to in-focus light, but signal from the whole specimen will contribute to the image. Another contributing factor is the Tyndall effect [54], especially for heterogenious samples like biological marterial: when the sample contains particles in the size of the wavelength used for illumination, these particles can scatter the light and redirect it towards the detector. Since these photons are originally coming from out-of-focus-areas they contribute to background noise, decreasing the contrast.

In the end, it was not only the wave-optical resolution limit, but especially the poor contrast of wide-field microscopes that made it obvious that new ways to increase the image quality had to be found in order to make microscopy more applicable.

### 3.1.2 ...And Going Beyond with the Evolution of Confocal Microscopy

A crucial step in order to improve the performance of light microscopy was undertaken roughly 100 years after Carl Zeiss in the late 1950s by the American mathematician Marvin Minsky. He developed a new type of microscope known as the *confocal microscope.* Although he is more known for his numerous and seminal works on artificial intelligence, it was actually his research on brain tissue that made him start to think about a way to improve optical microscopy. Misky's original intention was to study the functional principle of the human brain. He realized that microscopy on this relatively dense tissue was very difficult with conventional light microscopes due to the high image background that arises from the reasons mentioned above. In his new approach, he realized that illuminating the whole sample at once had to be replaced by illuminating the sample point-by-point and detecting the signal in the same manner. The solution for this problem was to overlay a focussed illumination spot with the region of interest in the sample and the detector - all three objects had to be in focus, or *con-focal.* This confocality was achieved by implementing pinholes in the excitation and detection path and thus blocking all light that was not originating from the desired focal plane. It was the implementation of the pinholes that lead to an amazing increase in contrast for images. The first prototype was presented in 1958 and a patent granted to Minsky in 1961 [55]. The light path and a

construction scheme is shown in figure 3.2.

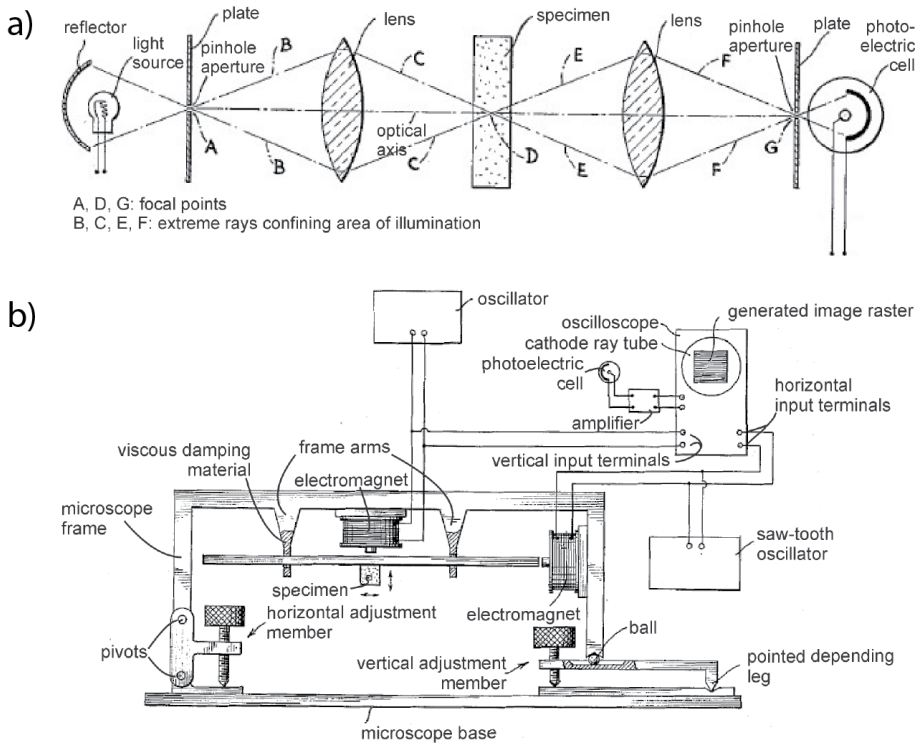


Figure 3.2: Confocal microscope prototype by Minsky, after [55]: (a) Optical beam path, (b) scanner construction

For the sake of integrity, it should be mentioned that there already existed a non-imaging scanning microscope that was built by the Japanese scientist Hiroto Naora in 1951 [56] for spectroscopic studies on nucleic acids. This instrument was only able to measure spectra and did not offer the possibility to record images.

Both systems had little success in the following years, a fact that can be largely attributed to the limited technical equipment available. The lack of coherent light sources and dichroic mirrors forced these early pioneers of confocal microscopy to accept several compromises: lasers only became available a decade later, high energy lamps had to be used. The best lamp at that time was a carbon arc lamp, but this light source required high maintenance efforts. Therefore, Minsky settled for an alternative and used a zirconium arc lamp in his setup.

Another severe drawback of confocal microscopy was its necessity to scan: in the absence of modern detectors like CDDs or APDs and fast scanners as we know them today, a compromise had to be found between a reasonable scanning performance and a sufficient pixel dwell time. The detection was based on a photomultiplier tube whose signal was made visible on the screen of a long-persistence radio oscilloscope. The foremost advantage of this particular method was that a whole image of the sample was visible at once, although it faded after a couple of seconds. To image the whole region of interest on the screen at once, very short dwell times had to be accepted due to the slow scanning

process. This resulted consequently in a decrease of image quality. Minsky mentioned once that *"In retrospect it occurs to me that this concern for real-time speed may have been what delayed the use of that scheme for almost thirty years."* [57]. He noticed further that his invention may have gotten a better start if he had used slower scan speeds, accompanied with a film to permanently record and store the acquired images.

In the following decades, technical advances helped confocal microscopy to obtain more and more acceptance in the scientific community. On the excitation side, especially the invention and availability of the first lasers in the 1960s has to be noted. They offered a bundled, high energetic, monochromatic and coherent light source that was effectively able to excite fluorescent samples. On the detection side, the development of the first dichroic mirrors in 1967 [58] decreased the complexity of the beam path greatly. With this technical advancement, it became possible to move away from the two-objective assembly that Minsky had to use (see figure 3.2), and allowed the use of only one objective for excitation and fluorescence detection at the same time. This had two effects: manufacturing costs decreased and the stability of the optical system increased.

Another challenge was inherent to the scanning process itself. While Minsky chose the slower option of moving the sample, a technique which is still used due to its wide applicability and the stability of the beam path, two different approaches have come into operation in the meantime. In the first approach, the laser beam used for excitation is moved over the sample with the help of galvanic mirrors (a variation of a classic galvanometer where a mirror can be moved by electric current), which allows very fast and accurate scanning. The second approach, the so called spinning disk confocal microscope (SDCM), was first presented by Egger and Pétran in 1967 [59]. They used an array of pinholes instead of a single one, placed on a spinning disk. Hence, they were able to scan several points of the image at the same time, increasing the speed of the scanning process up to video rate. Egger and Pétran successfully used their system to observe unstained cells and cell processes in brains of living, but anesthetized, salamanders.

This first work in practical application of confocal microscopy was followed by a steady progress in the development of the confocal microscope for another two decades. In 1987, two key publications meant the final breakthrough for confocal microscopy: The first work, published by John White *et al.* [60], showed the difference between conventional widefield and confocal microscopy. The images of various cells and larger tissue parts, repeated in this laboratory and displayed in figure 3.3, featured considerable improvement in contrast and resolution for the confocal microscope.

Here, it becomes clear that the widefield image shows only a cell without distinct features, while, in the confocal image of the same cell, it is apparent that the cell is undergoing mitosis.

In the second work, van Meer *et al.* [61] showed that it is not only possible to study structures in fixed cells, as in White's work, but that confocal microscopy is also suitable

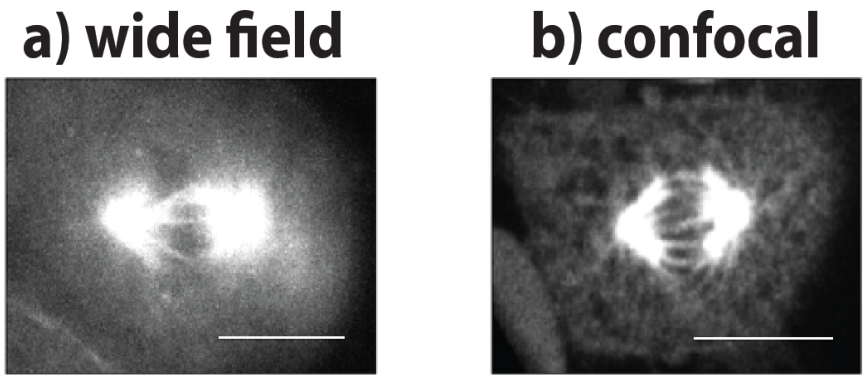


Figure 3.3: Conventional (A) and confocal (B) image of mitotic spindles in HeLa cells, the bar corresponds to 1µm, experiment repeated from [60].

to observe dynamic processes in living cells. They proved this by following the pathway of sphingolipids in epithelial cells.

Summarizing all the developments mentioned above, confocal microscopy has emerged as a powerful tool in the life sciences. It offers optical sectioning of the sample, and better contrast of the images at nearly the same imaging speed as conventional widefield microscopy. These features, along its applicability to *in vivo* microscopy, has made the confocal microscope into an integral part of the world of fluorescence microscopy.

## 3.2 The Theory of Confocal Microscopy

### 3.2.1 The principle of confocal microscopy

Confocal microscopy is based on the principle that all light has to pass through a pinhole before it reaches the detector. The idea behind this obstacle in the detection path was to create a small and very well defined detection volume. Hence, Minsky was able to reduce the out-of-focus light and increase the signal-to-noise ratio dramatically compared to bright-field methods. The schematic illustration of the beam path of a modern confocal scanning laser microscope is shown in Figure 3.4.

The first confocal microscopes suffered from the disadvantage that the loss of photons was rather drastic. Nowadays, this can be compensated with the use of lasers as excitation sources. This coherent light passes through the dichroic mirror that splits excitation light (green lines in figure 3.4a) and fluorescence (yellow lines). In the case of a beam scanning confocal microscope, the laser light is reflected by two mirrors that can be moved perpendicular to each other. Thus, the beam can be scanned in two dimensions. As a direct consequence to the movement of the beam, two identical lenses or a telescope have to be installed, where the second mirror is in focus of the first lens and the objective back focal plane is in the focus of the second lens. This is necessary because a movement of the mirrors results in stationary beam at the objective with only its incident angle varying (see figure 3.4b). Since the objective can be simplified as a normal lens, this change of angle results in a displacement of the focus, allowing to translate angular movement from the morrors into parallel displacement of the focus and, hence, a rastering of the focus over the sampel. The excitation beam passes through the objective and excites a spot of the specimen depending on the angle of the two mirrors.

Fluorescence generated out of the confocal volume, is not confocal with the pinhole and therefore its focus is before or behind the pinhole. This is illustrated in figure 3.4a) as the dashed, violet lines. The photons from the diffraction limited focus are collected with the same objective and pass in the identical angle through the telescope and the scanning mirrors. The dichroic mirror splits fluorescence and back scattered laser light through their different wavelengths. Accordingly, the beam is focused onto the pinhole. Here originates the advantage of confocal systems: fewer of photons are collected, but the amount of photons from out-of-focus regions passing through the pinhole is drastically reduced. This leads to a very high contrast and a high signal-to-noise ratio. As figure 3.4b) shows, the beam is collimated after the pinhole and can be separated by polarization and wavelength (indicated by the two hyphens) before it is focused onto a detector.

The detailed assembly of the confocal setups used in this thesis is given in chapters 5.1 and 5.2.

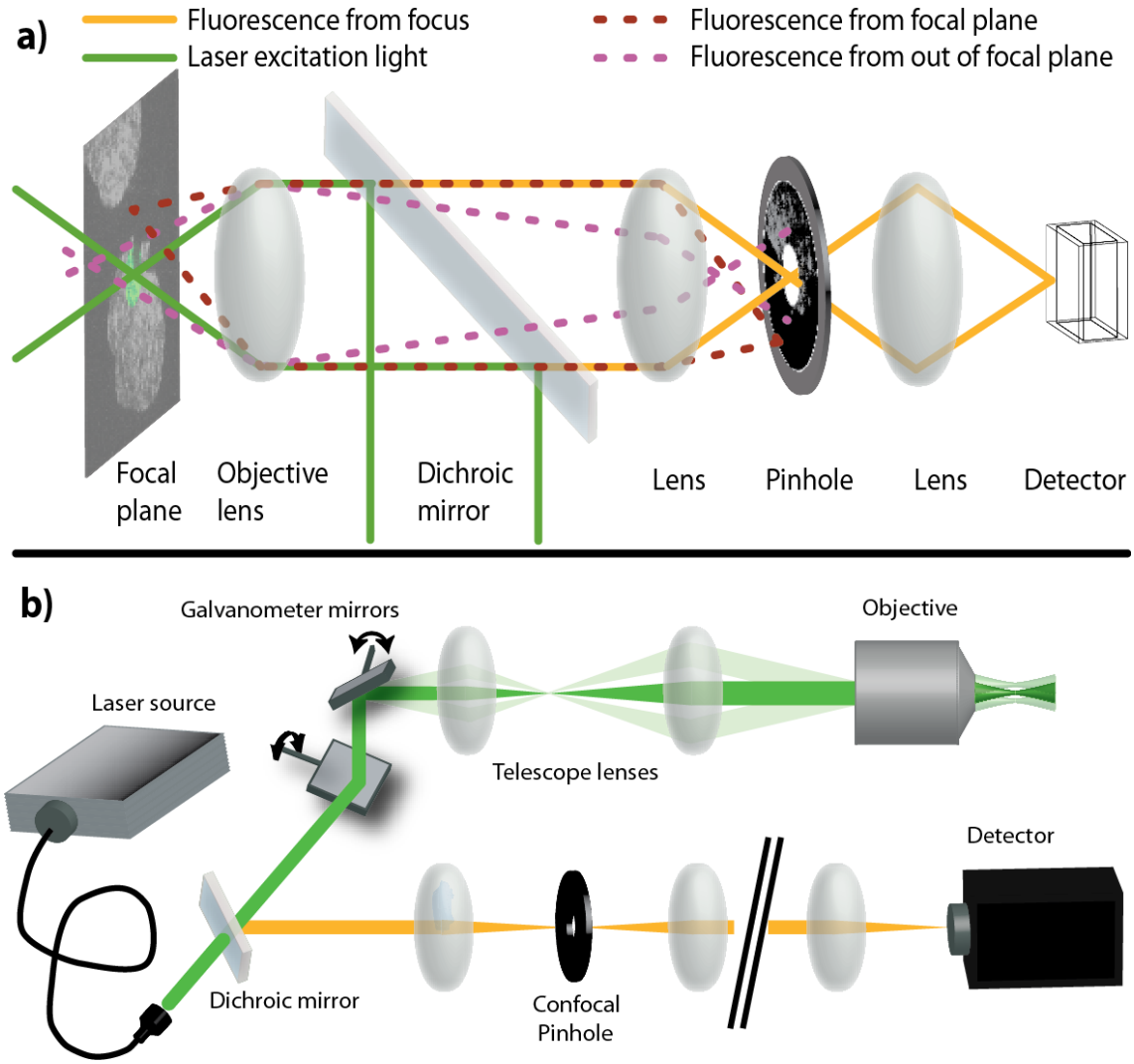


Figure 3.4: a) Principle of the function of the confocal detection pinhole: light originating from the excitation beam in the focal plane will pass through the pinhole and reach the detector whereas light originating from positions adjacent to the focal spot or from a different focal plane will be cut out by the pinhole. b) Principle of a Laser scanning confocal microscope. The excitation beam is deflected using two mirrors into the objective. The position of the beam at the back aperture of the objective is stationary during scanning and only the angle of the beam with respect to the objective changes during scanning, leading to focusing of the laser at different positions within the focal plane. The collected light is collimated with the same objective and guided back over the two mirrors, such that there is no divergence of the detection path upon reaching the confocal pinhole.

### 3.2.2 Radial and Axial resolution and the impact of the pinhole

In general, the resolution of a system is the minimum distance between two zero-dimensional (point) objects where they are still distinguishable. Abbé himself defined the minimum distance in a periodic grating, $d_{min}$, where not chromatic or spherical aberrations of the lenses are the limiting factor but diffraction itself, as:

$$d_{min} = \frac{\lambda_0}{NA_{objective} + NA_{condensor}} \tag{3.4}$$

where $\lambda_0$ is the wavelength of the light used, and $NA_{objective}$ and $NA_{condensor}$are the numerical apertures of the objective and condenser, respectively. The numerical aperture is the product of the index of refraction $\eta$ of the medium between objective and specimen ($NA_{objective}$) or between condenser and specimen ($NA_{condensor}$) and the sine of the half-angle $\theta$ of the maximum cone that is collected by the objective or exits the condenser:

$$NA = \eta \cdot sin\theta \tag{3.5}$$

Due to diffraction at a lens that doesn't have an infinite $NA$, a zero-dimensional point-object will not result in a point at the detector but rather in a bright, round spot in the middle, accompanied with a series of concentric bright and dark rings around it. This pattern is called the *Airy disk*. In general, the response of an optical system to luminescent point source is called the point spread function (PSF), illustrated in figure 3.6.

For a point source imaged using two perfect lenses, the Airy disk is the PSF. The Airy Pattern is given by:

$$I(r) = I_0 \cdot \left[\frac{2 \cdot J_1(2\pi r NA/\lambda_0)}{2\pi r NA/\lambda_0}\right]^2 \tag{3.6}$$

For confocal microscopy, the Airy disk has to be convoluted with the cutoff caused by the pinhole to gain the correct PSF. This means that the total PSF for the system is the convolution of both PSFs for excitation and detection which can be expressed by the product of both functions:

$$PSF_{confocal} = PSF_{excitation} \cdot PSF_{detection} \tag{3.7}$$

Figure 3.5 illustrates the Airy function from equation 3.6. It is obvious that, for the sake of simplicity, a Gaussian function can be used as a very good approximation for the Airy function.

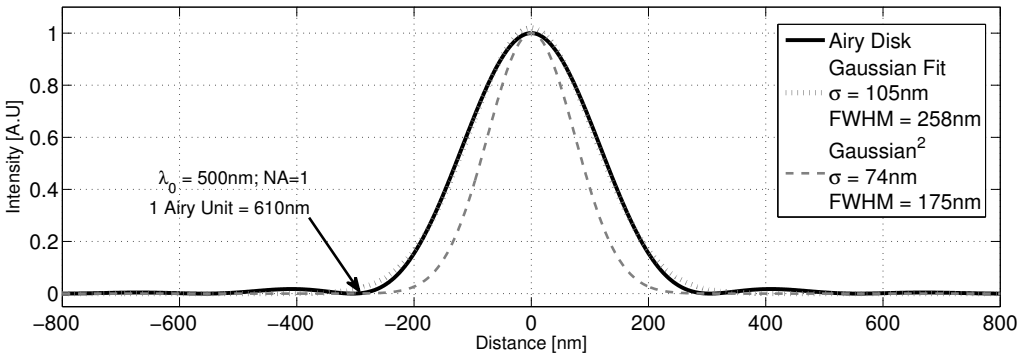


Figure 3.5: Airy function of the PSF and its Gaussian approximation. The Airy function is depicted as black line with the Gaussian fit shown as dotted grey line. The dashed grey line shows the squared Gaussian that results from equation 3.7 and, hence, the the reason for an increased resolution for confocal microscopes by a factor of $\sqrt{2}$ in the lateral dimension, compared to bright field microscopes, if very small pinhole sizes are chosen. For the sake of completeness it is worthy to note that for such small pinholes the SNR decreases radical and, hence, this measure to increase the resolution is rarely taken.

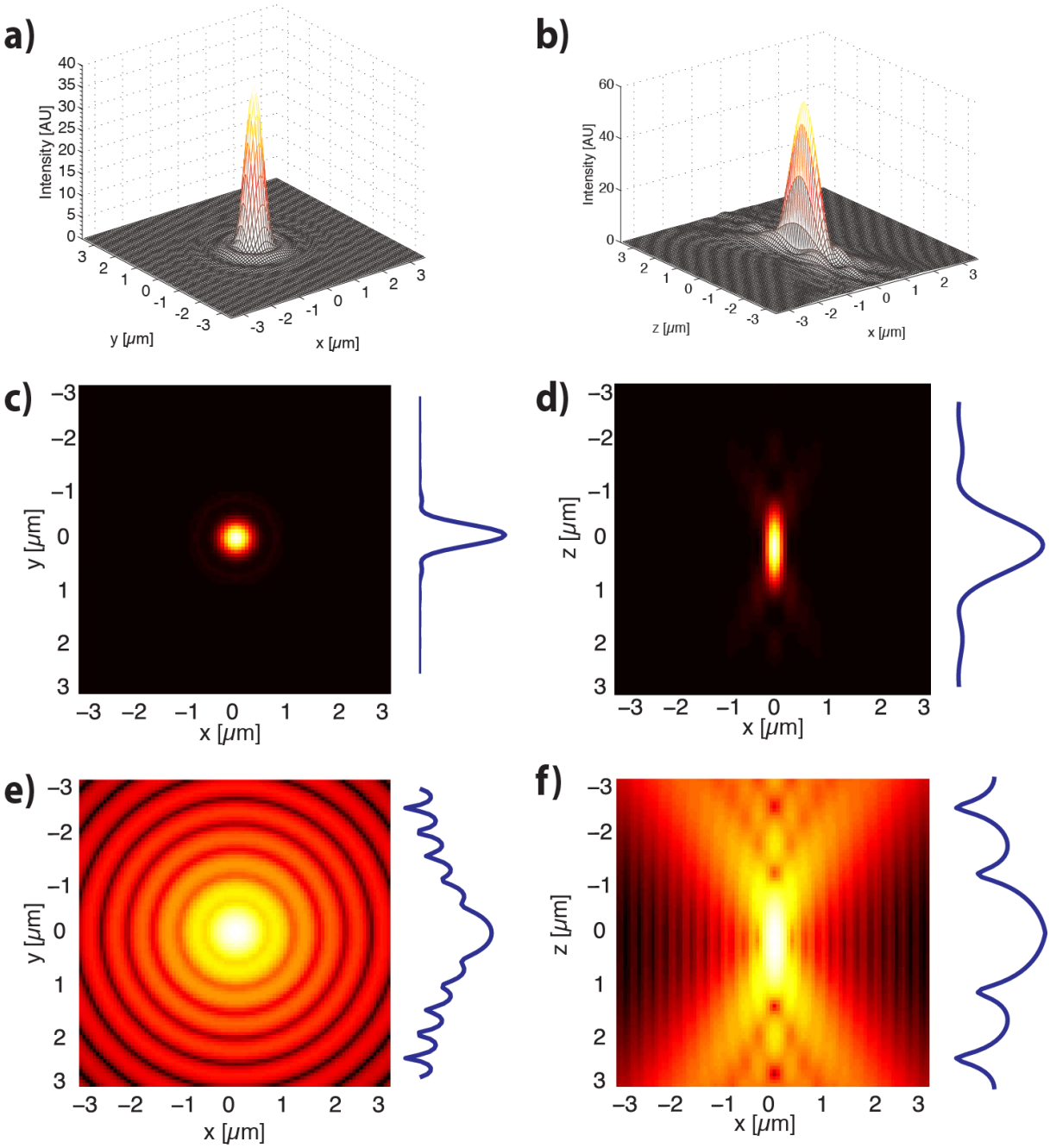


Figure 3.6: Illustration of the diffraction pattern, resulting of an illumination of a point source. Upper row: Cross-section through the middle of the a) $XY$- and b) $YZ$-plane. The middle panel shows projections of intensities in the corresponding planes on a linear scale, c) and d), while the same is shown in the lower panel on a logarithmic scale, e) and f). The plots to the right of parts c) to f) show cross-sections through the middle of the corresponding image.

If we now assume that both PSFs can be described in the simplest case by a Gaussian function to a first approximation, the intensity $I(x)$ at point $x$ for a one-dimensional system will be given as

$$I(x) = I_0 \cdot e^{-\frac{(x-x_0)^2}{2\sigma^2}} \tag{3.8}$$

where $x_0$ is the center of the Gaussian peak, $\sigma$ its standard deviation and $I_0$ the amplitude. Combining equations 3.7 and 3.8 yields the product of two Gaussian, which is in turn again a Gaussian function:

$$I'(x) = I_0^2 \cdot e^{-\frac{(x-x_0)^2}{2\sigma'^2}} \tag{3.9}$$

with $\sigma' = \sigma/\sqrt{2}$. As equation 3.9 shows, the standard deviation and therefore also the FWHM of the resulting function is smaller than the corresponding FWHM for wide-field microscopes by a factor of $\sqrt{2}$ . If this factor is now inserted into the classical equation for the Rayleigh criterion, this leads directly to the following expression for lateral resolution in confocal microscopy:

$$\Delta x_{confocal} = \frac{1}{\sqrt{2}} \cdot \Delta x_{widefield} \tag{3.10}$$

Since the confocal microscope shown schematically above doesn't use a condenser but illuminates the sample coherently through the objective, the NA of the objective and the condenser are identical. This changes equation 3.4 to:

$$r_{lateral} = 0.61 \cdot \frac{\lambda_0}{NA_{objective}} \tag{3.11}$$

where $r_{lateral}$ is the distance of the maximum of the Airy disk to the first minimum. This distance is referred to as 1 Airy Unit (AU). The radius of the Airy disk can be calculated when the result from the last equation is multiplied by the total magnification of the instrument, i.e. the product of the magnification of the objective and the lens system. To obtain the optimal signal-to-noise ratio, the pinhole size should be $\sim 0.85$ Airy Units. By increasing the pinhole size, the brightness of the picture increases, but this effect is accompanied with a loss of definition.

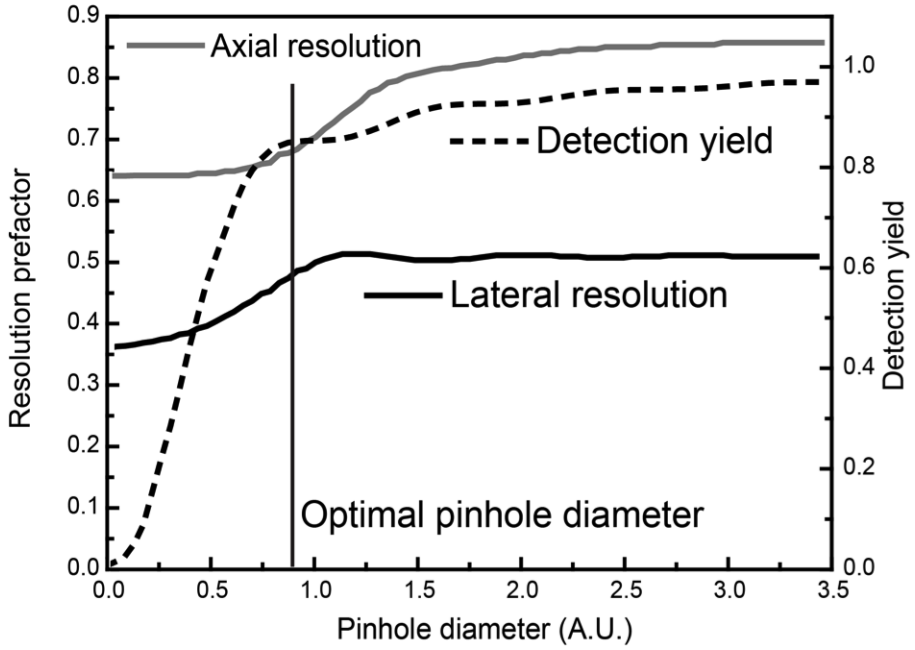


Figure 3.7: Resolution and signal throughput as a function of pinhole size. The solid black and gray lines show how the resolution prefactor changes for lateral and axial resolution, respectively (left scale). This depicts the transition from equation 3.11 to equation 3.12 for lateral resolution and the analog for the transition from equation 3.14 to equation 3.15 for axial resolution. Complimentary, the dotted black line shows the detection yield with increasing pinhole diameter (right scale). The vertical black line shows the best ratio of resolution to detection yield with a pinhole diameter of approximately $0.85AU$.

Figure 3.7 illustrates the dependence of detection yield and resolution on the pinhole size. It also demonstrates the transition from the different resolution prefactors shown in the equations below. It becomes apparent that the best compromise between resolution and detection yield is a pinhole size of $\sim 0.85AU$, where still most of the light is transmitted, but nearly the best resolution along the $Z$-axis is already achieved.

As already mentioned, the pinhole size can be varied to achieve a better resolution and hence can theoretically be downsized to a value infinitely close to zero (in practical approaches to $< 0.25AU$). In this case, the resolution can be improved by a factor of 1.4, since equation 3.11 changes to:

$$r_{lateral} = 0.37 \cdot \frac{\lambda_0}{NA_{Objective}} \tag{3.12}$$

Unfortunately, this advantage in resolution is often lost since the signal-to-noise ratio dramatically decreases and pictures taken with a pinhole that is smaller than 0.25 AU suffer from a very poor contrast. One has to keep in mind that resolution of a conventional wide-field microscope is nearly identical with $r_{lateral} = 0.61 \cdot \lambda_0 / NA_{Objective}$. But, as shown in the next paragraph, the pinhole size has a more significant influence on axial dimension of the Airy pattern, so its main function is to control the optical section thickness rather

than to gain the best possible lateral resolution.

In wide-field microscopy, optical slice thickness is in general not defined with optical elements. Sharp images of biological objects can only be generated if the specimen itself is thin enough; otherwise the sharp image of the focal plane is overlaid with the blurry signal that has its origin above or below the focal plane. The axial resolution in confocal microscopy is a widely discussed topic in the literature.

If the pinhole has a size considerably larger than necessary for the optimal SNR (on the order of $3-5AU$), the width of the detection volume is a result from the excitation diffraction pattern and the geometric-optical impact of the pinhole. Two terms contribute to the FWHM calculation for this case:

$$FWHM_{det,axial,PH>1AU} = \sqrt{\left(\frac{0.88\cdot\lambda_0}{\eta-\sqrt{\eta^2-NA^2}}\right)^2+\left(\frac{\sqrt{2}\cdot\eta\cdot PH}{NA}\right)^2} \tag{3.13}$$

where PH is the absolute size of the pinhole in $\mu m$. The first term, often called the wave-optical term, is constant as long as the corresponding parts at the setup – namely laser and objective - stay the same. The second term under the square root, the geometric-optical term, depends nearly linearly on the pinhole size. The larger the pinhole is chosen, the more prominent the second term gets. On the other hand, this also leads to the conclusion that in the case of a pinhole that has the diameter of $1AU$, the second term vanishes and equation 3.13 changes to:

$$FWHM_{det,axial,PH\cong 1AU} = \frac{0.88\cdot\lambda_0}{\eta-\sqrt{\eta^2-NA^2}} \tag{3.14}$$

when the size of the pinhole becomes very small ($< 0.25AU$), not only does the geometric-optical part of equation 3.13 vanish, but also diffraction effects of the pinhole play a severe role. If this is the case, equation 3.14 changes to:

$$FWHM_{tot,axial,PH<0.25AU} = \frac{0.64\cdot\lambda_0}{\eta-\sqrt{\eta^2-NA^2}} \tag{3.15}$$

In order to give a practical example based on the previous equations, table 3.1 compares the theoretically achievable resolution in wide-field and confocal microscopy assuming an excitation wavelength of $500nm$, a detection wavelength of $520nm$ and the usage of an air immersion objective ($NA = 0.95$, $n = 1$) compared to a high-NA water objective ($NA = 1.27$, $n = 1.33$).

We have not discriminated between excitation ($\lambda_{exc}$) and emission wavelength ($\lambda_{det}$) for the calculations, so far. Due to the Stokes shift, these two are usually separated by 20 to $50nm$. To obtain a result that better matches experimental conditions, $\lambda_0$ has to be replaced by an average wavelength:

| | Widefield (nm) | Confocal (nm) |
|---|---|---|
| NA=0.95, n=1 | | |
| Lateral | 557 | 393 |
| Axial | 4896 | 3348 |
| NA=1.27, n=1.33 | | |
| Lateral | 208 | 147 |
| Axial | 759 | 480 |

Table 3.1: Exemplary comparison of axial and lateral resolution limit for widefield and confocal microscopy. All values were calculated with $PH = 1AU$, $\lambda_{exc} = 500nm$ and $\lambda_{det} = 520nm$. These values were used to calculate the shape of the $PSF$ in figure 3.6. The lower values correspond to the best available water-immersion objectives that are available nowadays. Accordingly, $NA$ and $n$ were changed to 1.27 and1.33, respectively.

$$\lambda_{AV} = \sqrt{2} \cdot \frac{\lambda_{em} \cdot \lambda_{exc}}{\sqrt{\lambda_{exc}^2 + \lambda_{am}^2}} \tag{3.16}$$

While defining the excitation wavelength $\lambda_{exc}$ is easy, since some laser types feature a narrow excitation spectrum of only a few nanometers or are equipped with an appropriate dielectric mirror that narrows down the excitation spectrum, the emission wavelength $\lambda_{det}$ should be weighted by the emission spectrum to obtain the correct average wavelength.

For single molecule studies in solution, it is sometimes useful to work with a larger confocal volume, because it is possible to stretch the time a molecule, for example a globular protein, spends in the observation volume from one millisecond for the diffraction limited spot to the order of 10 to 15 milliseconds. This can be achieved if the back focus of the objective is not fully filled with the laser beam. Working with a spot that is increased due to change in effective $NA$ will result not only in a bigger volume in lateral dimension. It will also change the ratio of axial to radial size from approximately 2, as previously discussed, to a value between 3 and 8, depending on how much of the back aperture of the objective is filled with the laser beam.

## 3.3 Scanning Confocal Imaging

Since confocal microscopy typically uses one or several point detector, it is necessary to scan the PSF with respect to the sample in order to aquire an image. So, in addition to the unique feature of a pinhole, confocal setups have to be equipped with a scanner of some sort when images are to be recorded. Confocal microscopes can be classified by the technique with which the laser samples over the specimen. Whereas the MFD-setup built in the scope of this thesis features only a stationary laser spot that is placed in the sample and hence is only a spectroscopic tool, the STED setup is equipped with both types of scanners. While one scanner, a movable stage, is mainly used for $Z$-positioning, the beam scanner is used to acquire the images in the $XY$-plane. Besides the two most common approaches that are discussed below, other techniques like the early developed objective scanning [62] or slit scanning [1, 63] still exist.

### 3.3.1 Stage scanning

The simplest and most straight forward idea, also implemented successfully by Minsky in his first confocal microscope, was to leave the optics stationary but rather to move the sample and measure the intensity of the fluorescence for a certain amount of time and move then on to the next point. This technique is still widely used, especially in material science, and offers several advantages: the scanning can be very precise due to modern Piezo-scanners that offer a resolution on the sub-nanometer level. Piezo scanners allow the sample to be moved in all three dimensions in space. This is necessary if the main advantage of the confocal microscope, the superb resolution in the $Z$-direction compared to wide-field microscopes, is to be exploited and, for example, a 3D image of cell is recorded. However, this method also suffers from several drawbacks: biological samples are often sensitive to movement and the recorded image may be distorted due to wobbling of the specimen. Additionally, it is not possible to interact with the sample easily, for example to manipulate the sample with micropipettes. One should also consider that moving a sample is always slower than moving the beam as explained in the next section.

### 3.3.2 Laser scanning

The idea of leaving a sample stationary and instead raster scanning the beam over the sample is actually older than the idea of the confocal microscope [64]. It was first in 1987 that White *et al.* successfully combined the techniques of laser scanning and confocal microscopy [60]. The method of single-beam scanning, in contrast to, for example, spinning-disk-microscopy, uses a pair of galvanometric mirrors that are controlled by the acquisition software in order to move the beam in the $X$- and $Y$-directions. Figure 3.8 b) shows one possible line-up where the focus of the telescope is placed at the second

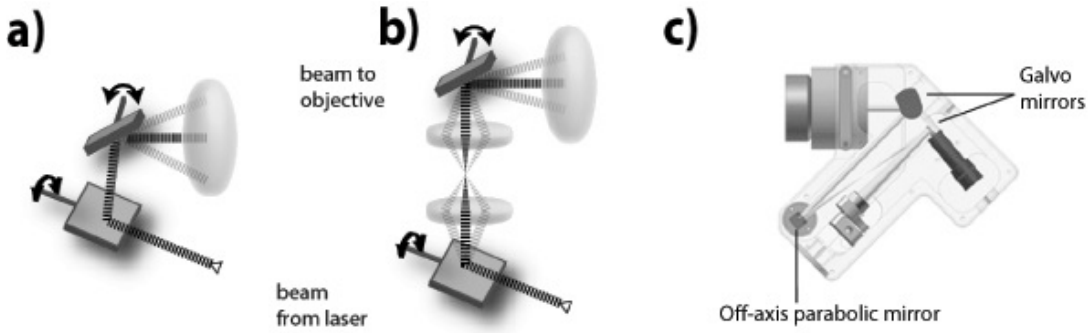


Figure 3.8: Beam scanner configurations: a) Standard way of using two galvo mirrors for scanning that induces aberrations due to the fact that only one of the galvo mirrors is in focus b) Inserting a telescope between the two scanning mirrors and focusing onto the scanners is the solution to work without any aberration caused by the scanning mirrors c) Using a off-axis parabolic mirror to project the image of one mirror onto the other (patent by Till Photonics, Gräfelfing)

mirror. This, together with placing the focus between the two mirrors or directly on one mirror (figure 3.8a) is often the only possible way to use such a scanning device since both mirrors are often assembled as one piece. A problem that occurs when this type of scanning device is chosen is that the focus of the second lens is not necessarily placed in the back aperture of the objective and therefore might cause aberrations. Figure 3.8 c) shows a solution that allows perfect alignment of the moving laser beam. Here, the two mirrors are spatially de-coupled and each of the mirrors is in-focus.

As already mentioned above, the biggest drawback of stage scanning, the very low acquisition speed, can easily be overcome when moving the laser beam rather than the sample. This allows scans speeds near video rates. To gain this advantage, one has to live with the fact that the beam is most of the time off-axis. This bears the problem that not only spherical- and chromatic aberrations from the optics have to be accounted for, but rather the fact that the outer regions of the lenses suffer usually from poorer quality.

## 3.4 Confocal Deconvolution

In every microscope, distortions will occur due to the fact that the picture, which arrives at the camera or is created through scanning, is convoluted with the point spread function of the system. Mathematically, the convolution for two functions $f$ and $g$ is defined as:

$$(f * g)(x) := \int_{R^n} f(\tau)g(x-\tau)d\tau \tag{3.17}$$

It is possible in confocal microscopy to determine the PSF, so it is also possible to deconvolute the picture and therefore decrease the fuzziness of the image. An example is shown in figure 3.4.

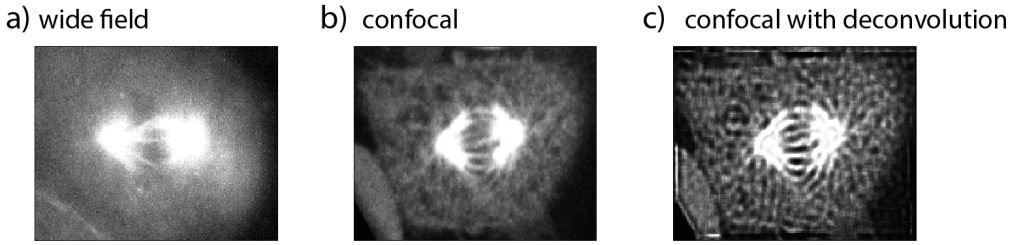


Figure 3.9: The affect of deconvolution. a) A standard wide field image of a tubulin labeled cell undergoing mitosis. b) A confocal image of the same cell as shown in a). c) The same image as shown in b) deconvoluted using the Richardson-Lucy algorithm.

For this example, the Richardson-Lucy algorithm was used [65, 66]. Every single pixel $d$ in the image is a product of the PSF $p_{ij}$ (that is the light intensity detected at location $i$ but originating from location $j$) and the original latent image intensity at pixel $u_j$:

$$d_i = \sum_i p_{ij} \cdot u_j \tag{3.18}$$

If $u_j$ is Poisson distributed, which is correct when the dominant noise source is the photon noise, one can iteratively calculate the most probable value for $u_j$ when all other parameters from equation 3.18 are known:

$$u_j^{(t+1)} = u_j^t \sum_i p_{ij} \cdot \frac{d_i}{\sum_j p_{ij} \cdot u_j^t} \tag{3.19}$$

It was shown that, if these iterations converge into a certain value, the result is the maximum likelihood estimation for $u_j$ [67]. Nevertheless, one should be aware that this algorithm can only be applied when the PSF is well characterized. Figure 3.4 c) shows that, especially for the bottom left corner, the PSF might change due to aberrations in the objective and the deconvolution does not yield the correct value for $u_j$ for this part of the image. Alternatively, the expectation-maximization algorithm [68, 69] can be applied, or if the PSF is not known, the method of blind deconvolution is still suitable to enhance the quality of the image [70, 71].

# Chapter 4

# Single-Molecule Methods

The following chapter deals with methods that are either hardware features of the setups descibed later on in this work or data analysis methods used in the applications section in order to gain relevant information about the sample.

## 4.1 Time-Correlated Single Photon Counting

Although Time-correlated single photon counting (TCSPC) is not necessarily restricted to single-molecule measurements, it adds valueable information to every measurement. TCSPC is not only applied in life-sciences, but generally applicable where the lifetime of a molecule has to be measured [72–76]. TCSPC was created due to the need of recording fluorescence decay curves, which were not possible to measure with an analog or digital detection card in the time-domain. The fluorescence decay, being in the range of a couple nano-seconds, was too fast to measure with ordinary instruments: With digital sampling of the arriving photons, it is necessary to have a reasonable resolution within the decay. Hence, the number of detected photons has to be read out at least every 50 pico-seconds, which in turn corresponds to a read-out frequency of $20GHz$. Only the latest equipment comes close to this sampling frequency. A reason against analog detection is the little amount of photons that arrive at the detector: the photons that arrive in each sampling cycle would simply vanish in the noise.

The solution to the stated problems is TCSPC [77]. The principle of TCSPC is shown in figure 4.1.

A periodic, pulsed excitation (as shown in figure 4.1 with 80MHz) is used to sample the specimen over at least a couple of seconds and a histogram of arrival times (see figure 2.4) is generated. TCSPC cards are usually run in reversed start-stop mode: the arrival of a signal from the detector is the start signal, whereas the reference clock, usually the excitation laser or an external clock, serves as stop signal. This has the advantage that the card is only busy when a photon is detected and avoids unnecessary use of the buffer.

Once a photon is detected, the card as well as the detector, go into a state where no

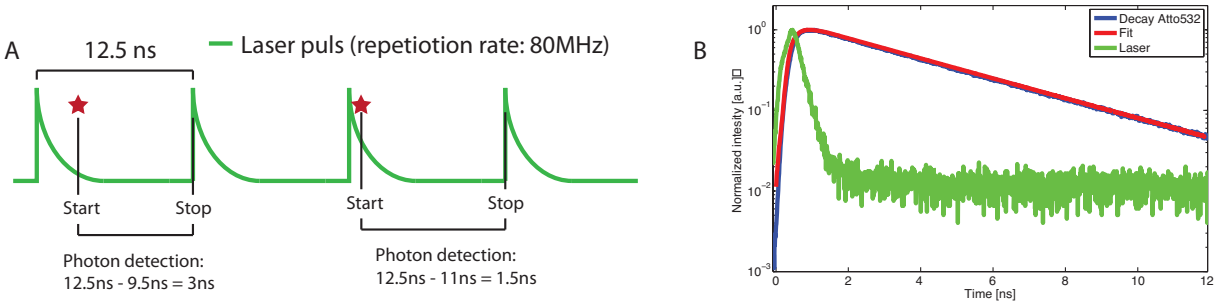


Figure 4.1: The principal of TCSPC in reversed start-stop mode: A) As soon as a first pulse arrives at the detection card - triggered by an arriving photon at the detector - the card starts measuring the time until a stop signal is detected, usually send by the excitation laser or an external clock. This time is then converted back into normal timing and in B) a histogram of all arrival times is built.

further photons can be detected, i.e. the dead time. Hence, one has to make sure that the probability of a second photon arriving during the dead time is small. As a rule of thumb, it is feasible that the count rate should be not higher than 1/1000 of the excitation laser rate - termed sync rate [78, 79]. When this condition is fulfilled, the created histogram corresponds to a lifetime histogram of the fluorophore, convoluted with the shape of the laser pulse of the excitation source. For the technical implementation on the counting board, the *Becker&Hickl "TCSCP handbook"* gives a detailed description [80]. TCSPC is also used for the implementation of Pulsed Interleaved Excitation (see chapter 4.4) [81].

## 4.2 Fluorescence Correlation Spectroscopy

Fluorescence Correlation Spectroscopy (FCS) is a versatile technique to extract information out of fluctuations in fluorescence intensity. Several detailed reviews can be found in the literature [82–86]. The description of FCS was published in the first half of the 1970s by Madge, Eldon and Webb [87–89]. The method is based on freely diffusing fluorescent molecules, either labeled with a dye or intrinsically fluorescent, that emit a burst of photons when they transit the PSF of a confocal microscope. Only with the development of ultra-sensitive detectors and stable light sources like lasers, together with a small detection volume it did become possible to apply the concepts developed by Madge *et. al* to single molecules. This sensitivity has made FCS easily applicable to a broad range of applications. Figure 4.2 shows the intensity time trace for two molecules with different brightness. While techniques like the photon counting histogram (PCH) [90], fluorescence intensity distribution analysis (FIDA) [91], and cumulant analysis [92] make use of the heights of the fluctuations, FCS uses the temporal changes to extract information from the intensity trace. Generally, FCS is used to extract information about the number of particles in the volume, as well as also the time it takes those molecules to traverse the confocal volume. When the PSF is calibrated and its size and shape known, it is also possible to obtain further information like average concentration [93], hydrodynamic radius [94], kinetic chemical reaction rates [84] and singlet-triplet dynamics with the help of FCS [95].

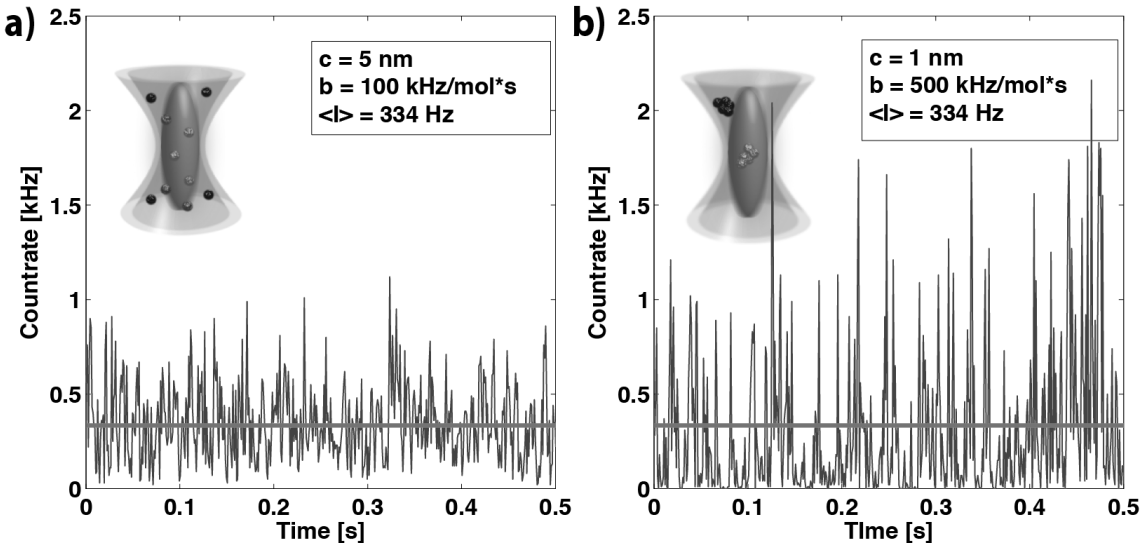


Figure 4.2: a) Simulation of a $5nM$ solution of particles with $100kHz$ brightness and b) a simulation of $1nM$ solution of particles with $500kHz$ brightness.

The concept of correlation analysis is used to determine via statistics the timescale on which two signals resemble each other. An exception is the auto-correlation, where not two, but a single signal is compared to itself. The idea behind this type of analysis is easy

to understand: the signal fluctuations, caused by the diffusion of molecules in and out of the focus, should be stochastically on the same timescale as the duration of a molecule crossing the confocal spot[1]. Hence, on timescales shorter or equal to $\tau_D$ the signal should exhibit a certain "self-similarity". This effect disappears as soon as the number of detected molecules changes and the duration of the self-resemblance contains information about the diffusion time $\tau_D$ of the molecule.

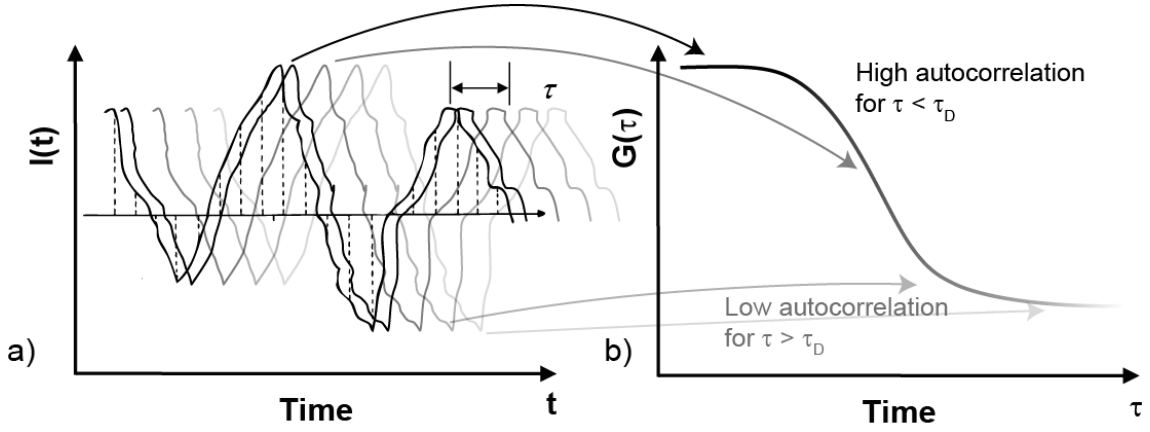


Figure 4.3: Auto-correlation (b) of an intensity trace, fluctuating about a mean value (black horizontal line) (a). The trace is duplicated and shifted by a certain time $\tau$ and for the auto-correlation the self-similarity is analyzed (the similarity decaying from black to grey).

The calculations behind the auto-correlation are moderately difficult, but a very good derivation is given in [96]. For a measurement as described above, with freely diffusing molecules in all three dimensions, the intensity of the fluorescence signal $F$ at a certain time $t$ is given as:

$$F(t) = \epsilon \cdot \int dr \overline{W(r)} \cdot c(r,t) \tag{4.1}$$

where $\epsilon$ is the molecular brightness, $C(r,t)$ is the number density of molecules at a certain position $r$ at a time $t$ and $\overline{W(r)} = W(r)/W(0)$ is the normalized PSF with $W(0)$ as the laser intensity in the center of the PSF. The molecular brightness is defined as:

$$\epsilon = \kappa \cdot \sigma_{Abs} \cdot \phi \cdot W(0) \tag{4.2}$$

where $\kappa$ is the total detection efficiency of the microscope, $\sigma_{Abs}$ is the absorption cross section of the fluorophore at the specific laser wavelength and $\phi$ is the fluorescence quantum yield of the dye. The autocorrelation (ACF) is given as:

$$G(\tau) = \frac{\langle \delta F(t) \cdot \delta F(t+\tau) \rangle}{\langle F(t) \rangle^2} = \frac{\langle F(t) \cdot F(t+\tau) \rangle}{\langle F(t) \rangle^2} - 1 \tag{4.3}$$

[1]The diffusion time $\tau_D$ in $\mu s$ depends on the size of the confocal volume, contrary to the diffusion constant D in $[\mu m^2/s]$.

with $\delta F(t) = F(t) - \langle F(t) \rangle$ and $\langle\rangle$ being the time averaged value. A graphical interpretation of the ACF is shown in figure 4.3. During the correlation analysis, the signal is shifted by different time intervals $\tau$, multiplied with the original curve and integrated over the fluorescence trace. The correlation analysis is normalized by the square of the average fluorescence intensity and, depending on the applied correction, one is subtracted. The PSF of a confocal microscope can be approximated as a three-dimensional Gaussian:

$$W(r) = W(0) \cdot e^{-\frac{x^2+y^2}{2\omega_r^2} - \frac{z^2}{2\omega_z^2}} \tag{4.4}$$

where $\omega_r$ and $\omega_z$ are the dimensions of the PSF from the center to the position where the intensity has decreased by a factor of $1/e^2$ in the lateral and axial directions respectively and $W(0)$ is the laser intensity at the center of the PSF. Substituting equation 21 into equation 23, we obtain an analytical form for the ACF of a freely diffusing particle:

$$G_D(N, D, \tau) = \frac{\gamma_{FCS}}{\langle N \rangle} \cdot \left( \frac{1}{1 + \frac{\tau}{\tau_d}} \right) \cdot \left( \frac{1}{1 + \left( \frac{\omega_r}{\omega_z} \right)^2 \cdot \frac{\tau}{\tau_D}} \right)^{\frac{1}{2}} \tag{4.5}$$

where $\langle N \rangle$ is the average number of particles in the confocal volume, $\gamma_{FCS}$ is a geometrical factor that depends on the shape of the confocal volume and $\tau_D$ is the diffusion time, which is given as:

$$\tau_D = \frac{\omega_r^2}{4D} \tag{4.6}$$

A very intuitive method to interpret the correlation function is as the probability of detecting a photon at a delay time $\tau$ when a photon was detected at the time $t = 0$. For timescales smaller than the diffusion time $\tau_D$, the molecule still remains in the confocal volume, so the probability of detecting a second photon is high. At longer timescales, this probability decreases since the molecule will diffuse out of the confocal volume, driven by Brownian motion. No further photon from this molecule will be detected, unless it diffuses back into the focus [97]. The ACF can be used to point out any correlating behavior in the signal. But the main applications are the determination of concentration and diffusion coefficient of freely diffusing molecules. A correlation analysis of the photon time trace in general is powerful as it is capable of detecting any type of fluctuation in fluorescence intensity that is not stochastic, i.e. correlated. Examples of processes that can be detected using FCS are shown in Figure 4.4.

A full correlation of a fluorescence signal will not only consist of the diffusion term, but can also include the triplet state of the fluorophore, rotational motion and photon antibunching. Fortunately, these influences take place at different time scales and are distinguishable, as figure 4.4 shows.

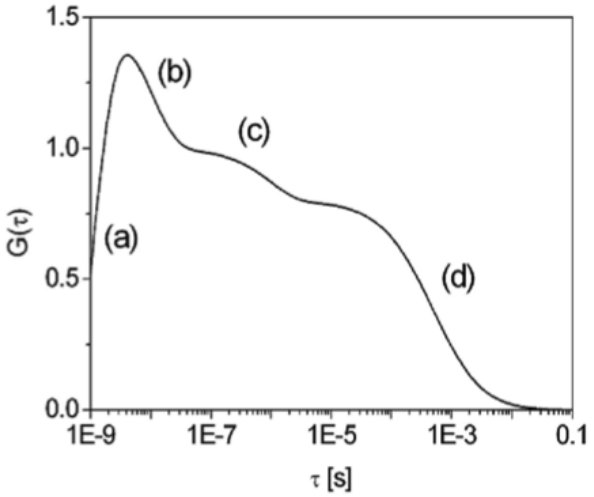


Figure 4.4: The Autocorrelation Function: A number of processes can be detected by FCS as shown schematically in the ACF: (a) antibunching, which emerges because the fluorophore has to be excited again before emission of a second photon, (to detect antibunching, two detectors are necessary to avoid the dead time of detectors and data collection card.) (b) rotational diffusion, (c) intra-molecular reactions like transitions between the singlet to the triplet states and (d) translational diffusion.

## 4.3 Fluorescence Cross-Correlation Spectroscopy

When considering the self-similarity of a signal, as done in FCS, the next logical step follows immediately: the comparison between two signals that are not *per se* identical. This method is known as cross-correlation, first described in 1994 [98] and experimentally realized in 1997 [99]. Two detection channels, e.g. sensitive to different wavelengths, are used and the fluorescence signals from the two channels are cross-correlated. This method of dual-color Fluorescence Cross-Correlation Spectroscopy (dcFCCS) is well suited for investigating the interaction of molecules [84, 100–102]. It is also possible to excite two fluorophores with one laser and, hence, have only separated detection channels. This modality of FCCS is known as single-wavelength FCCS (swFFCS) [103, 104].

The cross-correlation function (CCF), $G_x(\tau)$, for two channels $i$ and $j$ can be calculated analogous to the auto-correlation from equation 4.3:

$$G_x(\tau) = \frac{\langle F_i(t) \cdot F_j(t+\tau) \rangle}{\langle F_i(t) \rangle \cdot \langle F_j(t) \rangle} \tag{4.7}$$

where $F_i(t)$ and $F_j(t)$ are the corresponding fluorescence intensity signals for channel $i$ and $j$ at the time $t$, respectively. Figure 4.5 shows the auto- and cross-correlation of double-stranded DNA that is labeled on one strand with Atto532 and on the second strand with Atto647N. The strong cross-correlation is expected as the DNA is double-labeled with high efficiency and a fluctuation in the green channel due to a DNA molecule entering the confocal volume will be correlated with an increase in signal in the red channel, due to the presence of the red label.

The number of double-labeled molecules, $\langle N_{12} \rangle$, can be extracted from the amplitude of the cross-correlation function. Assuming two overlapping, 3D Gaussian confocal volumes and a cross-talk free system, the CCF is given by:

$$G_x(N, D, \tau) = \frac{\gamma_{FCS} \cdot < N_{12} >}{< N_1 + N_{12} > \cdot < N_2 + N_{12} >} \cdot \left( \frac{1}{1 + \tau/\tau_D} \right) \cdot \left( \frac{1}{1 + \left(\omega_r/\omega_z\right)^2 \cdot \tau/\tau_D} \right) \tag{4.8}$$

where $\gamma = 2^{-3/2}$ is The ACF can be used to point out any correlating behavior in the signal. But the main applications are the determination of concentration and diffusion coea geometrical factor when the PSF is approximated with a 3D Gaussian, $N_Y$ is the number of molecules of type $Y$, where $Y$ can be single-labeled particles visible in channel 1 (i.e. $N_1$), channel 2 ($N_2$) or double-labeled particles, visible in both channels ($N_{12}$). $\omega_r$ and $\omega_z$ are the lateral and axial dimensions of the PSF[2]. The diffusion time $\tau_D$ is given as:

$$\tau_D = \omega_r^2 / 4D_{12} \tag{4.9}$$

[2]The size of $\omega_r$ and $\omega_z$ is usually considered from the center of the focus with the maximum fluorescence intensity till the intensity has decayed to $1/e^2$ of the maximum in lateral ($\omega_r$) and axial dimensions ($\omega_z$).

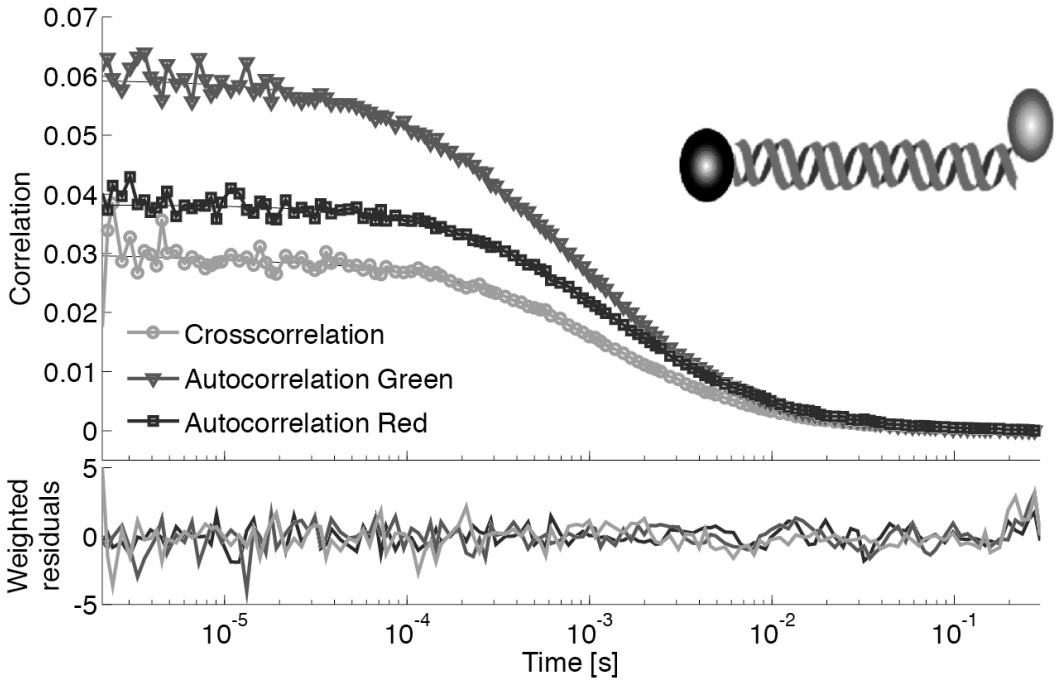


Figure 4.5: Cross-correlation of a double-labeled DNA-molecule. Double-stranded 60 base-pair DNA was labelled at its ends with Atto532 and Atto647N. The auto-correlation functions for Atto532 (dark grey, triangles), Atto647N (black, squares) and corresponding cross-correlation function (light grey dots) are shown. The weighted residuals are shown in the panel below the curves for each correlation curve in the corresponding color.

with $D_{12}$ being the diffusion constant of the double-labelled species. As already stated by Abbe's law, the size of the confocal volumes will depend on the wavelengths used for the excitation of the fluorophores. This means that in the best case the PSFs for channel 1 and 2 will be concentric, but differ in size. In this case, the effective cross-correlation volume $V_X$ is given by the geometrical average of the detection volumes $V_1$ and $V_2$:

$$V_x = (\pi/2)^{2/3}(\omega_{r,1}^2 + \omega_{r,2}^2) \cdot (\omega_{z,1}^2 + \omega_{z,2}^2)^{1/2} \tag{4.10}$$

Although the CCF is often used as a digital answer to a problem – whether or not two molecules interact - the amplitude of the CCF itself and its relative height to the auto-correlation amplitude contains information regarding the percentage of complexes carrying two fluorophores. A detailed description of how to perform quantitative analysis of FCCS data, in particular with fluorescent proteins, is given in chapter 7 and [105]. Since barely any optical microscope is truly cross-talk free, the next section will illustrate one way to recover the correct amount of cross-correlation in presence cross-talk and even FRET.

## 4.4 Pulsed Interleaved Excitation in Confocal Microscopy

The sensitivity of FCCS can be further enhanced with the use of pulsed interleaved excitation (PIE) [106–108]. By synchronizing the excitation lasers and delaying the respective lasers pulses by 12 to 20$ns$ (4-5 times the fluorescence lifetime of the dyes used), it is possible to assign every detected photon to its excitation source (figure 4.7a). The detected photons can be recorded using a counting board that is synchronized to the excitation lasers [109]. A more elegant possibility for data collection is to use time-correlated single-photon counting detection, which has the additional advantage that it is possible to generate and analyze the fluorescence lifetime histograms of the fluorophores. In this case, the fluorescence lifetimes of the fluorophores can be determined and the presence of quenching, for example due to FRET, can be determined. Figure 4.7b shows the ACFs and CCFs for two non-interacting fluorophores in solution. Crosstalk of the Atto532 signal into the Atto665 channel gives rise to a residual cross-correlation amplitude in the CCF. Spectral crosstalk arises from the long tail of the fluorescence emission spectrum of the green fluorophore that is detected in the red channel, shown in figure 4.6.

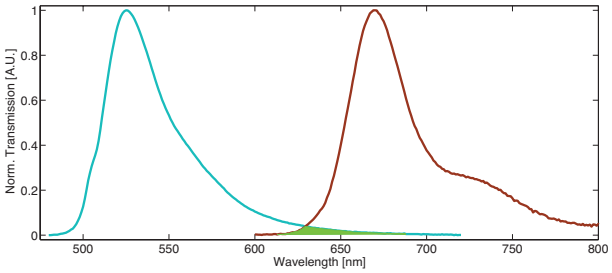


Figure 4.6: Spectral cross-talk: too far red-shifted photons (green area und the curve) are detected after spectral seperation in the incorrect detection channel.

In addition to the CCF, crosstalk also affects the amplitude of the red ACF. Spectral crosstalk cannot be totally suppressed in the red channel using the appropriate emission filter without significantly decreasing the sensitivity of the system to the red fluorophore. When green and red laser are delayed by $\sim$ 20$ns$, the effect of the spectral crosstalk can be removed by cross-correlating the photons detected in the green channel after green excitation with photons detected in the red channel after red excitation (light gold data, Figure 4.7b). The ACF of the red channel after red excitation increases upon removal of the crosstalk photons (red data, figure 4.7b) whereas the amplitude of the green ACF is not affected, even when crosstalk photons (photons detected in the red channel after green excitation) are included in the ACF analysis (light green data, figure 4.7b). In this case, direct excitation of Atto665 with the 530 nm laser is negligible. The crosstalk photons marginally increase the brightness, but the brightness does not influence the shape of the ACF when only a single species is present. The average number of molecules in the volume remains the same and hence the amplitude of the ACF does not change.

This improvement in FCCS is very important for interaction studies on biological samples, since PIE makes it possible to distinguish between a weak interaction of relevant

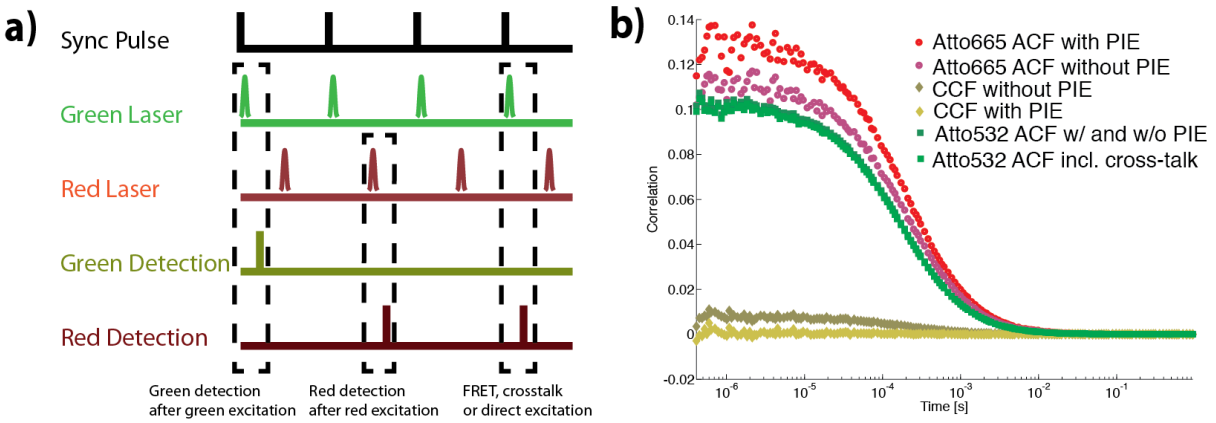


Figure 4.7: Pulsed Interleave Excitation. (a) Schematic principle of PIE and (b) ACF and CCF for Atto532 and Atto665 freely diffusing in solution determined with and without PIE. The influence of crosstalk and direct excitation on the red ACF and CCF can be observed, which is completely removed with PIE.

biomolecules and no interaction at all [110–112]. Since PIE records the detection channel and excitation source for each photon, different channels can be defined *ex facto* and "misplaced" photons can be reassigned to the correct channel. For example, cross-correlating all the photons detected after green excitation with photons detected after red excitation yields cross-correlation functions that can be evaluated quantitatively even in the presence of FRET [105, 108].

The impact of PIE on FRET experiments is explained in section 4.5.

## 4.5 Burst Analysis

Burst analysis is carried out - as all other methods described in this chapter so far - on a confocal microscope with its laser beam stationarily focussed into the aqueous solution of interest [113, 114]. The main difference here is that this method is the first true single-molecule technique. While in the previous described fluctuation techniques usually 1-10 molecules are in the femto-liter sized detection volume, in burst analysis most of the time no molecule is present. This is visible in the time trace of figure 4.8, where clearly separable burst of photons with the length of a couple milli-seconds disrupt the stream of background photons. This is achieved by diluting the sample 10x-100x from the nano-molar regime for FCS or PCH to 5 to 50$pM$.

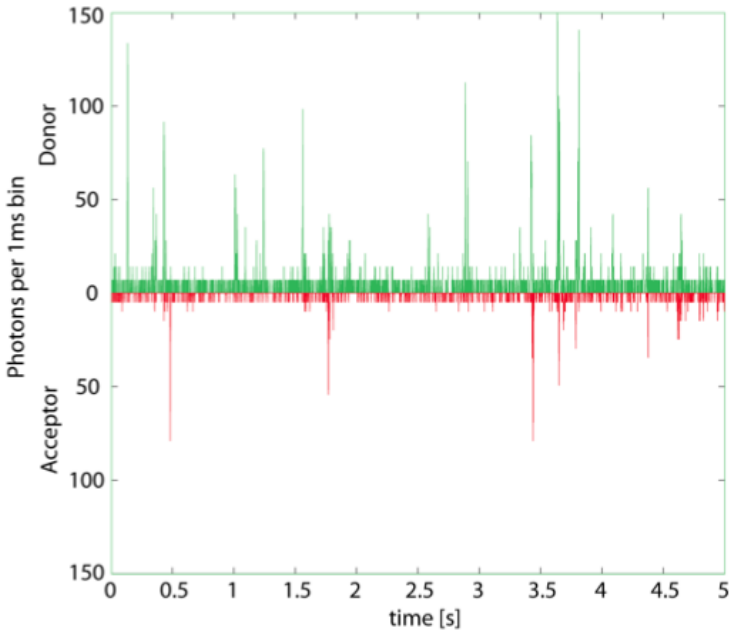


Figure 4.8: Photon time series of a double labelled DNA-molecule. Photons from the donor are represented in green, while photons that are detected in the acceptor channel are represented in red.

Burst Analysis, in general is the ideal tool to carry out single-molecule Förster resonance energy transfer experiments. Since each molecule is probed individually, no averaging can take place and sub-populations within one sample, along with other inhomogeneities are resolved. Each burst represents one molecule and accordingly all available molecular properties, like brightness, diffusion time, anisotropy and FRET efficiency can be calculated[3].

[3]Since the sample is very dilute, it is very likely that two neighboring burst come from the same molecule re-entering the confocal volume and one can even take advantage of these recurrence events [97].

The first challenge here is to correctly identify bursts. The most straight forward analysis is to apply a threshold placed above the background, thus separating the bursts. The disadvantages of this procedure come to mind instantly: for samples that suffer from a bad signal-to-noise ratio due to dim fluorophores or high background countrate, it might be hard to set the threshold correctly. Additionally, the beginning and end of a burst that fall below the threshold are cut off and hence not taken into further consideration. This later problem can at least be solved with the implementation of a second, lower threshold that is applied to both ends as soon as a burst is identified [115].

In this work, the more elegant *all-photon-burst-search* (APBS) algorithm is used [116]. Instead of considering the number of photons per time bin, but rather looking at the time in between arriving photons $\Delta t$, one can detect a strong decrease in the inter-photon time as soon as a molecule enters the outer regions of the PSF. If a few consecutive $\Delta t$ values are below a certain criteria, these photons are marked as belonging to a burst. Thus, a much higher precision for the burst search is achieved using the APBS.

For a FRET measurement, the donor is excited several 100 times while crossing the PSF and emits a burst of photons directly while some photons are transferred to an acceptor molecule that emits a burst of photons, with lower energy, as well. For each of the simultaneously occurring bursts of photons, a transfer efficiency is calculated. The FRET efficiency in its most basic form is defined as the number of transferred - or acceptor - photons $I_{FRET}$ divided by the total number of photons, i.e. those transferred and those emitted by the donor itself ($I_D$):

$$E = \frac{I_{FRET}}{I_{FRET} + I_D} \tag{4.11}$$

This very basic concept is true enough when only changes in FRET efficiency due to conformational changes are of interest. But as soon as the FRET efficiency has to be converted into absolute distances or changes in the chemical environment alter the properties of the dyes attached to the molecule of interest, it is necessary to implement several corrections that allow a more accurate determination of the apparent FRET efficiency.

The most obvious adjustment has to be made due to differences in quantum yield $\Phi$ and detection efficiency $\eta$ of donor and acceptor:

$$\gamma = \frac{\Phi_{Acc} \cdot \eta_{Acc}}{\Phi_{Don} \cdot \eta_{Don}} \tag{4.12}$$

When multiplying the donor photons $I_D$ with the correction factor $\gamma$, a more microscope- and fluorophore- independent result is achieved. $\gamma$ can be calculated with literature values, but is better evaluated directly with the molecule of interest itself [117]. Unfortunately, unlike in TIRF microscopy, it is not possible to correct each single molecule with its own $\gamma$ value. Therefore, one particular correction factor has to be applied to the whole mea-

surement, or, if it is possible to clearly distinguish sub-populations with different $\gamma$ values, treat each subpopulation individually [118, 119].

There are two more sources of error that have to be accounted for: As can be seen from figure 2.2, there is a certain amount of donor fluorescence that is red-shifted in such a manner that it extends into the acceptor emission region. These are called *spectral crosstalk* photons. They can pass the acceptor band width filter and hence are detected in the acceptor channel. In addition, it is also possible to excite the acceptor dye with the blue-shifted donor laser. Rather than transferred via FRET, these photons belong to *direct excitation* and are detected in the acceptor channel as well, despite originating from the donor laser.

For spectral crosstalk as well as direct excitation, it is possible to correct for with extra measurements of donor and acceptor alone to determine the amount of falsely assigned photons. Usually, the amount for both sources of error are each between 2% and 8%, depending of the fluorophore and filter combination used in the experiment. A more elegant way to calculate these contributions is offered with PIE: instead of calculating direct excitation and crosstalk photons in separate measurements, where conditions can vary, PIE offers the opportunity to directly determine both parameters in the analysis process after the measurement.

Combining Burst Analysis with PIE has profoundly increased the number of properties available for the analysis. Not only the lifetime of the dyes, or their anisotropies have added new characteristics for each burst, but also the *stoichiometry* $S$ has had an important impact [106–108, 115, 117, 120]. The stoichiometry $S$ is a counterpart to the FRET efficiency $E$ and allows an estimate of the ratio of donor to acceptor fluorophores attached to the molecule. This makes it possible, for the first time in a FRET histogram, to clearly separate between a low-FRET species and a donor-only population. In the same manner, molecules that only have a fluorescent acceptor that suffer from an ill defined efficiency, can be distinguished and excluded from the analysis[4].

As already explained in chapter 4.4, using PIE will not only offer the information of the channel the photon was detected in, but also the source of excitation, may it be FRET or the donor laser directly. Since the sample is illuminated with two lasers alternatingly, the need for a more precise nomenclature arises: $I_{XY}$ is the fluorescence in channel $Y$ after the excitation laser $X$. For example, the channel $I_{DA}$ contains all photons in the *acceptor* channel after excitation with the *donor* laser, i.e. all crosstalk, direct excitation and FRET photons. When taking the correction for crosstalk $\alpha$, the direct excitation $\beta$,

[4]In principle, it is also possible to get rid of donor-only and acceptor-only molecules with the *dual-channel-burst-search* (DCBS) [121], but this algorithm not only underestimates and discards low-fret molecules but also removes the molecules in such a way that no later control is given to whether this analysis was done correctly or not. Additionally, molecules with very low or very high FRET efficiency might also be discarded. The stoichiometry together with the FRET efficiency on the other hand creates a two-dimensional plot that offers full control over the all detected bursts.

the detection correction factor $\gamma$, and the new nomenclature into account, equation 4.11 changes to:

$$E = \frac{I_{DA} - \beta I_{DD} - \alpha I_{AA}}{I_{DA} - \beta I_{DD} - \alpha I_{AA} + \gamma I_{DD}} \tag{4.13}$$

As explained, the stoichiometry is, in essence, the ratio of green photons to all photons. Including again the correction factors, this yields the stoichiometry $S$:

$$S = \frac{I_{DA} - \beta I_{DD} - \alpha I_{AA} + \gamma I_{DD}}{I_{DA} - \beta I_{DD} - \alpha I_{AA} + \gamma I_{DD} + I_{AA}} \tag{4.14}$$

Figure 4.9 shows a typical two-dimensional histogram of an efficiency vs stoichiometry plot. The sample measured for this purpose was a mixture of two DNAs, described in detail in chapter 6, one with a low FRET value of around 0.1 and one high FRET species with 65% FRET efficiency. They were used on a daily basis to evaluate the performance of the microscope. Here, it becomes obvious that four different species were sampled: with a stoichiometry ratio close to one and a FRET efficiency around zero[5], the donor-only species is an always occurring species. This is due to stochastic and often incomplete labeling and mostly due to the fact that red dyes are more prone to bleaching or chemical reaction.

The second species is spread out in the efficiency space but has a stoichiometry around zero. It represents the acceptor-only population in the sample. The last two populations with a stoichiometry between $\sim 0.4$ and $\sim 0.5$ are the actual molecules of interest.

In principal, figure 4.9 can be used to determine the correction factors $\alpha$, $\beta$, and $\gamma$, if they are not known before. The donor-only peak has to be centered around zero FRET efficiency and can be adjusted with a changing crosstalk value. The acceptor-only fraction has to be spread around an stoichiometry value of 0 and can be realigned with a change in the direct excitation correction factor $\beta$. The efficiency ratio $\gamma$ is harder to determine: if a high-FRET and a low-FRET signal are present in the same sample or are mixed on purpose - and their fluorophores have the same quantum yields - the $\gamma$-value can be adjusted until both peaks have the same stoichiometry. Alternatively, it is suggested to plot 1/S vs. E and calculate the correction factor $\gamma$ from the slope $m$ and the $Y$-axis intercept $y_0$ [115, 117]:

$$\gamma = \frac{y_0 - 1}{y_0 + m - 1} \tag{4.15}$$

The calibration of all three correction factors should be done with extreme precaution. All of them influence the FRET histogram and hence have a heavy influence when converting the histogram into an actual distance. $\alpha$ and $\beta$ are straight forward and can

[5]Note that physically it doesn't make sense to have FRET values of single bursts that are smaller than one, but since the correction factors are determined stochastically and applied to all molecules, it can happen that bursts appear to have a FRET efficiency smaller than 0 or larger than 1.

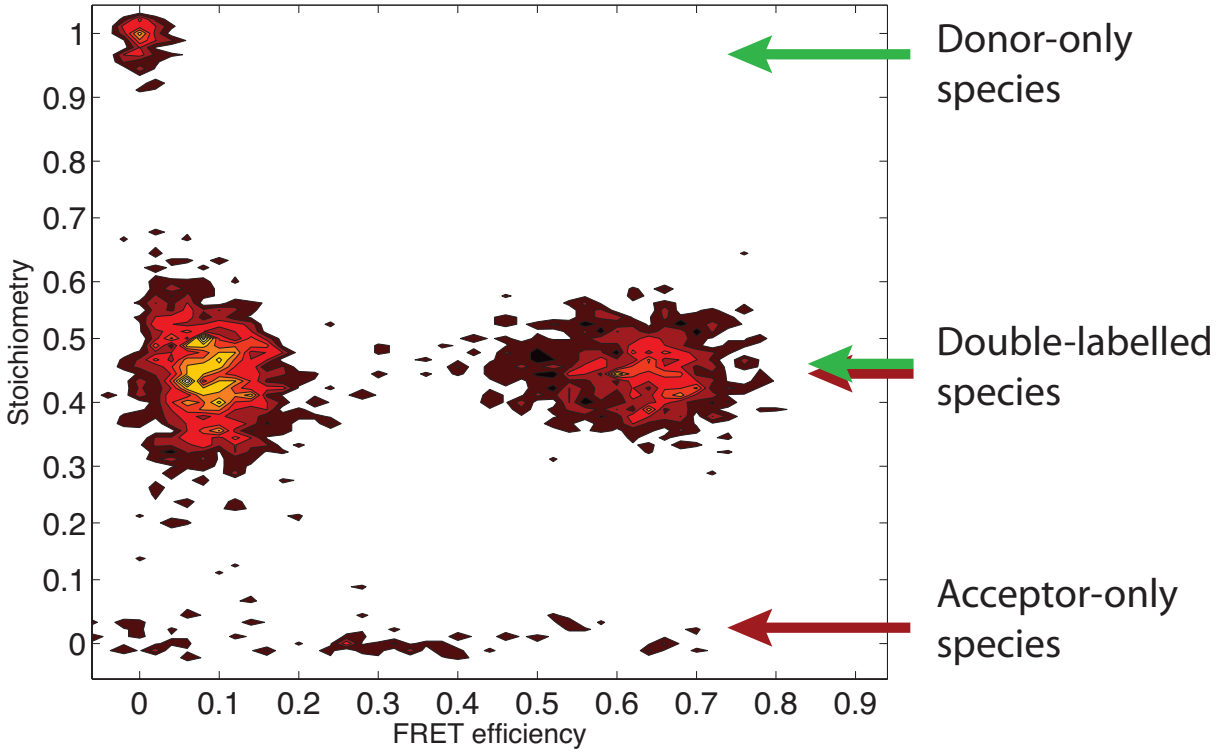


Figure 4.9: Two-dimensional efficiency vs. stoichiometry plot of two double-labelled DNA populations. Visible here are three species: donor-only (stoichiometry of one), acceptor-only (stoichiometry around zero), and the actual sample with a stoichiometry in the middle, consisting of a high-fret and a low fret species.

be adapted "on the fly" to every histogram. $\gamma$ offers more difficulties: even when using calibration samples. For example a high-FRET and a low-FRET - DNA with identical fluorophores to those attached to the bio-molecule of interest might have different life-times or spectra due to subtle changes of the chemical environment and, therefore, have a different gamma factor.

## 4.6 Photon Distribution Analysis

One very crucial point in single-molecule studies is dealing with the limited amount of photons. This holds especially for burst analysis studies of double labelled molecules [106, 122–125]. In general, the width of a single-molecule measurement carries additional information. The problem here is to distinguish broadening of the FRET histogram due to molecular motion or due to stochastic variations and dark counts. By taking the photon statistics into account, the method of probability distribution analysis (PDA) precisely models the shape of FRET histograms rather than fitting the overall shape to a Gaussian [118, 126–130]. Figure 4.10 shows clearly the influence of photon statistics onto the shape of a FRET histogram: a molecule with 50% FRET efficiency is shown with a total photon count of 10 photons (blue) and 100 photons (red). Normalized, the width of the histogram

is the broader the poorer the photon statistics get.

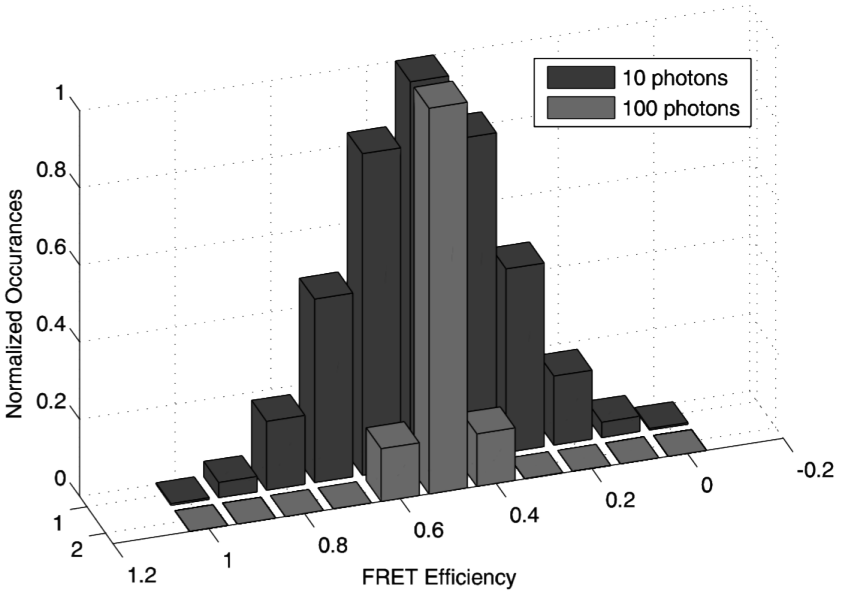


Figure 4.10: Influence of photon statistics onto the shape of a FRET histogram: a molecule with 50% FRET efficiency is simulated. The blue histogram has a total amount of 10 photons, while the red histogram contains 100 photons.

In general, FRET efficiencies describe the likelihood of transferring a photon from an excited donor molecule to an acceptor molecule and detecting the fluorescence of the second. Two discrete measurement observables correspond directly to the FRET efficiency: $S_G$, the number of detected "green" photons in the donor channel and $S_R$, the number of "red" photons in the acceptor channel. As already discussed in chapter 2.3, the FRET efficiency basically is the number of transferred photons divided by the sum of all photons (equation 4.11).

Instead of the FRET efficiency $E$, the ratio of green divided by red signal $S_G/S_R$ is often used because it does not limit significant results to a value between 0 and 1 and hence makes corrections easier to apply.

When converting FRET efficiencies to actual inter-dye distance, only in two cases this efficiency converges to one value: if the number of collected photons is indefinitely large, or the experiment is carried out only once. A single measurement usually includes thousands of analyzed bursts. Hence, the FRET efficiency will be distributed over a certain range. This is simply caused by the discrete and stochastic nature of photon emission, called *shot noise*. The signal per channel, $S_i$, consists not only of the fluorescence signal, $F_i$, itself but additionally the dark counts of the detector and the background from the buffer, summarized as $B_i$, contribute to the total counts:

$$S_i = F_i + B_i \tag{4.16}$$

The probability to observe a certain ratio of $S_G/S_R$ - in this case let's assume an examplary ratio $X$ - is the sum over all possible combinations of donor fluorescence $P(F_G)$, acceptor fluorescence $P(F_R)$, and the individual background contributions that yield exactly this ratio of $S_G/S_R = X$:

$$P(\frac{S_G}{S_R} = X) = \Sigma P(F_G, F_R, B_G, B_R) \tag{4.17}$$

Since background in each channel and fluorescence signals are independent, the right side of equation 4.17 can be split into $P(F_G, F_R)$ , $P(B_G)$ and $P(B_R)$, respectively. A very crucial step in PDA is to separate $P(F_G, F_R)$ into the probability to detect $F$ number of fluorescence photons with a subpopulation of $F_R$ acceptor photons at the same time.

$$P(F_G, F_R) = P(F)P(F_R|F) \tag{4.18}$$

Given the assumption that the data is binned into equal time bins, the probability for detecting a background photon follows a poissonian distribution. As characteristic for Poisson statistics, the average number of background counts $\langle B_i \rangle$ is the same as the width of the background photon distribution:

$$P_{B_i}(B_i) = \frac{\langle B_i \rangle^{B_i}}{B_i!} \cdot e^{-\langle B_i \rangle} \tag{4.19}$$

To calculate $\langle B_i \rangle$, it is necessary to run an experiment with buffer but no sample to estimate the total amount amount of background in each channel.

Measuring now $F_R$ photons, with $F$ total photons at the same time, can be expressed as the probability of a binomial distribution. This distribution can be characterized by a Bernoulli experiment of coin tossing $F$ times with a certain probability of getting an acceptor photon, in our case the apparent transfer efficiency $\epsilon$:

$$P(F_R|F) = \frac{F!}{F_R!(F - F_R)!}\epsilon^{F_R}(1 - \epsilon)^{F - F_R} \tag{4.20}$$

The challenge in this case is to model the distribution $P(F)$ correctly. Efforts have been undertaken to describe the photon per burst distribution analytically [131], but as long as the number of fluorescence photons is much higher than the number of background photons, it is easier and still legitimate to use the experimentally accessible distribution of $P(N)$, where $N = F + B_G + B_R$. During the duration of a burst under experimental conditions, the number of fluorescence photons exceeds the background photons by at least an order of magnitude or more[6]. This allows us to combine equations 4.17, 4.19 and

[6]If this is not the case anymore and the fluorescence signal is no longer strong enough to fulfill this statement,, $P(N)$ has to be deconvoluted with the probability of detecting background photons to receive a correct $P(F)$ [127].

4.20:

$$P(\frac{S_G}{S_R} = X) = \Sigma P(N) \cdot P(F_R|N - B_G - B_R) \cdot P_{\langle B_G \rangle}(B_G) \cdot P_{\langle B_R \rangle}(B_R) \tag{4.21}$$

The summation here includes all different combinations of $N, F_R, B_G$ and $B_G$ that yield one value of $S_G/S_R = X$. $\epsilon$ is left as the only free parameter and can be found by minimizing $\chi^2$, when fitting a model histogram based on equation 4.21 to the experimental data.

The problem of applying equation 4.21 to an experimental FRET histogram is that several other reasons exist that make it necessary to use more than a single FRET efficiency $\epsilon$: linker flexibility, conformational changes in the sample or photophysics of the dye make it necessary to describe the data with a distribution of FRET efficiencies. If no donor- or acceptor-only species is present, a gaussian distribution of $\epsilon$ is used with a mean of $\bar{R}_{DA}$ and a width of $\sigma_{DA}$. The probability of getting a certain $S_G/S_R$ ratio from equation 4.21 has to be integrated over all possible values of $\epsilon$ and accordingly weighted by the probability of $\epsilon$ as a function of inter-dye distance, $p(\epsilon(R_{DA}))$:

$$P\left(\frac{S_G}{S_R}\right) = \int p(\epsilon(R_{DA}))\Sigma P(N) \cdot P(F_R|N - B_G - B_R) \cdot P_{\langle B_G \rangle}(B_G) \cdot P_{\langle B_R \rangle}(B_R) \cdot d\epsilon \tag{4.22}$$

An example of a PDA fit with residuals to the small peptide AK14 (explained in depth in chapter 6), labelled with Atto488 and Atto647N is given in figure 4.11.

There are several things that became obvious when comparing the histograms in figure 4.11: the broadness of the histograms can be indeed induced by different underlying widths of the distance distributions, as can be seen by the two top histograms. While they have nearly the same center of 5 $nm$, the width in the case of pH 7 is much narrower, when compared to the case of pH 11. This behavior is mirrored in the FRET histograms.

But comparing the cases of $4M$ *GndCl* and $4M$ $NaClO_4$, it is apparent that the width of the underlying distance distribution is nearly the same for both cases, but the histogram appears much broader in the case of $4M$ *GndCl*. This is due to the fact that less photons were recorded per burst for *GndCl* and hence the distribution is more spread out.

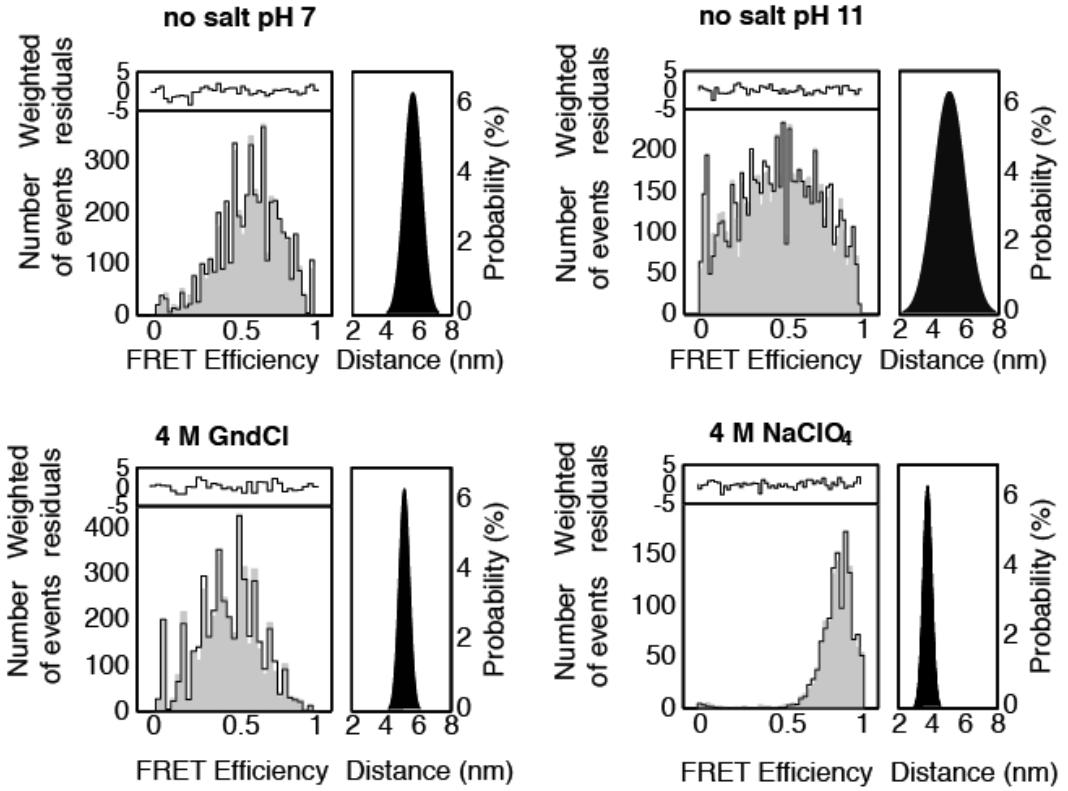


Figure 4.11: PDA analysis of a small peptide labelled with a donor and an acceptor dye: the protein exhibits different folding states due to change of the chemical environment. Different widths can be modeled by PDA with the underlying distance distributions shown to the right of each FRET histogram

## 4.7 The Photon Counting Histogram

The photon counting histogram (PCH) [90, 132, 133] is a technique that can be used on the identical data sets as FCS, but is somewhat a complementary technique in the analysis[7]. While FCS makes use of the length and the duration of fluctuations in a photon time series, PCH utilizes the height of these fluctuations to extract information. As stated before, with FCS it is possible to gain insight regards the *concentration* and *diffusion time* of fluorescent molecules. PCH, on the other hand, utilizes the hight of these fluctuations and is capable of determining the *concentration* and *molecular brightness* of a species diffusing through the confocal volume. The molecular brightness can be of particular use when two species with similar diffusion coefficients but different brightness - for example monomer and dimer [134] - are investigated.

A photon counting time series of freely diffusing molecules in a confocal volume never has a single value, but normally fluctuates around an average. This is due to two interwoven processes: the number of fluorescent molecules within the confocal volume varies due to brownian motion and the photon detection statistics (see chapter 4.6) itself. Both processes can be described by a Poisson distribution, but their convolution is broader and hence give rise to super-Poisson statistics. This is not the only reason for a broader histogram of counts: since the PSF is not uniformly shaped, the number of photons detected from a fluorophore will vary depending on its position in the confocal volume. The following equations take these complications into account and are the underlying basis for describing the final super-poisson distributions of counts. A very thorough discussion of the mathematics behind the PCH is given in [96]. For these principles to work, one has to make sure that the brightness of the sample does not change during the measurement and divide the photon stream into bins - containing the number of photons $k$ - that are small enough that during the time of the bin no noticeable change in the number of fluorophores and their respective brightness occurs. Usually, the bin size is on the order of 1µs.

A Poisson distribution is given by:

$$p(N) = \frac{\langle N \rangle^N \cdot e^{-\langle N \rangle}}{N!} \tag{4.23}$$

where $p(N)$ is the probability of detecting $N$ events. To describe the probability $p(k)$ of detecting $k$ photons within one time-bin, Mandels formula [135] is used:

$$p(k) = \int_0^\infty \frac{W^k e^{-W}}{k!} p(W) dW \tag{4.24}$$

[7]The optimal measurement conditions are slightly different: for PCH, the laser power should not be more than $5 - 10$µW and to compensate the lower signal, the measurement duration should be increased to $15 min$.

One has to differentiate here between $k$, which is the number of photons within a time bin and $W$, the time dependent number of counts that reach the detector. As mentioned before, the PSF is not illuminated homogeneously and additionally it doesn't make sense to integrate over the entire space up to infinity, so when taking the shape of the PSF into account, as well as the molecular brightness of the fluorophore $\epsilon$, equation 4.24 changes to:

$$\langle k \rangle = \frac{\epsilon}{V_0} \int_0 P\bar{S}F(r) \cdot dr = \epsilon \cdot \frac{V_{PSF}}{V_0} \tag{4.25}$$

The molecular brightness is the number of photons per molecule per second and is defined as the product of the detection efficiency $\eta$ of the the microscope, the maximum number of photons $I_0$ per second when the fluorophore is placed in the middle of the PSF, and additionally a coefficient $n$, which 1 for 1-photon excitation and 2 for 2-Photon excitation:

$$\epsilon = I_0^n \cdot \eta \tag{4.26}$$

Considering these basics of the photon counting histogram, it is possible to determine brightness and concentration of a single freely diffusion species. In this work, PCH is used purely qualitatively to show that the behavior of actin polymerization follows an electrostatic influenced diffusion controlled potential (see chapter 8).

# Chapter 5

# Single-Molecule Setups

## 5.1 Multi-parameter Fluorescence Detection Setup

### 5.1.1 Introduction to Multi-Parameter Fluorescence Detection

With a multi-parameter fluorescence detection (MFD) confocal setup (shown schematically in figure 5.2 and rendered in figure 5.1) it is not only possible to extract and analyze the fluorescence intensity, as discussed in the previous chapter, but ,in recent years, the full characterization of single molecules diffusing freely in solution became possible [122, 130].

To fully extract all information out of a transiting molecule, several fluorophore intrinsic properties have to be recorded: the fluorescence lifetime $\tau$, fluorescence anisotropy $r$, the molecular brightness $\eta$, and the spectral properties of absorption and emission [85]. Additionally, the fluorescence intensity $F$, and the exact arrival time of the photon after the start of the measurement are available. When two fluorophores are attached to the diffusing molecule and they are within the range of 100 Ångstroms, the distance between them is measurable since Förster energy resonance transfer (FRET) between these emitters will occur [27, 136, 137]. This phenomenon makes it possible to determine structural features of proteins and other biological relevant molecules in vivo with a resolution down to a few Ångstroms, which is otherwise achieved only by X-ray measurements.

### 5.1.2 Instrumentation of the MFD Setup

To carry out smFRET and PIE-FCCS experiments, we used a home-build confocal multi-parameter fluorescence setup with pulsed interleaved excitation. To recorded all available photon-characteristics, making it possible to determine the FRET efficiency, fluorescence lifetime of various components, time resolved and steady state anisotropy and stoichiometry, the system built during this work was constructed with certain aims: the detection efficiency should be greatly improved compared to the setup built during the previous work [19] [118] along with improved thermal, mechanical and, hence, optical stability

while the permeability towards light from the environment should be greatly decreased. Therefore, all optical elements that are placed in the detection path after the pinhole are incorporated into a 30mm cage/tube system (ThorLabs, Dachau, Germany).

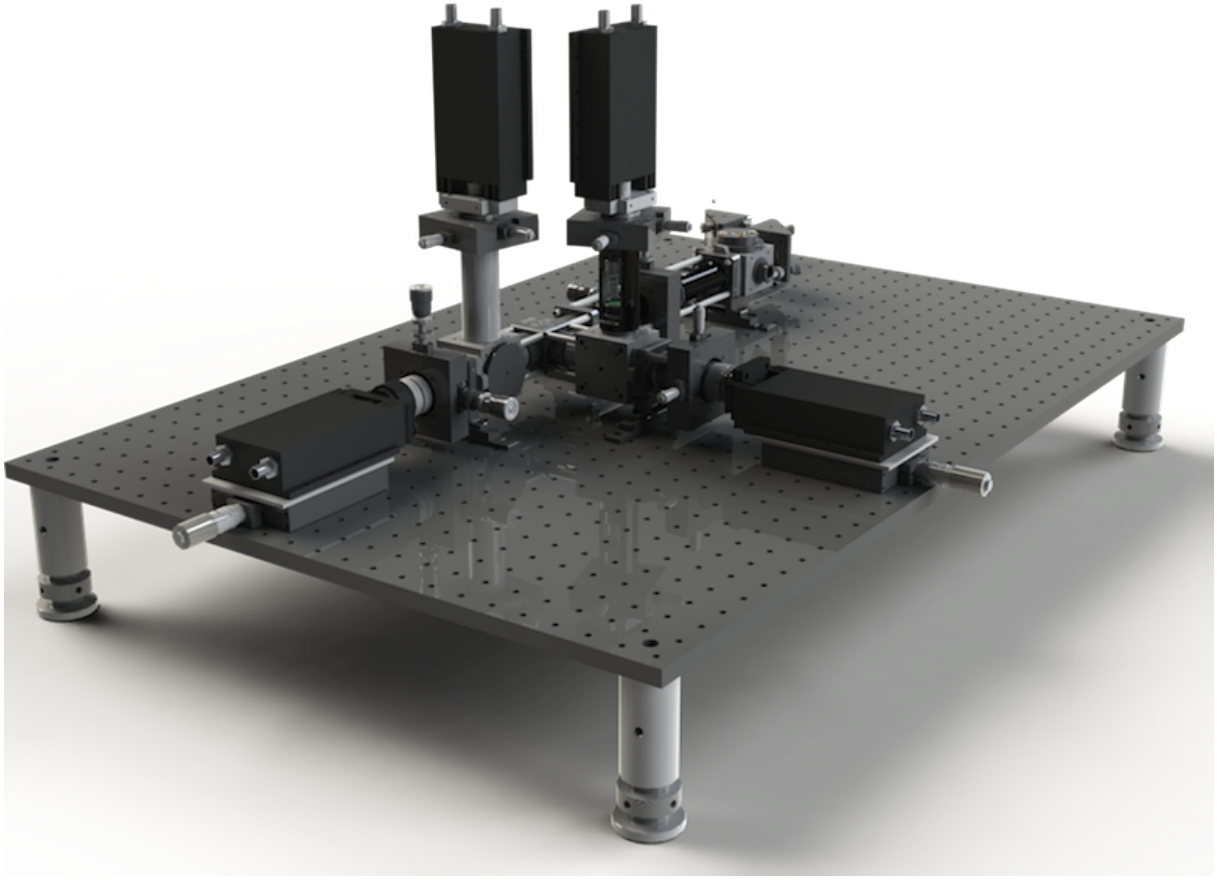

Figure 5.1: Rendered image of the MFD-setup

The microscope base is a Nikon Ti Eclipse (Nikon, Tokyo, Japan). Diode lasers were used as picosecond, pulsed excitation sources at 488 nm (LDH-P-C- 485, PicoQuant, Berlin, Germany) or 532 nm (LDH-P-FA-530, PicoQuant, Berlin, Germany) for donor excitation and at 635 nm for acceptor excitation (LDA635, PicoQuant, Berlin). The lasers were combined into a single-mode fiber (AMS Technologies, Planegg, Germany) within a fiber coupling unit (FCU II, PicoQuant, Berlin, Germany), collimated (60SMS-1-4-RGBV, Schäfter und Kirchhoff, Hamburg, Germany) and reflected via two mirrors for alignment (BB1-E02, Thorlabs, Dachau, Germany). It is reflected with the help of a 99% silver mirror (F21-005, AHF Analysentechnik, Tübingen, Germany) through the 60× 1.2NA water immersion objective (Plan Apo VC 60x WI, Nikon, Tokyo, Japan) and focused on the sample. The fluorescence is collected by the same objective and passes the dichroic mirror (DualLine z488/635, AHF Analysentechnik, Munich, Germany) separating excitation and emission beam paths. The collected fluorescence is focused on a 50µm pinhole (P50s, Thorlabs, Dachau, Germany) with a 60 mm achromatic doublet lens

(G322322000, Linos, Göttingen, Germany) and afterwards collimated with an identical lens. A polarizing beamsplitter cube (CM1-PBS251, Thorlabs, Dachau, Germany) separates the two polarization planes followed by spectral separation in donor and acceptor fluorescence by two dichroic mirrors (BS 650, AHF Analysentechnik, Tübingen, Germany) and four individual emission filters (2x BrightLine HC 525/45 and 2x ET 700/75, AHF Analysentechnik, Tübingen, Germany). Fluorescence is collected by four single photon counting avalanche photodiodes (2x SPQR-14 and 2x SPQR-16, Perkin Elmer, Waltham, Massachusetts) and registered by four individual TCSPC data collection cards (SPC-154, Becker&Hickl, Berlin, Germany). Measurement cards and lasers were synchronized by the laser controller (Sepia 2, Picoquant, Berlin, Germany). The laser pulses were delayed with respect to each other by $18ns$, allowing determination of the excitation source by the arrival time of the detected photon using TCSPC. To avoid different starting times of the four TCSPC cards, a TTL trigger box (Ni6009, National Instruments, Austin TX, USA) is used to synchronize them and start an experiment.

Figure 5.1 shows a rendered image of the setup without the microscope base itself. This image reveals another very important advantage of the setup: the setup is mounted on a breadboard (MB3060/M, Thorlabs, Dachau, Germany), which is itself mounted on four adjustable height posts (BLP01/M, Thorlabs, Dachau, Germany). This has the immediate consequence that the fiber output, pinhole and two of the detectors have the same height as the entrance point into the microscope. This means that no alignment in this axis is necessary as soon as the whole breadboard is adjusted to the correct height.

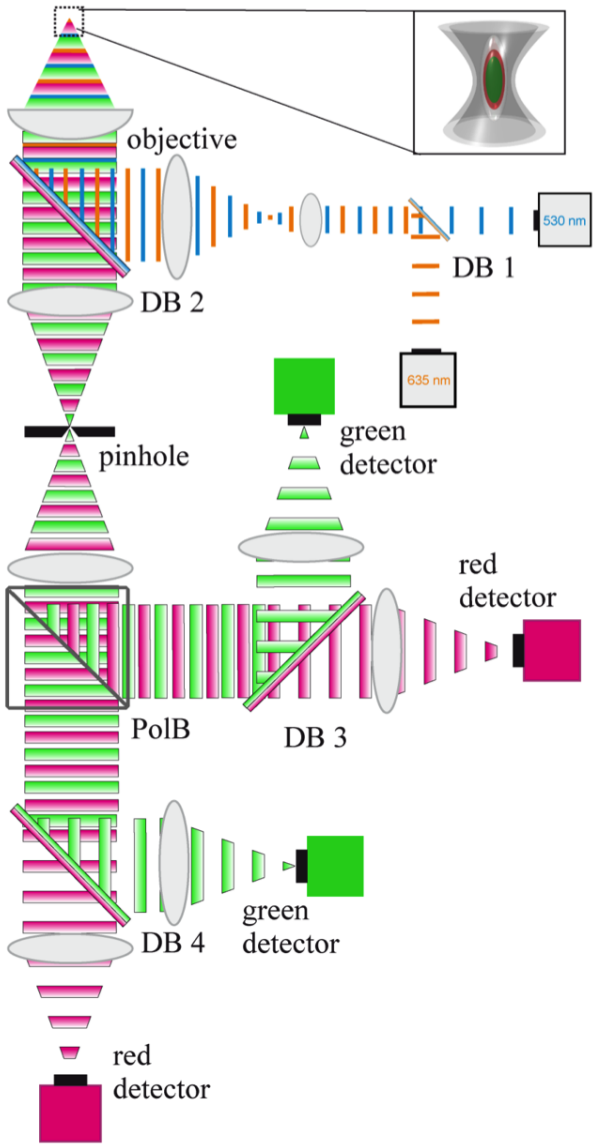


Figure 5.2: Schematic illustration of the MFD setup's beam path. The excitation lasers are combined with a dichroic beamsplitter (DB1) and focused into the sample. DB2 separates fluorescence from excitation photons. The polarizing beam splitter (PolB) divides photons based upon their respective polarization and the dichroics 3 and 4 separate blue/green fluorescence from red fluorescence.

### 5.1.3 Characterization of the MFD setup

#### 5.1.3.1 Optical Properties of the Setup

The choice of optical elements is crucial for a MFD setup, because the implemented elements determine the amount and the properties of the photons that arrive at the different detectors. Figure 5.3 shows the range of wavelengths that arrive at the detectors for the donor and for the acceptor channels. It is essential to know that the filter for the blue region can't be expanded, because at approximately $575nm$ is a Raman line of the blue laser. To avoid any Raman light being collected, the filter excludes these wavelength regions.

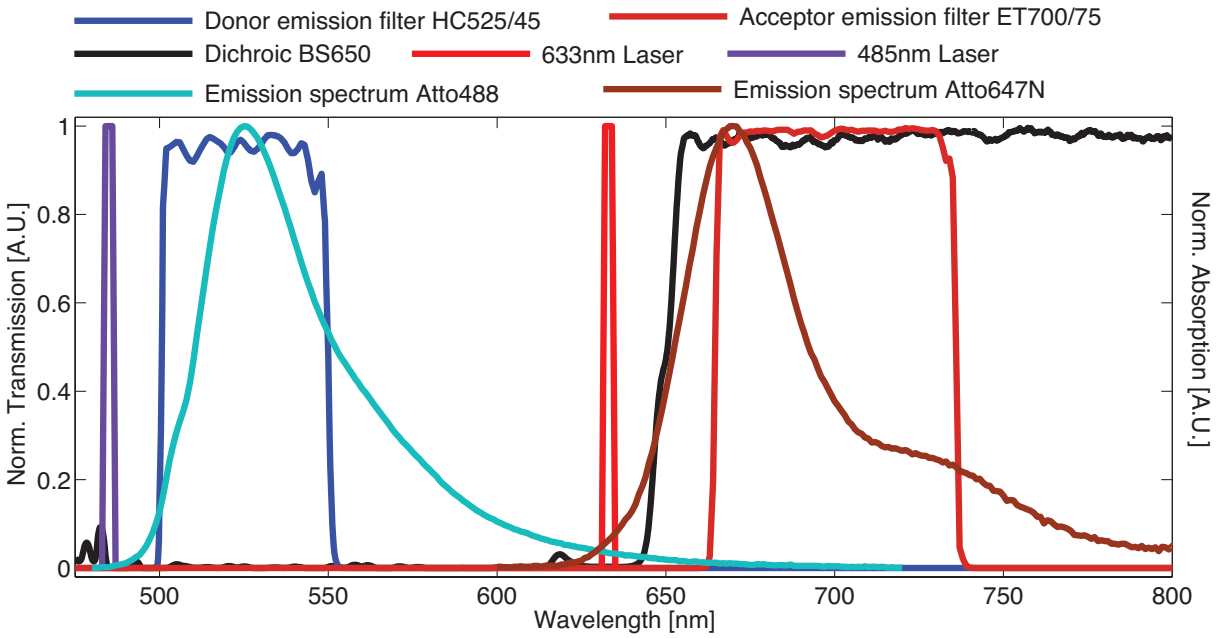


Figure 5.3: Optical properties of the MFD setup. The spectra are shown for the configuration that was used for the measurements in chapter 6. The emission filter of the blue dye could not be broadened, because otherwise a Raman line of water, generated by the red laser, appeared and increased the background about tenfold.

#### 5.1.3.2 Focus Size and Overlap of the Foci

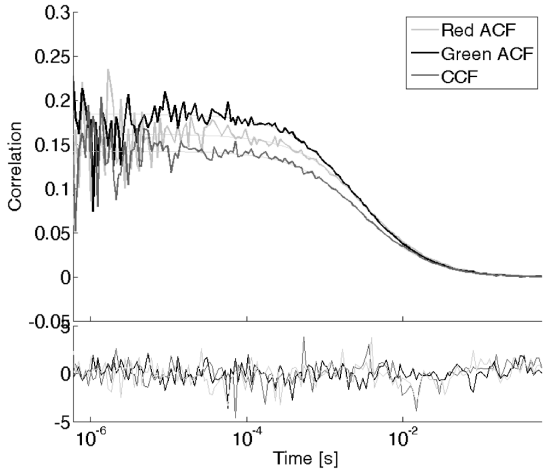


Figure 5.4: Fluorescence (cross-) correlation curves of double labeled DNA. The three curves are fitted only with a diffusional term due to the absence of any photo-physical effects. Fits are shown in red and the residues to the fit of all three curves below.

Due to the setting of the MFD setup, in particular the two excitation lasers originating from the same single-mode fiber, the overlap of the two resulting foci, as well as their size, is predetermined. A truly diffraction limited laser focus requires the incident laser wave front to be completely flat. Since all point sources, like a single-mode fiber in combination with a collimator, produce a gaussian shaped intensity distribution, the beam diameter has to be larger than the back-aperture of the objective ($8mm$ for the Nikon Plan-Apo). In the case of the MFD setup, a collimator is used that yields a beam diameter of $2.5mm$. This means that the objective is heavily under-filled. As a result, the PSF of this setup is stretched in all three dimensions, compared to the smallest possible configuration. The actual size of the PSF can be calculated with a sample that has a known diffusion coefficient [138]. For this purpose, a sample of free carboxylic acid variant of Atto488 with a diffusion constant of $400\mu m^2/s$ has been measured. The three resulting correlation curves - autocorrelation of parallel and perpendicular channel, as well as their cross-correlation in figure 5.5 - are then fitted with equation 4.5.

The results from this fit determine the confocal volume to an $\omega_{R,Green} = 0.96 \pm 0.01\mu m$ and an $\omega_{Z,Green} = 5.10 \pm 0.41\mu m$. The effective confocal volume is calculated by:

$$V_{conf} = \left(\frac{\pi}{2}\right)^{\frac{3}{2}} \cdot \omega_R^2 \cdot \omega_Z \tag{5.1}$$

This yields a total detection volume for the green channel of $V_{conf,Green} = (9.25 \pm 0.93) \cdot 10^{-15} L$.

This experiment can be repeated for the red detection channel. The sample that is investigated here is Atto655-NHS ester with a diffusion coefficient of $425\mu m^2/s$. The fits from the correlation curve yield the size parameters of $\omega_{R,Red} = 1.07 \pm 0.01\mu m$ and an $\omega_{Z,Red} = 5.53 \pm 0.46\mu m$, resulting in a total red detection volume $V_{conf,Red} = (11.19 \pm 1.31) \cdot 10^{-15} L$. Looking at the wavelength differences of the exciting lasers of 25%, it makes sense that the red excitation volume is larger compared to the green one. This also explains why in figure 5.4 the green ACF is higher than the red ACF: since the

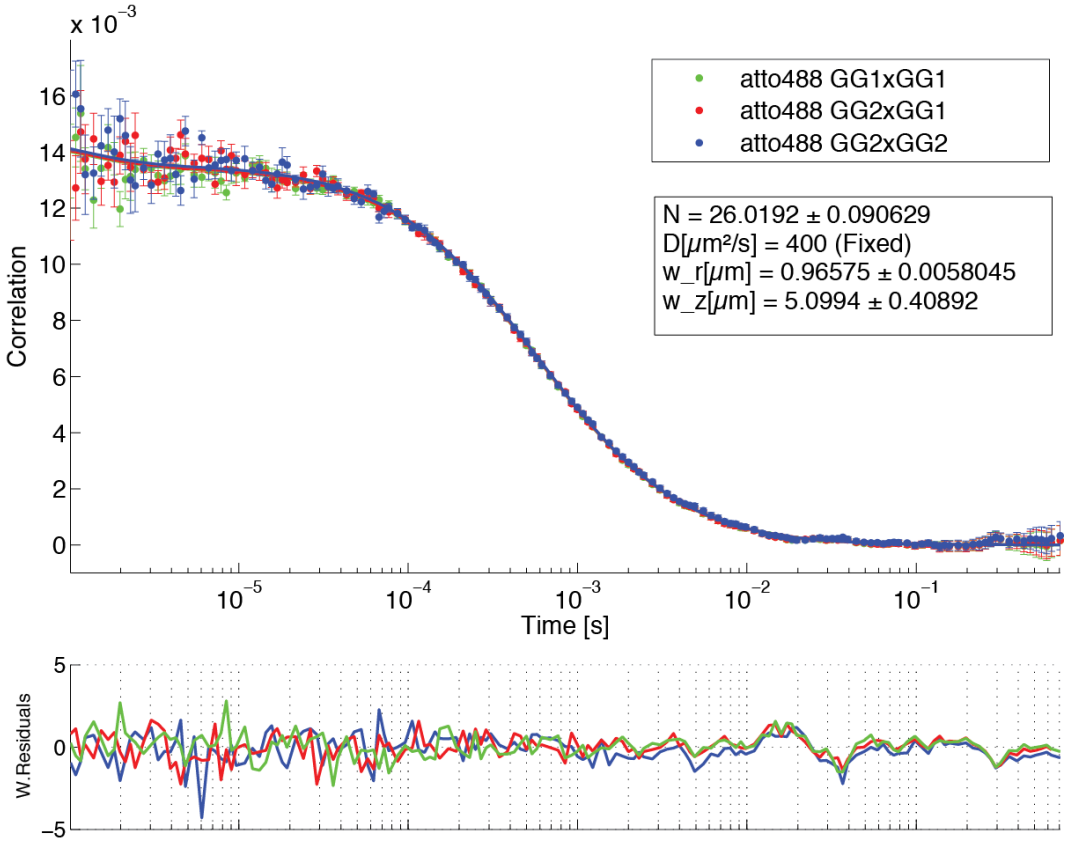


Figure 5.5: FCS measurements to determine the foci size. Atto488 carboxylic acid with a known diffusion coefficient of $400\mu m^2/s$ has been measured and the resulting correlation curves were fitted globally with equation 4.5.

green confocal volume is smaller, less molecules are detected at the same time and the auto-correlation is higher.

## 5.2 Stimulated Emission Depletion Setup

### 5.2.1 Introduction to STED Nanoscopy

Every stimulated emission depletion setup to date is based on and hence is an evolution of a confocal microscope. As already described in the historical synopsis about confocal microscopy, Ernst Abbe showed that the optical refraction capacity of a lens is not improvable beyond the point of the diffraction limit. To develop a microscope that can resolve structures with a size smaller than the point spread function, several approaches have been developed. They can be divided into three groups[1]:

1. True super-resolution techniques - like *near-field optical microscopy* [141], *4pi-Microscopy* [142], or *structured illumination microscopy* [143].

2. Stochastic functional techniques - like *Super-resolution optical fluctuation imaging (SOFI)* [144], *Stochastic optical reconstruction microscopy (STORM)* [145] or *photoactivated localization microscopy (PALM)* [146].

3. Deterministic functional techniques - like *ground state depletion (GSD)* [147] or *Stimulated emission depletion (STED)* [148].

Except the near-field techniques, all of these techniques have in common that the diffraction limit in itself is still present, but rather circumvented in one or the other way. Figure 5.6 shows the Jablonski scheme, extended with an incoming STED photon.

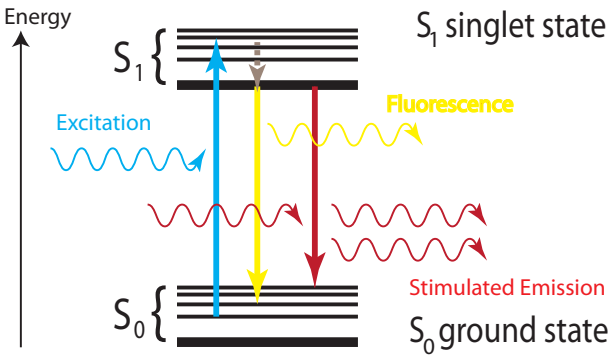


Figure 5.6: Jablonski scheme with stimulated emission.

Like many super-resolution techniques, STED makes use of two states that a fluorophore frequently visits: the ground state $S_0$ and the first excited state $S_1$. With the help of an excitation laser and a STED laser, molecules can now be switched between these two states. Figure 5.7 shows the principle that stands behind every STED microscope.

The STED setup in this thesis is operated with pulsed lasers, although CW-mode is also possible [149]. A 150ps long 640nm excitation pulse (see figures 5.8 and 5.10) is used to excite molecules from the ground state $S_0$ to the $S_1$ level. This happens in a diffraction limited PSF. A second PSF is then created with a 736nm STED laser. These two PSFs are concentric, but have different shapes.

[1]Stefan Hell later on summarized most of them in the RESOLFT -REversible Saturable OpticaL Fluorescence Transitions - principle[139][140]: the common ground here is that as long as only one emitter per PSF is in a fluorescent state, the location accuracy only depends on the number of detected photons.

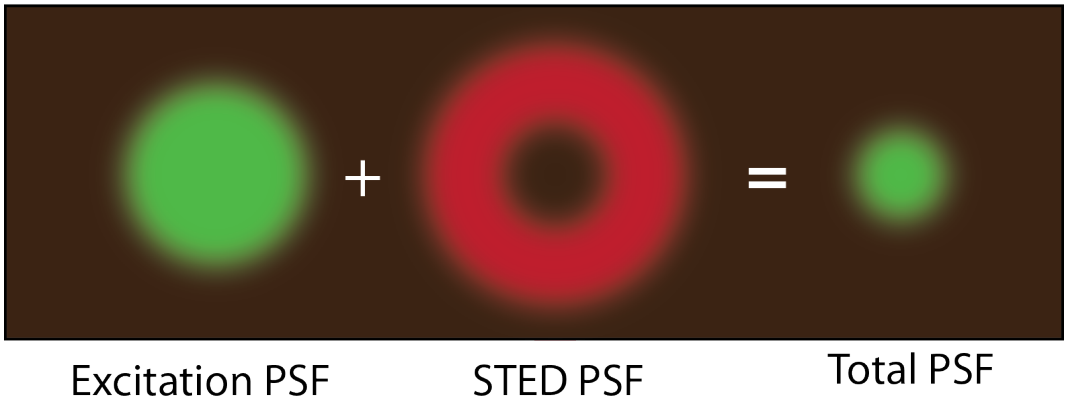


Figure 5.7: Principle of STED microscopy. The green PSF is used to switch fluorophores to an "on" or $S_1$-state. A second PSF is used to stimulate the emission in outer regions of the original PSF - switching molecules to an "off" state, back to $S_0$ - and hence suppresses fluorescence in this area. This results in a smaller effective PSF that is, in itself, no longer diffraction-limited anymore, unlike excitation and STED PSFs.

As figure 5.7 illustrates, the STED PSF features an intensity of zero at its center. This effect, often described as a donut, is created by a $2\pi$-phase plate [150]. This vortex type phase filter, placed in a conjugated back focal plane of the objective, changes with a 0 to $2\pi$ clockwise phase shift the phase front of the beam, creating a zero intensity at its center.

Oftentimes, a 2-photon laser is used as STED laser. This light source originally has a pulse width of approximately $150fs$. In order to not compete with 2-photon excitation, the pulse width is elongated to approximately $300ps$ by focussing the beam into a $120m$ long polarization-maintaing single-mode fiber. The excitation and STED lasers are timed in such a way that excited molecules are allowed $400ps$ to relax to the vibrational ground state of $S_1$ before the STED pulse arrives.

The photons that origin from stimulated emission have the same properties as the laser photons and are therefore excluded by the filters. In order to guarantee an efficient de-excitation to the ground state within the desired region of the STED-PSF, stimulated emission rates have to be favorable compared to spontaneous emission. When this condition is fulfilled, the resolution can be increased to:

$$\Delta r \approx \frac{\lambda}{2 \cdot n \cdot sin\alpha \sqrt{1 + \frac{I}{I_{sat}}}} \tag{5.2}$$

This equation is essentially an extension of Abby's formula, equation 3.3, where $I$ is the intensity of the STED laser beam and $I_{sat}$ is the laser power needed to quench half of the molecules. Considering a standard dye with a lifetime of $\tau = 4ns$: the spontaneous decay rate from the $S_1$ state is given by the inverse of this lifetime, so $I_{sat}$ can be approximated

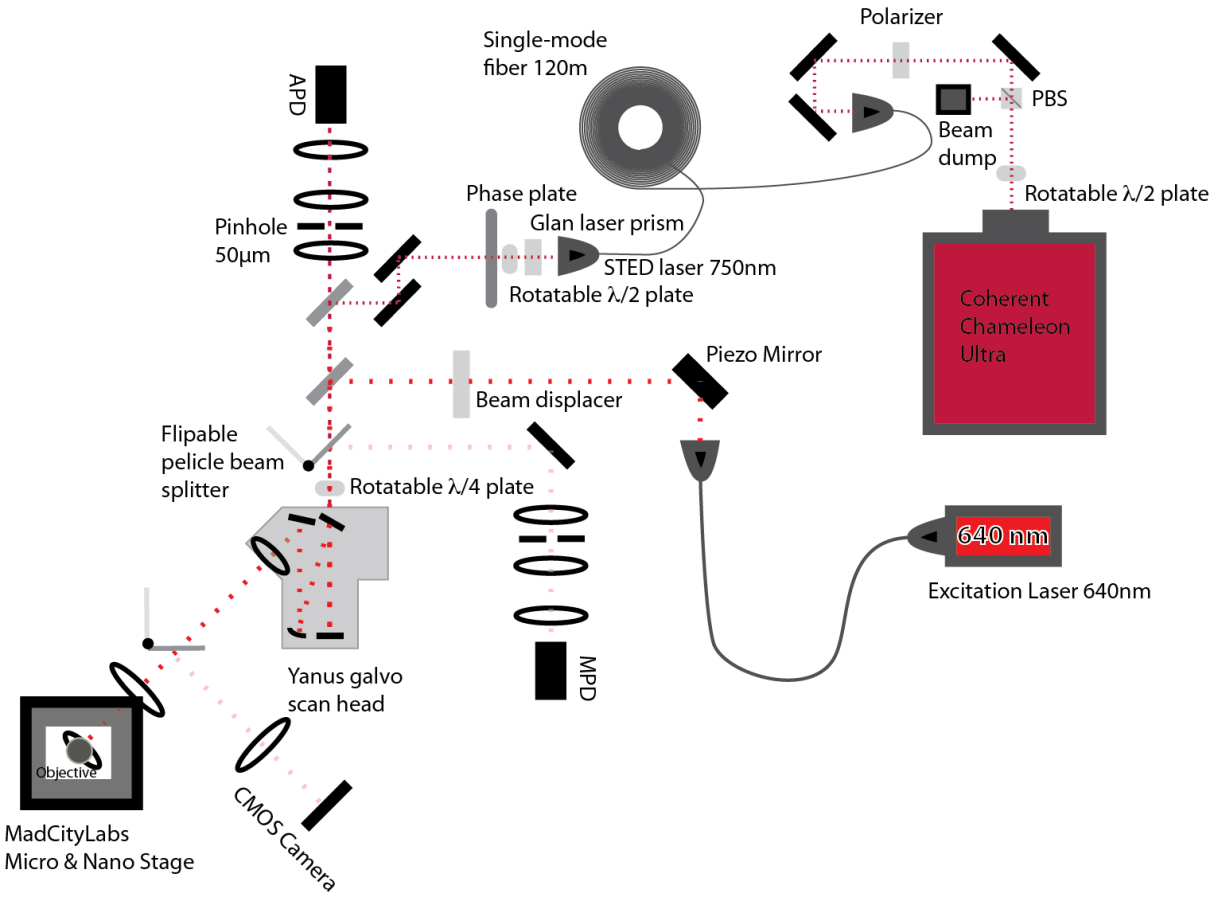


Figure 5.8: Schematic of the STED beam path: The STED laser is focussed into a $120m$ single-mode fiber to stretch it in order to avoid competition with 2-photon processes. Accordingly, STED and excitation beam path are overlaid and focussed into the sample. The detection is achieved by descanning and fluorescence photons are collected by an APD.

by:

$$I_{sat} = \frac{1}{\tau \cdot \sigma} \tag{5.3}$$

where $\sigma$ is the optical cross section of this transition. A typical cross-section is in the order of $\sigma = 10^{-16} cm^2$. This leads to a value of $I_{sat} = 0.7 MW/cm^2$. The eventually achievable distance $\Delta r$ inbetween two emitters that are still distingiushable from equation 5.2 is only limited by the following factors:

1) The fraction of $I/I_{sat}$, i.e. the quality of the zero intensity in the center of the STED beam.

2) How quickly a fluorophore photobleaches, i.e. the maximum number of emitted photons.

3) How much STED laser intensity is available and reasonable for a certain type of specimen.

4) The size of the fluorophore itself and its ability to switch between $S_1$ and $S_0$.

A very thorough mathematical description can be found in [151], but in essence the

probability $P_i$ for finding a molecule in the state $S_i$ is given by the following differential equation:

$$\frac{dP_1}{dt} = -k_{10}P_1 + k_{01}P_0 = -\frac{dP_0}{dt} \tag{5.4}$$

where $k_{ij}$ are the transition rates from $S_i \rightarrow S_j$. The total decay rate consists of spontaneous and stimulated emission:

$$k_{10} = k_{10,non-STED} + \sigma I_{STED} \tag{5.5}$$

where $k_{10,non-STED}$ is the decay rate uninfluenced by STED and $\sigma$ is the transition cross-section at the STED wavelength. For a sufficient depletion in the desired region, stimulated emission rates have to exceed the spontaneous emission, $k_{10,non-STED}$ by an order of mgnitude. For a fluorophore that is in state $S_0$ at time $t_0$, the probability of finding it in $S_1$ in a time $t > t_0$ is given by:

$$P_1(t) = \frac{k_{01}}{k_{10} + k_{01}}(1 - e^{-(k_{10}+k_{01})t}) \tag{5.6}$$

In order to reach an equilibrium, times that are longer than the inverse of the sum of both rates ($t \gg (k_{10} + k_{01})^{-1}$) have to be considered and therefore the second part of equation 5.6 vanishes:

$$P_1 = \frac{k_{01}}{k_{10} + k_{01}} = \frac{1}{1 + (\frac{k_{10}}{k_{01}})} \tag{5.7}$$

This equation is the mathematical description of the above mentioned fraction of $I/I_{sat}$: since the ratio of the excitation and de-excitation rates mostly depends on the STED laser power, the molecules in the fluorescent state can be quenched more effectively at higher laser power.

### 5.2.2 Instrumentation of the STED Setup

Figure 5.8 gives an overview of the layout of the STED setup: the setup is build for the 640nm excitation laser (LDH-D-C-640, PicoQuant, Berlin, Germany) and the 736nm STED laser (tunable from 680nm to 1200nm, Chameleon Ultra II, Coherent, Göttingen, Germany). To modulate the intensity of the STED beam, it goes through a rotatable half-wave plate (AQWP05M-600, Thorlabs, Dachau, Germany) and accordingly through a polarizing beam splitter (PBS052, Thorlabs, Dachau, Germany). The part of the laser beam that is not needed is safely disposed of in a beam dump (BT600, Thorlabs, Dachau, Germany). The remaining STED laser is coupled with three NIR mirrors (G340803000, QIOPTIQ, Paris, France) into a 120m long single-mode polarization-maintaining fiber (PMC-CAS-780-001 fiber cassette, 60FC-4-A6.2S-02 laser to fiber coupler, 60FC-T-4-M40-54 fiber to laser collimator, Schäfter&Kirchhoff, Hamburg, Germany). After the fiber, the beam is collimated again and the STED beam polarization is cleaned up by a Glan-Thompson laser prism (GTLP, Melles Griot, Carlsbad CA, USA) with a ratio of extinction for $p$- over $s$-polarization of $10^5 : 1$. In order to get a perfectly circular polarization at the objective, the beam passes a half-wave plate (AQWP05M-600, Thorlabs, Dachau, Germany) and the vortex phase plate (VPP-1a, RPC Photonics, Rochester NY, USA) to create the donut-shaped STED beam. It is guided over two mirrors (G340803000, QIOPTIQ, Paris, France) for alignment and a 5 mm thick dichroic mirror (zt625-745 rpc, AHF Analysentechnik, Tübingen, Germany) that only reflects the STED wavelength and lets fluorescence pass. The spectra of the filter and dichroics used are shown in figure 5.9.

The excitation laser, which is powered by a Sepia laser driver (Sepia I, PicoQuant, Berlin, Germany) and synchronized to the STED laser, is directly fiber coupled and collimated with a shiftable 30 mm lens (AC254-030-A, Thorlabs, Dachau, Germany) in order to correct for chromatic aberrations by the objective. The beam is reflected by a piezo mirror (E-500.00 Chassis, E-503.00S LVPZT amplifier, E-509.S3 Sensor/Servo Controller DMS, E-808.90 Monitorcable for E-809, Physik Instrumente, Karlsruhe, Germany) and passes a beam displacer (PD01, PicoQuant, berlin, Germany). The beam is then combined with the STED beam using a dichroic mirror (zt640 RDC, AHF Analysetechnik, Tübingen, Germany), passed through an achromatic quarter-wave plate (RAC 4.4.15, B.Halle, Berlin, Germany) and afterwards both beams enter the galvo scanner (Yanus, digitally driven, Till Photonics, Gräfelfing, Germany). The scanner has a fixed scanning lens of 40 mm and a 200 mm lens (AC508-200-A, Thorlabs, Dachau, Germany) is used to collimate the beam and act as tube lens. The laser beams enter the objective (60x, 1.27 NA Water, Nikon, Tokyo, Japan) that focusses the light into the sample, which is mounted on two stages, one for large $X$-$Y$ movements and the other for $Z$-positioning (MCL MicroStage and MCL NanoStage, Mad City Labs, Madison WI, USA).

Since no microscope body with occulars is present and in order to have a measure for

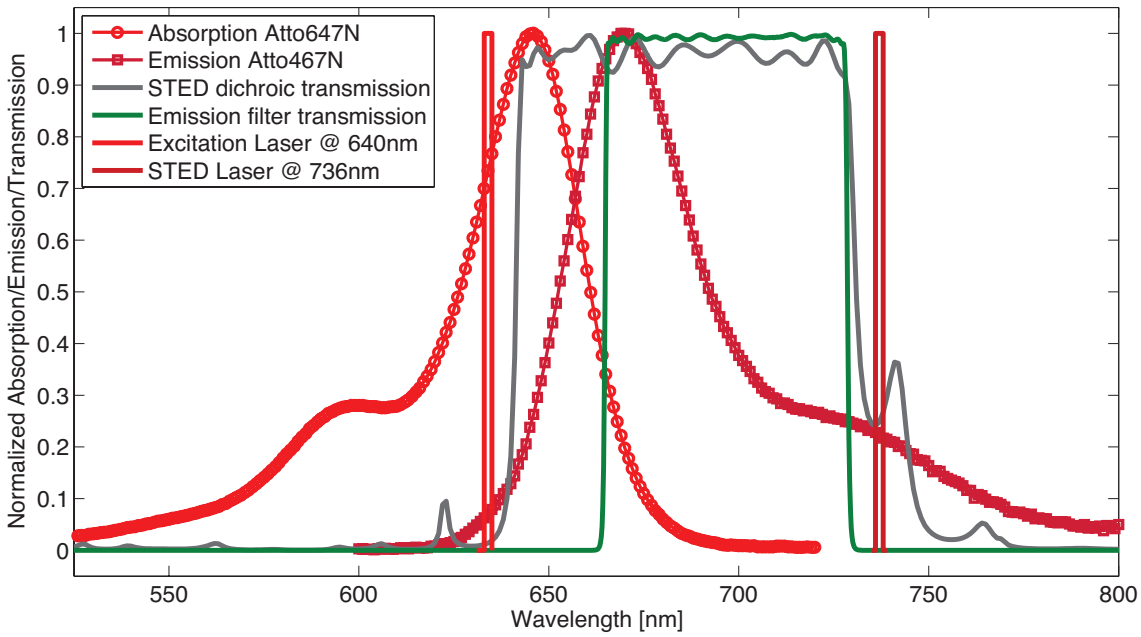


Figure 5.9: Spectral properties of the STED setup: The absorption and emission spectra of the dye Atto647N, with its corresponding excitation and depletion wavelength (light and dark red, respectively). The spectrum of the dichroic mirror, used to overlay excitation and emission, is depicted in grey and the spectrum of the emission filter in green.

the actual z-position of the focus with respect to the sample surface, a part of the back-scattered light is split by a pellicle beam splitter (BP108, Thorlabs, Dachau, Germany) and focussed with a 100 mm lens (AC254-100-A, Thorlabs, Dachau) onto a CMOS camera (DCC1545M,Thorlabs, Dachau, Germany).

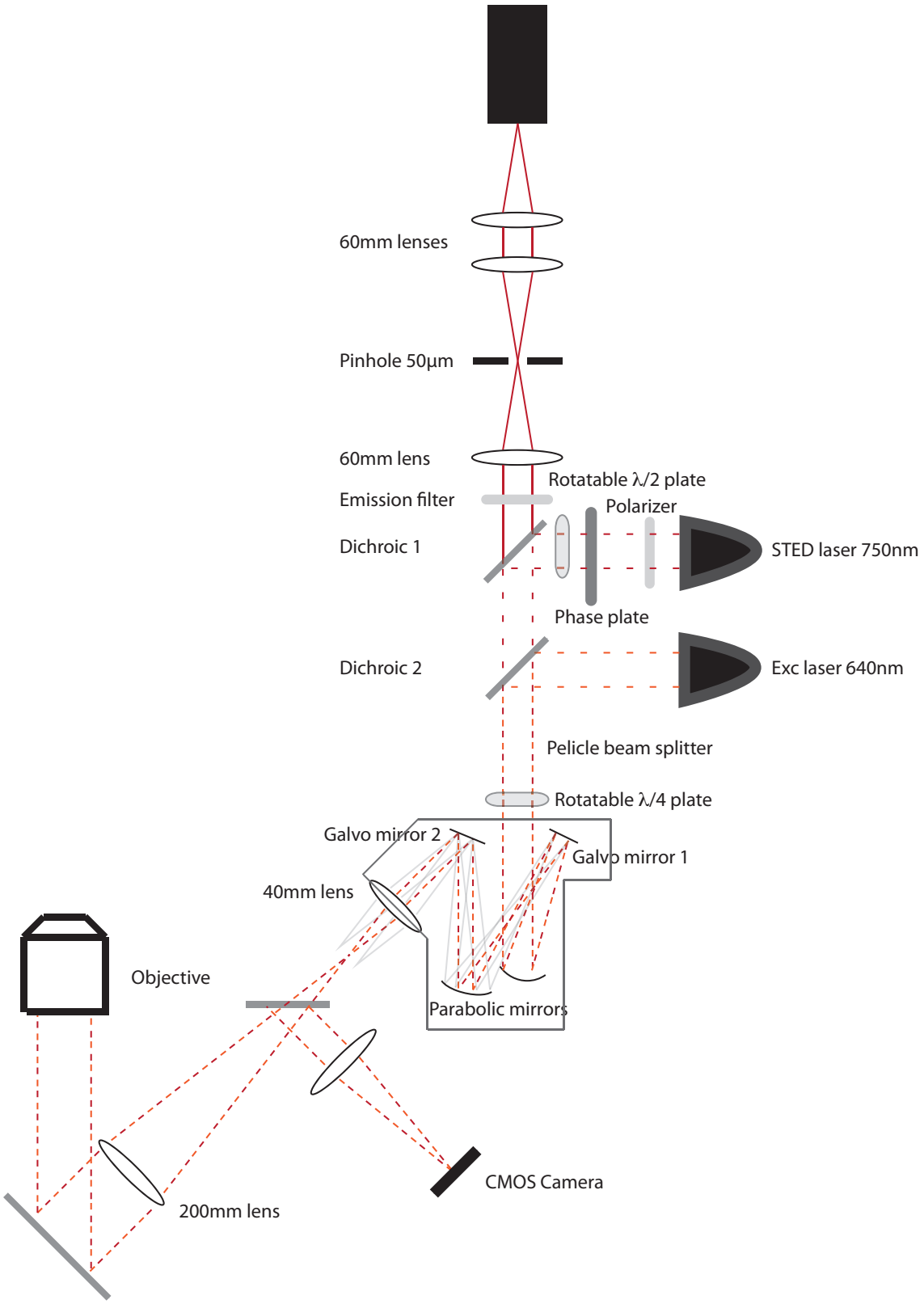


Figure 5.10: The detailed laser path, showing especially the beam path in the scanner: the collimated beam is focussed by a parabolic off-axis mirror onto the first galvo scanner, collimated and reflected by a second parabolic off-axis mirror and focussed again by the 40mm scan lens. The 200mm tube lens collimates the beam again and the objective focussed the beam into the sample.

The fluorescence of the sample is collected with the same objective and descanned through the entire beam path till it passes both dichroic mirrors and then an emission filter (Brightline HC697/25, AHF Analysetechnik, Tübingen, Germany). Two 60 mm lenses (G322306322, QIOPTIQ, Paris, France) are used to focus the fluorescence through a 50 µm pinhole (P50s, Thorlabs, Dachau, Germany) and collimate the beam afterwards again. A third lens of this type is used to focus the fluorescence onto an avalanche photo detector (AQRH16, Perkin Elmer, Hamburg, Germany). The TTL signal of the detector is split and on one end recorded by a TCSPC card (TimeHarp200, Picoquant, berlin, Germany) and on the other side counted by a field programmable gate array (FPGA, Spartan-6 FPGA SP605, Xilinx, San Jose CA, USA). This FPGA is used for quick and accurate count-rate display and as a hardware FCS correlator [152]. Hardware control and recording of the incoming signals is done with the home-written C# software *FabSurf*.

### 5.2.3 Characterization of the setup

The following paragraphs are not only meant to characterize the setup, but can also be used as a step-wise guide to align the setup.

#### 5.2.3.1 Backreflection onto CMOS camera

As a first step of the alignment procedure and in order to gain a rough idea how well the confocal excitation volume and the STED PSF overlap, a part of the back-reflection of both lasers that are focussed onto a glass coverslip is guided with a removable pellicle beam splitter onto a Thorlabs CMOS camera. The crosshairs for both images are kept at the same pixel in of the images for figure 5.11. Hence, the un-illuminated area of the STED donut is exactly concentric with the normal PSF of the excitation laser. As an additional measure to check the alignment, the opening and closing of the diffraction pattern, when focussing through the glass cover slip, has to be concentric, symmetric and has to stay stationary in the lateral plane.

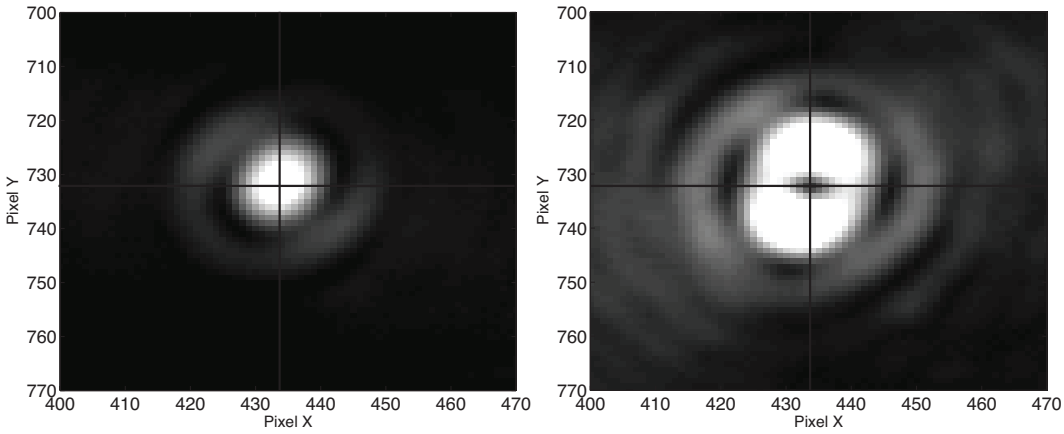


Figure 5.11: Backreflection of excitation beam (left) and STED beam (right) onto the CMOS camera. Two criteria can be applied to decide whether the beams are aligned and going straight into the objective: when focussing through the coverslip-water boundary, the diffraction pattern has to be concentric and the intensity of the diffraction pattern has to be symmetric to all sides.

In general, if this overlap is done correctly, only slight changes to the placement of the excitation PSF have to be undertaken when overlapping the two PSFs later on with gold beads.

#### 5.2.3.2 Polarization

To create a donut-shaped PSF, it is crucial to change the polarization of the STED laser to circular right before the beam enters the objective [153] [154]. This is ensured in this setup by replacing the objective with a Glan-Thompson laser prism (G033217000, QIOPTIQ, Paris, France) in a rotational mount with servodrive (G065117000, QIOPTIQ, Paris,

France). The aperture is decreased with an iris (SM1D12D, Thorlabs, Dachau, Germany) in such a manner that the laser prism is not overfilled with the expanded beam. A conventional power meter head (S120C, Thorlabs, Dachau, Germany) is connected to an USB analogue signal input box (NI6009, National Instruments, Austin TX, USA) and the incoming signal is analyzed with NI Signal Express. This process is shown in figure 5.12.

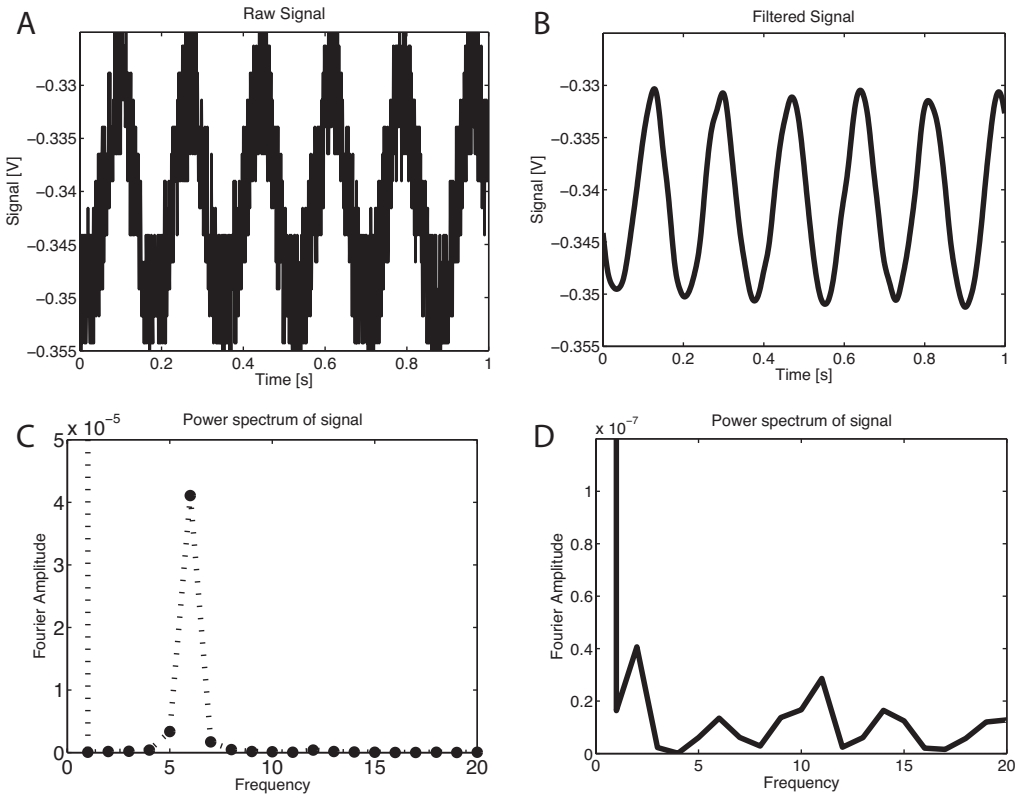


Figure 5.12: Signal processing for circular polarization: A) the raw data is filtered B) with a low-pass filter to get rid of the noise and C) afterwards fourier-transformed. To achieve optimal polarization, the half-wave and the quarter-wave plate are turned in such a manner that the peak at 6 Hz gets in the same range as the noise ($\sim 10^{-7}$), as shown in D).

The servo motor is supplied with 10V and turns with six rotations per second. The incoming signal from the power meter head is smoothed and Fourier transformed. With the help of this generated power spectrum, it is possible to turn the half-wave plate and the quarter-wave plate in such a way that the remaining polarization of the incoming STED beam is negligible. To fully achieve a circular polarization, it is also necessary not only to rotate the quarter-wave plate, but to also tilt it with regard to the beam. This leads to a fourier amplitude that is in the range of approximately $10^{-7}$.

#### 5.2.3.3 Alignment of detection path

In order to ensure that the excitation and detection volumes overlap, detector and pinhole are aligned with a *3 nM* sample of Atto655 (ATTO-TEC GmbH, Siegen, Germany).

This concentration yields a correlation height *G(0)* of *0.06 - 0.09*, dependent upon the penetration depth of the focus into the sample. This dependence is caused by the use of an oil immersion objective and hence the PSF is the more distorted the deeper the focus is inside an aqueous sample. Figure 5.13 depicts that the diffusion time of this dye can be influenced by switching on or off the STED laser beam, as visible when comparing the red and blue curve.

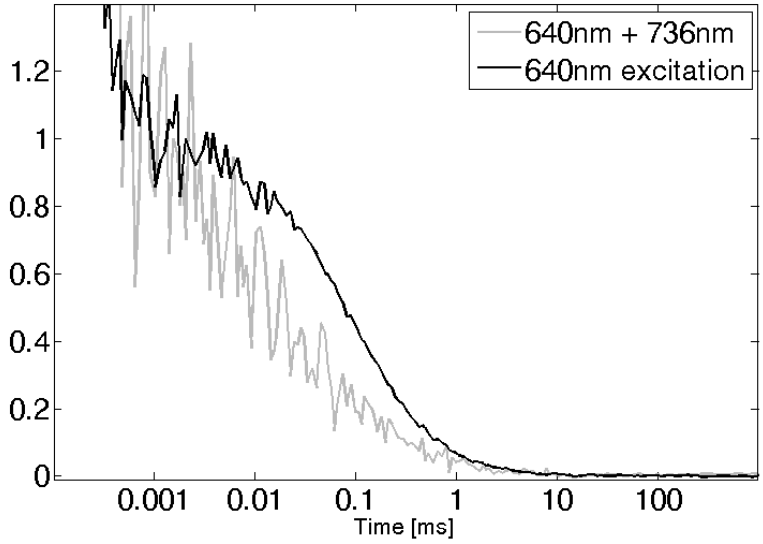


Figure 5.13: FCS curves with and without the STED laser. As clearly visible, the diffusion time decreases when the STED laser is switched on. At the same time, the statistics gets worse due to a decrease in count-rate. The measurement time was kept constant at 45s.

When decreasing the confocal volume with the help of the STED laser, the diffusion time decreases as well, but at the same time the signal-to-noise ratio goes down as well for the same measurement time. This caused by two effects: First, the desired effect of depletion in the outer PSF regions diminishes the number of photons, but at the same time the STED laser contributes significantly with background photons to the amount of collected photons. As shown recently by *Hendrix et. al* [155], the significant amount of laser light bleaching through the emission filters also decreases the height of the correlation curve. This is not visible in this graph, since both curves are normalized to 1, but should be considered when aligning the detection path with this method.

#### 5.2.3.4 Timing of the lasers

For an efficient STED process to take place, it is crucial that the timing between the incoming excitation laser and the depletion laser is correct. The excitable electron has to have enough time to relax to the ground state of the $S_1$-level. But it should not to be allowed enough time to fluorescence spontaneously. This means that the optimal timing of the STED laser is $400ps$ after the excitation laser. But this timing is highly dependent

on the duration of the excitation laser pulses itself. In order to most efficiently check the timing of the two lasers, the emission filter in front of the detector is replaced with an OD 4 filter (Thorlabs, Dachau, Germany) and the power of the STED laser is additionally reduced with an OD 5 filter (Thorlabs, Dachau, Germany). Accordingly, both lasers are focussed onto the boundary surface between a glass coverslip and a drop of water. Figure 5.14 a) shows the IRF of both lasers. By measuring scattered light rather then fluorescence, the two histograms are not convoluted with the lifetime of a dye. In order to see, when the depletion is most efficient, the following procedure was carried out: all ND filters were removed and to the emission filter for Atto655 was installed again. The arrival of the STED laser was kept fixed, while the timing of the incident excitation pulse was varied with different cable lengths between the trigger pulse of the STED laser and the excitation laser.

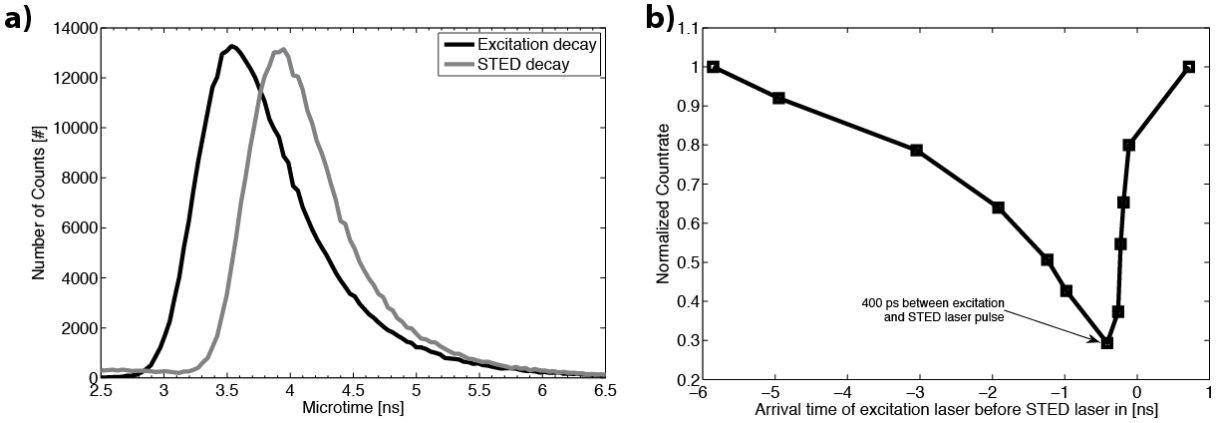


Figure 5.14: a) Lifetime histograms of both lasers, focussed onto the boundary surface of glass coverslip and a water droplet. b) Count rate as a function of time between laser pulses and depletion of a $3nm$ Atto655 solution.

Figure 5.14 b) shows the drop in the countrate due to depletion by the STED laser with respect to its arrival time after excitation. Here, it is obvious that there is an optimal timing between laser pulses of 400 ps. If the STED laser follows to closely to the excitation, the STED process is not sufficient due to the molecule not having relaxed to the $S_1$-ground state (right side of the minimum). If the STED laser arrives too late, most of the fluorescence has already occurred and no effect is visible. Hence, the timing is a crucial part of the alignment of the setup and should be carried out on a daily basis.

#### 5.2.3.5 Gold bead scans

The scan of 150*nm* gold beads (SigmaAldrich, Taufkirchen, Germany) is carried out in order to visualize the PSF. Here, the filters are again changed as described above: the emission filter is replaced by an OD 4 filter and the power of the STED laser is diminished with an OD 5 filter in front of the fiber. Accordingly, single gold beads are scanned in all three dimensions (*XY*, *YZ* and *XZ)* in order to optimize the donut and the excitation PSF.

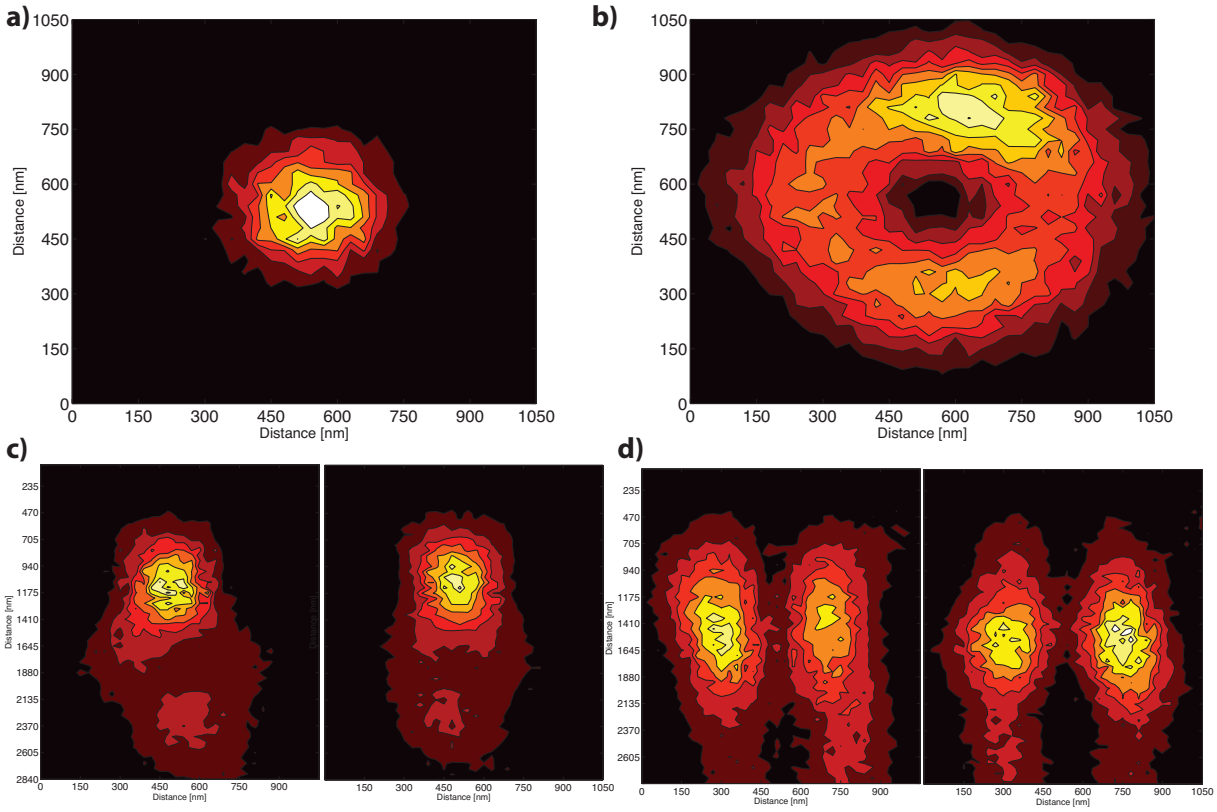


Figure 5.15: Bead scan of a 150nm gold bead. a) Excitation PSF in the *XY*-plane b) STED PSF in the *XY-plane* c) the *XZ*- (left) and *YZ* (right) plane of the excitation PSF d) the *XZ*- (left) and *YZ* (right) plane of STED PSF.

There are two reasons why this step is carried out: one the one hand, it becomes very easy to tell whether the excitation PSF is exactly concentric with the donut of the STED PSF. As can be seen from figure 5.15 c) and d), the excitation PSF is placed slightly higher than the STED PSF. This is not a real concern, but should be changed with an adaptable collimator for the red 640nm laser. On the other hand, one can check on the shape of especially the STED PSF. If the donut is not concentric or would be tilted in space, one has to correct that with alignment of the phase plate.

#### 5.2.3.6 Crimson bead scan

In order to finally check the functionality of a the STED microscopy, a sample of sparsely spread fluorescent beads (Crimson beads, 20nm, Life Technologies, Carsbad, CA) is imaged with and without the STED laser.

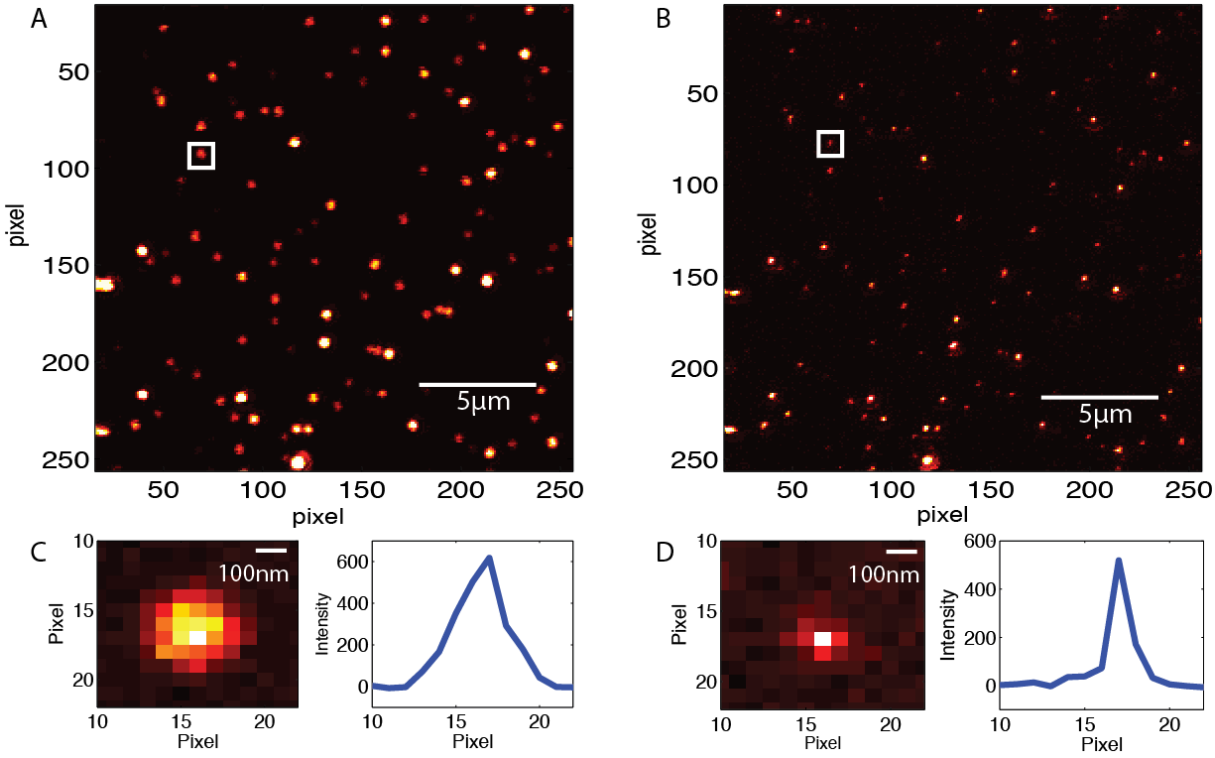


Figure 5.16: Image of a 20nm Crimson beads on the surface of a glass coverslip. A) 20 x 20µm scan with excitation laser only B) Same region of interest with the STED laser at $25mW$ at the backfocal plane of the objective C) Zoom-in on a single bead with excitation laser only and corresponding cross-section with $FWHM = 270nm$ D) Zoom-in with activated STED laser resulting in a $FWHM = 87nm$. Remarkably, the intensity in the brightest pixel is barely decreased. This hints to a perfect donut, leaving no residual intensity in the middle of the STED PSF.

Figure 5.16 A and B show a number of crimson beads that are visible in a ROI of $20x20$µm. The difference here is already clearly visible, but becomes more apparent when imaging a single bead, as shown in 5.16 C and D with the corresponding cross-sections. One feature of the cross-section of both beads should be considered: the intensity in the middle of the bead - with or without STED beam - should not differ by more than 10 percent. If the STED image suffered from a general diminished brightness, this would be a hint that the middle of the donut is not exactly zero and hence the polarization of the STED beam should be adjusted. In this set of images, the width (FWHM) of the PSF from a single bead decreases from $270nm$ to $87nm$ with a STED intensity of $40mW$ at the back aperture of the objective.

Figure 5.17 demonstrates the resolving power of the microscope. While in panel A)

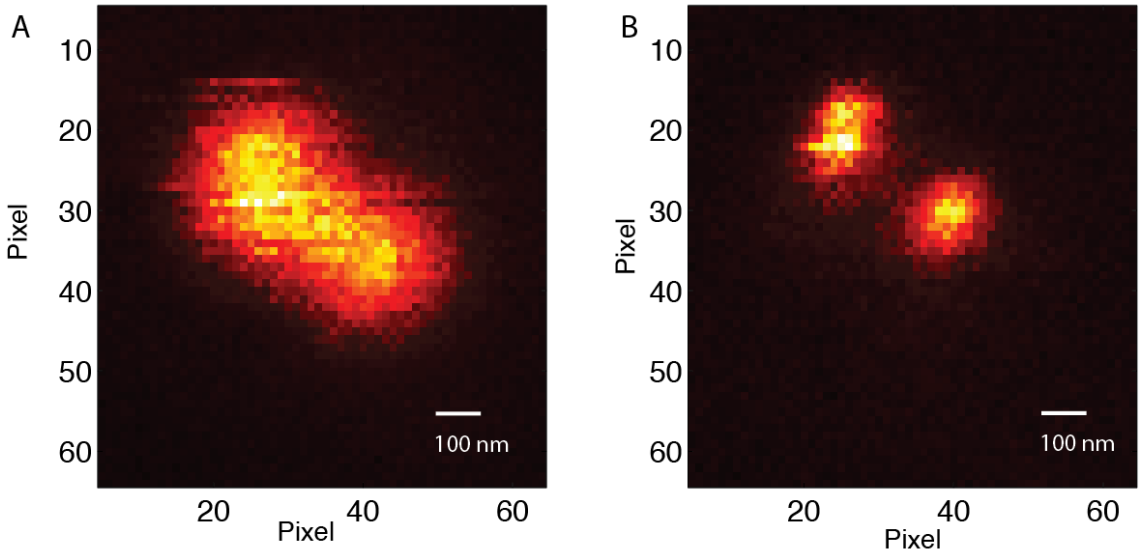


Figure 5.17: Demonstration of the resolving power of the microscope: While the shape of the fluorescent region in A) can only be guessed as two beads, B) shows clearly that only two beads are accountable for the resulting fluorescence. Image B) was taken with 25mW of STED laser power.

it is not possible to clearly identify the number of fluorescent beads, panel B) shows that two individual beads are responsible for the resulting image. This figure is at the same time an impressive demonstration for the Sparrow criterion, discussed in chapter 3. While the distance of $290nm$ is close to the width of one PSF, the two peaks are not resolvable anymore and do not meet the Sparrow criteria. With the STED image, the two fluorescent beads are easily discernible.

As already mentioned, a crucial point is the laser power of the STED laser. In order to test the gain in resolution with increasing amount of depletion photons, a series of images is taken with varying laser power. Figure 5.18 shows a crimson bead scan with $0mW$, $25mW$, $40mW$ and $60mW$ STED laser power, respectively. While the FWHM of the bead scan shrinks from $290nm$ to $80nm$ and further down to $75nm$ at $40mW$, it increases for the highest STED power to $90nm$. There are two things certifiable from the cross-sections: first, while the STED donut has an acceptable residual intensity in its middle for $25mW$ - the intensity of the bead scan image decreases only from 400 to 360 counts in the brightest pixel - the number of counts diminishes significantly for $40mW$ and $60mW$, showing that at these laser powers the zero at the middle of the donut of the STED beam is not given anymore. Second, the background contribution of the STED laser is approx. 20, 23 and 60 counts per pixel, respectively. Both points taken together lead to a decreasing signal-to-noise ratio for increasing laser powers. When measuring the $FWHM$s of the individual STED images, the result is $80nm$, $75nm$ and $90nm$. This means that although the resulting resolution appears smaller in panel D) than in B), the measurable gain is annihilated by the decreasing signal-to-nise ratio. Hence, the laser

power of both lasers should be well adjusted to the sample and great care should be taken to optimize the signal-to-noise ratio.

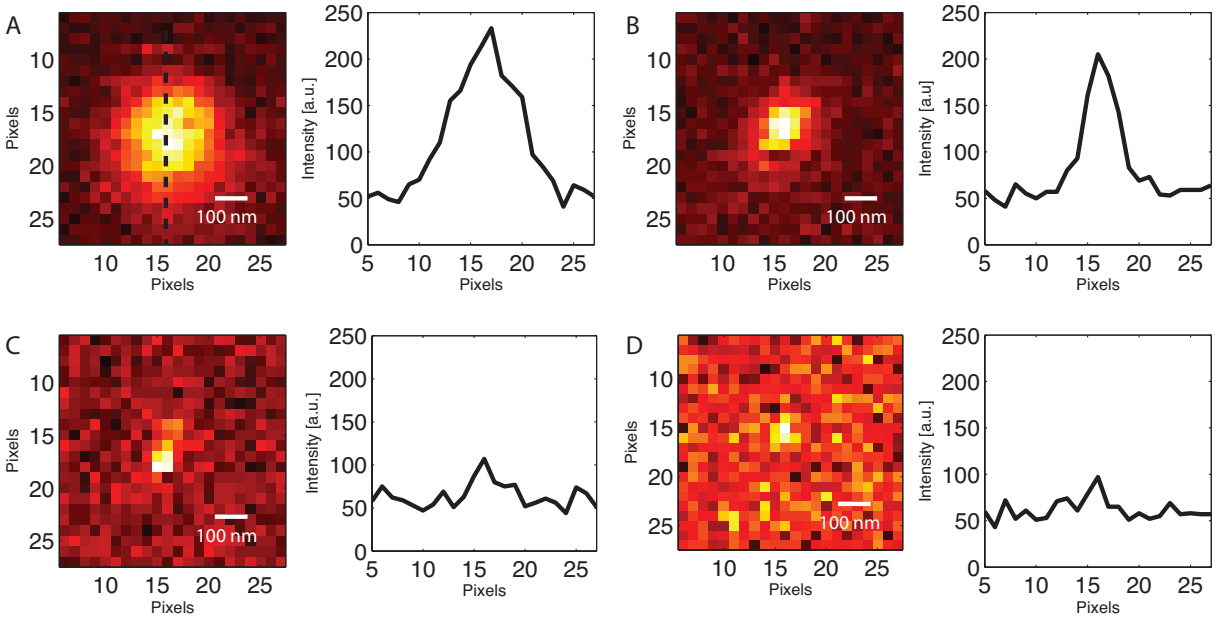


Figure 5.18: Crimson bead scan with increasing depletion laser power and the corresponding cross-section (indicated in image A for all cross-sections) through the center of the bead. A) Diffraction limit PSF with $FWHM = 290nm$ B) STED laser power of $25mW$ and resulting PSF with $FWHM = 80nm$ C) STED laser power of $40mW$ and resulting PSF with $FWHM = 75nm$ D) STED laser power of $60mW$ and resulting PSF with $FWHM = 90nm$

### 5.2.4 Outlook for the STED Setup

This chapter has given a thorough theoretical description of the basis of the stimulated depletion emission and accordingly specified the instrumentation of the setup assembled during this work. While all necessary steps to characterize and align the setup have been described, it should be mentioned that the timing of the lasers, their optimal overlap and the STED PSF design are the key steps to achieve a working STED setup. While all these requirements have been met and the functionality and the reliability of the setup have been shown, there are several ways to improve the capabilities of the setup:

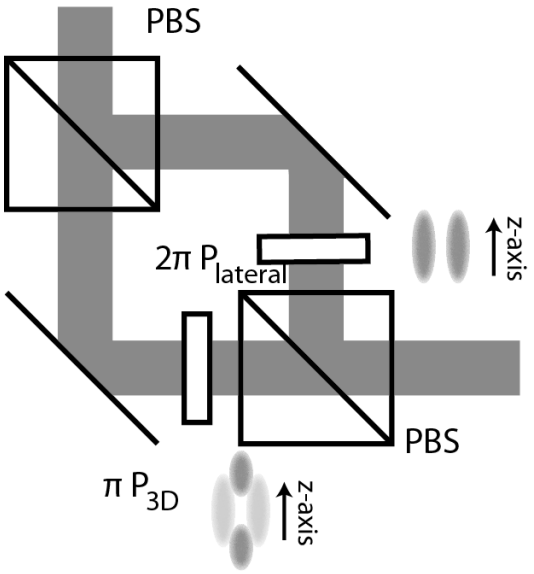


Figure 5.19: STED beam path with a second phase plate for a depletion above and below the actual excitation focus. The resulting PSFs are shown next to the phase plates.

The first improvement would be to implement a second phase plate that modulates the focus in such a way that depletion above and below the focus would also occur [156]. The design of such a beam path, including a $2\pi$-vortex phase plate and a $\pi$-phase retardation plate is shown to the right. The STED beam is split by a polarizing beam splitter, passes the corresponding phase plate and is combined again with a polarizing beam splitter. In essence, three beams have to be overlaid in the focus, but the result is a depletion in all three dimensions, making a resolution of down to $100nm$ along the z-axis possible.

The second improvement would be to expand the setup to a second or even third wavelength. A three-color setup would be realized for example by expanding the current setup with a laser at $490nm$, exciting EGFP and mCherry, depleting them at $590nm$ and splitting their fluorescence into two detection channels. This allows e.g. collocalization studies on the nanometer scale, making predictions about interactions of molecules and their placement more accurate and reliable. One possible way to achieve this, thereby maximizing the use of the available resources, would be to convert the Chamelion Ultra II laser with the help of a supercontinuum generation kit into a supercontinuum laser, i.e. creating white light with the spectrum of $400nm - 1200nm$ from the $800nm$ output of the laser. Accordingly, it is easy to split of the necessary excitation and depletion wavelengths with filters or an acousto-optical tunable filter. The disadvantage of combing several colors on the STED setup is clearly that for every color two, or in the case of 3D-STED even three PSFs have to

be overlaid, generating up to nine PSFs for three colors. Making such a setup insensitive against drift, may it derive from temperature fluctuations or mechanical vibrations, would have the highest priority and might make alignment a challenging task.

# Chapter 6

# Effect of Salts onto the Unfolding of an $\alpha$-Helix

The results of this chapter have been published in the Biophysical Journal [157].

## 6.1 Proteins - Assembly, Structure and Folding

Besides the fact that up to 70% of all the mass in living cells is actually water, four groups of molecules play the most important roles [158]: *lipid bilayers*, formed for example by phosphatidylcholine and phosphatidylethanolamine, enclose the contents of the cell and provide a barrier to separate inner and outer compartments of cells. At the same time they serve as an anchoring spot for the cytoskeleton to supply stability and communication with the environment. *Carbohydrates*, often uptaken in the form of various sugars and converted into the universally accepted currency of *ATP*, serve as the energy supply. Chains of *nucleic acids* (deoxyribonucleic acid - DNA and ribonucleic acid - RNA), as a third group, are used to store and pass on information. Given the need for keeping this information well protected, it is not surprising that of all four classes, this one is particularly stable when it comes to environmental influences like heat or chemicals. The last group, *proteins,* are nature's "workhorses" and fulfill most of the functions within a cell [159]. Unlike the first three groups, proteins are far more complex and hence it is not so easy to deduce their function from the chemical structure. However, for the viability of the cell, it is crucial that proteins fulfill their designed duty. For this step to successfully happen, proteins have to fold from a polymer into their active state. This transition will be discussed in this chapter.

### 6.1.1 Protein Assembly and Structure

The structure of proteins is encoded in the DNA. In essence, three basepairs stand for one of the twenty-two amino acids (aa), which are the building blocks of all proteins. Twenty

of these are used ubiquitously, while the remaining two, selenocysteine and pyrrolysine, are used in only very special organisms. For the production of proteins, DNA is first transcribed to messenger RNA (ribonucleic acid) and, accordingly, translated with the huge machinery of the ribosome to a polypeptide chain. Monomeric amino acids, each containing an amine- ($-NH_2$) and a carboxy- ($-COOH$) group, form a very stable peptide bond upon reaction (as displayed in figure 6.1 a). The number of connected amino acids can range from ten to several thousand units [160].

As already visible from figure 6.1, all amino acids feature the same backbone. Only in position, at the central carbon atom, each amino acid features a characteristic substituent. This fourth substituent contains either polar, charged or hydrophobic groups. The number and the order of the amino acids combined in one peptide chain determine the unique *primary structure* of each protein.

The *secondary structure* of protein results from parts of the primary structure folding into local, specific 3D structures. There are two types of secondary structures that are prominent due to their stability: the first one is the $\alpha$-helix, a right-handed spiral with $\approx$ 3.6 amino acids per turn (figure 6.1b displays an $\alpha$-helix made of 14 repetitions of alanine and lysine, see chapter 6). This structure is stabilized through a hydrogen-bond of a backbone $N-H$ group interacting with another backbone $C=O$ group, four AA down the chain. Peptides that are rich in the AA alanine are prone to form $\alpha$-helices while, for example, the AA proline is too rigid to be integrated into a helix and, hence, is used by nature to break up such a structure. The second most common secondary structure is the $\beta$-(pleated) sheet. Those structures are not completely flat, but rather pleated, e.g. like the bellows of an accordion. To create this structure, several parts of the poly-peptide chain are oriented in a parallel or anti-parallel manner, so that sheets result as an overall structure. A famous example for a protein which contains $\beta$-sheets is fluorescent protein eGFP, a so-called $\beta$-barrel (a zoom-in on one of the $\beta$-sheets of eGFP [162] is displayed in figure 6.1c). Easy identifiable is the parallel line up of oxygen atoms (red) that form bonds to the hydrogen atoms attached to the nitrogen atoms in blue. These bonds are responsible for the rigid charakter of the $\beta$-sheets. Besides these two prominent secondary structures, also $\pi$-helices, $3_{10}$-helices, left-handed $\alpha$-helices, $\beta$-turns and random coil motives exist.

Normally, one peptide chain folds into several secondary structure elements. The secondary structure elements, in turn, fold into a 3D *tertiary structure*. Folding of secondary structure elements into a compact globule is mainly driven by the exclusion from water from hydrophobic amino acid side chains. These non-specific hydrophobic interactions form a core, and accordingly the overall structure is stabilzed by tertiary interaction, e.g. salt bridges, $\pi$-$\pi$ stacking of side chains and disulfide bonds. The thermodynamic hypothesis [8], formulated by nobel laurate Christian Anfinsen and hence called Anfinsen's Dogma, states that this tertiary structure is already determind by the sequence of

amino acids. This is at least true for smaller proteins and is a very crucial step in protein folding, because the tertiary structure is responsible for the correct functionality of the protein. Figure 6.1d) shows the correctly assembeled actin monomer that consists of several $\alpha$-helices (purple), $\beta$-sheets (yellow), $3_{10}$-helices (blue), turns (cyan) and random coils (white).

The highest order structure, the *quaternary structure,* is reached, when several folded poly-peptide chains are assembled into a multi-subunit complex. Figure 6.1e) shows a filament of actin that consists of several monomers. The higher order structures are held together by non-covalent bonds and often disulfide bridges, as described for the tertiary structure.

### 6.1.2 Protein Folding

Proteins fulfill a vast variety of functions within living organisms and are involved in nearly every step. This ranges from metabolism over sensing and reacting to the environment to duplication of the DNA and production of other protins, only to name a few. Biosynthesis, the assembly of proteins by the ribosome machinery, yields unfolded chains of polypeptides. In order to carry out their preset task, nearly all nascent chains have to fold into their unique, native form[1]. This fully functional form is accompanied by a free-energy ($\Delta G$) minimum, when all possible conformations of the chain are considered on a free-energy landscape.

There are severe consequences that result from incorrectly folded proteins: not only the intended function is disturbed in most cases, but misfolded proteins may also exhibit toxic behaviour. It is believed that several neurodegenerative diseases result from agglomerating amyloid fibers that originate from misfolded proteins [163] .

As already stated above, the sequence of an AA poly-peptide chain already determines the native conformation after folding. While a number of proteins fold while or after biosynthesis, one should consider that this process is heavily dependend on the environment like the hydrophobicity of the solvent, pH, ion concentration, or the presence of proteins that assist in folding, so called chaperons. There are two big driving forces behind protein folding: one is the reduction of contacts of hydrophobic AAs with the hydrophilic environment (water) and the other is the formation of intramolecular hydrogen bonds[2]. Since proteins can't screen all possible conformations (Lenvinthal's paradox [7]), there are two mechanisms that are at the moment debated in literature. These two result directly from the two driving forces that minimize the free energy. The first one is

[1] Intrinsically unstructured proteins broke up the paradigm that well defined structure is indeed needed for functionality. These disordered proteins often fold into a fixed structure upon binding to other proteins.

[2] Deechongkit *et al.* [164] showed that the contribution of individual hydrogen bonds is not equivalent for the minimization of the energy landscape: while hydrogen bonds of hydrophobic side chains with other hydrophobic residues contribute more, hydrophilic aa can exhibit hydrogen bonds with water as well and therfore contribute less to the overall stability.

the *diffusion collision model* [165], where a initial molten globule core is formed on the basis of hydrophobic interactions. Afterwards, secondary structures are formed and, by diffusion and collision,ß bind in the correct conformation. The *nucleation-condensation model*, on the other hand, suggests that secondary structures as well as tertiary structures are formed at the same time and nearly all residues in the chain form bonds that stabilize the native structure [166]. Examples of proteins that fold in one or the other way are known and which mechanism is predominant seems to depend on the amount of secondary structure present and the ratio of hydrophilic to hydrophobic residues.

Chapter 6 of this work will focus on the process that takes place when proteins are forced to unfold and chapter 7 will discuss several influences on the folding efficiency of the fluorescent proteins eGFP and mCherry.

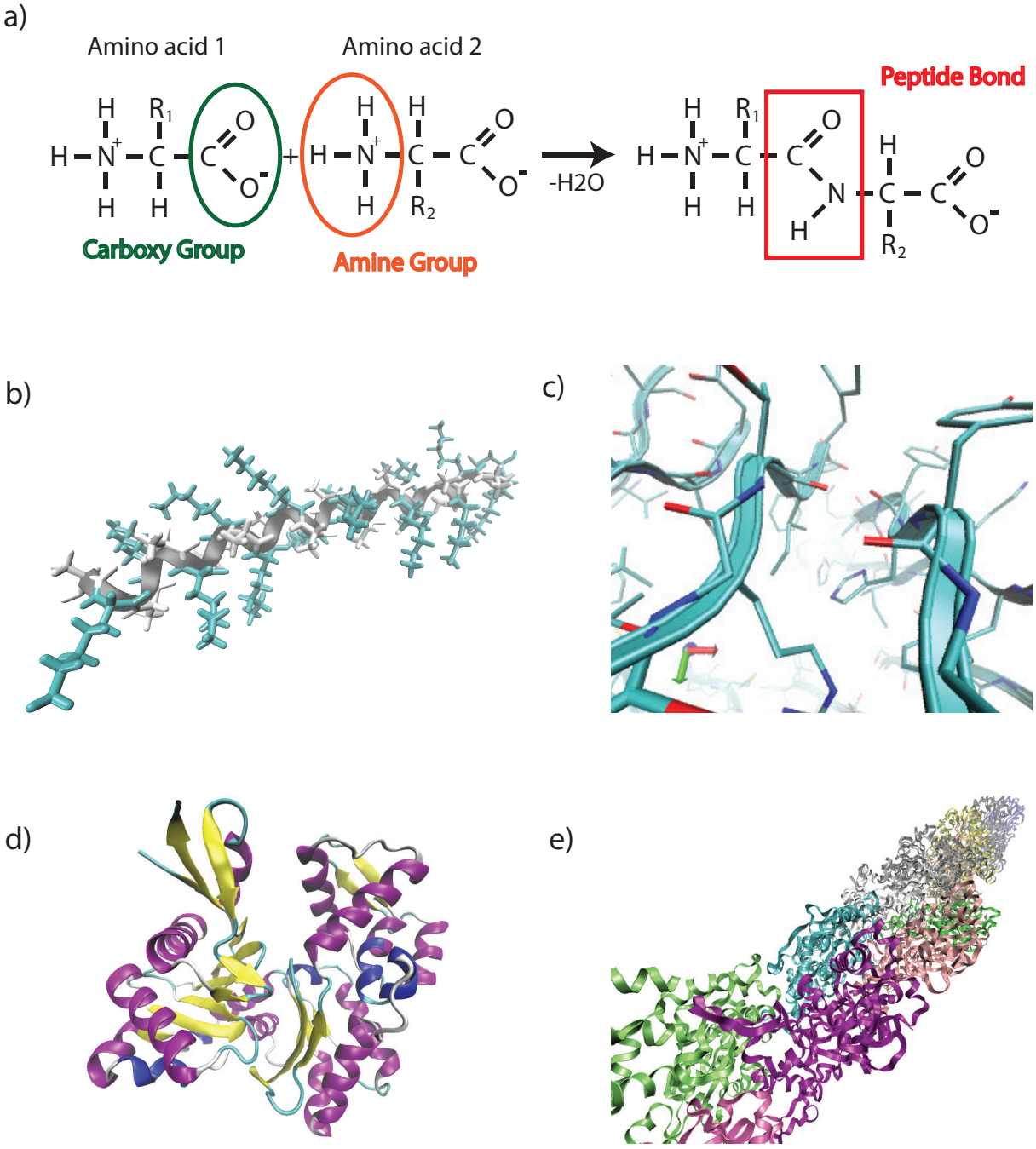


Figure 6.1: Structure of proteins: a) Origin of the primary structure. The poly-peptide is composed of individual amino acids that react and form a polymer. This process is thermodynamically driven mainly by the production of water and the energeticaly favourable formation of the peptide bond. b) and c) Two examples of secondary structure. While the $\alpha$-helix, in this case a sequence of 14 repetitions of alanine and lysine, gives flexibility to the system, the $\beta$-sheets are able to form a rigid layer (excerpt from the PDB structure of eGFP: 3EVP). Noticeable is the parallel line-up of oxygen atoms (red) that form bonds to the hydrogen atoms attached to the nitrogen atoms in blue. d) Tertiary structure of actin with different secondary structures forming one globular protein (PDB structure: 3HBT). $\alpha$-helices are displayed in purple, $\beta$-sheets in yellow, $3_{10}$-helices in blue, turns in cyan and random coils in white. e) Quaternary structure of an actin filament with each individual peptide chain in a different color (PDB structure: 3B63). Structures were taken from the RSC protein database http://www.rcsb.org and visualized using VMD [161]

## 6.2 Scope of this Project

Franz Hofmeister described in 1888 the ability of different salts to precipitate or dissolve proteins on an empircial basis [167]. In despite of the ensuing 125 years of scientific research, a coherent understanding of ion-specific (Hofmeister) effects in biochemical processes remains a challenging task [168–172]. Salt effects are in particular important for the characterization of intermediate states during the process of protein folding. For instance, salts such as $NaSO_4$ or $KF$ typically stabilize native protein conformations whereas $GdmCl$ is a widely used as denaturandtwhose molecular mechanism of action is still being debated [173]. Other ions, such as $ClO_4^-$, $I^-$, or $SCN^-$ are known to promote denatured states. The structural character of these denatured states, however, remains obscure and is often loosely interpreted as compact dry molten globule [174] - "an expanded form of the protein that lacks appreciable solvent" [175]. Due to the complexity of competing nonpolar and polar solvation at biological surfaces, the detailed molecular understanding of the action of those salts on protein structures is still a subject of intense investigation.

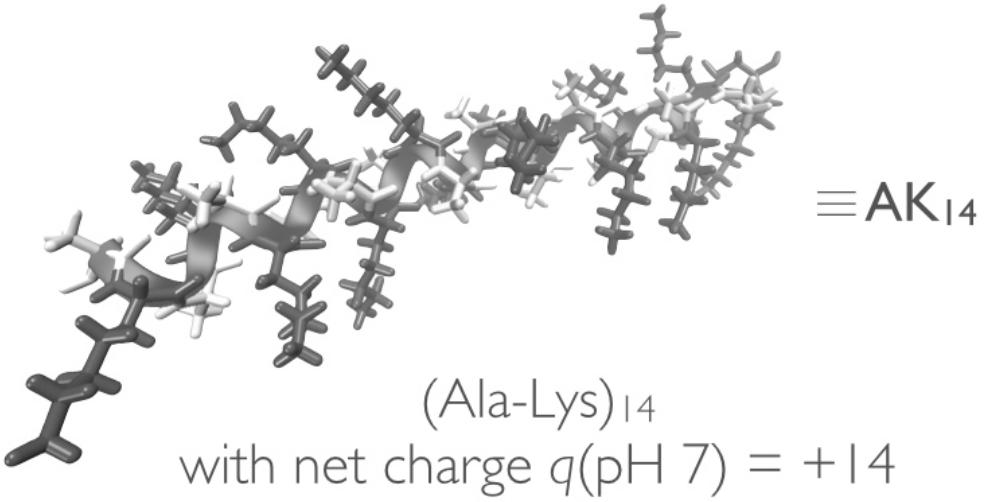


Figure 6.2: Schematic of the model peptide $(AK)_{14}$ peptide investigated in this chapter, shown in its fully folded state.

In the following chapter of this work, the ion-specific effect of various salts ($KCl$, $NaClO_4$, and $GdmCl$) on the structure of a model peptide $(AK)_{14}$ are elucidated. Single-molecule Förster resonance energy transfer (smFRET) experiments as a function of salt concentration are performed in order to investigate contradtictions that arise from circular dichroism measurments and atomistic computer simulations. Further molecular dynamics (MD) simulations give molecular insight into the binding mechanism of these particiular salts. In a final step, MD and smFRET experiments are combined to elucidate the strong

structural diversity of denatured states that are induced by the different unfolding reagents $NaClO_4$ and $GdmCl$.

## 6.3 Status Quo of CD-Spectroscopy and MD-Simulations with $(AK)_{14}$

To investigate the effect of different Hofmeister salts (KCl, NaClO4, and GdmCl) on the secondary structure of a model $\alpha$-helix (a net-charged $[(AK)_n]$), circular dichroism (CD) measurements were performed. All CD measurements and MD simulations in this paragraph were carried out with a chain length of $n = 6$. This was necessary to reduce computational efforts for the simulations. smFRET experiments were carried out with a longer peptide of $n = 14$ in order to achieve a reasonable inter-dye distance $R_{DA}$. Despite the differences in chain lengths, the results for both peptides provide the same trend.

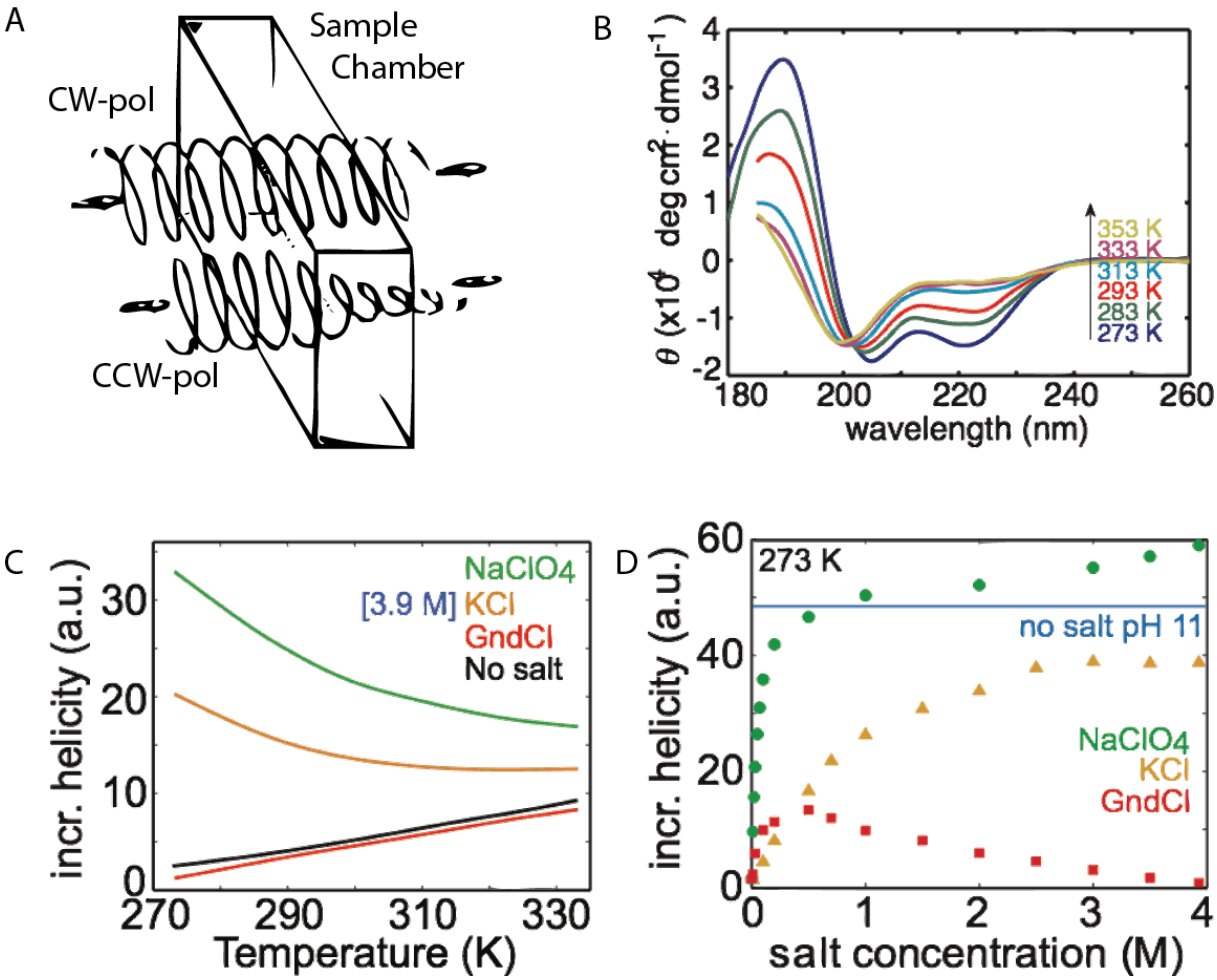


Figure 6.3: CD measurements of $(AK)_{14}$ measurements: A) Principle of CD spectroscopy: the sample is irradiated with clockwise and counter-clockwise polarized light and the delta absorbance as a function of wavelength is measured. B) CD spectrum of $(AK)_{14}$ with $3.9M$ $KCl$ as a function of temperature: the characteristic dip at $222nm$ flattens out with temperature C) Temperature behavior for $(AK)_{14}$ peptide with different salts: For $NaClO_4$ and $KCl$, where helicity is already present at $273K$, this helicity decreases, wheareas, for the other conditions, it becomes possible to form initial helical structures. D) Amount of helicity for the $(AK)_{14}$ peptide as a function of salt and at pH 11 where all side chains are not charged at $273K$.

The principal of CD spectroscopy is shown in figure 6.3A. The CD spectrum of proteins in the far UV region is often used to determine the amount of secondary structure [176]. This works well for structures like the $\alpha$-helix, $\beta$-sheets or random coil structures. Since CD spectroscopy can be used to determine the amount of a particular secondary structure present in a sample, but not their position within the protein, it is extremely usefull for detecting changes in conformation[3]. Figure 6.3B shows the result of a CD spectrum of $(AK)_6$ in $KCl$ for different temperatures. The characteristic double well with a dip at $222nm$ gets shallower with increasing temperature, indicating that more and more helical turns are broken up.

The investigated $(AK)_n$ peptides carries a net charge of either +6 or +14 elementary charges. Thus, in the case of no salt (6.3C, black line), compact helical states are energetically forbidden due to electrostatic repulsion between the side chains. As anticipated, the stabilization of the helical state due to electrostatic screening is observed in CD measurements, as shown in 6.3D. With the exception of $NaClO_4$, the stabilization of the peptides is nonspecific for salt concentrations $c < 0.5M$. Hence, it is a purely screening effect and strong ion-peptide interactions can be ruled out for these concentrations. For higher concentrations, the stabilization is highly salt specific and we observe the order $NaClO_4 \sim KF > KCl \sim NaCl > GdmCl$. $GdmCl$ destabilizes $\alpha$-helical content for the peptide at concentrations above $0.5M$, giving rise to a remarkable nonmonotonic helicity versus concentration curve. Submolar $NaClO_4$ concentrations appear to be especially strong at stabilizing positively charged peptides (6.3D, green dots), in line with previous work [177]. This indicates that screening of the positively charged side chains by binding of the $ClO_4^-$ anion is very effective. To test this hypothesis, CD spectra of $ClO_4^-$ with a negatively charged peptide are taken, where lysine is exchanged with glutamate (data not shown). The charge pattern is therefore the same, but the positively charged $(AK)_6$-peptide features a 10% better helix stabilization. Figure 6.3D shows another measurement condition: the case of a salt free buffer at pH 11. This is above the isoelectric point of lysine and hence the helix is charge-free, enabling full formation of the helix without any salt. This condition provides a positive control for the highest possible helicity without any salt pertubating the measurement.

At molar concentrations, however, the behavior of $NaClO_4$ for the $(AK)_6$-peptide, is in contrast to what is expected from the Hofmeister series ranking [170]: the $NaClO_4$ stabilization capacity is much larger than for $KF$ in the case of $(AK)_6$. The expectation for $NaClO_4$ comes from its high salting-in constant [171] and its strong interaction with the peptide (amide) group. This places the $ClO_4^-$ ion in a similar location to $Gdm^+$ in the Hofmeister series and far from $F^-$ in opposition with the observations made here.

[3]Usually the delta absorption $\Delta A = A_{counter-clockwise} - A_{clickwise}$ is measured. Due to historical reasons $\Delta A$ is converted via Beer's law into the molar circular dichroism $\Delta\epsilon$: $\Delta\epsilon = \Delta A * C * l$ and further into the molar ellipticity $[\theta] = 3298.2 * \Delta\epsilon$

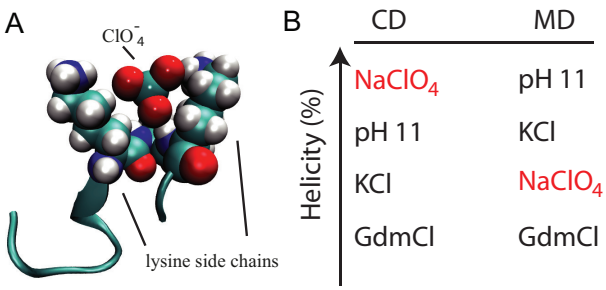


Figure 6.4: (A) A $ClO_4^-$ -ion hydrogen bonded to the backbone amide and embedded by lysine side chains in the $(AK)_6$ peptide. (B) Concrete comparison of helicity between CD measuremeants and MD simulations.

In order to quantify the interaction of the $Gdm^+$-ion with the peptide, which leads to the highest helicity at molar concentration, all-atom molecular dynamics simulations were carried out. As already suggested from the CD measurements, the ionic density distribution provides a consistent molecular picture: $ClO_4^-$ strongly interacts with the polar (amide) group and has a distinct affinity to hydrophobic groups. A representative MD snapshot for a $ClO_4^-$-ion bound to the peptide with long lifetimes ($> 1ns$) is shown in figure 6.4A. $ClO_4^-$ hydrogen-bonds to the amide while at the same time embedded between nonpolar groups, such as ALA methyl groups or the greasy lysine side chain. For $NaClO_4$, both ions have a strong affinity to the backbone, resulting in a concerted binding to multiple peptide groups.

Figure 6.4B gives a concrete comparison between the results derived from CD measurements and the corresponding MD simulations. The agreement for the order of $pH11 > KCl > GdmCl$ is striking. But the most noticable element in this comparison is $NaClO_4$: it is the ion that leads to highest helicity in the CD measurements but shows the least helicity in the MD simulations. In order to resolve this contradiction, smFRET on the $(AK)_{14}$-peptide in different environments were carried out.

## 6.4 Throwing sm-FRET Measurements into the Mix

To further elucidate structural characteristics of the peptide and the curious behavior of $NaClO_4$ in its impact of the $\alpha$-helical structure, the global conformation of the $(AK)_{14}$ peptide via smFRET was monitored. For this purpose, burst analysis measurements were performed with $\sim 10pM$ of $atto488-(AK)_{14}C-atto647N$ $[\equiv (AK)_{14}]$ in solution with increasing amounts of $NaClO_4$. They were compared with measurements in the presence of $KCl$ or $GdmCl$. Using the photon distribution analysis (PDA) on the experimentally measured FRET efficiency histograms, the donor-acceptor separation $R_{DA}$ was estimated together with the residual distribution width beyond shot noise. Figure 6.5 shows a representative FRET histogram and the corresponding distance distribution for $4M$ $KCl$. Additional FRET histograms and their PDA fits are shown in figure 4.11.

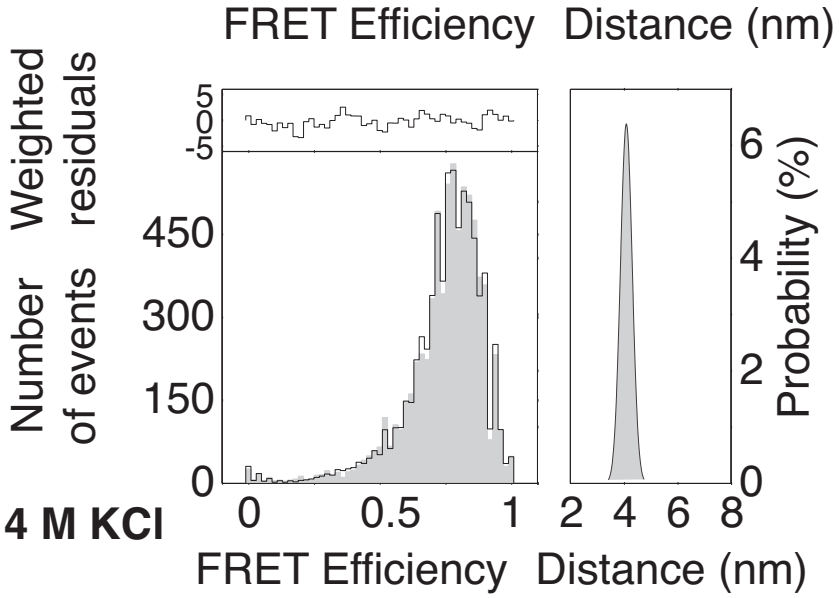


Figure 6.5: PDA of $(AK)_{14}$ in 4M KCl. Results from PDA fit (solid line) for experimental histogram (bars) with weighted residuals are shown. The estimated gaussian distance probability distribution for this condition is displayed next to the respective histogram.

Figure 6.6A gives an overview of all measured conditions: In the absence of any salt, the $R_{DA}$ of the $(AK)_{14}$-peptide is $4.7nm$, where MD-simulations indicate a slightly swollen coil due to the electrostatic repulsion. For comparison, FRET measurements have also been performed in a reference state at $pH = 11$ (where deprotonation of lysine residues should allow full $\alpha$-helix formation) yielding a $R_{DA} = 4.9nm$. Thus, $\alpha$-helical states without salt seem to have extensions similar to a coil state. Adding $GdmCl$ first increases $R_{DA}$ to $5.0nm$ and then decreases and settles at an average distance of 4.9 nm. At 4 molar $GdmCl$, the $R_{DA}$ is $5.1nm$ implying slight swelling of the coil. Submolar amounts of $KCl$ have a similar behavior as $GdmCl$, initially increasing $R_{DA}$ with salt and then reducing it at higher salt concentrations. Molar amounts of $KCl$ compact the peptide

to $4.1nm$ (figure 6.6A) while increasing helix formation (figure 6.6C and D). $NaClO_4$ starts to collapse $R_{DA}$ even at submolar amounts. This compression is considerably stronger for 4-molar $NaClO_4$ where $R_{DA}$ further goes down to $3.6nm$. Figure 6.6B shows the corresponding distribution widths beyond the shot noise from the PDA fit for the measurements in panel A.

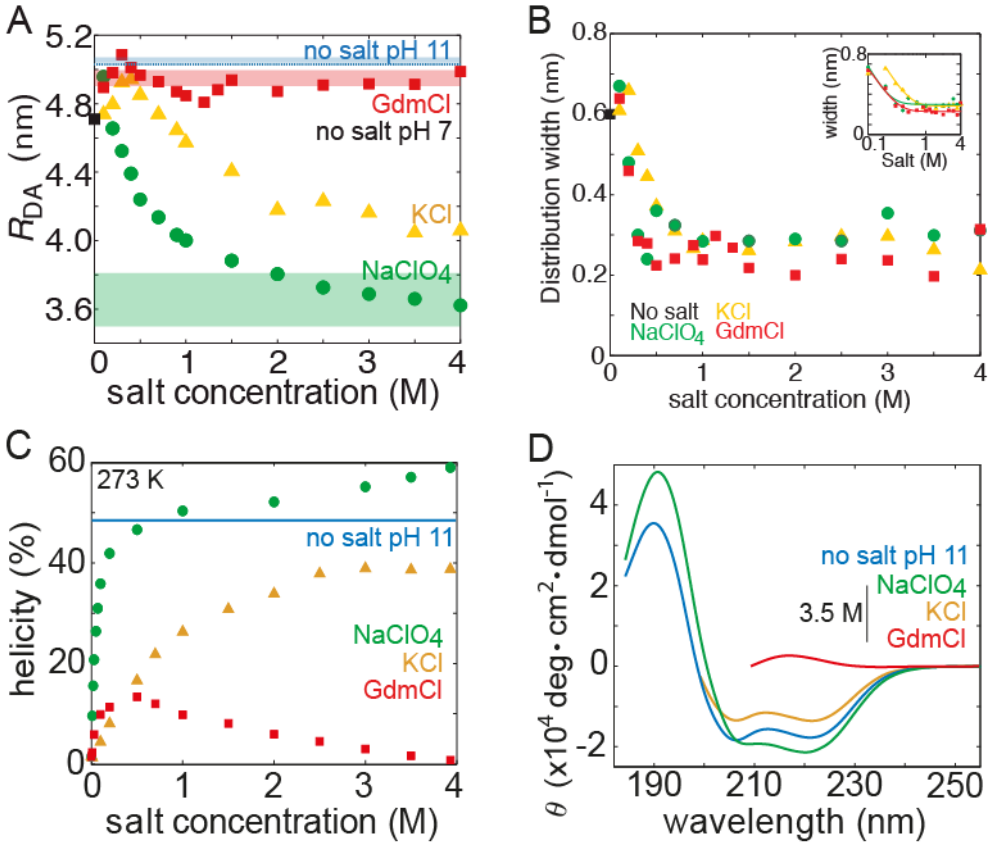


Figure 6.6: Ion specitfic effect on the CD spectra and donor-acceptor fluorophore separation $R_{DA}$ of $(AK)_{14}$. (A) Measured $R_{DA}$ (symbols) in the absence of salt at pH 7 (black), with $KCl$ (yellow upper triangles), $GdmCl$ (red squares), $NaClO_4$ (green circles), and no salt pH 11 (light blue line). Standard deviations from several measurements are smaller than the size of the symbol ($0.05nm$). Estimated range of $R_{DA}$ from MD-derived structures at $3.5M$ salt is represented as shaded areas depicting the upper and lower limits. (B) Structural dynamics of $(AK)_{14}$ vs. salt. The residual broadening of the single molecule FRET distribution of $R_{DA}$, beyond shot noise is plotted as a function of salt concentration. Inset, semilog plot of the data. (C) The salt-dependent helicity (derived from the signal at $222nm$) of $(AK)_{14}$ in the absence of salt at pH 7 (black), with $KCl$ (yellow), $GdmCl$ (red), $NaClO_4$ (green), and no salt pH 11 (light blue). The average value is a dotted line while the thickness of the shaded area represents the upper and lower boundaries. (D) CD spectra of $(AK)_{14}$ in the absence of salt at pH 7 (black), with $KCl$ (yellow), $GdmCl$ (red), $NaClO_4$ (green), and no salt pH 11 (light blue).

Although CD indicates a similar helicity for the peptide in $NaClO_4$ at $\sim 1.5M$ (or $KCl$ at $4M$) and $pH = 11$, FRET points to much more compact states in the $NaClO_4$ solution. To compare the FRET measurements with the results from CD, the CD spectra

of the $(AK)_{14}$-peptide are shown in 6.6B. As a reference measurement, we performed CD for $(AK)_{14}$ in the absence of salt at a $pH = 11$ where all side chains are deprotonated and the peptide is neutral, i.e., perfectly screened. In this case, the peptide displays $\sim 50\%$ helicity, less than in molar $NaClO_4$ at $pH = 7$. In 6.6C, the raw CD spectrum in $3.5M$ salt solution is shown. In comparison to the salt-free data at $pH = 11$, $NaClO_4$ displays unusual features: the maximum around $190nm$ is red-shifted and the helix-typical double-wells between 200 and $230nm$ are less resolved. This red-shift has been interpreted as originating from helix distortion [178]. To corroborate the interpretation of the FRET data with the simulations, the following approach is taken:

i), the following three, highly complementary structural states are taken: 1) a fully $\alpha$-helical structure; 2) fully coiled structures, and 3) a compact structure with a minimum radius of gyration;

ii) the accessible volume of linker and dye at each end are calculated;

iii) the mean distance between dyes is then estimated and corrected for dye linker length and dynamics [179]. The range of distances for each structural state 1) –3) is depicted in 6.6A. The fully helical state has a calculated $R_{calc,DA}$ of $5.12nm$, the coiled states feature very similar extensions with a mean of $R_{calc,DA}$ of $4.95nm$. The two compact state configurations result in a mean $R_{calc,DA}$ of $3.63nm$. Therefore, the distances measured with FRET correspond extremely well with the MD data. This is visualized in figure 6.7, where snapshots of the MD simulations are overlaid with the AV-calculations.

The combined FRET and MD analysis thus provide significant evidence for an abundance of tightly packed peptide states at molar $NaClO_4$ concentrations in contrast to swollen coils in molar $GdmCl$ or extended helices at $pH = 11$. Comparison to pH 11 shows that the high compaction at molar $NaClO_4$ cannot be explained by electrostatic screening of the side chains. The previously described trends can be compared to the average end-to-end distances $R_{ee}$ for the well-converged simulations of the shorter $(AK)_6$ peptides. The peptides in molar $GdmCl$ show the highest extension in molar salt. The swelling of peptides and proteins upon denaturation in molar $GdmCl$ is in fact a common phenomenon, even observed for purely hydrophobic model polymers [180].

$NaClO_4$-induced compact states are not new as they have been observed in what was interpreted as a molten globule state [181]. Of importance, compression with $NaClO_4$ is accompanied by a significant increase in $3_{10}$ and turn secondary structure elements as calculated from MD simulations. This implies that CD measurements in the presence of $ClO_4^-$ should be avoided, since overestimation of helical structure elements will influence any further analysis.

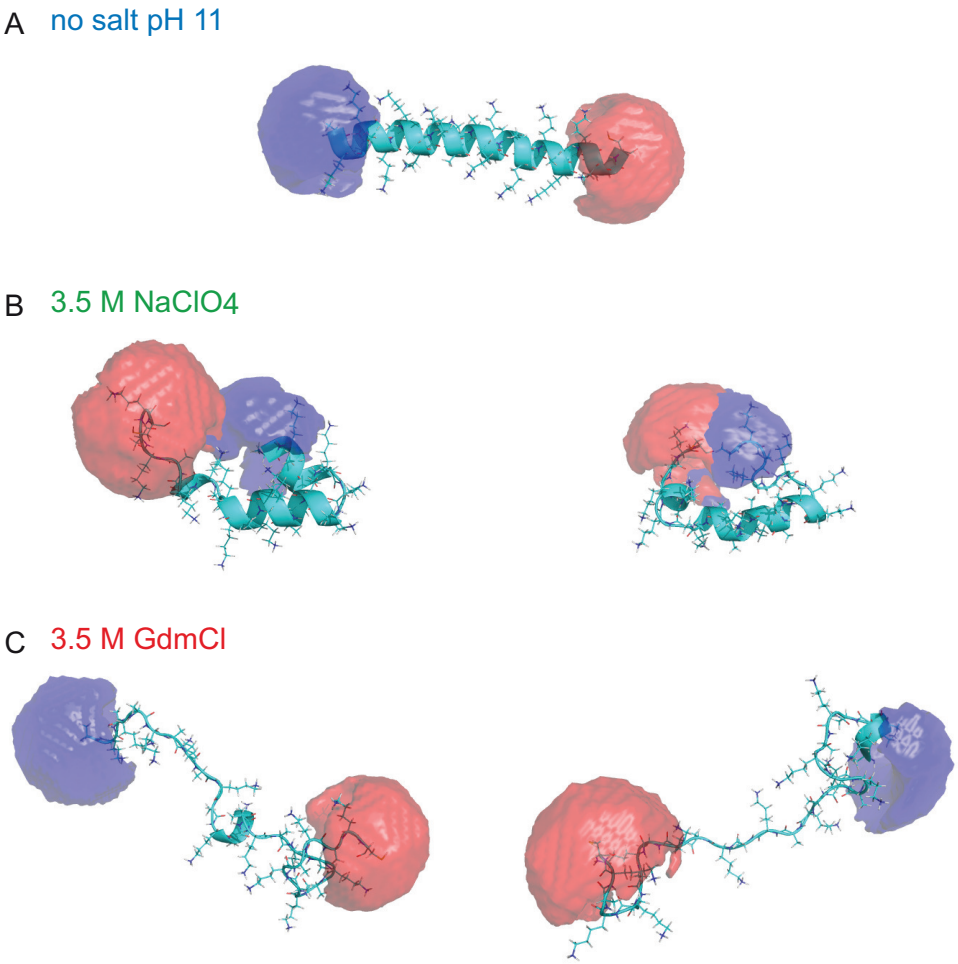


Figure 6.7: Dye Accessible Volume calculation using MD-derived structures. (A) $(AK)_{14}$ in no-salt pH 11, full α-helical state. Donor (blue) dye attached to N-terminus and acceptor (red) to C-terminus. (B) Collapsed states in $3.5M$ $NaClO_4$. (C) Coil-like structures formed at $3.5M$ GdmCl.

## 6.5 Sodium perchlorate, CD spectra, and the diversity of denatured states

The CD analysis of the $(AK)_n$-peptide indicates high $\alpha$-helicity in molar $NaClO_4$ whereas MD simulations do not. Despite its popularity, the interpretation of CD spectra is not always unique and has led to controversies in the past [182]. For instance, it is not possible to unambiguously distinguish between partial contributions of an $\alpha$-helix and a $3_{10}$-helix to a CD spectrum with multiple components. In particular, Scholtz and Baldwin [183] showed that for the $ClO_4^-$-induced denatured state of *ribonuclease A*, CD suggested secondary structure formation although it did not provide measurable protection against amide proton exchange, and it does not belong to the class of structured molten globules. Their interpretation was that compact states were induced possibly leading to a change in the far-ultraviolet CD spectra, and caution was advised in the interpretation of CD data in molar concentrations of $ClO_4^-$. Along this line, pioneering work from the 70s demonstrated that direct binding of ions may change the spectral and vibrational properties of the amide chromophore, *i.e.*, the double bond character of the peptide group [184]. The relative effectiveness of the salts in altering CD (or NMR) spectra was presumed to correspond to the strength of relative amide binding. In fact, $NaClO_4$ has one of the largest binding constants of typical Hofmeister salts even exceeding that of the divalent $CaCl_2$ [168, 171]. Mattice showed that very short alanine peptides (1–3 residues), which are unable to form $\alpha$-helical $i, i+4$ amide bonds, exhibit a decreasing ellipticity at $\lambda = 222nm$ with addition of molar amounts of $NaClO_4$ [184]. It may not be only CD that suffers from problems at molar concentrations of salt, because strong binding to the amide chromophore may also alter the physical properties of the molecule [185]. Judging from literature and our results, the following picture of peptide structure in molar concentration of $NaClO_4$ emerges: Both ions, $Na^+$ and $ClO_4^-$ favorably bind to the backbone in a concerted fashion as reflected by the MD simulations. The binding affects both the optical and structural properties of the peptide: First, spectral properties of the amide chromophore are altered, at least for some sequences, such that ellipticity curves are shifted toward more helical distributions. Second, the observed binding to multiple and adjacent amide groups induces bends and kinks in the chain, thereby leading to compaction and distortion of ordered fragments as demonstrated by FRET and MD. The red-shift in the CD spectrum (figure 6.6D) supports the interpretation as $\alpha$-helical distortion. The binding of $ClO_4^-$ ions facilitates sampling of $3_{10}$- and turn configurations, which cannot easily be distinguished from the $\alpha$-helix in CD measurements. The $3_{10}$-helix is actually the most hydrophilic secondary structure for short peptide fragments, much more open to the solvent than an $\alpha$-helix. The higher exposure of amide groups can better satisfy both internal $H$-bonds and an increase coordination number (i.e., the accumulation of the ions). Thus, the denatured state in molar $NaClO_4$ must be regarded as a compact, highly heterogeneous

mixture of $\alpha$-, $3_{10}$-, and turn-elements with much less $\alpha$-helical content as indicated by CD. On the basis of these results, the $ClO_4^-$-induced compact denatured state cannot be viewed as a canonical molten globule state.

Why is there such a big difference in the structure of the denatured states in molar $GdmCl$ (swollen coil) versus $NaClO_4$ (compact)? MD simulations provide two plausible explanations: First, $GdmCl$ is hardly excluded from the nonpolar groups of the peptide. A coil state gives maximum exposure of favorable amide groups while hydrophobic parts are covered by $Gdm^+$ (consistent with swelling of a purely hydrophobic polymer). $NaClO_4$ is more excluded from nonpolar regions while binding strongly to the peptide backbone. Second, due to the large affinity of both $Na^+$ and $ClO_4^-$ to amide groups, binding to multiple backbone groups in a concerted fashion is possible (figure 6.4A). This, in turn, leads to kinks and turns and overall compression of the chain. Thus, due to their specific and direct binding properties, $GdmCl$ and $NaClO_4$ are both destabilizers of ordered secondary structures but lead to extremely different denatured states, where one is close to a random coil, the other one is a compact, structurally heterogeneous state.

## 6.6 Conclusion

The action of specific ions on protein structure is a highly complex issue. However, the direct comparison between experimental CD data and MD simulations of model peptides shows that computer simulations are qualitative enough to provide the right trends and give molecular insights. Destabilization of secondary structure is therefore induced by individual ion binding to specific peptide sites, perturbing hydrogen bonds and salt bridges and drawing peptide groups into solution. Strong ion-specific destabilization typically occurs at salt concentrations larger than $0.5M$, where nonspecific charge effects, such as helix charge-ion or helix dipole-ion interactions, are screened. Interestingly, the CD data contrast the MD results for $NaClO_4$. Subsequent use of smFRET allows validation of results from MD simulations versus those obtained from CD, which was unable to distinguish heterogeneous collapsed states from homogeneous secondary structure content. The present analysis, in combination with previously reported results, points to a highly disordered class of compacted states in strongly accumulating salts such as $NaClO_4$. These collapsed states have been in the past erroneously taken as molten globule intermediaries during protein unfolding and not as a denatured end-species, as previously surmised by Baldwin and co-workers [183]. Thus, although both $NaClO_4$ and $GdmCl$ interact strongly with peptides, this does not necessarily imply a swollen, random coil-like denatured state. As shown in this chapter, the detailed, specific and local binding structure makes the difference.

# Chapter 7

# FCCS Applications to Biomolecular Interactions

The results of this chapter, except section 7.5, have been published in the Biophysical Journal [105].

## 7.1 Scope of this Project

All biomolecules are involved in some type of interaction as they perform their functions. Fluorescence cross-correlation spectroscopy (FCCS) is therefore a widely used technique to determine interactions and dissociation constants ($K_d$s) of biomolecules. The quantitative analysis of this interaction strongly depends on the ratio of the auto- and cross-correlation function (ACF and CCF) amplitudes.

If all fluorescent molecules diffuse through the confocal volume with a binding partner attached, the ratio of of the CCF/ACF amplitudes should be 1. As figure 7.1 shows, the CCF/ACF ratio is 0.75, although this double-labelled DNA is purified twice via a size exclusion column and as close to an ideal sample as possible. When analyzing measurements performed on tandem fluorescent proteins (FPs), in which two different FPs are linked, the CCF/ACF amplitude ratio is around 0.5, or less for different FCCS schemes. Figure 7.1 pinpoints several possible reasons for suboptimal cross-correlation.

The following part of this work will utilize this suboptimal ratio to deduce the folding efficiency of different FPs and the influence that Förster resonance energy transfer has on the CCF curve. Several optical parameters will be assessed that influence the amplitude of the CCF and, finally, a comprehensive overview of the possible sources of error (figure 7.1) and their respective corrections will be given.

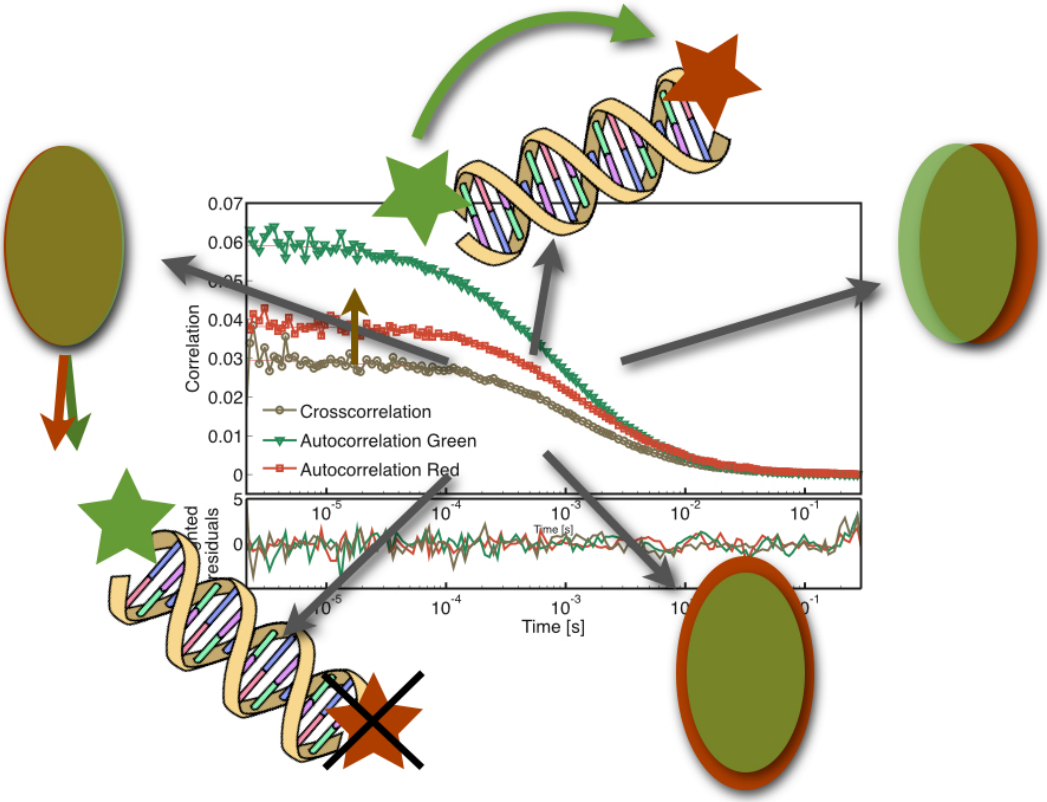


Figure 7.1: Possible reasons for the ACF/CCF ratio being less than 1 (from top clockwise): FRET, displaced excitation volumes, different sizes for confocal volumes, suboptimal samples, not identical detection volumes.

## 7.2 Description of Parameters and their Denotation

The theory on FCS and FCCS is described in chapter 4.2 and 4.3. The observation volumes and diffusion times are given in the green *(G)*, red *(R)*, and cross-correlated (X) channels as $V_G$, $V_R$, and $V_X$, and $\tau_{D,G}$, $\tau_{D,R}$, and $\tau_{D,X}$, respectively. The amplitudes for the autocorrelations are given by $G_G(0)$ and $G_R(0)$; the amplitude of the cross correlation is given by $G_X(0)$. If the observation volumes are not concentric but are shifted in respect to each other the cross-correlation volume $V_X$ is affected and the determined cross-correlation observation volume will have an apparent size $V_{X,app}$ [186].

The discussion of the size and the displacement of the observation volumes $V_G$, $V_R$, $V_x$, and $V_{x,app}$, and the influence of FRET on FCS are provided in the next paragraph. Once the observation volumes have been determined and corrected for artifacts, the concentrations $C_g$, $C_r$, and $C_{gr}$ of the free green-labeled molecules, free red-labeled molecules, and their complex, respectively, can be determined.

Of particular importance in this work are the FCCS amplitude ratios. Although the amplitudes are influenced by cross talk, background, and FRET, the ratios of the amplitudes are used as an empirical observation between different sets of measurements. Later on, when all the parameters have been accounted for, the values of the individual concentration $C_i$, which are a more accurate representation of the observations, will be used.

The ratio $G_X(0)/G_G(0)$ refers to the CCF/green-ACF amplitude ratio. It depends on the amount of red molecules in complex, and the ratio of nonfluorescent green labels in a tandem FP.

The ratio $G_X(0)/G_R(0)$ refers to the CCF/red-ACF amplitude ratio. It depends on the amount of green molecules in complex, and the ratio of nonfluorescent red labels in a tandem FP.
Both ratios also depend upon the overlap of the two effective volumes. The ratio $G_G(0)/G_R(0)$ refers to the ratio of the amplitudes of the green/red ACFs. This ratio depends on the relative size of the two effective volumes and ratio of the amount of red to green molecules.

## 7.3 Influence of FRET on the correlation amplitudes

Another factor that can influence the ACF and CCF amplitudes in FCCS experiments, when using FP tandems, is FRET between the FPs [187]. Under measurement conditions where photobleaching is present or not all fluorescent constructs have matured, two populations exist. One complex that exhibits FRET and one that does not, due to the nonphotoactive acceptor. For the mCherry-14-EGFP construct[1], two molecular

[1]The linker length of 14 AA was chosen in this case to give the FPs enough freedom to rotate and, hence, average out the orientation behavior of FRET

brightnesses will be observed for EGFP and mCherry, one for the constructs that do not undergo FRET and a second for those that do. To see how FRET reduces the ratio of $G_X(0)/G_G(0)$, PIE-FCCS on mCherry-14- EGFP in CHO cells and in cell lysate is performed. The variant with 14 aa between the fluorescent proteins is chosen because literature hints that too short linkers inbetween FPs lead to a higher misfolding rate [188].

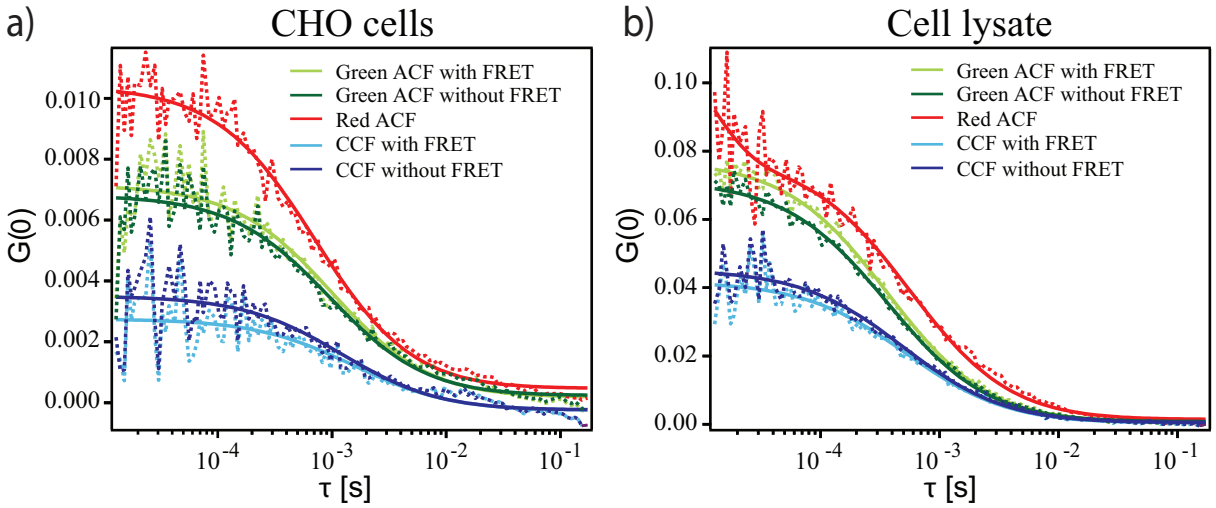


Figure 7.2: PIE-FCCS experiments in the presence of FRET are represented by the light green curve for EGFP, the red curve for mCherry, and the light blue curve for the cross-correlation. PIE-FCCS experiments after correcting for FRET are represented by the dark green curve and the dark blue curve. The lines are the corresponding fits to the data. (a) mCherry-14-EGFP in live CHO cells and (b) mCherry-7-EGFP in cell lysate are shown. The influence of FRET is observable in both experiments.

Intrinsically in the methodology of PIE is the possibility to correct for any occurance of FRET, cross-talk or direct excitation, as explained in chapter 4.4 and successfully applied in chapter 7.5. Since in PIE the excitation source of every photon is known, the increased amount of photons given out by the acceptor due to FRET can be corrected for by reallocating them back to the donor channel. The ACF and CCF amplitudes can then be calculated under non-FRET conditions. Figure 7.2a shows the PIE-FCCS measurement of mCherry-14-EGFP in CHO cells. $G_X(0)$ increases after FRET correction, whereas $G_G(0)$ does not change as much as $G_X(0)$. The reason for this is that the two species that are in solution - one that shows FRET, the other that doesn't - are combined to one species, which influences the green ACF. The $G_X(0)/G_G(0)$ ratio, which is influenced by FRET, is $0.51 \pm 0.07$ with a traditional FCCS analysis, whereas the ratio increased by 0.08 to $0.59 \pm 0.04$ after correcting for FRET. The same trend is observed for mCherry-7-EGFP in cell lysate (figure 7.2b) with an increase of $G_X(0)/G_G(0)$ from $0.55 \pm 0.07$ to $0.65 \pm 0.07$. A rather interesting development is the change of the ratio of the two ACFs: the higher value of $G_G(0)/G_R(0)$ of $0.94 \pm 0.17$ *in vitro* compared to $0.78 \pm 0.15$ in cells is due to the reduction of bulk photobleaching and the longer time available for maturation of mCherry in the cell lysate. These measurements show that a quantitative analysis of a CCF curve

is only possible with the help of PIE, since the ratios of ACF/CCF are not only influenced by the fluorescent state of the FP, but also by the energy transfer inbetween them. A method to determine the FRET-free correlation amplitude is given in chapter 7.4.2.

## 7.4 Correction of Artefacts

### 7.4.1 Correction of Spacially Shifted Volumes

When $V_G$ and $V_R$ are spatially shifted, for example due to chromatic aberrations, the amplitude of the CCF due to the imperfect overlap is given by [186]:

$$G_X(0) = \frac{C_{gr}}{N_A V_X \cdot (C_{gr}+C_g)\cdot(C_{gr}+C_r)} \cdot e^{-\frac{d_x^2+d_y^2}{\omega_{0,x}^2}-\frac{d_z^2}{z_{0,x}^2}}$$

$$= \frac{C_{gr}}{N_A V_{X,app} \cdot (C_{gr}+C_g)\cdot(C_{gr}+C_r)} \tag{7.1}$$

where $d_x$, $d_y$ and $d_z$ are the center-to-center distances between $V_G$ and $V_R$ in the $x$, $y$ and $z$ directions, respectively. Usually the CCF is fitted with models without the displacement of the two volumes as the displacement distances are not known, resulting in an apparent overlap volume $V_{X,app}$ which has a value larger than the actual $V_X$. This gives a lower amplitude $G_X(0)$ and a longer diffusion time $\tau_{D,X}$. The parameters of $d_x$, $d_y$ and $d_z$ can be determined when the emission filters for all detectors are replaced by OD filters and a scan of a gold bead is performed for all detection channels. With this method, the overlap of the detection volumes can be easily tested. Gold bead scans for the 3-color MFD PIE setup show no detecable shift between the detection volumes for EGFP and mCherry.

### 7.4.2 Correction of the Amplitudes in the Case of FRET

In the presence of FRET, a proper analysis of the amplitudes of the CCF becomes more complicated. As no sample features a 100% labeling with two fluorophores due to difficulties with the labeling procedure, lack of maturation of the fluorophore or photobleaching, there are always multiple species present in the measurements (donor only molecules, acceptor only molecules and double-labeled molecules that undergo FRET). The amplitude of the CCF with FRET contribution is given by [108]:

$$G_X(0) = \left(\frac{1-f_E}{1-f_E\cdot f_{gr,g_i}}\right)\cdot\left(\frac{1+q_r}{1+q_r\cdot f_{gr,r_i}}\right)\cdot\frac{C_{gr}}{N_A\cdot V_{GR}\cdot(C_{gr}+C_g)\cdot(C_{gr}+C_r)} \tag{7.2}$$

where $f_{gr,g_i} = C_{gr}/(C_{gr}+C_g)$ is the fraction of the species that undergo FRET to the total

number of green labels and $f_{gr,r_i} = C_{gr}/(C_{gr} + C_r)$ is the fraction of species that undergo FRET to the total number of red fluorophores. The FRET efficiency is determined by the decrease in molecular brightness of the donor which is given by $f_E = 1 - q_g$ where $q_g = \eta_{gr,G}/\eta_{g,G}$. This decrease is proportional to the FRET efficiency and the increase in sensitized emission of the acceptor due to FRET and is given by $q_r = \eta_{gr,R}/\eta_{r,R}$. $\eta_{i,j}$ is the molecular brightness of the $i^{th}$ molecule detected in the $j^{th}$ detection channel given in counts per particle per second (cps). The subscript $i$ represents free or complexed molecules ($g$ for green, $r$ for red, and $gr$ for the complex). The subscript $j$ represents either the green ($G$) or red ($R$) detection channels. Taking into account background, crosstalk, FRET and different effective volumes, the ACFs and CCF of a system that binds with a stoichiometry of $1:1$ are given by [103]:

$$G_G(0) = \frac{(q_G\eta_{g,G} + q_r\eta_{r,G})^2 \cdot C_{gr} + \eta_{g,G}^2 C_g + \eta_{r,G}^2 C_r}{N_A V_G \left[(q_G\eta_{g,G} + q_r\eta_{r,G}) \cdot C_{gr} + \eta_{g,G} C_g + \eta_{r,G} C_r + B_G/N_A V_G\right]^2} \tag{7.3}$$

$$G_R(0) = \frac{(q_G\eta_{g,R} + q_R\eta_{r,R})^2 \cdot C_{gr} + \eta_{g,R}^2 C_g + \eta_{r,R}^2 C_r}{N_A V_G \left[(q_G\eta_{g,R} + q_R\eta_{r,R}) \cdot C_{gr} + \eta_{g,R} C_g + \eta_{r,R} C_r + B_R/N_A V_R\right]^2} \tag{7.4}$$

$$\begin{aligned} G_X(0) = {} & \frac{(q_G\eta_{g,G} + q_r\eta_{r,G})(q_G\eta_{g,R} + q_R\eta_{r,R})C_{gr} + \eta_{g,G}\eta_{g,R}C_g + \eta_{r,G}\eta_{r,R}C_r}{N_A V_{GR,app}\left[(q_g\eta_{g,G} + q_r\eta_{r,G})C_{gr} + \eta_{g,G}C_g + \eta_{r,G}C_r + B_G/N_A V_G\right]} \cdot \\ & \cdot \left[(q_g\eta_{g,R} + q_r\eta_{r,R})C_{gr} + \eta_{g,R}C_g + \eta_{r,R}C_r + B_R/N_A V_R\right]^{-1} \end{aligned} \tag{7.5}$$

where $G_G(0)$ and $G_R(0)$ are the amplitudes of the green and red ACF respectively. $B_G$ and $B_R$ are the count rates of the uncorrelated background of the green and red detection channels.

## 7.5 Investigation on the Folding Efficeincy of FPs

The folding efficiency of fluorescent proteins is a widely discussed topic in literature [189–191]. A relatively straight forward way to test the degree of maturation of FPs is with the help of FCCS. One mistake that is often made is to underestimate the amount of information that is available from the cross-correlation curve itself. Although the cross-correlation volume is already determined by the two auto-correlation volumes (see equation 4.10), the cross-correlation can be used to refine this result. This corresponds mathematically to an over-determined problem, for three unknows with four equations, but unlike an equation system, the additional information can be used in this experiment to make the fit for the CCF more robust.

The first step is to determine the volume of the green effective Volume $V_G$ with a sample with known diffusion constant. In this case, the ACF of Atto488-carboxylic acid with a diffusion constant of $400\mu m^2/s$ was fitted with a single component and an additional triplet term. All measurements in this chapter are carried out on the 3-color scanning PIE setup (see Methods and Materials, chapter 11.2). This yields a diffusion time $\tau_D = 32.29 \pm 0.98\mu s$, a structure parameter $p = 4.50 \pm 0.52$ and a $V_G$ of $0.54 \pm 0.05 fL$. For $V_R$, there is no red fluorophore with an emission maximum similar to mRFP/mCherry with a known diffusion coefficient. Hence, the differences of the diffusion times $\tau_{D,R}$ and $\tau_{D,G}$ measured on the tandem FPs in the different detection channels are utilzed for this purpose. The average $\tau_{D,R}/\tau_{D,G}$ value for the mRFP/ mCherry-EGFP tandems is 1.24, which translates into $V_R/V_G$ of 1.4 ($\tau_D$ is proportional to $\omega_0^2$, whereas $V$ is proportional to $\omega_0^3$). This means that 1.4 times more red molecules will be detected compared to the green. $V_R$ is therefore $0.76 fL$.

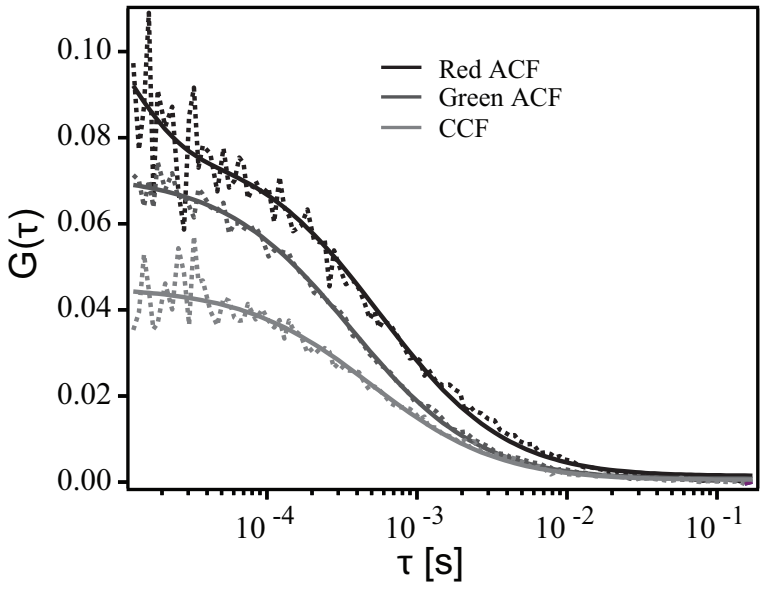


Figure 7.3: ACFs (green: EGFP, red:mCherry) and CCF (blue) of mCherry-7-EGFP tandem. The corresponding fits are displayed as solid lines.

The second step is to measure a tandem FP construct consisting of two FPs that emit into spectral distinguishable detection channels. Figure 7.3 shows the ACFs/CCF for the mCherry-7-EGFP tandem FP. '7' is the number of linker-amino acids and the sequence of this linker is: 'GSRMGTG'. The shown measurement is performed in cell-lysate, giving the FPs another 24h to mature compared to live-cell measurements. Since this experiment is carried out with pulsed interleaved excitation, all FRET, cross-talk and direct excitation photons are sorted back into the EGFP channel.

The three correlation curves have to be fitted globally. This means that not only the diffusion constant $D$ in $\mu m^2/s$ is identical for all three curves, but that the cross-correlation volume is calculated via equation 4.10 and not treated as an independent fitting parameter. This is a crucial step, because it eliminates the possibility that two spacially shifted observation volumes lead to a bigger volume. This bigger volume would be compensated by the fit with a lower number and lead to subsequent error for calculating the correct ratio of labelled to unlabelled particles. The fit calculates the number of single labelled species and the number of double labelled species. For each case the the number of particles is coverted into its respective concentration and, accordingly, the number of double-labelled particles is substracted from the single labelled species. The fit results in an average concentration of $c_{EGFP} = 9.80 \pm 1.49nM$. Repeating this step for the red ACFresults in $c_{mCherry} = 2.81 \pm 0.52nM$. The fit to the CCF curve with a cross-correlation volume of $0.65fL$ results in a number of double-labelled molecules of $N_{double} = 4.22 \pm 0.70$ and a concentration of $c_{double} = 10.82 \pm 1.80nM$. The conversion of number of particles per volume into concentration is necessary to make numbers comparable and independent of the focus size.

The only assumption that has to be made for the following conclusions is that the active state of the two FPs is independent of each other and that bleaching of one of the two fluorescent proteins does not influence the fluorescent state of the other. Combining the numbers from above, the total concentration of mCherry is $c_{mCherry,total} = 13.63 \pm 2.32nM$. Of this total concentration $c_{mCherry,total}$, $10.82 \pm 1.80nM$ carry also a fluorescent EGFP. This means that in this case, $79 \pm 11\%$ of all mCherry carry a fluorescent EGFP and, hence, the folding efficiency of EGFP is at least $79 \pm 11\%$.

The same calculation can be carried out for the other FP, mCherry, where the total concentration of EGFP is $c_{EGFP,total} = 20.62 \pm 3.21nM$. Of these molecules, $10.82 \pm 1.80nM$ carry also a fluorescent mCherry, resulting in minimal folding efficiency of mCherry of $52 \pm 7\%$. Repeating this step in live-cells proves difficult because of heavy bleaching and inhomogenous expression throughout a cell. Raster image correlation spectroscopy is here a more suited tool to answer this question in a more accurate way. When carrying out this experiment nevertheless, folding efficiencies go down for both FPs, for EGFP to $62 \pm 9\%$ and for mCherry to $40 \pm 6\%$. The experiment can also be carried out with a fusion construct of mRFP-7-EGFP, resulting in an *in vivo* folding efficiency for mRFP of

$30 \pm 6\%$, going down *in vivo* to $22 \pm 4\%$.

These results show clearly that FCCS is idealy suited to investigate the folding efficiency of FPs and that EGFP is superior to all other investigated FPs here.

## 7.6 Compilation of Parameters that Influence the Correlation Function

| Factors | Equations | Effects | Solutions |
|---|---|---|---|
| Size of the effective volumes $V_G$ and $V_R$. | Eq. 4.11 | • The size of $V_G$ and $V_R$ determines the correlation volume $V_x$ (Eq.4.1), which should have a value in between $V_G$ and $V_R$.<br>• The volumes directly affect the diffusion time observed.<br>• These volumes directly affect the concentrations of the molecules determined. | • This is a property of the optical system and can be determine by a calibration of the system with a dye of known diffusion coefficient. |
| Overlap of the green and red effective volumes | Eq. 7.1. | • A non-ideal overlap (the centers of the green and red effective volumes do not overlap) leads to a lower than expected $G_x(0)$ and larger $\tau_{D,x}$ when fitted with a model that does not account for the non-ideal overlap resulting in an apparent cross-correlation volume ($V_{x,app}$)<br>• This in terms leads to an underestimate of the amount of complex. | • A molecule with a green and red label (tandem) should be used to check for the maximum $G_x(0)/G_{ACF}(0)$.<br>• The maximum cross-correlation amplitude result can be used to normalize or correct for the lower than expected $G_x(0)/G_{ACF}(0)$ in the actual experiments. |
| Non-fluorescent labels (photobleached, non- maturated FPs and<br>labels in long-lived dark states) | | • Leads to lower than expected $G_x(0)/G_{ACF}(0)$ and an underestimate of the number of molecules (both, free and in complexes)<br>. | • Non-maturated FPs or the presence of dark states is a nature of the fluorophore. Hence the choice of the FPs is important. EGFP is one of the best GFPs. mCherry is far from ideal, but is probably one of the better RFPs available.<br>• Bulk photobleaching of the FPs in cells is difficult to prevent. It can be minimized by use of photostable FPs (eg. EGFP) and use of lower laser powers. Shorter exposure times and unnecessary scanning helps (eg. "blind" search).<br>• The amount of non-fluorescent labels can be characterized from the tandem experiments and corrected for in the actual binding experiments. |
| FRET | Eqs. 7.3 - 7.5 | • Leads to lower than expected $G_x(0)/G_{ACF}(0)$. | • Apply PIE-FCCS.<br>• Estimate the FRET efficiency of the complex (e.g. by measuring the brightness in the presence and absence of binding) and apply correction factors to the brightness of the labels involved. |

# Chapter 8

# Electrostatics Influences Actin Behavior

The results of this chapter have been published in the Journal for Biological Chemistry [192].

## 8.1 Overview

Actin is a 42 kDa structural protein that is present in every eukaryotic cell and posses the ability to polymerize upon hydrolyzation of adenosine triphosphate (ATP), which makes it a member of the family of ATPases. The monomeric form of globular actin (G-actin) can be implemented into filaments, so called filamentous actin (F-actin). Filaments can be implemented into two different types of higher order structures [193]: The first are actin bundles, which are part of the contractile apparatus in muscle cells. In these structures, actin filaments are closely packed into parallel arrays by crosslinkers. The second type are actin networks where a different set of crosslinkers orders the filaments in a more orthogonal way, hence forming a three-dimensional network, which is responsible for motility, contraction and stability of the cells [194]. At the same time, these filaments serve as track for the transport of cargo with the help of the motor protein family of myosins and are involved in cell signaling.

Actin filaments provide the mechanical scaffold for the whole cell. The ability to remodel this network in a very short time allows fast adaption to stimuli either from within the cell or from the environment. Cell migration can already occur by fast polymerization of actin in a certain direction. So far, it is not fully understood how such a highly dynamic behvior is acheived by the cell.

Although actin has already been known since 1887 and many important functions of actin within the cell are already known, the mechanism by which the nucleation occurs is still unknown. Very recently, Oda *et al.* [195], could show that the transition of G- to F-actin involves a change in conformation and a twist of the molecule. The scope of his work was to investigate the dynamics that underly the polymerization process and determine the influence of possible changes in the environment of filaments onto these

polymerization dynamics.

## 8.2 Structure

Interestingly, the aa sequence of actin is highly conserved throughout evolution. As already mentioned, actin needs ATP in order to polymerize, but without the presence of ATP or ADP, actin can't maintain in its native form. As already seen from the number of functions it is involved in, its unique structure enables it to establish more interactions than any other protein. Actin exists in globular, monomeric form (G-actin) or incorporated into filaments (F-actin).

### 8.2.1 G-Actin

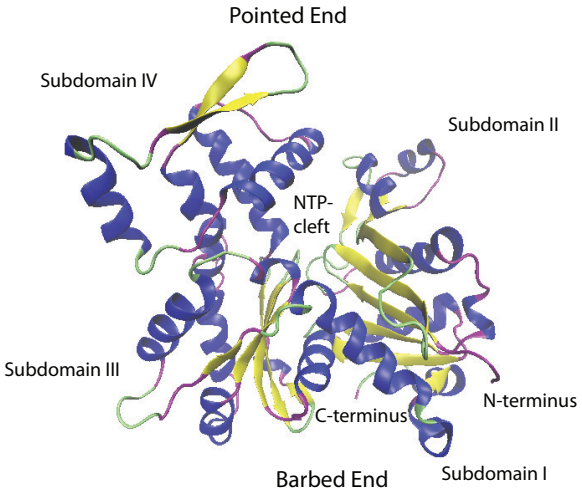


Figure 8.1: Detailed NewCartoon representation of G-actin (PDB file 1J6Z). Clearly visible is the nucleotide binding cleft in the middle that gives G-actin its asymetry.

The monomeric form of actin is known to exhibit a globular shape in solution. This assumption was supported by electron transmission microscopy images [196]. Figure 8.1 shows the crystal structure of a G-actin molecule. In this representation, however, it is clearly visible that the monomer consists of two lobes with a cleft in the middle. This fold is characteristic as an ATP binding motif that is needed for the interaction with nucleotides and, hence, can be found in several enzymatic catalases, e.g. in the HSP70 family.

Actin posseses another binding site for small molecules besides the ATP binding motif: just below the nucleotide binding side, there is a divalent cation binding site, which is usually occupied by $Ca^{2+}$ or $Mg^{2+}$. Additionaly, there are several regions located at the surface of each monomer that show characteristica for binding sites of divalent cations. Remidios *et al.* [197] suggested that, upon binding of cations to these sites, actin might be activated and thus be triggered to polymerize.

One monomeric unit of actin has a volume of $\approx 60nm^3$, an estimated isoelectric point of $pH = 5.2$, and is charged at neutral pH with a net charge of -7 [192]. The detailed influence of pH onto the charge distribution on the surface of the protein will be discussed in section 8.4.3. These specifications were also used for the calculations in chapter 8.4.3.

### 8.2.2 F-Actin

The transition of G-actin to F-actin is induced *in vitro* by an exchange of the buffer: while the storage buffer contains only $0.2mM$ $CaCl_2$ and $0.1mM$ of ATP, the polymerization buffer contains $50mM$ $KCl$, $1mM$ $MgCl_2$, $1mM$ $EGTA$ and $10mM$ $imidazole \cdot HCl$. This necessary increase of the salt concentration is the underlying basis of the assumption stated above that the weaker binding sites at the surface of each monomer may play a role in the polymerization process.

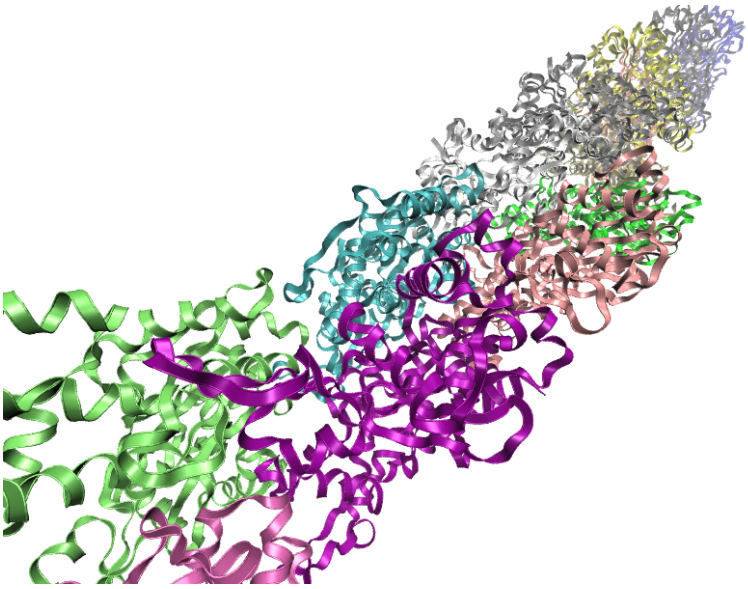

Figure 8.2: Ribbon representation of a repetition of a part of an actin filament model proposed by [198].

The structure of filamentous actin is not easy explicable. The reason is that an actin filament is a highly dynamic structure, unlike the snapshot of the fixed filament shown in figure 8.2. This makes it hard to pinpoint or predict the exact structure for a filament. Classically, F-actin is considered as double stranded, counter-clockwise rotating helix[1] with 166° turn around the filament axis and $\approx 2.7nm$ ascent along the axis per subunit. Over time, it was shown that while the axial translation stays relatively constant, the turn around the filament axis is not fixed and deviations from $\pm 10\%$ are normal for F-actin. The underlying phenomenon might be distinct structural states that are needed for the polymerization process to adapt to different requirements, which are dictated by the environment.

Each actin filament is build up in an asymmetrical manner. This polarity arises from the fact that all monomers that are implemented into the polymer orient their cleft for nucleotide binding into the same direction. The end that has an actin subunit attached with its cleft pointing away from the polymer is called the “pointed”-end, while the end that has a subunit with a covered cleft by the rest of the polymer is called the “barbed”-end. This nomenclature arises from transmission electron microscopy, where filaments are “decorated” with myosin S1. The samples form a structure that resembles an arrow, where the shaft is the actin and the myosins are the feathers. Hence, the common nomenclature for the different ends is “pointed”- and “barbed” -end.

An interesting property of actin filaments is treadmilling: whether actin filaments

[1]Since each monomer is shifted laterally with respect to its neighbour, the helix appears to be a double helix.

grow or shrink depends on the critical concentration $c_c$. This concentration is defined as the number of monomers in solution where neither growth nor shrinking occurs. The critical concentrations for the individual ends are not identical: for the pointed end, $c_c^-$ is roughly $600nM$, while for the barbed end $c_c^+$ is around $200nM$. At high cytosolic actin concentrations, both ends grow while at concentrations below $200nM$, both ends shrink. In the middle, there are conditions, where the pointed end shrinks, the barbed end elongates and the overal length of the filament stays the same. One particular interesting result of treadmilling is effective movement in the direction of the growing end. Some cells are able to make use of this directed motion for force generation at the leading edge.

The dynamics of the elongation of the pointed and the barbed end, especially in dependence of the $pH$, and how this dynamic can be correctly modelled will be discussed in this chapter.

## 8.3 Scope of this Project

The key feature of the cellular actin network is its dynamic nature, known to be involved in a multitude of cellular processes. As already mentioned, the polymerization state of actin is highly sensitve to the ion concentration in solution. One ion that has been shown to influence the polymerization, but is overlooked in most studies is the oxonium ion, $H_3O^+$ [199, 200]. This ubiquitous parameter, equivalent with the pH of the solvent, is involved in several biological processes, e.g. it plays a role in the fertilization of sea urchin eggs [201] and on the acrosomal reaction of echinoderm sperms [202]. The pH of the medium has also been identified as one possible modulator for actin turnover [203] and for force generation in cells [204].

Not only is actin itself heavily influenced by variations in pH, also proteins that are closely tied to actin react to changes in the oxonium ion concentration. Cofilin, for example, one of the key players for actin severing and depolymerization has been shown to be blocked by low pH. Talin, which is responsible for linking actin to integrins in focal adhesions and thus plays a role in force generation, is regulated by pH in a similar way. In mammalian cells, the intracellular pH ($pH_i$) is mainly regulated by the $Na^+/H^+$ *exchanger 1* (NHE1, often also called "sodium–hydrogen antiporter"). For migrating cells, it is localized at the leading edge of a cell, where turnover and continuous polymerization of actin is most prominent [205]. *Denker et al.* [206] could show that by modulating $pH_i$ with the help of NHE1, cell migration can be directly affected.

Nature strictly controls the internal pH of cells to ensure the normal pathways for basic cell functions like ATP maintenance, cellular metabolism, enzyme activity, membrane permeabilty, cell proliferation, and apotosis. If these control mechanisms fail, misregulated pH can lead to pathogenic conditions. A prominent example are cancer cell lines that are shown to exhibit a higher $pH_i$ compared to non-cancer cells [207–209].

There have been efforts to understand the influence of $pH_i$ on the actin dynamics at the cellular level, but many questions are left unanswered. A nearly countless number of proteins are involved in cellular actin behavior, most of which are sensitive to pH in one or the other way. Pure actin, under *in vitro* conditions, polymerizes faster at lower pH [199, 200]. The reason for this can be found in the underlying effect of pH on every actin monomer: pH alters protein electrostatics by changing the protonation state of amino acid side chains, thereby changing the interaction potential of monomers. This implies that protein electrostatics have the potential to influence the reaction rate of proteins, being able to enhance or slow down polymerization of actin.

This work will focus on the development of a method to investigate actin polymerization behavior for freely diffusing molecules in solution with the help of a confocal microscope. This fluorecence fluctuation method has the tremendous advantage that the results are not biased by the influence of the tethering protein that is necessary for TIRF

microscopy to attach actin to the surface. The results are combined with *in vivo* observations and results from TIRF microscopy. The combined findings are then brought into context with the help of a theoretical generic model.

## 8.4 Results

### 8.4.1 Replacing Pyrene-Actin with pH insenitive Atto-488-Actin

A well established method within the actin community to investigate actin polymerizaiton is the bulk pyrenyl fluorescence assay. For this purpose, actin - extracted from muscle or non-muscle tissue - is labelled at high pH with N-(1-pyrene)-iodoacetamide at the only surface cystein available. The resulting monomeric actin fluoresces weakly at $384nm$, but when the local environment of the dye is changed upon polymerization of actin, the fluorescence is increased 20-fold. The exact mechanism for the increase in fluorescence yield is not known, but the the amount of formed polymer can be measured with the increase of fluorescence in a fluorimeter.

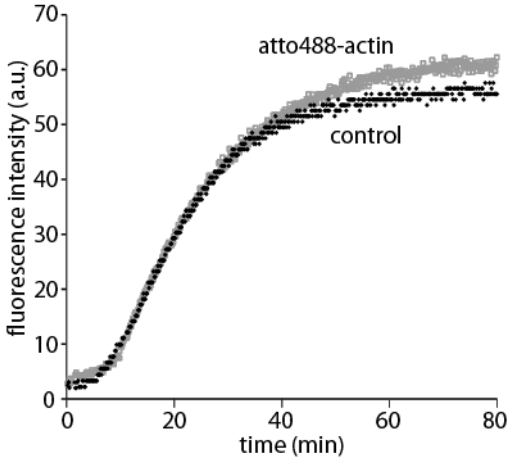


Figure 8.3: Comparison between standard pyrene actin (control, black) and actin labelled with Atto488 (grey). 5% of all actin monomers are labelled with pyrene in both cases. As can be seen from the comparison between the curves, the reaction kinetics stay the same, only the total mass of incorporated monomers vary in the plateau phase.

This technique is well established but only provides information about the total polymer mass without revealing any details about individual species that are present in solution. Figure 8.3 shows a typical pyrene assay curve. In this case, 2 µM total actin, of which 5% is pyrene-labeled actin, was polymerized under standard conditions in the presence of 95% unlabeled actin (control, black). One can clearly distinguish the characteristic shape of such a curve: an inital lag phase, where mostly nucleation of filaments takes place, followed by a near linear phase with growth of the filaments and a leveling off to a plateau, when nearly all of the monomers are incorporated into polymer mass. One particular problem with this essay and one possible reason why pH has evaded much attention so far is due to the fact that pyrene itself is pH dependent. The excited state of pyrene features a different, non-planar shape and hence fluorescent lifetime, spectrum and quantum yield are highly sensitive to any changes in the environment [210]. Due to this reason, pyrene has been replaced for the following

experiments with dyes that have a matching excitation maximum for the MFD setup and are not pH sensitive. A practical limitation in the use of fluorescently labeled actin is its overall lower polymerization capacity when labeled at the cystein residue 375 [211]. Therefore, we used lysine-labeled actin [212]. To check whether the attachment of Atto488 has a drastic effect on the actin polymerization behavior, 2 µM total actin, of which 5% is pyrene-labeled actin, was polymerized under standard conditions in the presence of 95% atto-488 labeled actin (figure 8.3, atto488-actin, red). Labeling of the actin did not alter polymerization kinetics, only the total mass of incorporated monomers varied, as can be seen from the different plateau heights.

To test whether actin labelled with Atto488 is suitable for the whole pH range where actin is stable (pH 5-9), the following control experiments have been carried out: one particularly sensitive parameter for investigating the photophysics of a fluorophore is its lifetime. When fluorescence is quenched, e.g. by heavy atoms, the lifetime is shortened, or if the local environment of a dye leads to an increase in fluorescence, the lifetime is prolonged. To evaluate whether the proposed fluorophore atto-488 is pH independent over the desired range, TCSPC lifetime measurements were carried out on Atto488 in solution at various pH values. Figure 8.4A shows the normalized lifetime histograms of atto-488 in the desired pH range. The fitted lifetimes are $3.91 \pm 0.01$, $4.32 \pm 0.02$ and $4.39 \pm 0.02$ ns, for pH 6.3, 7.1, and 8.3, respectively. To further analyze these deviations and show that they are likely to be caused by different influences of the background, rather than pH, the brightness of the fluorophore was measured in the range of pH 4 - 9. The molecular brightness is defined as the number of photons per molecule per second at a particular laser power (equation 4.2). For the inset of figure 8.4A, the laser power was kept constant at $10\mu W$. The error bars are in the range of the graphical representations and the inset shows that there is no correlation between pH and molecular brightness, supporting the suggestion from the lifetime histograms. The small deviations between 2.1 $counts/(second \cdot molecule)$ and 2.4 $counts/(second \cdot molecule)$ may rather result from errors diluting the stock solutions down to the final desired concentrations.

The logical next step is to show that the countrate measured with a confocal setup is directly related to the amount of fluorophores in solution. For this purpose, the mean countrate of atto488-actin in G-buffer at varying concentrations from $75nM$ to $1\mu M$ was recorded. As can be seen from the main panel of figure 8.4B, the fluorescence intensity increases linearly with the amount of actin used for the experiment. At the same time, with the help of FCS and PCH, the number of actin monomers within the confocal volume can be determined (upper inset). Both methods show a good agreement in the number of fluorescent molecules. To rule out further photo-physical effects of the laser, the laser power for a sample of $100nM$ atto488-actin was varied from 1 to 20µW. The lower inset of figure 8.4B shows a linear relationship in this regime. The laser power should not be further increased, since dead time effects of the detector and the TCSPC electronics start

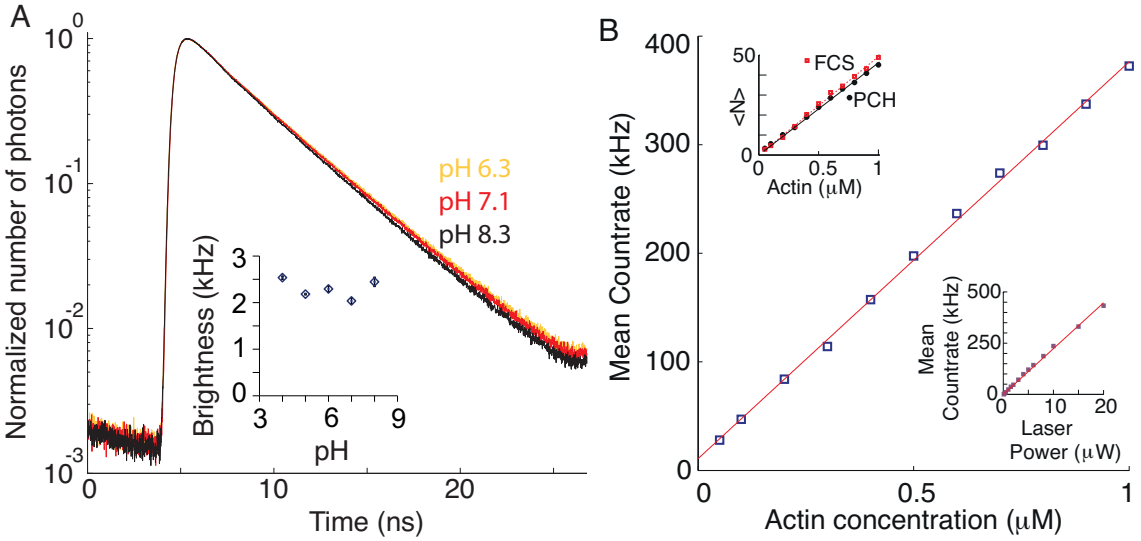


Figure 8.4: A) Normalized TCSPC histogram of 400 nM atto488 labeled actin in F-buffer at pH 6.3 (yellow), 7.1 (red) and 8.3 (black). The fluorescence lifetimes are $3.91 \pm 0.01$, $4.32 \pm 0.02$ and $4.39 \pm 0.02$ ns, respectively. Inset, Brightness of atto488 measured at 10 μW determined using PCH. Bars represent s.e.m. of 3 independent measurements. B) Mean countrate as a function of actin concentration at cosntant illumination power. The red line is a linear to the data; Upper inset, the mean number of molecules in the observation volume $< N >$ (as determined by PCH or FCS) versus actin concentration are shown. Lower inset, the linear relationship between laser power and the mean count rate of a sample of $100nM$ atto488-actin.

to take over and a significant amount of photons are no longer detected. These dead-time effects also explain the small discrepancies in the determination of the numbers by PCH or FCS for more than 30 molecules in the confocal volume at the same time.

The figures 8.3 and 8.4 show a full characterization of actin labelled with atto488 on the MFD setup. From these figures, it becomes evident that atto488-actin is is suitable replacement for pyrene-actin, with the advantage that atto488 is not pH-sensitive in the desired range.

### 8.4.2 Decreasing pH Promotes Spontaneous Nucleation of Actin Filaments

For polymerization experiments, the same rules no longer apply as for standard free-diffusion experiments that are mentioned before, e.g. FCS or PCH. The reason is that rare events are detected and not all species in the sample are stochastically sampled.

When a filament diffuses through the observation volume, the fluorescence intensity increases well beyond what is observed due to the statistical fluctuations in monomer concentration (figure 8.5A, beginning of the trace) and is detected as a spike (figure 8.5B and C). The time from the start of the experiment until initial spikes appear vary for experiments carried out with constant actin concentration at different pH values. As can be seen from figure 8.5B not only the frequency of the spikes increases, but also the hight.

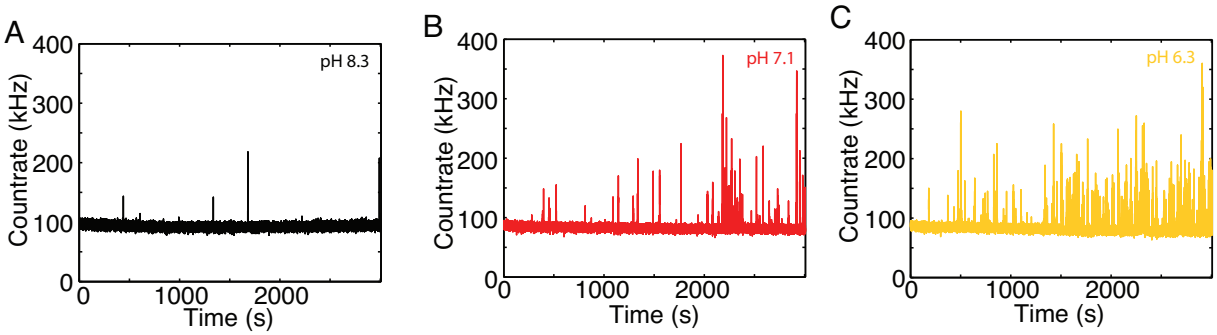


Figure 8.5: Monitoring pH-sensitive actin polymerization dynamics with fluorescence fluctuation spectroscopy: The time course of polymerization during the first 3000 seconds of 400 nM of atto488-labeled actin by addition of 1/10 of final volume of 10x KMEI buffer. Final solution pH values are 8.3 (A), 7.1 (B) and 6.3 (C).

Figure 8.6 illustrates the principle that stands behind the observations from figure 8.5 and the following experiments. The top panel of figure 8.6B and the beginning of the second correspond to the first case of figure 8.6A: a pool of monomers will result in a countrate, which fluctuates around a constant mean due to Brownian motion. A zoom-in with a histogram of the countrates is shown in figure 8.6C. This histogram is well described with a Gaussian distribution, as predicted from other fluctuation experiments. The timeline to the right of the graph, in minutes, indicates the addition of polymerization buffer and at which time after the start the photon traces of 300$s$ are shown. As can be seen from the second time trace in 8.6B, already after 15 minutes, polymers have formed that are clearly distinguishable as spikes from the pool of monomers (zoom-in in panel D, red box). When polymerization advances and more and more monomers are incorporated into polymers, spikes not only appear more frequently (figure 8.6B, third panel), but the heigth of the spikes also increases in heigth, until after five hours, a constant fluctuation of polymers is visible (forth panel of 8.6B).

In order to find a way to compare our results with a standard pyrene essay, the

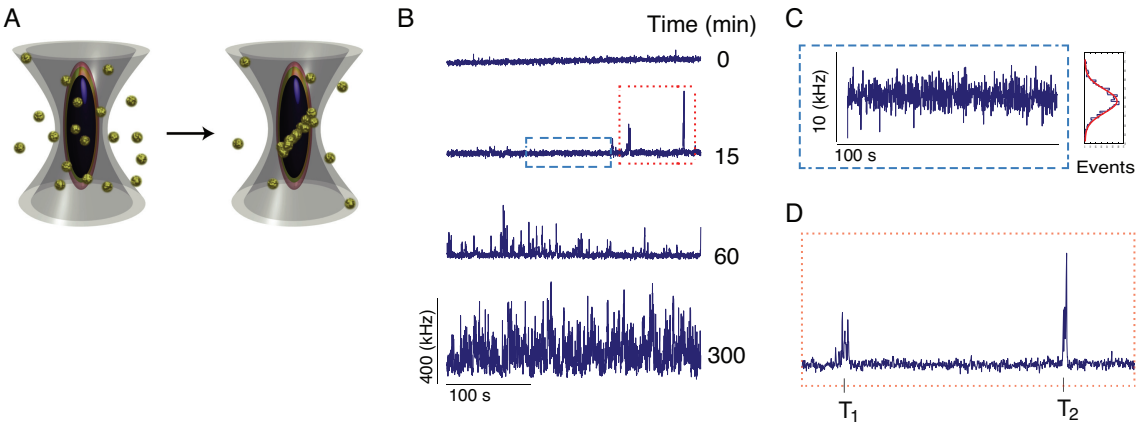


Figure 8.6: Monitoring actin polymerization dynamics with fluorescence fluctuation spectroscopy. (A) Schematic of the experiment. Actin molecules, each labeled with a single atto-488 fluorophore (i.e. 95% labeling efficiency), are free in solution as monomers and filaments. The fluorescence intensity will fluctuate as the particles diffuse through the observation volume. (B) Fluorescence intensity arising from the sample as a function of time after polymerization. Filaments form as a function of time after the start of polymerization. As filaments contain multiple labeled actin molecules, they will be observed as a spike in fluorescence intensity. 400 nM of atto488-labeled actin was polymerized by the addition of 1/10 volume of 10x KMEI at pH 7.1. (C) Zoom in of the blue box from panel B. At 1s temporal binning, the fluorescence signal is absent of spikes and is well described by a Gaussian distribution of intensities. (D) Zoom in of the red box from panel B showing the first two spikes. Each individual spike has associated an arrival time T, a duration-time and a total number of photons.

spikiness parameter was introduced: it is defined for every measurement as the percentage of counts with values higher than three standard deviations beyond the mode of the signal. The mode and its standard deviation are retrieved as shown in 8.6C: A histogram of all countrates is generated and this histogram fitted with a Gaussian function, yielding the mentioned parameters. Interestingly, separating spikes from the pool of monomers by this method proves robust, even at later time points where an evaluation by eye shows a clear dominance of spikes.

When plotting the spikiness of over time, these curves in turn resemble the sigmoidal shape of the well established pyrene essay (figure 8.7A): after addition of poylmerization buffer, the trace was spike-free, showing similarity to the lag phase of a pyrene experiment. Afterwards, the formation of polymers could be observed as spikes in the countrate. For concentrations higher than $400nM$ of labeled actin, only the first 12 minutes could be observed since polymers were so bright that the detectors had to be shut off to prevent permanent damage to the APDs. The lower concentrations show a good agreement between confocal and fluorometer experiments and, hence, prove that fluorometer bulk assays can be adapted to confocal microscopes that offer higher precission and more-dimensional information.

A very unique feature of conducting polymerization experiments on a confocal setup

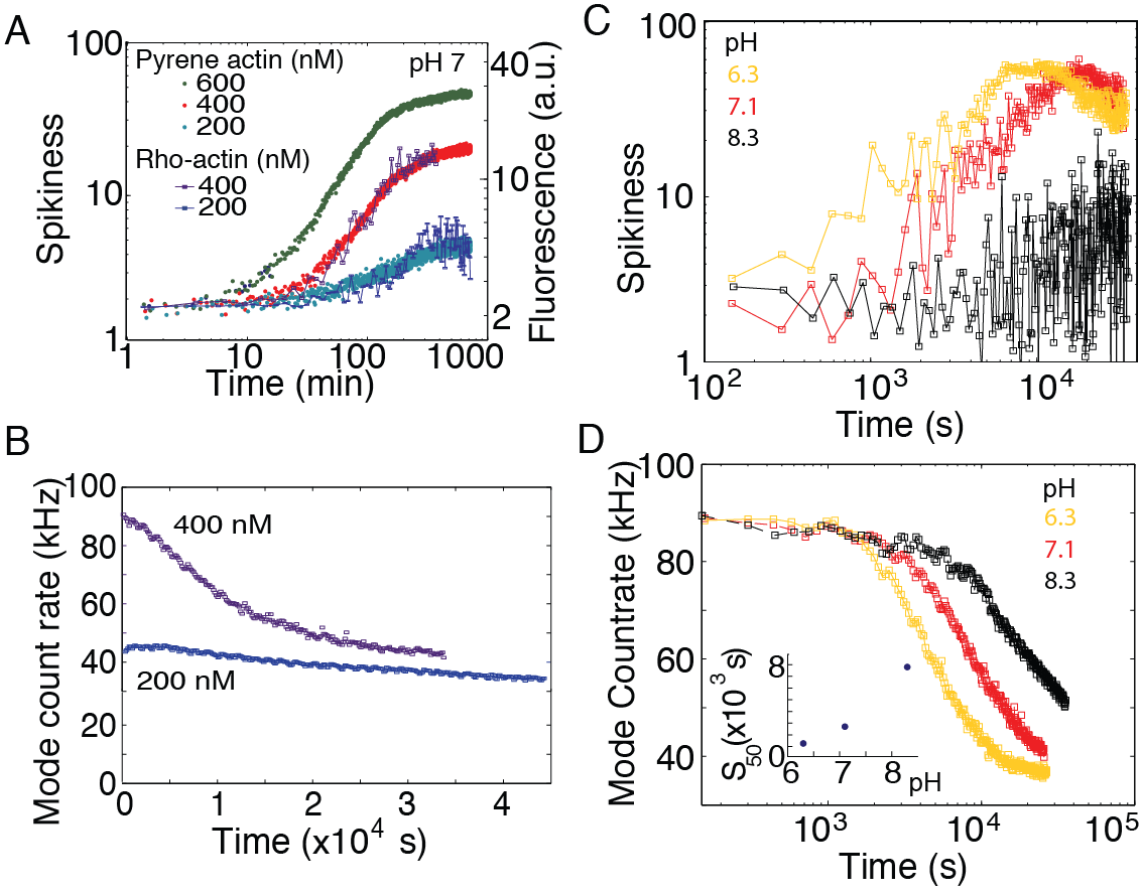


Figure 8.7: (A) Spikiness (i.e. percentage of counts $> 3\sigma$) vs. time for 200, 400 and $600nM$. For $600nm$ only the overlay of first $10min$ is shown, because after this time the polymers were already so bright that the detectors had to be shut down to prevent permanent damage. Shown on the right axis is the pyrene fluorescence increase for a similar concentration of actin. (B) Mode of counts vs. time showing the decrease in monomer concentration upon filament formation. (C) Spikiness of polymerization at three different pH values. (d) The decrease of the mode vs. pH (data from figure 8.5). (Inset) Time that has elapsed between beginning of the experiment and appearance of the first 50 spikes in seconds as a function of pH.

is that not only the formation of polymer mass is observable, but the parameter of the mode of the countrate resembles the monomer concentration (figure 8.7B). The mode, i.e. the monomer concentration, decreased during the course of the experiments untill the critical concentration was reached and an equlibrium between polymerization and depolymerization is reached. This method is the first of its sort where within a single experiment the formation of polymer mass can be observed and at the same the critical concentration is determinable (figure 8.7D).

The critical concentration calculated from confocal measurements is in good agreement with separately carried out TIRF experiments and is $160nM$ at pH 7.1. Repeating these experiments at different pH values shows that the critical concentration is pH sensitive. At pH 6.3, the critical concentration is below $100nM$, whereas at a higher pH value of

8.3, it increases to more than $300nM$.

Figure 8.7C shows the calculated spikiness for the experiments shown in figure 8.5. At pH 6.3, there was practically no lag phase observed while, at pH 8.3, the lag phase lasted for more than an hour. When comparing the polymer behavior (i.e. the spikiness) with the behavior of the monomer species (i.e. the mode of the countrate), it becomes apparent that a lag phase exists for the whole pH range (figure 8.7C). But interestingly, the lag phase, as estimated from both, pyrene essay and monomer concentration, was not devoid of filaments. For example, at pH 7, the first filaments were observed around $500s$ whereas the lag-phase lasted for ca. $1000s$.

In order to quantify the amount of monomer interactions around the critical concentration at pH 7 (˜150 nM), FCCS experiments with a mixture of $80nM$ atto488-actin and $80nM$ atto647-actin were carried out. Any complex, where the two fluorophores would diffuse in or out of the volume together, would give rise to a cross-correlation of the two colors and reveal the the existence of actin filament nuclei and short oligomers. Figure 8.8A and B show the countrates for a total of $160nM$actin split into the two different detection channels for pH 5.8 and pH 7.1, respectively. Longer filaments that have incorporated red and blue fluorophores can be seen as spikes that appear simultaneously.

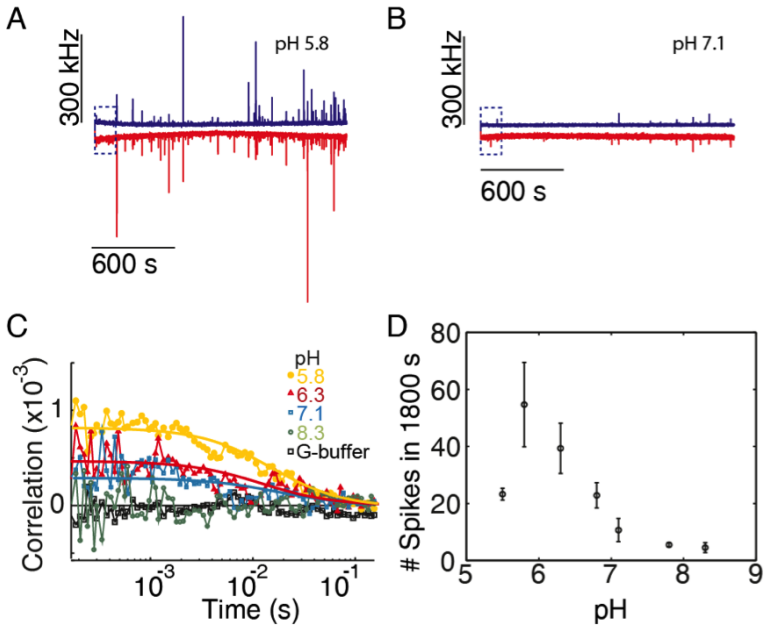


Figure 8.8: Actin nucleation is pH sensitive: $80nM$ of atto-488 and atto-647 labeled actin (95% and 50% labeled, respectively) were mixed and polymerization was started by addition of 1/10 of 10x KMEI buffer. (A-B) The count rate for the first 1800 s of polymerization at pH 5.8 (A) and 7.1 (B) are shown. In blue is the signal from the blue detection channel, red is the signal from the red channel. (C) The cross-correlation curves from the first $150s$ of the above measurements (blue dashed boxes in panels A and B). Solid lines are fits to a single diffusion species in a 3D Gaussian volume to guide the eye. A control sample was measured using G-buffer, where no polymerization occurs. (D) The number of spikes vs. pH during the first $15min$ after initiation of polymerization. The error bars are the S.D. from three independent measurements.

At a pH value of 5.8, a higher number of two-color coincident spikes, that had a larger size, are observed within minutes after the initiation of polymerization (figure 8.8A). In contrast, fewer coincident spikes are observed at pH 7.1 (figure 8.8B). When performing cross-correlation analysis of the collected data on the MFD setup during the very early times (spike-free) of the lag-phase, the CCF shows that larger amounts of double-labeled complexes prior to filament emergence are observed at lower pH values (figure 8.8C). A global fit of both, the ACFs and the CCF, suggest that there is, at most, 1 complex out of 100 molecules at the highest cross-correlation amplitude observed at pH 5.8. The amount of filaments formed (i.e. the number of spikes detected) within the first 15 min after the start of polymerization is shown in figure 8.8D as a function of pH and has a maximum at pH 5.8. Considering figure 8.8C and D, it becomes clear that pH modulates the kinetics of nuclei formation. This modulation of nuclei formation, in turn, leads to more individual filaments at lower pH values.

### 8.4.3 pH dependent electrostatics control actin polymer formation

The next logical step is to identify the reason for the pH sensitivity of the monomer association rate and how this rates compares with the general predictions for typical diffusion-controlled reactions.

The basis for the following steps is the fact that the net charge of a protein depends on the surrounding environment of the protein. The higher the pH, the more negative a protein is charged and vice versa (figure 8.9A). This means that the higher the absolute value of the charge of a protein is, the higher is the electrostatic potential in-between those molecules. Figure 8.9B illustrates the surface of an actin monomer with respect to its charge, where positive isosurfaces are displayed in blue (+2 kT/e) and negative in red (-2 kT/e). The top panel shows clearly that the dependence of the surface charge on pH is pronounced for the low salt conditions of G-Buffer, where charges cannot be screened so easily and monomer-monomer contacts are harder to establish. In contrast, as the lower panel of figure 8.9B shows, there are barely any differences visible at the distribution of surface charges of the protein between pH 5 and 8 for high salt conditions of F-Buffer. This means that higher salt concentrations are able to screen the charges better and, hence, facilitate polymerization.

A generic model of protein-protein association provides a way of rationalizing the observed pH effects. Assuming isoreactive spheres (5 nm in size), an attractive potential of $5 \cdot k_B T$ and a homogeneous charge distribution, the diffusion-limited on-rates can be calculated as a function of pH and salt concentration (figure 8.9C). With this simple model, two trends are visible: First, the diffusion-limited $k_{on}$ has a maximum at the isoelectric point where charge repulsion completely vanishes. Second, as the salt concentration increases, the charge repulsion (calculated from equation 11.6, materials and methods) is more efficiently screened and the reaction rate increases considerably even for pH values far from the isoelectric point. At high salt concentrations (c = 0.03M and above), the pH dependence decreases and actin polymerization becomes possible at higher pH values.

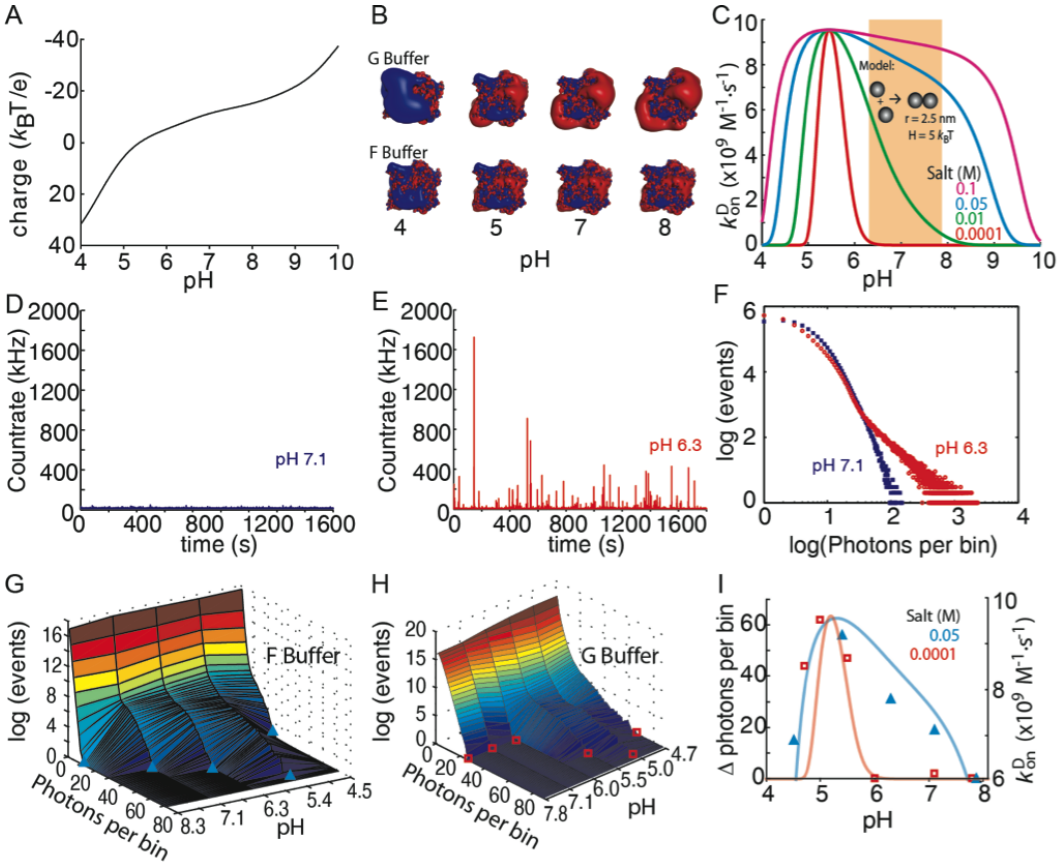


Figure 8.9: pH-dependent actin electrostatics control polymer formation. (A) The protein net charge prediction from the atomic structure of muscle actin (PDB 1J6Z) as a function of pH using the Protein Calculator (The Scripts website). (B) Electrostatic map made with the Adaptive Poisson-Boltzmann Solver (APBS) visualized with PyMol. Isosurfaces displayed are 2 kT/e in blue and -2 kT/e in red. (C) The diffusion-controlled $k_{on}$ for dimer formation with actin's pH-defined net charge determined using isoreactive spheres as an approximation for the actin interactions. The orange shadowed region indicates the physiological pH range (see text). (D) Fluorescence intensity trace for 60 nM of atto532-actin in F-buffer at pH 7.1. (E) Fluorescence intensity trace for 60 nM of atto532-actin (80% labeled) in F-buffer at pH 6.3. (F) A photon counting histogram analysis (with 1 ms bin size) of the traces shown in panels (D) and (E). (G-H) Photon counting histogram vs. pH in F-buffer (G) and G-buffer (H). (I) Difference of the maximum number of photons detected per bin during a measurement at the given pH value with respect to the measurement at pH 8.3. The light solid curves are taken from (C) for the same salt concentrations for comparison with its association rate axis on the right.

This generic model already reproduces the overall trend observed for monomer association rates as a function of pH (figure 8.8D). Also, it predicts that even in the absence of salt, polymerization can occur at pH values close to the $pI$ value of actin. To further validate our model, a PCH analysis (chapter 4.7) of our fluorescence fluctuation spectroscopy data (figure 8.9D-F) was carried out. The histogram of photon counts directly reveals the effect of pH on the polymerization process (figure 8.9F). The spikes visible in the countrate for the case of pH 6.3 affect especially the bins with more than a hundred

photons. When considering the case of pH 7.1, there are practically no bins with more than hundred photons, whereas when a bigger filament diffuses through the confocal volume, up to 1000 photons can be emitted within one bin-time of 1µs. As already stated before, with FFS it is possible to measure at pH values below 6 and, in contrast to the surface-restricted polymerization in TIRFM assays, maximal polymer mass generation in solution was observable at pH 5.4 (figure 8.9G), close to the calculated $pI$ of actin. In the absence of salts (G-buffer), there is no observable polymer mass above pH 5.5 (figure 8.9H). Figure 8.9 makes a connection between model and experiment - although it should be emphasized that the model predicts a diffusion controlled on-rate in $[M^{-1} \cdot s^{-1}]$, whereas the experimental data results in $[photons/bin]$. The solid lines are taken from the model, which is visualized in figure 8.9C, for $0.1mM$ and $50mM$ of salt concentration and normalized with the blue triangles and red squares[2] from the experimental results, shown in figure 8.9G and 8.9H, respectively. The predicted trend of association rates from the model therefore closely coincides with the observed polymer formed in solution at different salt concentrations (figure 8.9I). This leads to the conclusion that electrostatics indeed have a massive influence on the actin polymerization and that active control of the pH can regulate polymer formation.

[2]In order to achieve comparability between model and experiental data, the blue triangles and red squares are set in the histogram where the first time a photon-per-bin with 0 photons appears. Larger spikes result in outlayers along the x-axis that would render the figure illigable.

### 8.4.4 $pH_i$ modulates actin-driven pathogen motility in vivo

In order to place the findings that have been described so far in biological context, with the help of our cooperation partners at the UCSF, an essay is developed to test the influence of pH on actin polymerizaiton in an *in vivo* environment. One possible approach is the pH-dependence of Listeria monocytogenes motility in a cellular environment. Listeria is a bacterial pathogen that hijacks the host actin cytoskeleton to move through the cytoplasm and escapes immune response by spreading from cell to cell without extracellular exposure. These pathogens do not move actively, but rather express the protein ActA at their back end, which results in activation of the protein complex ARP2/3. This, in turn, leads to actin nucleation at the Listeria surface and, with the help of the driving force of this nucleation and elongation of actin, the bacteria are propelled forward [213], leaving a 'comet tail' of actin behind. It has been shown before that the speed of Listiria corelates with the rate of actin polymerization in cells [214]. Hence, the Listiria motility can be used to directly measure of any parameter that influences actin polymerization.

To create environments with varying $pH_i$ for the bacteria, one fibroblast cell line was engineered to stably express wild-type NHE1 (PSN cell line) and another was mutated to express an inactive NHE1 (E266I cell line). NHE1 is the sodium/hydrogen exchanger 1 and as ubiquitous membrane-bound protein involved in the regulation on the $pH_i$ (figure 8.10A). This results in two different cytosolic pHs for these two cell lines: 7.4 for the wild-type PSN cell line and a lower pH of 7.1 for the non-functional E266I cell line. To make actin filaments visible, both cell-types stably expressed the actin marker Lifeact-GFP. Listeria internalization was visualized by ActA-RFP expression once they entered the cytosol (figure 8.10B). The velocities for individual trajectories in both cell lines are measured (figure 8.10C and D). The average transport velocities increased from $0.31 \pm 0.03 \mu m \cdot s^{-1}$ in PSN control cells to $0.42 \pm 0.04 \mu m \cdot s^{-1}$ for E266I ($mean \pm s.e.m$, $N = 46$ each, $p < 0.01$, figure 8.10E). This change, of ~20%, of Listeria actin-driven motility in fibroblasts agrees well with the change in elongation measured *in vitro*, also of ~20%

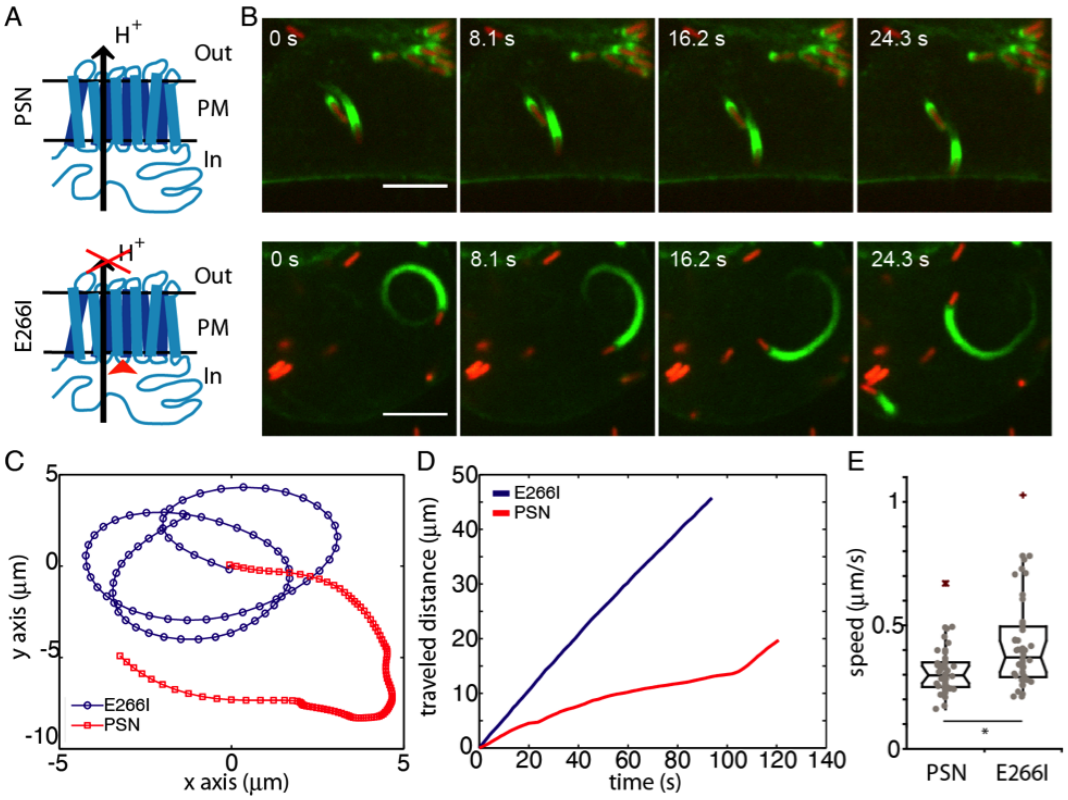


Figure 8.10: Effect of $pH_i$ on actin polymerization-driven motility of Listeria monocytogenes. (A). Schematic of NHE1 and the point mutation which blocks ion translocation of NHE1 while maintaining its ability to interact with adaptor proteins through its long cytoplasmic tail and thereby bind to the cytoskeleton. 'PM' refers to the Plasma membrane, 'Out' to the extracellular space and 'In' to the cytosol. (B) Single bacteria cells moving in either a PSN cell (upper panels) or an E266I cell (lower panels). Scale bar 5 µm. (C) Representative trajectories of bacterial transport in PSN cells and E266I cells (blue) (D) The travelled distance as a function of time for the trajectories shown in panel (C). (E) Boxplot of Listeria monocytogenes speeds in PSN or E266I cells. N = 46 for each condition, * p =0.009.

## 8.5 Discussion

In this work an extensive evaluation of the direct pH effects on the polymerization of actin and actin assemblies is performed, independent of actin regulatory proteins. By bridging the gap between bulk fluorimetric measurements and confocal fluorescence fluctuation spectroscopy, it becomes possible to reveal mechanistic details on actin filament nucleation and explain the observed pH effects with a simple model of electrostatic protein-protein interaction.

### 8.5.1 Nucleation

The variety of FFS techniques to study actin nucleation show, in their simplest application (i.e. spikiness), that FFS data provide an equivalent readout to the established pyrene method. It reliably reproduces the typical sigmoidal polymerization kinetics. In addition, FFS provides direct information on monomer concentration (i.e. the mode of the count rate) and can be applied over long time scales and a wide range of pH values. When applying these FFS techniques, a strong effect of pH on the nucleation is apparent. The high sensitivity of FFS clearly shows that short filaments already form during the lag-phase of polymerization. This is predicted by the kinetic model for actin polymerization [215] [216] but had not been proven experimentally. The early existence of such rapidly elongating filaments leads to a direct competition with newly forming nuclei - a critical aspect of the nucleation-elongation model [216]. Fluorescence cross-correlation spectroscopy is able to detect actin complexes formed prior to filament appearance, suggesting that these species represent the actual polymerization nuclei. The findings that nuclei are present preceding filament emergence agree with and support the expectations based on pyrene experiments. Finally, something that also became obvious from using ultra-sensitive FFS techniques (in particular at low molecule concentrations) is that extensive actin polymerization dynamics occur below the critical concentration. Hence, FFS opens up new possibilities for elucidating mechanisms of nucleation.

### 8.5.2 Electrostatics

The strong pH-dependence of polymerization suggests an important role of electrostatic forces in filament formation. Consistent with this hypothesis, it is shown here that screening of charges by the addition of salt increased the association rate for actin (figure 8.9). A similar explanation for the effect of salt on actin was proposed more than 50 years ago [217] [218]. The generic theoretical model proposed in this work quantitatively correlates now the effects of pH and salt on a monomer and for the resulting electrostatic potential. Hence, polymerization of actin can either occur in the presence of sufficient amounts of screening salts, or if the net charge is reduced, i.e. close to the pI of actin. Interestingly,

salt has been reported to have a non-monotonic effect on actin polymerization: at high salt concentrations, the elongation rate decreases monotonically with increasing salt [219]. This is possibly due to a reduction of intra-strand contacts that mostly consist of salt-bridges [220]. On the other hand, at low salt concentrations, screening allows inter-strand contacts to be formed, which are largely based on hydrophobic interactions. Altogether, the results shown here explain the overall polymerization response to pH within a general framework of electrostatic forces and provide a basis to understand the non-specific effects of salt on actin polymerization.

### 8.5.3 Implications within a cellular environment

This work presents an extensive analysis of pH effects on polymerization of pure actin. However, actin in cells always functions within complex assemblies that are regulated by a vast number of modulating factors. This diversity could help to regulate mechanical properties of local cellular environments such as stress fibers, lamellipodia or the isotropic actin cortex. In this way, a cell could modulate its mechanical properties and contractility by locally changing its $pH_i$ [221] in time scales that are only limited by proton diffusion within the cytoplasm. For dynamic processes that are determined by the rate of actin polymerization, such as cell migration or bacteria moving through the cytosol, changes in $pH_i$ could be expected to have a direct effect. Indeed, in collaboration with the Barber lab at UCSF, we show that velocities of Listeria in fibroblast are higher at lower $pH_i$ values (figure 8.10), which agrees with the increased polymerization rates of actin measured in vitro. Although in this particular way of probing the pH dependece of actin polymerization many different factors and proteins are involved in actin dynamics, this experiment offers one possibility to test for the pH dependence of actin *in vivo*. In contrast, the increased motility and metastatic capacity of cancer cells with an increased pHi [209] is likely dominated by pH-sensitive actin regulators, such as cofilin [203]. Careful evaluation of all involved regulators will therefore be required to fully understand the effects of pH on the complex machinery generating cellular motion and how it is harnessed by cancer cells. So far, our results suggest that actin polymerization-driven cellular processes will be sensitive to the $pH_i$ and suggest that pH modulation can be used to finely tune the intracellular environment to promote and assist the vast variety of cellular behaviors.

# Chapter 9

# Super Resolution Imaging of Actin Filaments

## 9.1 Scope of this Project

Crucial cellular processes, like cell migration, cytokinesis, cell polarization and the perception of forces, rely heavily on actin-based force generation and constant actin filament assembly and turnover. At the same time, actin is involved in the regulation of a vast number of processes ranging from gene expression to cytoskeletal remodeling. The nearly unmanageable amount of interaction partners and their involvement in the mentioned processes explains why it has been highly conserved during evolution.

Actin is not only able to form long fibers that stretch over several µm, but there is also the particular structure of the "branched actin network" [222, 223]. Networks are able to create forces, which react on compartments of the cellular membrane. This can introduce a change of shape, but also help building cellular membranes during endocytosis [224]. In general, branching is involved where a motile patch of actin network is needed, e.g. in phagocytosis and in the migration of fibroblast monolayers for wound-healing. When a growing actin network experiences external force in the direction of growth, e.g. by the cytoplasmic membrane, it will start to compress, distributing the pressure within the network and filaments within the network will start to bend [225, 226]. Recently, it was shown that this curvature influences the direction of newly emerging branches [227]. It is assumed that the reason for the preferential branching to the convex side is established by preferential binding of the 'actin related complex 2/3' ARP2/3 to this side. ARP2/3 is a protein that consits of seven subunits and is mainly responsible for the branching of actin. While the complex binds to the side of an already existing 'mother' filament, its subunits 2 and 3 resemble the structure of an actin monomer and facilitate the emergence of a new 'daughter' filament. Very little information is presently available about the dynamics and the cooperative effects of different actin binding partners onto the branching behavior.

Crevenna et al. [paper in revision] could recently show that the polymerization behavior of actin itself is heavily influenced by the tethering protein used to attach actin filaments to the surface.

The scope of this project is to show that the STED microscope built in this work is able to image growing actin filaments and also to produce super-resolution images of actin networks, which are not limited by the diffraction barrier anymore. The long-term goal would be to investigate the influence of different tethering proteins in combination with ARP2/3 on the branching behavior of actin filaments.

## 9.2 Imaging of Actin Filaments on the STED Setup

In order to successfully visualize the growth of actin filaments, flow cells were made using a sandwich of a cover slip ($20x20mm$, #1, VWR, Ismaning, Germany), parafilm (Brand, Wertheim, Germany) and a cover slide (VWR, Ismaning, Germany). To achieve a tight sealing of the chamber, the sandwich is heated with the heat gun for a short period, until the parafilm becomes transparent. After cool-down, the flow cells are passivated by incubating them with 10% BSA in PBS for 10 minutes. The channel is washed three times with $90\mu L$ of G-buffer. Then the tethering protein filamin is applied for 5 minutes and afterwards washed again three times with $90\mu L$ of G-buffer. Atto647-actin was incubated for 5 minutes on ice with 1/10 volume of 10x ME buffer ($MgCl_2$ and EGTA) to exchange $Ca^{+2}$ for $Mg^{+2}$. The actin-containing solution was mixed after the ion exchange with the imaging buffer (Catalase, β-mercapto-ethanol, glucose oxidadase, D-glucose, 0.25% (w/v) Methylcellulose, and 1/10 of $10x$ KMEI buffer, with a final pH of 7.1) and introduced into the flow cell. The flow cell is sealed off with vacuum grease. Imaging was performed using a self-written measurement program in FabSurf on the STED setup. For images that are acquired with the MCL Nano-positioner, the pixel dwell time has to be $2ms$ for images that are at least 20x20µ$m$. For images that are smaller, longer dwell times of $10ms$ have to be chosen because of non-linear movements of the scanner at shorter time scales. The analysis is either done using ImageJ, or in the self-written Matlab software iSTEhaufDi.

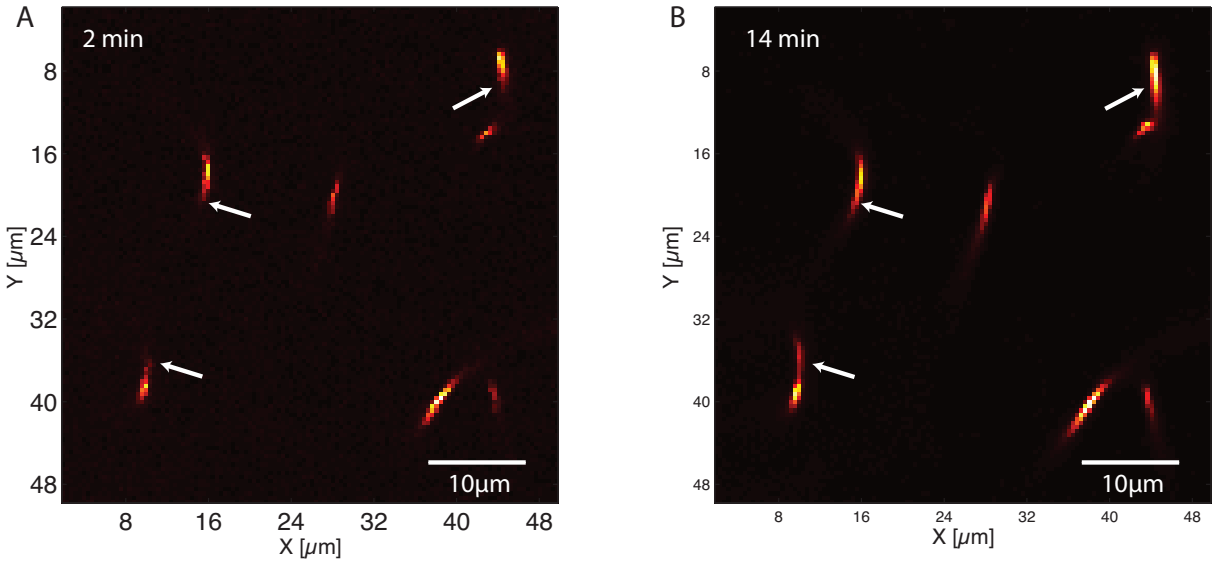


Figure 9.1: Growth of actin filaments, visualized with the confocal part of the STED setup. Actin filaments are tethered to the surface with filamin. The image on the left is imaged 2 minutes after addition of actin into the flow cell, while the image on the right is a time-projection of 20 images over the course of 12 minutes. The white arrows are positioned at the same place in both images and at the end of the filaments at $t = 2min$.

Figure 9.1 gives an example of the growth of atto647-actin, tethered to the surface of

the glass cover slip with filamin. Panel A is imaged 2 minutes after addition of actin into the flow cell, while panel B is a time-projection of 20 images over the course of the next 12 minutes. The white arrows are positioned at the same place in both images and at the end of the filaments at $t = 2min$. The time projection is necessary because, during the process of imaging, already imaged F-actin bleaches away and thus leaving the impression that filaments migrate over the surface.

This image series proves that it is possible to image actin growth on a surface with the confocal part of the STED setup. Seperate experiments with different tethering proteins like $\alpha$-actinin, VASP or NEM-myosin show that also these proteins are suited to produce images of growing F-actin.

## 9.3 Super-Resoultion Images of Actin Networks

The next logical step is to prove the ability of the STED setup to produce super-resolution images of atto647-actin networks. One particular problem that occured during the realization of these experiments is the absorption spectrum of atto647-actin. While the capability of the setup is proven to successfully deplete atto647, figure 9.2 shows that atto647-actin is still slightly excitable with the STED wavelength at $736nm$ and a depletion laser power of $25mW$ before the objective.

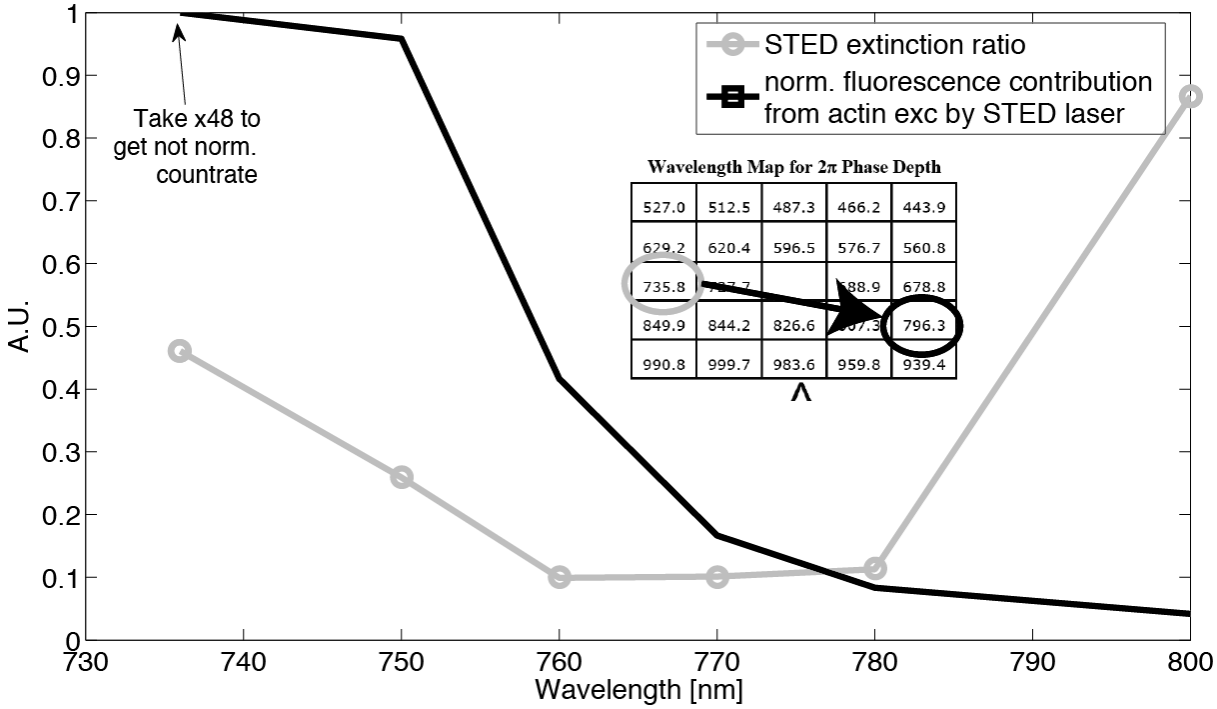


Figure 9.2: The residual countrate of atto647-actin by the STED laser vs the wavelength of the STED laser is shown (blue line). Not normalized, $25mW$ STED laser power lead to $48kHz$ of countrate, making any STED imaging impossible. In the same line, the depletion efficiency vs the wavelength shows that higher wavelength, compared to the normally used $736nm$ lead to a better depletion (blue line). As a result, the STED laser wavelength has to be moved to $780nm$ and, hence, the STED beam path has to be changed when going through the vortex phase plate, from $735.8nm$ to $796.3nm$ (inset).

$25mW$ STED laser power lead to $48kHz$ of countrate, making any STED imaging impossible (red line, normalized to make it comparable to the depletion efficiency). At the same time, the depletion efficiency becomes more efficient at higher wavelength, compared to the normally used $736nm$ (blue line). As a result, the STED laser wavelength has to be moved to $780nm$ and, hence, the wavelength is not suited anymore for the previously used path through the phase plate. The inset of figure 9.2 shows the configuration with the respective wavelength that the phase plate is made for. For atto647-actin, the phase plate is moved in such a way that the beam passes through the $796.3nm$ window instead of the $735.8nm$ window. As a consequence, the alignment, especially the polarization and the

collimation of the STED laser has to be adjusted. Accordingly, the efficiency of the STED setup has to be tested with 'Dark Red' beads (20nm, Life Technologies, Carsbad, CA), because the previously used 'crimson beads' are not suited for this wavelength anymore.

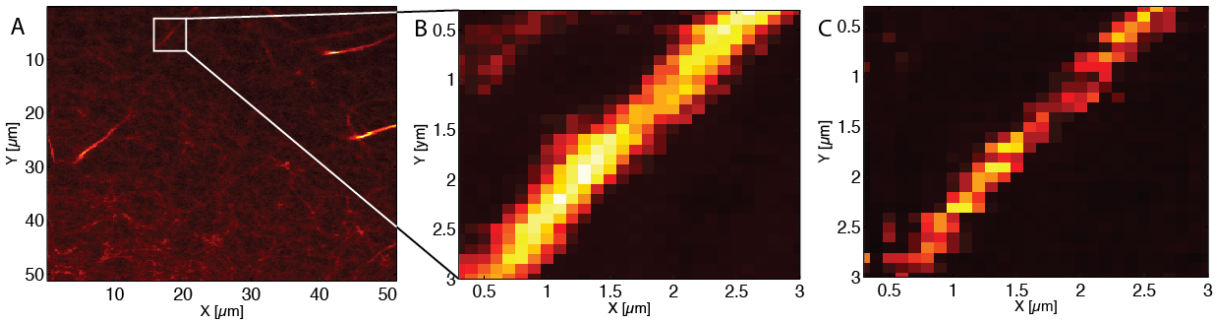


Figure 9.3: A) Image of Atto647-actin filaments, tethered with filamin to the surface. Brightest filaments are most likely already bundled up actin strands. B) Zoom-in on a single fiber, image taken only with excitation laser, $FWHM = 292nm$ C) STED image of the same filament, $FWHM = 112nm$.

Figure 9.3A shows actin filaments (bundling up and development of an network is already visible in the buttom righthand corner), tethered with filamin to the surface. The nominal actin concentration in the flow cell is 0.5µm. The brightest parts of the image, visible on both sides, are already bundled up fibers of actin. Panel B) shows a zoom-in of a single filament, resulting in a FWHM of $292nm$. From the brightness and the width, it is reasonable to suppose that this depicts a single filament growing on the surface. Figure 9.3C shows the same region of interest with the STED laser activated. The STED image decreases the FWHM to $112nm$, resulting indeed in the desired effect of producing a super-resolution image of atto647-actin.

There are several reasons why the maximum achievable resolution of approximately $75nm$ is not visible in this image. One particular reason is the amount of methyl-cellulose present in the solution. The higher its content is, the more viscous the F-Buffer and the less fluctuation of filaments on the surface. However, the amount of methyl-cellulose that finally reaches the flow cell varies strongly due to experimental difficulties. One possible solution would be to increase the amount of methyl-cellulose, making imaging easier and having a positive effect on the resolution, but increasing the complexity of the preparation of the sample before imaging.

## 9.4 Outlook

The results so far have shown that it is indeed possible in principle to follow the polymerization of actin under varied conditions with the STED setup, achieving a resolution that is far beneath the diffraction limit. To achieve meaningful results about the branching of actin as stated in the scope of the project, several experimental parameters need to be optimized: the first is for sure the actin concentration. The higher the actin concentration, the faster the polymerization takes place and the more statistics about branching can be achieved. The disadvantage of high actin concentrations are the high number of nuclei and the need for speed between sample preparation and the start of the measurement. Otherwise, only the already formed polymers and branches can be counted but the emergence of branches can not be followed. Another reason against high actin concentration is the background contribution of freely diffusing actin in the flow cell. This means that a compromise between statistics and high speed has to be found.

Another parameter that needs optimization is the concentration of ARP2/3, which is needed to initiate branching. In the first experiments that were carried out with a final ARP2/3 concentration of $0.5\mu M$, no branches were visible, either in TIRF or STED microscopy. This fact can either be caused by ARP2/3 being to old or by too few branches. As already suggested in the outlook of the STED setup, with the help of a second color, it would be possible to label ARP2/3 and determine by colocalization whether the protein is still active. Another option with two-color STED would be to seed e.g. atto488-actin filaments and accordingly add ARP2/3 and atto647-actin and follow the process of branching in greater detail, since the starting point of the branching experiment could be exactly determined.

The main goal still is to characterize the influence of the different tethering proteins on the branching behavior of actin with ARP2/3 and determine whether the discrepancy that can be found in literature arrives from different protocols that are used for imaging. This can only be investigated when the difficulties described in this paragraph can be overcome and varying branching conditions can be reliably imaged with the STED setup.

# Chapter 10

# Conclusion and Summary

In this work, two different types of confocal microscopes were assembled, characterized and applied to different biological problems. The first one, a multi-parameter fluorescence detection (MFD) setup that is equipped with the previously developed pulsed interleaved excitation (PIE) technique, is a powerful spectroscopic tool that offers a number of fluorescent fluctuation spectroscopy (FFS) techniques like fluorescence (cross-) correlation spectroscopy (F(C)CS), single-pair Förster resonance energy transfer (spFRET), and spike analysis spectroscopy (SAS). The instrument is also capable of utilizing brightness fluctuation methods like the photon counting histogram (PCH), fluorescence intensity distribution analysis (FIDA), and the number and brighness (N&B) analysis. These techniques together offer the capability to characterize fluorescent molecules with respect to their number, diffusion coefficient, anisotropy, FRET efficiency, lifetime, stoichiometry and their interaction partner, only to name a few parameters. The setup assembly is described in detail and the accordingly the size of the confocal volumes was determined with the help of freely diffusing fluorophores. The overlap of the two different laser excitation and the four detection volumes is shown with a double labeled DNA.

The second setup that was assembled in the scope of this work is a stimulated emission depletion (STED) microscope setup. This type of setup, theoretically described at the end of the 1990s and realized a few years later, was among the first to successfully circumvent the diffraction limit, formulated by Ernst Abbe 150 years ago. One of its key features is the fact that its resolution is, in principle, only limited by the bleaching of the fluorophore and even nowadays a resolution on the single-digit nanometer scale is possible. The setup in this work consists of a excitation and a depletion laser and is capable of super resolution imaging on one fluorophore in 2D. A full description of the theoretical background is first given, followed by a detailed description of the setup. The subsequent characterizaiton of the setup serves two purposes: on the one hand it demonstrates the properties of the setup, but on the other hand it serves as guide for the alignment of the setup. All steps - from backreflection on the CMOS camera, polarization of the STED beam, alignment of the detection path, timing of the two lasers to the scaning of gold- and fluorescent beads -

should be carried out on a daily basis to ensure the full operational reliabilty of the setup.

The MFD setup is then used to test the influence of different salts from the Hofmeister series - $NaClO_4$, $KCl$, and $GdmCl$ - on the folding state of a 29 amino acid long helical model peptide $AK_{14}$. This peptide consists of 14 repetitions of alanine and lysine. Lysine is positively charged at neutral pH and, hence, the folded state is forbidden without the addition of salts that screen this charge or by changing the pH to 11, which is above the isoelectric point of lysine. Combining circular dichroism (CD) and all-atom molecular dynamics (MD) simulations with spFRET measurements, several fundamental findings emerge: on the one hand, every salt, also salts that are well known as unfolding reagents like $GdmCl$ or $NaClO_4$, acts in small concentrations up to $0.5M$ as screening reagent and induces folding. One the other hand, it is shown that, although CD shows high helical content for high concentrations of $NaClO_4$, the combination of CD and spFRET prove that actual a highly collapsed state of the peptide is existent. The reason why CD specroscopy leads to wrong results is cleared up by MD simulations: the $ClO_4^-$-ion binds tighly to the backbone of the peptide and alters the CD fluorophore structure, rendering CD spectroscopy useless in the case of perchloride ions in the buffer.

Furthermore, with the help of FCCS and a global fit to both autocorrelation - and the cross-correlation curve, the folding efficiency of fluorescent proteins is investigated. Although the cross-correlation volume is already determined by the two auto-correlation volumes, THE CCF itself delivers aditional information about the cross-correlation volume. A global fit to all three curves offers the advantage that this overdetermined problem is solved more precisely by using the additional information to fit the three parameters with higher precision. To determine the folding efficiency, EGFP is fused with mCherry and with the help of FCCS, the number of EGFP-only, mCherry only and double-labeled molecules is available. This makes it possible to calculate a minimum folding efficiency of EGFP of 79% and mCherry of 52%. These values are calculated from samples that are extracted and purified from cell lysate, giving them more time to mature than in a live-cell experiment. This means that for in vivo experiments, the folding efficeincy will be lower.

The third topic that is covered in this work is the polymerization of actin. Actin and its highly dynamic polymerizaiton behavior is crucial for processes like cell migration, cytokinesis, cell polarization and the perception of forces. The results here show that it is possible to transfer bulk experiments to a confocal microscope. This opens up a new dimension for polymerization essays, because not only the generated polymer mass is available, but, for the first time, also the monomer concentration is a measurable parameter. This makes it possible to determine the critical concentration for the polymerization for every individual measurement, for the case that polymerization equlibrium is reached. In addition, the influence of pH on the polymerization is investigated. By developing a simple model of electrostatic protein-protein interaction and combining it with different

FFS techniques, it becomes clear that polymerization of actin can either occur in the presence of sufficient amounts of screening salts, or when the net charge is reduced, i.e. close to the pI of actin. These results explain why it is necessary to switch from low-salt buffer to high-salt buffer for the start of the polymerization.

The final chapter shows that it is indeed possible to visualize the polymerization of actin not only on a confocal scanning microscope, but that the STED setup assembled in this work is able to follow the growth of actin filaments and image them with a resolution of $110nm$. This will enable us in further studies to investigate the influence of different thethering proteins, which are used to bind actin filaments specifically to the surface, on the branching behavior of actin.

Clearly, the setups assembled in this work in combination with the variety of fluorescence techniques that they offer, and the resulting applications yield significant new insights into problems that have been strongly debated in literature. Especially bridging the gap between imaging and spectroscopy, which is possible on a STED setup, becomes more and more relevant. The technological advances in the recent decade are leading towards a confocal microscope that offers the capabilty to image a biological specimen under *in vivo* conditions with a resolution on the single-digit nanometer scale at nearly video-rate and at the same time serving as spectroscopic tool that offers information about the sample on the nanosecond time resolution. This microscope does not yet exist and the amount of information that is achievable is mainly limited by the amount of collectable photons from the fluorophores. Looking at the step increase of interest in biology on the single-molecule level in combination with technical advances, it will possible in the near future to follow a single biological molecule within its natural environemt from its emergence throughout its whole lifecycle, gaining thereby information about its interaction pathway and helping us understand how life on the nanometer scale takes place.

# Chapter 11

# Materials and Methods

## 11.1 Exp. Proc. for the Unfolding Study of AK14

### Peptide synthesis and purification

The $(AK)_{14}$ peptide was synthesized using standard Fmoc chemistry with N-terminal acetylation and C-terminal amidation. Peptide purification was done by C8 reverse phase HPLC and the sequence was confirmed by electrospray mass spectroscopy. Labeling was done in solution with atto488 succinimidyl ester and atto647N maleimide fluorophores. Labeled peptides were purified via anion exchange chromatography followed by liquid condensed/lung surfactant mass spectrometry.

### Circular Dichroism Spectroscopy

CD experiments were done with a JASCO 715 spectropolarimeter (Jasco, Gross-Umstadt, Germany) and thermal denaturation with a Peltier-thermostat. Peptide concentrations between 30-60 μM were used. The helical fraction was determined assuming the standard linear relationship between spectra at 222 nm and the average peptide α-helicity, i.e. $([\theta]_{222} - E_U)/(H - E_U)$, where $H = -44000 \cdot (1 - (3/N))$ is the maximum helical content corrected for finite size effects, N is the number of amino acids, and EU is the ellipticity of a fully unfolded state (2220). We did not included temperature corrections of the unfolded state signal since all analyses for added salts were done at 273 K.

### MD computer simulations

MD simulations were performed as described previously for brute-force and replica-exchange MD. Calculation of $R_{DA}$ based on MD-derived structures is done as follows: In order to compare results from single molecule FRET and MD, the positions of the fluorophores with their linkers need to be accounted for in the MD-derived structures. To do this we first, representative snapshots of specific classes of structures (1. fully helical, 2. fully

coiled, 3. highly compact, i.e., minimum radius of gyration) were taken from the MD simulation. Due to the difficulty in achieving equilibrium conditions, we could not choose 'average' states but instead we chose prominent classes of 3 well-defined, structural states. Second, the end cap Trp residues were removed. The donor dye was located at the N atom of the Ala residue of the N-terminus and the acceptor dye was positioned on the S atom of the Cys residue at the C-terminus. It was done this way to resemble the amino coupling at the N-terminus, and the maleimide labeling at the C- terminus of the $(AK)_{14}$ peptide for experiments. Dye sizes of 7Ålinker length of 10Åand linker widths of 4.5Åwere used. The accessible volume (AV) of the dyes was then calculated using 'Prior positions' with FRETnpsTools. The AV's on the MD- derived structures are displayed using PyMol (24). A mean position, $< R_{DA} >_{mp}$, was calculated assuming equal probabilities of the dye position within the AV using 100000 samples and taking into consideration the measured residual anisotropies (0.12 for atto488 and 0.08 for atto647N) and a Förster radius of 51Å. The $< R_{DA} >_{mp}$ was transformed into $R_{DA}^{exp}$ assuming isotropic averaging.

## 11.2 Exp. Proc. for the Quantification of FCCS curves

### Proteins

Two types of GFPs were used in this part of the work. One is the commonly used EGFP from Clontech. The other is a modified version of the mgfp5 in the GFP.RN3 vector, which are called $GFP^{RN3}$ in this work [228]. We also used two RFPs in the article, mRFP1 and mCherry. The constructs mRFP-GSRMGTG-EGFP (mRFP-7-EGFP) and mRFP-GSRMGTG-$GFP^{RN3}$ (mRFP-7-$GFP^{RN3}$) have been previously used [229]. The number between both FPs refers to the number of amino acids between them. The plasmids are all sub-cloned in a pXJ40 plasmid. mCherry-GSRMGTG-EGFP (mCherry-7-EGFP) was made by replacing mRFP1 with mCherry on mRFP-7-EGFP between the EcoRI and BamHI sites. mCherry-GGAGGAGGSRMGTG- EGFP (mCherry-14-EGFP) was made by replacing mRFP1 with mCherry plus additional 21 base pairs behind the mCherry gene. mCherry-GGAGGAGGSRMGTG-$GFP^{RN3}$ (mCherry-14- $GFP^{RN3}$) was made by replacing EGFP with $GFP^{RN3}$ between the BamHI and NotI sites. The EGFP and $GFP^{RN3}$ dimer were made by replacing the mRFP with EGFP or $GFP^{RN3}$ in mRFP-7-EGFP and mRFP-7-$GFP^{RN3}$ respectively between the EcoRI and BamHI sites. EGFP-10- mCherry was made by replacing the EGFP at the C-terminal in the EGFP dimer by mCherry between the BamHI and NotI sites.

CHO-K1 cells were cultured in F-12K Kaighn's modification medium (Invitrogen) containing 10% fetal bovine serum and 1% penicillin, and streptomycin and cultured at 37 oC in 5 % CO2. Cells were transfected with 5 μg of plasmid DNA using electroporation following the preprogrammed protocol for CHO cells (Gene Pulser Xcell; Bio-Rad, Hercules, CA). The cells were then seeded onto glass slides (30 mm in diameter; Lakeside, Monee, IL) and grown in the culture medium for 18–24 h. They were washed and measured in phosphate-buffered saline (PBS) in a POC minichamber (Carl Zeiss, Jena, Germany).

### Optical setup

Dual-color FCCS experiments with pulsed interleaved excitation were performed on a home-build confocal setup, assembled by Matthias Höller [96]. A pulsed fiber laser with a fixed repetition rate of 27.4 MHz (FFS.SYS-CONT-COMP-TSHG, TOPTICA Photonics, Gräfefilng, Germany) was tuned to a wavelength of 561 nm for mCherry excitation. The laser served as a synchronization source and master clock for the entire setup. The system is built around a Nikon TE200 microscope base. As a second picosecond, pulsed excitation source for excitation of EGFP, a 476 nm diode laser was used (LDH-P-C-470, PicoQuant, Berlin, Germany). The lasers were combined into a single-mode fiber (AMS Technologies, Munich, Germany) using a dichroic mirror (500DCXR, AHF Analysetechnik, Tübingen, Germany). The output of the fiber was collimated (60FC-4-RGB11- 47,

Schäfter & Kirchhoff, Hamburg, Germany) and focused on the sample by a 60× 1.2NA water immersion objective (Plan Apo VC 60x WI, Nikon, Japan). The average excitation powers used were 2 µW for experiments in live cells, measured before the dichroic mirror (Brightline HC 482/563/640, AHF Analysentechnik, Munich, Germany) separating excitation and emission beam paths. For scanning of the cells, a galvanometric scanner unit with two mirrors for x and y (scanner: 6210H, controller: MicroMax 673 series, Cambridge Technology, Cambridge, USA) in combination with a telescope was installed to scan the beam. The collected fluorescence was focused on a 50µm pinhole with a 60 mm achromatic doublet lens (G322322000, Linos, Göttingen, Germany), and the signal of different FPs was separated using a dichroic mirror (565DCXR, AHF Analysetechnik). Each channel has an appropriate emission filter (HQ 525/20 and ET595/50, AHF Analysetechnik) before the single photon counting avalanche photodiodes (SPQR-16, Perkin Elmer, Waltham, Massachusetts) used for detection. The detected photons were registered by two individual but synchronized TCSPC data collection cards (SPC-144, Becker&Hickl, Berlin, Germany). The laser pulses were delayed with respect to each other by 18 ns allowing determination of the excitation source by the arrival time of the detected photon using TCSPC.

## 11.3 Exp. Proc. for the Actin Polymerization

### Proteins

G-actin was purified from rabbit or chicken skeletal muscle [230] [231] and stored at 4°C for up to two weeks. Myosin was purified and chemically inactivated with NEM according to [232]. Actin was labeled in random surface lysines with atto-488 or atto532 or it was purchased already labelled from Hypermol (Bielefeld, Germany).

### Bulk assays

Polymerization of actin was induced by addition of 1/10 of the final volume of 10x KMEI buffer (1x contained: $50mM\ KCl$, $1mM\ MgCl_2$, $1mM\ EGTA$ and $10mM\ imidazole \cdot HCl$ at pH 7.0) and incubation for at least one hour at room temperature. For the polymerization assays, 20% pyrene-labelled actin was used [233] [234]. $Ca^{+2}$ to $Mg^{+2}$ exchange was done by adding 1/10 of the final volume of 10x ME buffer ($50\mu M\ MgCl_2$, $0.2mM\ EGTA$) for 5 min. Polymerization was promoted by addition of 1/10 of the final volume 10x KMEI buffer. The final volume was 100 µl. Pyrene fluorescence was monitored by excitation at 365nm and emission at 407nm with a Cary Varian Spectrofluorometer. Lag-times were extracted as the intercept from the slope at the inflection point of the polymerization curve. Depolymerization was carried out by diluting $1\mu M$ of 100% pyrene-actin (polymerized for 2 h at RT in the desired pH) in F-buffer pH 7.1 to $10nM$. Data from Zimmerle and Frieden was digitized using the freely-available program grabit (http://www.mathworks.com/matlabcentral/fileexchange/7173-grabit) in MATLAB.

### Circular Dichroism and Electron Microscopy

CD spectra from 195 to 260 nm were acquired with a Jasco J-715 spectropolarimeter (Jasco). A protein concentration of $10\mu M$ in G-buffer at the desired pH value was used. The measurements were performed at a bandwidth of 5nm, a response time of 2s, and a scan rate of $0.1nm \cdot s^{-1}$. For Electron Microscopy, a 3 µL drop of polymerized actin was incubated for 90 s on a copper grid previously plasma cleaned for 30 s and stained with 3% uracyl acetate for 30 s.

### Rate Calculations

In general, protein-protein (e.g. A and B) complex formation (AB) is described by:

$$A + B \underset{k_{-D}}{\overset{k_{+D}}{\rightleftarrows}} A \cdot B \underset{k_{-C}}{\overset{k_{+C}}{\rightleftarrows}} AB \tag{11.1}$$

where $A * B$ is the transient complex defined with a separation and orientation close to the native complex but where short-range interactions still have to be formed. $k_{+D}$ and $k_{-D}$ are the diffusion-limited rate constant for transient complex formation and the reverse process, respectively. $k_{+C}$ and $k_{-C}$ are the rate constants from the transient complex to tight native complex through conformational changes and the reverse process, respectively. The association rate constant, $k_{on}$, is then defined as:

$$k_{on} = \frac{k_D \cdot k_C}{k_{-D} + k_C} \tag{11.2}$$

and the off rate, $k_{off}$ is given by:

$$k_{on} = \frac{k_{-D} \cdot k_{-C}}{k_{-D} + k_C} \tag{11.3}$$

If the conformational rearrangement is very fast upon transient complex formation, it is said that the reaction is diffusion-limited or diffusion-controlled (i.e. when $k_C \gg k_{-D}$).

In order to rationalize the experimental trends in the pH and salt concentration dependence of the rate constants, we make use of a simple generic theory. We assume the reaction is completely diffusion-controlled and isotropic, and the two reactive constituents $A$ and $B$, say, two actin proteins or one dimer and one actin protein, can be effectively modeled as two spheres with size (diameter) $\sigma_i = 2R_i$ with $i = A, B$, where $R$ is equal to $2.5nm$. The reaction size is then given by $\sigma_{AB} = (\sigma_A + \sigma_B)/2$. We further assume that the two spheres interact with an isotropic pair potential $V_{AB}(r)$ for center-to-center distances $r > \sigma_{AB}$. The steady-state result for the diffusion-controlled rate constant $k_D$ is then given by [235] [236]:

$$k_D^{-1} = \frac{1}{4\pi D_0} \int_{\sigma_{AB}}^{\infty} dr \frac{exp(k_B \cdot T \cdot V_{AB}(r))}{r^2} \tag{11.4}$$

where $D_0$ is the mutual diffusion constant between the reactants and is assumed to be given by Stokes' relationship:

$$D_0 = \frac{\Sigma_i k_B T}{6\pi\eta R_i} \tag{11.5}$$

in a solvent with the viscosity $\eta$. As the proteins carry a (pH-dependent) net charge, the leading order interaction between the spheres can be modeled by the so-called DLVO potential [237]:

$$V_{AB}(r) = V_{DLVO}(r) = V_{disp}(r) + V_{dl}(r) \tag{11.6}$$

which is the sum of attractive dispersion interactions ($V_{disp}(r)$) and the repulsive electrostatic double-layer interaction ($V_{dl}(r)$). Higher order multipoles are neglected in our approach, but can be included in principle in equation 11.6 by resolving angular degrees of freedom in the integral. To a good approximation for short distances, where $r \ll \sigma_{AB}$,

the attractive forces can be described as:

$$V_{disp} = -\frac{H}{24} \cdot \frac{\sigma_A \sigma_B}{\sigma_{AB} \cdot (r - \sigma_{AB})} \tag{11.7}$$

where $H$ is a material constant called the Hamaker constant and is typically between $3-10k_BT$. In this work, a Hamaker constant of $5k_BT$ is used. The double layer interaction between two charged spheres in a solution with salt concentration $c$ is given by:

$$k_BT \cdot V_{dl} = Z_i \cdot Z_j \cdot \lambda_B \cdot \frac{exp(\kappa R_A)}{1 + \kappa R_A} \cdot \frac{exp(\kappa R_B)}{1 + \kappa R_B} \cdot \frac{exp(\kappa r)}{1 + \kappa r} \tag{11.8}$$

with $\lambda_B = e^2/4\pi\epsilon_0 k_B T = 0.71nm$ is the Bjerrum length in water, $\kappa = \sqrt{8\pi\lambda_B c}$ is the inverse (Debye- Hückel) screening length, and $Z_i$ the valency of reactant $i$. In our case is $Z_i = n_i z_i(pH)$, where $n_i$ is the degree of polymerized actin of reactant $i$, for instance $i = 2$ for a dimer. The actin net charge $z_i(pH)$ has been estimated by the Scripps APBS software for the actin protein structure (PDB: 1J6Z) and is shown in figure XX. Actin has an isoelectric point at a $pH \backsimeq 5.4$. This analysis is very generic and the trends with pH and salt should hold for every step during polymerization, i.e, dimerization, trimerization, etc., where the reactive size $\sigma_{AB}$ has to be effectively adjusted. Quantitatively, the analysis ignores a few details such as anisotropic reactivity (the 'patchiness'), hydrodynamic corrections to the diffusion constant and rotational diffusion. These extensions will only slow down the reaction. Other refinements, such as a more accurate approximation of the dispersion interactions (Eq. 11.6) or inclusion of multipoles will also not change the calculated trends. At higher salt concentrations (above 0.1 M), nontrivial ion-specific effects may occur [238] as well as a reduction of any favorable electrostatic-mediated interactions that stabilize filament formation [195]. The observed maximal association rates at a pH of 6.3, which are higher than the predicted $pI$ of actin at 5.4, may be due to the anisotropic reactivity of the monomer to a particular filament end.

## Cell line construction and Listeria infection

Lentiviral constructs of Lifeact-mEGFP were generated according to the protocol of Untergasser [239], using the ViraPower™ II Lentiviral Gateway® Expression System (Invitrogen). Cellular $pH_i$ was determined using the fluorescent $H^+$-sensitive dye $2,7 - biscarboxyethyl - 5(6) - carboxyfluorescein$ (BCECF; Invitrogen) as described previously [240] [241].

*L.monocytogenes*10403*S* strain expresses red fluorescent protein (RFP) under the actA promoter (pactA-RFP). Upon entry of the bacteria into the cytosol of the host cell, transcription of RFP is up-regulated 200-fold (42). Hence, the expression of RFP in this strain correlates with entry of bacteria into the cytoplasm. Before infection with L. monocytogenes, cells were plated in MatTek dishes containing an inserted coverslip, main-

tained in growth medium for 24 to 48 h and then washed 3 times with PBS and incubated with DMEM containing 10% FBS without antibiotics. A culture of *L.monocytogenes* incubated overnight at 30$^{o}$C was diluted 1:100 in PBS and 5 µl of this dilution was added to the MatTek dishes and incubated for 8 to 14 hours to achieve 90% infection. Just before imaging, the cells were washed 2X with PBS and maintained in Hepes buffer ($25mM\ Hepes$, $140mM\ NaCl$, $5mM\ KCl$, $10mM\ Glucose$, $1mM\ KPi$ buffer, $1mM\ MgSO_4$, $2mM\ CaCl_2$, pH7.4) for 2 to 3 min during imaging.

## Imaging and image analysis of Listeria motility

The pH-dependent motility of L. monocytogenes was tested using PSN and E266I fibroblasts cells (Table S1). Cells were imaged at 37$^{o}$C using a 100x objective on an inverted microscope system (Nikon eclipse TE2000 Perfect Focus System; Nikon Instruments, Melville, NY), equipped with a spinning-disk confocal scanner unit (CSU10; Yokogawa, Newnan, GA), 488-nm solid-state laser (LMM5; Spectral Applied Research, Richmond Hill, Canada), 561-nm solid state laser (MPB VFL-P-series), multipoint stage (MS-2000; Applied Scientific Instruments, Eugene, OR), a CoolSnap HQ2 cooled charge-coupled device (CCD) camera (Photometrics, Tucson, AZ), and camera-triggered electronic shutters controlled with NIS-Elements Imaging Software (Nikon). A single confocal plane of cells was imaged for 3 min, 1 image/s, with an exposure time from 50 to 100 ms for both 488 nm and 561 nm excitation. Forty-six L. monocytogenes trajectories per cell line were tracked by the manual tracking command in the NIS elements software.

# Bibliography


[1] J B Pawley and B R Masters. Handbook of biological confocal microscopy. *Journal of biomedical optics*, 2008.

[2] Alan Van Orden, Keir Fogarty, and Jaemyeong Jung. Fluorescence fluctuation spectroscopy: a coming of age story. *Applied spectroscopy*, 58(5):122A–137A, May 2004.

[3] Takeshi Suzuki, Toshiyuki Matsuzaki, Haruo Hagiwara, Takeo Aoki, and Kuniaki Takata. Recent advances in fluorescent labeling techniques for fluorescence microscopy. *Acta histochemica et cytochemica*, 40(5):131–137, December 2007.

[4] S Weiss. Fluorescence spectroscopy of single biomolecules. *Science*, 1999.

[5] E Abbe. Beiträge zur Theorie des Mikroskops und der mikroskopischen Wahrnehmung. *Archiv für mikroskopische Anatomie*, 9(1):413–418, December 1873.

[6] B Huang, H Babcock, and X Zhuang. Breaking the diffraction barrier: super-resolution imaging of cells. *Cell*, 2010.

[7] C Levinthal. Are there pathways for protein folding. *J Chim phys*, 1968.

[8] C B Anfinsen. Principles that govern the folding of protein chains. *Science*, 181(4096):223–230, July 1973.

[9] A Einstein. Zur Quantentheorie der Strahlung. *Physikalische Gesellschaft Zürich*, 1916.

[10] A Jaboski. Efficiency of Anti-Stokes Fluorescence in Dyes : Abstract : Nature. *Nature*, 1933.

[11] Markus Sauer, Johan Hofkens, and Jörg Enderlein. *Handbook of Fluorescence Spectroscopy and Imaging*. From Ensemble to Single Molecules. John Wiley & Sons, December 2010.

[12] M Born and R Oppenheimer. Zur Quantentheorie der Molekeln. *Annalen der Physik*, 389(20):457–484, 1927.

[13] Edward Condon. Nuclear Motions Associated with Electron Transitions in Diatomic Molecules. *Physical Review*, 32(6):858–872, December 1928.

[14] J Franck and E G Dymond. Elementary processes of photochemical reactions. *Transactions of the Faraday Society*, 1926.

[15] Michael Kasha. Characterization of electronic transitions in complex molecules. *Discuss. Faraday Soc.*, 9:14–19, 1950.

[16] D C Harris and M D Bertolucci. Symetry and Spectroscopy: An Introduction to Vibrational and Electronic Spectroscopy. 1978.

[17] J M Hollas. Modern spectroscopy. 2004.

[18] P W Atkins and J De Paula. Atkins' physical chemistry. 2006.

[19] Nikolaus Naredi-Rainer. Multi Parameter Fluorescence Spectroscopy - Setup, Assembly and Applications. Master's thesis, Ludwig-Maximilians-Universität, München.

[20] G G Stokes. On the change of refrangibility of light. *Philosophical Transactions of the Royal Society of ...*, 1852.

[21] R Ladenburg. Untersuchungen über die anomale Dispersion angeregter Gase. *Zeitschrift für Physik*, 1928.

[22] J P Gordon, H J Zeiger, and C H Townes. Phys. Rev. 99, 1264 (1955): The Maser—New Type of Microwave Amplifier, Frequency Standard, and Spectrometer. *Physical Review*, 1955.

[23] Theodore H Maiman. Stimulated optical radiation in ruby. *Nature*, 187(4736):493, 1960.

[24] R M Clegg, O Holub, and C Gohlke. [22] Fluorescence lifetime-resolved imaging: Measuring lifetimes in an image. *Methods in enzymology*, 2003.

[25] Th Förster. Zwischenmolekulare Energiewanderung und Fluoreszenz. *Annalen der Physik*, 437(1-2):55–75, 1948.

[26] P R Selvin. The renaissance of fluorescence resonance energy transfer. *Nature structural biology*, 2000.

[27] Robert M Clegg. Fluorescence resonance energy transfer. *Current opinion in biotechnology*, 6(1):103–110, January 1995.

[28] Xavier Michalet, Achillefs N Kapanidis, Ted Laurence, Fabien Pinaud, Soeren Doose, Malte Pflughoefft, and Shimon Weiss. The power and prospects of fluorescence microscopies and spectroscopies. *Annu Rev Biophys Biomol Struct*, 32:161–182, 2003.

[29] D C Lamb. Single-Pair FRET: An Overview with Recent Applications and Future Perspectives. *... Tracking and Single Molecule Energy Transfer*, 2009.

[30] Kazuhiro Aoki, Yuji Kamioka, and Michiyuki Matsuda. Fluorescence resonance energy transfer imaging of cell signaling from in vitro to in vivo: Basis of biosensor construction, live imaging, and image processing. *Development, growth & differentiation*, 55(4):515–522, May 2013.

[31] J Hohlbein, S J Holden, and A N Kapanidis. Single-molecule FRET: Methods and biological applications. *Handbook of Single- ...*, 2009.

[32] B Schuler and W A Eaton. Protein folding studied by single-molecule FRET. *Current opinion in structural biology*, 2008.

[33] R M Clegg and P C Schneider. Fluorescence lifetime-resolved imaging microscopy: a general description of lifetime-resolved imaging measurements. *Fluorescence microscopy and ...*, 1996.

[34] Th Förster. Experimentelle und theoretische Untersuchung des zwischemmolekularen Übergangs von Elektronenanregungsenergie. *Zeitschrift Naturforschung Teil A*, 4:321, 1949.

[35] R M Clegg. The history of FRET. *Reviews in Fluorescence 2006*, 2006.

[36] R Emerson and W Arnold. A SEPARATION OF THE REACTIONS IN PHOTOSYNTHESIS BY MEANS OF INTERMITTENT LIGHT. *The Journal of general physiology*, 15(4):391–420, March 1932.

[37] R Emerson and W Arnold. The photochemical reaction in photosynthesis. *The Journal of general physiology*, 1932.

[38] H Kallmann and F London. Zur Quantenmechanik der Energieübertragung. *Zeitschrift für Physik A Hadrons and Nuclei*, 1930.

[39] P Auger and F Perrin. La répartition dans l'espace des directions d'émission des photoélectrons. *J Phys Radium*, 1927.

[40] F Weigert. Über die spezifische Wirkung der polarisierten Strahlung. *Annalen der Physik*, 1920.

[41] E Gaviola and P Pringsheim. Über den Einfluß der Konzentration auf die Polarisation der Fluoreszenz von Farbstofflösungen. *Zeitschrift fuer Physik*, 1924.

[42] F Perrin. Interaction entre atomes normal et active. Transferts d'activation. Formation d'une molecule activee. *Annales de l'institut Henri Poincaré*, 1933.

[43] W Arnold and J R OPPENHEIMER. Internal conversion in the photosynthetic mechanism of blue-green algae. *The Journal of general physiology*, 33(4):423–435, March 1950.

[44] T Förster. Energiewanderung und fluoreszenz. *Naturwissenschaften*, 1946.

[45] PAM Dirac. The quantum theory of the emission and absorption of radiation. In *Proceedings of the Royal Society of London Series A*, 1927.

[46] M Shinitzky and Y Barenholz. [CITATION][C]. *Biochimica et Biophysica Acta (BBA)-Reviews ...*, 1978.

[47] Steven S Vogel, Christopher Thaler, Paul S Blank, and Srinagesh V Koushik. Time Resolved Fluorescence Anisotropy. *FLIM Microscopy in Biology and Medicine*, 1:245–288, 2009.

[48] U Kubitscheck. Fluorescence Microscopy: From Principles to Biological Applications. 2013.

[49] Robert Hooke. Micrographia: or, some physiological descriptions of minute bodies made by magnifying glasses. With observations and inquiries thereupon, 1667.

[50] A Van Leeuwenhoek. Epistolae physiologicae super compluribus naturae arcanis. 1719.

[51] G B Airy. On the diffraction of an object-glass with circular aperture. *Transactions of the Cambridge Philosophical Society*, 1835.

[52] L Rayleigh. XXXI. Investigations in optics, with special reference to the spectroscope. *The London*, 1879.

[53] C M Sparrow. On spectroscopic resolving power. *The Astrophysical Journal*, 1916.

[54] N G Jerlov and B Kullenberg. The Tyndall effect of uniform minerogenic suspensions. *Tellus*, 1953.

[55] M Minsky. Microscopy apparatus. US Patent Office, 1961.

[56] H NAORA. Microspectrophotometry and cytochemical analysis of nucleic acids. *Science*, 114(2959):279–280, September 1951.

[57] M Minsky. Memoir on inventing the confocal scanning microscope. *Scanning*, 1988.

[58] J S Ploem. The use of a vertical illuminator with interchangeable dichroic mirrors for fluorescence microscopy with incident light. *Z Wiss Mikrosk*, 1967.

[59] M D Egger and M Petrăn. New reflected-light microscope for viewing unstained brain and ganglion cells. *Science*, 157(3786):305–307, July 1967.

[60] J G White, W B Amos, and M Fordham. An evaluation of confocal versus conventional imaging of biological structures by fluorescence light microscopy. *The Journal of cell biology*, 105(1):41–48, July 1987.

[61] G van Meer, E H Stelzer, R W Wijnaendts-van Resandt, and K Simons. Sorting of sphingolipids in epithelial (Madin-Darby canine kidney) cells. *The Journal of cell biology*, 105(4):1623–1635, October 1987.

[62] P Davidovits and M D Egger. Scanning laser microscope for biological investigations. *Applied optics*, 10(7):1615–1619, July 1971.

[63] Y S Sabharwal, A R Rouse, L Donaldson, M F Hopkins, and A F Gmitro. Slit-scanning confocal microendoscope for high-resolution in vivo imaging. *Applied optics*, 38(34):7133–7144, December 1999.

[64] J Z YOUNG and F ROBERTS. A flying-spot microscope. *Nature*, 167(4241):231, February 1951.

[65] W H Richardson. Bayesian-based iterative method of image restoration. *JOSA*, 1972.

[66] Nicolas Dey, Laure Blanc-Feraud, Christophe Zimmer, Pascal Roux, Zvi Kam, Jean-Christophe Olivo-Marin, and Josiane Zerubia. Richardson–Lucy algorithm with total variation regularization for 3D confocal microscope deconvolution. *Microscopy Research and Technique*, 69(4):260–266, 2006.

[67] H Bi and G Boerner. When does the Richardson-Lucy deconvolution converge? *arXiv.org*, 1994.

[68] A P Dempster, N M Laird, and D B Rubin. Maximum likelihood from incomplete data via the EM algorithm. *Journal of the Royal Statistical Society ...*, 1977.

[69] J A Conchello. Superresolution and convergence properties of the expectation-maximization algorithm for maximum-likelihood deconvolution of incoherent images. *Journal of the Optical Society of America. A, Optics, image science, and vision*, 15(10):2609–2619, October 1998.

[70] Praveen Pankajakshan, Bo Zhang, Laure Blanc-Feraud, Zvi Kam, Jean-Christophe Olivo-Marin, and Josiane Zerubia. Blind deconvolution for thin-layered confocal imaging. *Applied optics*, 48(22):4437–4448, August 2009.

[71] P Pankajakshan and B Zhang. Blind deconvolution for diffraction-limited fluorescence microscopy. *... Imaging: From Nano ...*, 2008.

[72] W Becker, A BERGMANN, and M KACPRZAK. Advanced time-correlated single photon counting technique for spectroscopy and imaging of biological systems. *Progress in biomedical ...*, 2005.

[73] DJS Birch and R E Imhof. Time-domain fluorescence spectroscopy using time-correlated single-photon counting. *Topics in fluorescence spectroscopy*, 2002.

[74] Michael Wahl, Tino Röhlicke, Hans-Jürgen Rahn, Rainer Erdmann, Gerald Kell, Andreas Ahlrichs, Martin Kernbach, Andreas W Schell, and Oliver Benson. Integrated multichannel photon timing instrument with very short dead time and high throughput. *Review of Scientific Instruments*, 84(4):043102, April 2013.

[75] Wolfgang Becker, Axel Bergmann, and Christoph Biskup. Multispectral fluorescence lifetime imaging by TCSPC. *Microscopy Research and Technique*, 70(5):403–409, May 2007.

[76] W Becker, A BERGMANN, H Wabnitz, and D Grosenick. High count rate multichannel TCSPC for optical tomography. *Proc SPIE*, 2001.

[77] D O'Connor. Time-correlated single photon counting. 1984.

[78] M Wahl, H J Rahn, I Gregor, and R Erdmann. Dead-time optimized time-correlated photon counting instrument with synchronized, independent timing channels. *Review of Scientific ...*, 2007.

[79] S Felekyan and R Kuhnemuth. Full correlation from picoseconds to seconds by time-resolved and time-correlated single photon detection. *Review of Scientific ...*, 2005.

[80] Wolfgang Becker. *The bh TCSPC handbook*. Becker & Hickl GmbH, 2005.

[81] D C Lamb, B K Müller, and C Bräuchle. Enhancing the sensitivity of fluorescence correlation spectroscopy by using time-correlated single photon counting. *Current pharmaceutical biotechnology*, 6(5):405–414, October 2005.

[82] E Haustein and P Schwille. Fluorescence correlation spectroscopy: novel variations of an established technique. *Annu Rev Biophys Biomol Struct*, 2007.

[83] O Krichevsky and G Bonnet. Fluorescence correlation spectroscopy: the technique and its applications. *Reports on Progress in Physics*, 2002.

[84] S T Hess, S H Huang, A A Heikal, and W W Webb. Biological and chemical applications of fluorescence correlation spectroscopy. *Biochemistry*, 2002.

[85] J R Lakowicz. Principles of fluorescence spectroscopy. 2009.

[86] Miguel ngel Medina and Petra Schwille. Fluorescence correlation spectroscopy for the detection and study of single molecules in biology. *BioEssays*, 24(8):758–764, July 2002.

[87] E L Elson and D Magde. Fluorescence correlation spectroscopy. I. Conceptual basis and theory. *Biopolymers*, 1974.

[88] D Magde and EL Elson. Fluorescence correlation spectroscopy. II. An experimental realization. *Biopolymers*, 1974.

[89] D Magde, E Elson, and W W Webb. Thermodynamic fluctuations in a reacting system—measurement by fluorescence correlation spectroscopy. *Physical review letters*, 1972.

[90] Yan Chen, Joachim D Müller, Peter T C So, and Enrico Gratton. The Photon Counting Histogram in Fluorescence Fluctuation Spectroscopy. *Biophysical journal*, 77(1):553–567, July 1999.

[91] P Kask, K Palo, D Ullmann, and K Gall. Fluorescence-intensity distribution analysis and its application in biomolecular detection technology. *Proceedings of the National Academy of Sciences of the United States of America*, 96(24):13756–13761, November 1999.

[92] Joachim D Müller. Cumulant Analysis in Fluorescence Fluctuation Spectroscopy. *Biophysical journal*, 86(6):3981–3992, June 2004.

[93] K M Berland, P T So, Y Chen, W W Mantulin, and E Gratton. Scanning two-photon fluctuation correlation spectroscopy: particle counting measurements for detection of molecular aggregation. *Biophysical journal*, 71(1):410–420, July 1996.

[94] Ashok Pabbathi, Shalini Ghosh, and Anunay Samanta. FCS Study of the Structural Stability of Lysozyme in the Presence of Morpholinium Salts. *The Journal of Physical Chemistry B*, 117(51):16587–16593, December 2013.

[95] P Schwille and J Ries. Principles and applications of fluorescence correlation spectroscopy (FCS). *Biophotonics: Spectroscopy*, 2011.

[96] Matthias Hoeller. Advanced Fluorescence Fluctuation Spectroscopy with Pulsed Interleaved Excitation. February 2011.

[97] Armin Hoffmann, Daniel Nettels, Jennifer Clark, Alessandro Borgia, Sheena E Radford, Jane Clarke, and Benjamin Schuler. Quantifying heterogeneity and conformational dynamics from single molecule FRET of diffusing molecules: recurrence analysis of single particles (RASP). *Physical chemistry chemical physics : PCCP*, 13(5):1857–1871, February 2011.

[98] M Eigen and R Rigler. Sorting single molecules: application to diagnostics and evolutionary biotechnology. *... of the National Academy of Sciences*, 1994.

[99] P Schwille, F J Meyer-Almes, and R Rigler. Dual-color fluorescence cross-correlation spectroscopy for multicomponent diffusional analysis in solution. *Biophysical journal*, 72(4):1878–1886, April 1997.

[100] M Rarbach, U Kettling, A Koltermann, and M Eigen. Dual-color fluorescence cross-correlation spectroscopy for monitoring the kinetics of enzyme-catalyzed reactions. *Methods*, 2001.

[101] Kirsten Bacia, Sally A Kim, and Petra Schwille. Fluorescence cross-correlation spectroscopy in living cells. *Nature methods*, 3(2):83–89, February 2006.

[102] K Bacia and P Schwille. Practical guidelines for dual-color fluorescence cross-correlation spectroscopy. *Nature protocols*, 2007.

[103] Ling Chin Hwang and Thorsten Wohland. Dual-color fluorescence cross-correlation spectroscopy using single laser wavelength excitation. *ChemPhysChem*, 5(4):549–551, April 2004.

[104] Ling Chin Hwang and Thorsten Wohland. Single wavelength excitation fluorescence cross-correlation spectroscopy with spectrally similar fluorophores: resolution for binding studies. *The Journal of chemical physics*, 122(11):114708, March 2005.

[105] Yong Hwee Foo, Nikolaus Naredi-Rainer, Don C Lamb, Sohail Ahmed, and Thorsten Wohland. Factors affecting the quantification of biomolecular interactions by fluorescence cross-correlation spectroscopy. *Biophysical journal*, 102(5):1174–1183, March 2012.

[106] Achillefs N Kapanidis, Ted A Laurence, Nam Ki Lee, Emmanuel Margeat, Xiangxu Kong, and Shimon Weiss. Alternating-Laser Excitation of Single Molecules. *Accounts of Chemical Research*, 38(7):523–533, July 2005.

[107] Jelle Hendrix and Don C Lamb. Pulsed interleaved excitation: principles and applications. *Methods in enzymology*, 518:205–243, 2013.

[108] Barbara K Müller, Evgeny Zaychikov, Christoph Bräuchle, and Don C Lamb. Pulsed interleaved excitation. *Biophysical journal*, 89(5):3508–3522, 2005.

[109] D C Lamb, A Schenk, C Röcker, and C Scalfi-Happ. Sensitivity enhancement in fluorescence correlation spectroscopy of multiple species using time-gated detection. *Biophysical . . .*, 2000.

[110] Ettore Bismuto, Enrico Gratton, and Don C Lamb. Dynamics of ANS Binding to Tuna Apomyoglobin Measuredwith Fluorescence Correlation Spectroscopy. *Biophysical journal*, 81(6):3510–3521, December 2001.

[111] A J García-Sáez and P Schwille. Fluorescence correlation spectroscopy for the study of membrane dynamics and protein/lipid interactions. *Methods (San Diego*, 2008.

[112] T Ohrt, J Mutze, W Staroske, L Weinmann, J Hock, K Crell, G Meister, and P Schwille. Fluorescence correlation spectroscopy and fluorescence cross-correlation spectroscopy reveal the cytoplasmic origination of loaded nuclear RISC in vivo in human cells. *Nucleic Acids Research*, 36(20):6439–6449, September 2008.

[113] C Zander, M Sauer, K H Drexhage, D S Ko, and A Schulz. Detection and characterization of single molecules in aqueous solution. *Applied Physics B*, 1996.

[114] A A Deniz, M Dahan, J R Grunwell, T Ha, A E Faulhaber, D S Chemla, S Weiss, and P G Schultz. Single-pair fluorescence resonance energy transfer on freely diffusing molecules: observation of Förster distance dependence and subpopulations. *Proceedings of the National Academy of Sciences of the United States of America*, 96(7):3670–3675, March 1999.

[115] Barbara Katrin Müller. Die gepulste alternierende Anregung in der konfokalen Fluoreszenzspektroskopie. January 2007.

[116] C Eggeling, S Berger, L Brand, J R Fries, J Schaffer, A Volkmer, and C A Seidel. Data registration and selective single-molecule analysis using multi-parameter fluorescence detection. *Journal of biotechnology*, 86(3):163–180, April 2001.

[117] Nam Ki Lee, Achillefs N Kapanidis, You Wang, Xavier Michalet, Jayanta Mukhopadhyay, Richard H Ebright, and Shimon Weiss. Accurate FRET measurements within single diffusing biomolecules using alternating-laser excitation. *Biophysical journal*, 88(4):2939–2953, April 2005.

[118] Volodymyr Kudryavtsev, Martin Sikor, Stanislav Kalinin, Dejana Mokranjac, Claus AM Seidel, and Don C Lamb. Combining MFD and PIE for Accurate spFRET Measurements. *ChemPhysChem*, 13(4):1060–1078, 2012.

[119] Martin Sikor. Single-molecule fluorescence studies of Protein Folding and Molecular Chaperones. 2011.

[120] Steffen Rüttinger, Rainer Macdonald, Benedikt Krämer, Felix Koberling, Martin Roos, and Eberhardt Hildt. Accurate single-pair Förster resonant energy transfer through combination of pulsed interleaved excitation, time correlated single-photon counting, and fluorescence correlation spectroscopy. *Journal of biomedical optics*, 11(2):024012, March 2006.

[121] Eyal Nir, Xavier Michalet, Kambiz M Hamadani, Ted A Laurence, Daniel Neuhauser, Yevgeniy Kovchegov, and Shimon Weiss. Shot-noise limited single-molecule FRET histograms: comparison between theory and experiments. *The Journal of Physical Chemistry B*, 110(44):22103–22124, November 2006.

[122] Jerker Widengren, Volodymyr Kudryavtsev, Matthew Antonik, Sylvia Berger, Margarita Gerken, and Claus A M Seidel. Single-Molecule Detection and Identification of Multiple Species by Multiparameter Fluorescence Detection. *Analytical Chemistry*, 78(6):2039–2050, March 2006.

[123] S J Holden and A N Kapanidis. Alternating-laser excitation and pulsed-interleaved excitation of single molecules. *Single Particle Tracking and Single ...*, 2009.

[124] A N Kapanidis and S Weiss. Single-molecule Fret analysis of the path from transcription initiation to elongation. *RNA Polymerases as Molecular ...*, 2009.

[125] Martin Sikor. *Single-molecule fluorescence studies of Protein Folding and Molecular Chaperones*. PhD thesis, LMU Munich, Munich.

[126] Matthew Antonik, Suren Felekyan, Alexander Gaiduk, and Claus A M Seidel. Separating structural heterogeneities from stochastic variations in fluorescence resonance energy transfer distributions via photon distribution analysis. *The Journal of Physical Chemistry B*, 110(13):6970–6978, April 2006.

[127] S Kalinin, S Felekyan, and M Antonik. Probability distribution analysis of single-molecule fluorescence anisotropy and resonance energy transfer. *The Journal of Physical ...*, 2007.

[128] S Kalinin, S Felekyan, and A Valeri. Characterizing multiple molecular states in single-molecule multiparameter fluorescence detection by probability distribution analysis. *The Journal of Physical ...*, 2008.

[129] Stanislav Kalinin, Alessandro Valeri, Matthew Antonik, Suren Felekyan, and Claus A M Seidel. Detection of structural dynamics by FRET: a photon distribution

and fluorescence lifetime analysis of systems with multiple states. *The Journal of Physical Chemistry B*, 114(23):7983–7995, June 2010.

[130] Koyeli Mapa, Martin Sikor, Volodymyr Kudryavtsev, Karin Waegemann, Stanislav Kalinin, Claus A M Seidel, Walter Neupert, Don C Lamb, and Dejana Mokranjac. The conformational dynamics of the mitochondrial Hsp70 chaperone. *Molecular cell*, 38(1):89–100, April 2010.

[131] J R Fries, L Brand, C Eggeling, and M Köllner. Quantitative identification of different single molecules by selective time-resolved confocal fluorescence spectroscopy. *The Journal of ...*, 1998.

[132] J D Müller, Y Chen, and E Gratton. Resolving heterogeneity on the single molecular level with the photon-counting histogram. *Biophysical journal*, 2000.

[133] Yan Chen, Joachim D Müller, QiaoQiao Ruan, and Enrico Gratton. Molecular brightness characterization of EGFP in vivo by fluorescence fluctuation spectroscopy. *Biophysical journal*, 82(1 Pt 1):133–144, January 2002.

[134] Yan Chen, Li-Na Wei, and Joachim D Müller. Probing protein oligomerization in living cells with fluorescence fluctuation spectroscopy. *Proceedings of the National Academy of Sciences of the United States of America*, 100(26):15492–15497, December 2003.

[135] L Mandel. Fluctuations of photon beams and their correlations. In *Proceedings of the Physical Society*, 1958.

[136] Kausik Chakraborty, Manal Chatila, Jyoti Sinha, Qiaoyun Shi, Bernhard C Poschner, Martin Sikor, Guoxin Jiang, Don C Lamb, F Ulrich Hartl, and Manajit Hayer-Hartl. Chaperonin-Catalyzed Rescue of Kinetically Trapped States in Protein Folding. *Cell*, 142(1):112–122, July 2010.

[137] Benjamin Schuler, Everett A Lipman, and William A Eaton. Probing the free-energy surface for protein folding with single-molecule fluorescence spectroscopy. *Nature*, 419(6908):743–747, October 2002.

[138] P Kapusta. Kapusta: Absolute diffusion coefficients: compilation... - Google Scholar. *Application note*, 2010.

[139] Michael Hofmann, Christian Eggeling, Stefan Jakobs, and Stefan W Hell. Breaking the diffraction barrier in fluorescence microscopy at low light intensities by using reversibly photoswitchable proteins. *Proceedings of the National Academy of Sciences of the United States of America*, 102(49):17565–17569, December 2005.

[140] S W Hell. Far-Field Optical Nanoscopy. *Science*, 316(5828):1153–1158, May 2007.

[141] D W Pohl, W Denk, and M Lanz. Optical stethoscopy: Image recording with resolution lambda/20. *Applied physics letters*, 1984.

[142] C Cremer and T Cremer. Considerations on a laser-scanning-microscope with high resolution and depth of field. *Microscopica acta*, 1974.

[143] B Bailey, D L Farkas, D L Taylor, and F Lanni. Enhancement of axial resolution in fluorescence microscopy by standing-wave excitation. *Nature*, 366(6450):44–48, November 1993.

[144] T Dertinger, R Colyer, G Iyer, S Weiss, and J Enderlein. Fast, background-free, 3D super-resolution optical fluctuation imaging (SOFI). *Proceedings of the National Academy of Sciences of the United States of America*, 106(52):22287–22292, December 2009.

[145] Michael J Rust, Mark Bates, and Xiaowei Zhuang. Sub-diffraction-limit imaging by stochastic optical reconstruction microscopy (STORM). *Nature methods*, 3(10):793–795, October 2006.

[146] Eric Betzig, George H Patterson, Rachid Sougrat, O Wolf Lindwasser, Scott Olenych, Juan S Bonifacino, Michael W Davidson, Jennifer Lippincott-Schwartz, and Harald F Hess. Imaging intracellular fluorescent proteins at nanometer resolution. *Science*, 313(5793):1642–1645, September 2006.

[147] Andriy Chmyrov, Jutta Arden-Jacob, Alexander Zilles, Karl-Heinz Drexhage, and Jerker Widengren. Characterization of new fluorescent labels for ultra-high resolution microscopy. *Photochemical & photobiological sciences : Official journal of the European Photochemistry Association and the European Society for Photobiology*, 7(11):1378–1385, November 2008.

[148] S W Hell and J Wichmann. Breaking the diffraction resolution limit by stimulated emission: stimulated-emission-depletion fluorescence microscopy. *Optics letters*, 19(11):780–782, June 1994.

[149] K I Willig, B Harke, R Medda, and S W Hell. STED microscopy with continuous wave beams. *Nature methods*, 2007.

[150] Y Xia and J Yin. Generation of a focused hollow beam by an 2pi-phase plate and its application in atom or molecule optics. *JOSA B*, 2005.

[151] M Dyba, J Keller, and S W Hell. Phase filter enhanced STED-4Pi fluorescence microscopy: theory and experiment. *New Journal of Physics*, 2005.

[152] Stanislav Kalinin, Ralf Kühnemuth, Hayk Vardanyan, and Claus A M Seidel. Note: A 4 ns hardware photon correlator based on a general-purpose field-programmable gate array development board implemented in a compact setup for fluorescence correlation spectroscopy. *Review of Scientific Instruments*, 83(9):096105, 2012.

[153] Bhanu Neupane, Fang Chen, Wei Sun, Daniel T Chiu, and Gufeng Wang. Tuning donut profile for spatial resolution in stimulated emission depletion microscopy. *Review of Scientific Instruments*, 84(4):043701, April 2013.

[154] Silvia Galiani, Benjamin Harke, Giuseppe Vicidomini, Gabriele Lignani, Fabio Benfenati, Alberto Diaspro, and Paolo Bianchini. Strategies to maximize the performance of a STED microscope. *Optics express*, 20(7):7362–7374, March 2012.

[155] J Hendrix, W Schrimpf, M Höller, and D C Lamb. Pulsed interleaved excitation fluctuation imaging. *Biophysical journal*, 2013.

[156] B Harke, C K Ullal, J Keller, and S W Hell. Three-Dimensional Nanoscopy of Colloidal Crystals - Nano Letters (ACS Publications). *Nano letters*, 2008.

[157] Alvaro H Crevenna, Nikolaus Naredi-Rainer, Don C Lamb, Roland Wedlich-Söldner, and Joachim Dzubiella. Effects of Hofmeister Ions on the $\alpha$-Helical Structure of Proteins. *Biophysical journal*, 102(4):907–915, February 2012.

[158] J M Berg and J L Tymoczko. Stryer Biochemie. 2012.

[159] B Alberts. Molecular biology of the cell. 2000.

[160] Luciano Brocchieri and Samuel Karlin. Protein length in eukaryotic and prokaryotic proteomes. *Nucleic Acids Research*, 33(10):3390–3400, 2005.

[161] William Humphrey, Andrew Dalke, and Klaus Schulten. VMD – Visual Molecular Dynamics. *Journal of Molecular Graphics*, 14:33–38, 1996.

[162] Qi Wang, Bo Shui, Michael I Kotlikoff, and Holger Sondermann. Structural basis for calcium sensing by GCaMP2. *Structure (London, England : 1993)*, 16(12):1817–1827, December 2008.

[163] Dennis J Selkoe. Folding proteins in fatal ways. *Nature*, 426(6968):900–904, December 2003.

[164] Songpon Deechongkit, Houbi Nguyen, Evan T Powers, Philip E Dawson, Martin Gruebele, and Jeffery W Kelly. Context-dependent contributions of backbone hydrogen bonding to beta-sheet folding energetics. *Nature*, 430(6995):101–105, July 2004.

[165] R L Baldwin. How does protein folding get started? *Trends in Biochemical Sciences*, 14(7):291–294, July 1989.

[166] L S Itzhaki, D E Otzen, and A R Fersht. ... transition state for folding of chymotrypsin inhibitor 2 analysed by protein engineering methods: evidence for a nucleation-condensation mechanism for protein folding. *Journal of Molecular Biology*, 1995.

[167] F Hofmeister. Zur lehre von der wirkung der salze. *Archiv für experimentelle Pathologie und ...*, 1888.

[168] P H Von Hippel and T Schleich. Ion effects on the solution structure of biological macromolecules. *Accounts of Chemical Research*, 1969.

[169] P K Nandi and D R Robinson. The effects of salts on the free energies of nonpolar groups in model peptides. *Journal of the American Chemical Society*, 94(4):1308–1315, February 1972.

[170] R L Baldwin. How Hofmeister ion interactions affect protein stability. *Biophysical journal*, 71(4):2056–2063, October 1996.

[171] L M Pegram and M T Record, Jr. Thermodynamic origin of Hofmeister ion effects. *The Journal of Physical Chemistry B*, 2008.

[172] Y Zhang and P S Cremer. Chemistry of Hofmeister anions and osmolytes. *Annual review of physical chemistry*, 2010.

[173] Edward P O'Brien, Ruxandra I Dima, Bernard Brooks, and D Thirumalai. Interactions between hydrophobic and ionic solutes in aqueous guanidinium chloride and urea solutions: lessons for protein denaturation mechanism. *Journal of the American Chemical Society*, 129(23):7346–7353, June 2007.

[174] Haripada Maity and Maurice R Eftink. Perchlorate-induced conformational transition of Staphylococcal nuclease: evidence for an equilibrium unfolding intermediate. *Archives of biochemistry and biophysics*, 431(1):119–123, November 2004.

[175] Robert L Baldwin, Carl Frieden, and George D Rose. Dry molten globule intermediates and the mechanism of protein unfolding. *Proteins*, 78(13):2725–2737, October 2010.

[176] N Berova, K Nakanishi, and R W Woody. Circular dichroism: principles and applications. 2000.

[177] Eliana K Asciutto, Ignacio J General, Kan Xiong, Kang Xiong, Sanford A Asher, and Jeffry D Madura. Sodium perchlorate effects on the helical stability of a mainly alanine peptide. *Biophysical journal*, 98(2):186–196, January 2010.

[178] M C Manning, M Illangasekare, and R W Woody. Circular dichroism studies of distorted alpha-helices, twisted beta-sheets, and beta turns. *Biophysical chemistry*, 31(1-2):77–86, August 1988.

[179] S Sindbert, S Kalinin, and H Nguyen. Accurate distance determination of nucleic acids via Forster resonance energy transfer: implications of dye linker length and rigidity. *Journal of the ...*, 2011.

[180] Rahul Godawat, Sumanth N Jamadagni, and Shekhar Garde. Unfolding of hydrophobic polymers in guanidinium chloride solutions. *The Journal of Physical Chemistry B*, 114(6):2246–2254, February 2010.

[181] L M Pegram, T Wendorff, and R Erdmann. Why Hofmeister effects of many salts favor protein folding but not DNA helix formation. In *Proceedings of the ...*, 2010.

[182] N H Andersen, Z Liu, and K S Prickett. Efforts toward deriving the CD spectrum of a 3(10) helix in aqueous medium. *FEBS letters*, 399(1-2):47–52, December 1996.

[183] J M Scholtz and R L Baldwin. Perchlorate-induced denaturation of ribonuclease A: investigation of possible folding intermediates. *Biochemistry*, 32(17):4604–4608, May 1993.

[184] W L Mattice. The effect of temperature and salt concentration on the circular dichroism exhibited by unionized derivatives of L-alanine in aqueous solution. *Biopolymers*, 13(1):169–183, January 1974.

[185] D Balasubramanian and B C Misra. Effects of metal ions on the structure and spectra of the peptide group. *Biopolymers*, 1975.

[186] T Weidemann and M Wachsmuth. Analysis of ligand binding by two-colour fluorescence cross-correlation spectroscopy. *Single ...*, 2002.

[187] R Kuhlemann and A Koltermann. A protease assay for two-photon crosscorrelation and FRET analysis based solely on fluorescent proteins. In *Proceedings of the ...*, 2002.

[188] R Heim and R Y Tsien. Engineering green fluorescent protein for improved brightness, longer wavelengths and fluorescence resonance energy transfer. *Current Biology*, 1996.

[189] Geoffrey S Waldo. Improving protein folding efficiency by directed evolution using the GFP folding reporter. *Methods in molecular biology (Clifton, N.J.)*, 230:343–359, 2003.

[190] N C Shaner, G H Patterson, and M W Davidson. Advances in fluorescent protein technology. *Journal of cell science*, 2007.

[191] Nathan C Shaner, Paul A Steinbach, and Roger Y Tsien. A guide to choosing fluorescent proteins. *Nature methods*, 2(12):905–909, December 2005.

[192] A H Crevenna, N Naredi-Rainer, A Schonichen, J Dzubiella, D L Barber, D C Lamb, and R Wedlich-Soldner. Electrostatics Control Actin Filament Nucleation and Elongation Kinetics. *The Journal of biological chemistry*, 288(17):12102–12113, April 2013.

[193] T D Pollard, W C Earnshaw, and J Lippincott-Schwartz. Cell biology. 2007.

[194] G M Cooper and R E Hausman. The cell. 2000.

[195] T Oda, M Iwasa, T Aihara, Y Maéda, and A Narita. The nature of the globular-to fibrous-actin transition. *Nature*, 2009.

[196] C A Larabell and K A Nugent. Imaging cellular architecture with X-rays. *Current opinion in structural biology*, 2010.

[197] D Chhabra and C G dos Remedios. Actin: An overview of its structure and function. *Actin-Binding Proteins and Disease*, 2008.

[198] K C Holmes, D Popp, W Gebhard, and W Kabsch. Atomic model of the actin filament. *Nature*, 347(6288):44–49, September 1990.

[199] F Wang, R V Sampogna, and B R Ware. pH dependence of actin self-assembly. *Biophysical journal*, 55(2):293–298, February 1989.

[200] C T Zimmerle and C Frieden. Effect of pH on the mechanism of actin polymerization. *Biochemistry*, 1988.

[201] D A Begg and L I Rebhun. pH regulates the polymerization of actin in the sea urchin egg cortex. *The Journal of cell biology*, 83(1):241–248, October 1979.

[202] L G Tilney, D P Kiehart, C Sardet, and M Tilney. Polymerization of actin. IV. Role of Ca++ and H+ in the assembly of actin and in membrane fusion in the acrosomal reaction of echinoderm sperm. *The Journal of cell biology*, 77(2):536–550, May 1978.

[203] Christian Frantz, Gabriela Barreiro, Laura Dominguez, Xiaoming Chen, Robert Eddy, John Condeelis, Mark J S Kelly, Matthew P Jacobson, and Diane L Barber. Cofilin is a pH sensor for actin free barbed end formation: role of phosphoinositide binding. *The Journal of cell biology*, 183(5):865–879, December 2008.

[204] J Srivastava, G Barreiro, S Groscurth, A R Gingras, B T Goult, D R Critchley, M J S Kelly, M P Jacobson, and D L Barber. Structural model and functional significance of pH-dependent talin-actin binding for focal adhesion remodeling. *Proceedings of the National Academy of Sciences*, 105(38):14436–14441, September 2008.

[205] Anne J Ridley. Life at the leading edge. *Cell*, 145(7):1012–1022, June 2011.

[206] Sheryl P Denker and Diane L Barber. Cell migration requires both ion translocation and cytoskeletal anchoring by the Na-H exchanger NHE1. *The Journal of cell biology*, 159(6):1087–1096, December 2002.

[207] Rosa A Cardone, Valeria Casavola, and Stephan J Reshkin. The role of disturbed pH dynamics and the Na+/H+ exchanger in metastasis. *Nature reviews. Cancer*, 5(10):786–795, October 2005.

[208] R J Gillies, N Raghunand, and G S Karczmar. MRI of the tumor microenvironment. *Journal of Magnetic ...*, 2002.

[209] Bradley A Webb, Michael Chimenti, Matthew P Jacobson, and Diane L Barber. Dysregulated pH: a perfect storm for cancer progression. *Nature reviews. Cancer*, 11(9):671–677, September 2011.

[210] M W Geiger and N J Turro. Pyrene fluorescence lifetime as a probe for oxygen penetration of micelles. *Photochemistry and photobiology*, 22(6):273–276, December 1975.

[211] J R Kuhn and T D Pollard. Real-time measurements of actin filament polymerization by total internal reflection fluorescence microscopy. *Biophysical journal*, 2005.

[212] D Didry, R Lipowsky, M F Carlier, and G Romet-Lemonne. Individual actin filaments in a microfluidic flow reveal the mechanism of ATP hydrolysis and give insight into the properties of profilin. *PLoS biology*, 2011.

[213] Cat M Haglund and Matthew D Welch. Pathogens and polymers: microbe-host interactions illuminate the cytoskeleton. *The Journal of cell biology*, 195(1):7–17, October 2011.

[214] J A Theriot, T J Mitchison, L G Tilney, and D A Portnoy. The rate of actin-based motility of intracellular Listeria monocytogenes equals the rate of actin polymerization. *Nature*, 357(6375):257–260, May 1992.

[215] C Frieden. Polymerization of actin: mechanism of the Mg2+-induced process at pH 8 and 20 degrees C. In *Proceedings of the National Academy of ...*, 1983.

[216] D Sept and J A McCammon. Thermodynamics and kinetics of actin filament nucleation. *Biophysical journal*, 2001.

[217] R F Steiner, K Laki, and S Spicer. Light scattering studies on some muscle proteins. *Journal of Polymer Science*, 1952.

[218] A Narita, T Oda, and Y Maéda. Structural basis for the slow dynamics of the actin filament pointed end. *The EMBO journal*, 2011.

[219] D Drenckhahn and T D Pollard. Elongation of actin filaments is a diffusion-limited reaction at the barbed end and is accelerated by inert macromolecules. *Journal of Biological Chemistry*, 1986.

[220] T Oda, K Makino, I Yamashita, K Namba, and Y Maéda. Distinct structural changes detected by x-ray fiber diffraction in stabilization of F-actin by lowering pH and increasing ionic strength. *Biophysical journal*, 2001.

[221] Simone Köhler, Kurt M Schmoller, Alvaro H Crevenna, and Andreas R Bausch. Regulating contractility of the actomyosin cytoskeleton by pH. *Cell reports*, 2(3):433–439, September 2012.

[222] Thomas D Pollard and Gary G Borisy. Cellular motility driven by assembly and disassembly of actin filaments. *Cell*, 112(4):453–465, February 2003.

[223] M D Welch and R D Mullins. Cellular control of actin nucleation. *Annual review of cell and ...*, 2002.

[224] E N Firat-Karalar and M D Welch. New mechanisms and functions of actin nucleation. *Current opinion in cell biology*, 2011.

[225] M L Gardel, J H Shin, F C MacKintosh, and L Mahadevan. Elastic behavior of cross-linked and bundled actin networks. *Science*, 2004.

[226] O Lieleg, J Kayser, G Brambilla, L Cipelletti, and A R Bausch. Slow dynamics and internal stress relaxation in bundled cytoskeletal networks. *Nature materials*, 10(3):236–242, March 2011.

[227] Viviana I Risca, Evan B Wang, Ovijit Chaudhuri, Jia Jun Chia, Phillip L Geissler, and Daniel A Fletcher. Actin filament curvature biases branching direction. *Proceedings of the National Academy of Sciences*, 109(8):2913–2918, February 2012.

[228] M Zernicka-Goetz, J Pines, K Ryan, K R Siemering, J Haseloff, M J Evans, and J B Gurdon. An indelible lineage marker for Xenopus using a mutated green fluorescent protein. *Development (Cambridge, England)*, 122(12):3719–3724, December 1996.

[229] Xianke Shi, Yong Hwee Foo, Thankiah Sudhaharan, Shang-Wei Chong, Vladimir Korzh, Sohail Ahmed, and Thorsten Wohland. Determination of dissociation constants in living zebrafish embryos with single wavelength fluorescence cross-correlation spectroscopy. *Biophysical journal*, 97(2):678–686, July 2009.

[230] J A Spudich and S Watt. The regulation of rabbit skeletal muscle contraction I. Biochemical studies of the interaction of the tropomyosin-troponin complex with actin and the proteolytic .... *Journal of Biological Chemistry*, 1971.

[231] S MacLean-Fletcher and T D Pollard. Identification of a factor in conventional muscle actin preparations which inhibits actin filament self-association. *Biochemical and biophysical research communications*, 96(1):18–27, September 1980.

[232] Dennis Breitsprecher, Antje K Kiesewetter, Joern Linkner, and Jan Faix. Analysis of actin assembly by in vitro TIRF microscopy. *Methods in molecular biology (Clifton, N.J.)*, 571:401–415, 2009.

[233] T D Pollard. Measurement of rate constants for actin filament elongation in solution. *Analytical biochemistry*, 134(2):406–412, October 1983.

[234] T A Holak, Z Werb, M Sixt, and R Wedlich-Soldner. Lifeact: a versatile marker to visualize F-actin. *Methods*, 2008.

[235] P Debye. Reaction rates in ionic solutions. *Transactions of the Electrochemical Society*, 1942.

[236] M Smoluchowski. Studien über Kolloidstatistik und den Mechanismus der Diffusion. *Colloid & Polymer Science*, 1916.

[237] J L Barrat and J P Hansen. Basic concepts for simple and complex liquids. 2003.

[238] H Kang, M J Bradley, and B R McCullough. Identification of cation-binding sites on actin that drive polymerization and modulate bending stiffness. In *Proceedings of the ...*, 2012.

[239] Untergasser A. Cloning - TOPO-Reaction.

[240] T Tominaga, T Ishizaki, S Narumiya, and D L Barber. p160ROCK mediates RhoA activation of Na–H exchange. *The EMBO journal*, 1998.

[241] T Voyno-Yasenetskaya, B R Conklin, and R L Gilbert. G alpha 13 stimulates Na-H exchange. *Journal of Biological ...*, 1994.

# Nomenclature

| | |
|---|---|
| aa | amino acid |
| APBS | all-photon-burst-search |
| DCBS | dual channel burst search |
| DNA | deoxyribonucleic acid |
| FRET | Förster resonance energy transfer |
| IRF | instrument response function |
| MFD | multi-parameter fluorescence detection |
| PCH | photon counting histogram |
| PIE | pulsed interleaved excitation |
| PSF | point spread function |
| RNA | ribonucleic acid |
| SDCM | spinning disc confocal microscopy |
| STED | stimulated emission depletion |
| TCSPC | time-correlated single photon counting |
| TIRF | total internal reflection fluorescence |

# Chapter 12

# Acknowledgements

Ich möchte meinem Chef, Prof. Don C. Lamb, nicht nur dafür danken, dass ich meine Doktorarbeit in dieser Gruppe machen durfte: ich wurde auch schon für die Diplomarbeit herzlich aufgenommen und habe bei allen Fragen - sei es bei Datenauswertung oder bei Anschaffungen die mein Leben leichter gemacht haben - immer ein offenes Ohr gefunden. Auch die Unterstützung, die ich bei von mir angestossenen Projekten erfarhen habe, ist nicht selbstverständlich und die Kompetentz mit der wissenschaftliche Probleme angegangen wurden hat mich tief beeindruckt. Am meisten möchte ich Dir aber dafür danken, dass Dir die Weiterentwicklung Deiner Studenten wichtig ist, auch in Hinsicht auf Reisen zu Konferenzen, was viele wissenschaftliche Rück- und Tiefschläge wieder wett macht!

Auch möchte ich Prof. Christoph Bräuchle dafür danken, dass er sich ohne Umschweife dazu bereit erklärt hat mein Zweitbegutachter zu sein. Auch für die schönen Seefeste, die Infrastruktur im Labor und nicht zu vergessen die Aufgaben an Rechner Karl und dem iPad, die mich manchmal zu äußerstem Erfindungsreichtum herausgefordert haben, ein aufrichtiges Dankeschön.

Ich möchte hier auch die vielen Geldgeber - SFB 749, 1032, 1035, SPP 1464, NIM, CeNS - dankend erwähnen, ohne die nicht nur der Setup-Bau unmöglich gewesen wäre, sondern auch die Reisekosten zu vielen Konferenzen kamen aus diesen Töpfen.

Ich möchte meinen vielen Kooperationspartnern danken: Yong-Hwee und Thorsten für das FCS Projekt, bei dem ich selber über FCS glaube ich am meisten gelernt habe.

Alvaro, für unzählige brilliante Ideen und eine nicht zu bremsende Begeisterung für die Wissenschaft im Allgemeinen. Es hat mich immer umgehauen wie viel Literaturwissen Du schon angesammelt hast und welche Verbindungen Du überal in die Welt hin hast. Aber vor allem möchte ich Dir dafür danken, dass deine Ideen immer zwar hochtrabend aber nie unrealistisch waren. Die Zusammenarbeit hat mir immer unglaublichen Spaß gemacht!

Und nicht zuletzt meinen tiefen Dank an Marcus Knopp, auch wenn wir gar keine Kooperation zusammen hatten. Aber ohne die Hilfe am STED wäre ich hier wirklich nicht rausgekommen! Du warst nie genervt von mir auch wenn ich 5 Mal am Tag angerufen

hab, weil das Setup wieder irgendwas gemacht hat und mir geduldig alle zu beachtenden Finessen erklärt hast. Auch für unzählige Leihgaben und witzige außeruniversitäre Kontakte ein herzliches Dankeschön.

Bei den vielen Kollegen, die ich über die Jahre hatte, weiß ich gar nicht, wo ich anfangen soll: Ich glaube bei Matthias, den ich noch aus meiner Zeit als F-Praktikant hier kenne, der mir alle Grundlagen über Konfokalmikroskopie, FCS und Programmierung beigebracht hat. Aber eigentlich möchte ich mich bei Dir für deine Leidenschaft für Fußball (auch auf dem Gang), unzählige Kaffeepausen (bei dir ohne Kaffee), aberwitzige Gespräche bei so manchem Feierabendbierchen, und insgesamt dafür bedanken, dass Du ein Bürokollege warst, wie man ihn sich nicht besser hat vorstellen können. Wolfi, vielen Dank dafür dass Du meinen Leidensweg seit der 7. Klasse geteilt hast und wir jetzt den Spaß noch haben werden auf mindestens zwei Junggesellenabschieden noch gemeinsam teilzunehmen. Danke, Martin, dass Du immer (naja, fast immer!) das Telefon abgehoben hast, wenn ich mal wieder Justage-Fragen hatte und dafür dass Du mir gezeigt hast, wie man die Jahre hier überstehen kann, ohne komplett am Rad zu drehen. Herzliches Vergelts-Gott an Gregor, meinen symphatischen Landsmann, der immer eine unglaubliche Geschichte parat hatte und von dem ich in Sachen Schlitzohrigkeit noch einiges lernen konnte. Vielen Dank an Iko, der mich stets davor gewart hat in diesem Arbeitskreis anzufangen. Vielen Dank, liebe Doro, dass Du stets Zeit für Kaffeepausen hattest, die immer mit höchst amüsanten Gesprächsthemen gefüllt waren. Vielen Dank an die Ostblockmafia, Sergey und Vova, für viel Prgrammierung, aber auch Fach- und Fußballgespräche. Vielen Dank auch an meine F-Praktikanten, Gerhard und Wehne. Gerhard vor allem dafür dass er das "unsterbliche" Bild vom MFD setup gerendert hat und Wehne dafür, dass Du meine Laufbahn nachahmst und das volle Programm hier ablieferst. Und nicht nur danke dafür, dass du mein STED setup am Leben erhalten wirst, sondern vor allem dafür, dass Du von mir die Ansicht übernommen hast, dass Gruppengefühl das Leben hier leichter macht. Vielen Dank an Aurelie, die nicht nur eine Kompetenz ausgestrahlt hat, sondern immer einen Trick auf Lager hatte, um Dinge am Laufen zu halten. Herzlichen Dank, Jens, dass Du mir bei vielen gemeinsamen Morgentees bei wirklich jedem Thema zugehört hast. Danke Jelle für manche Sturheit, ohne die einige Fehler nie aufgefallen wären. Vielen Dank an Monika, die mir gezeigt hat, dass man auch noch mit 65 mehr flirten kann, als manch 25-jährigem lieb ist. Vielen Dank, Waldi, dass Du immer ein offenes Ohr für meine Programmierprobleme hattest und faktisch jede Pause mit Dingen erheitern konntest, über die Du dich aufgeregt hast. Dankeschön Vroni, für Deinen unvergleichlichen Sarkasmus und unzählige Kommentare, die mich zu grinsen gebracht haben. Vielen Dank an Sushi, Du hast unsere Gruppe um viele fern-östliche Einflüsse bereichert, sei es Essen, oder eine Vielzahl an an Infos, warum es bei uns gar nicht so schlecht ist. Vielen Dank, Lena, dafür dass Du mir unzählige kleine oder große Tätigkeiten abgenommen hast und mir immer das Gefühl vermittelt hast, dass Du dich über Wissen das ich Dir weitergeben

konnte, gefreut hast. Danke, Giulia, für das gewisse italienische Flair in unserer Gruppe und die Leichtigkeit mit der Du Arbeit wegsteckst. Da gehört natürlich auch Adriano dazu: vielen Dank Dir, denn ohne Dich hätte ich den Pilao nie kennen gelernt. Ellen, vielen Dank für Massen an Kuchen, die an Genialität nicht zu überbieten waren. Vielen Dank, Daniela, für abenteuerliche Geschichten aus dem Ruderclub, die meine Laune stets erheitert haben. Dankeschön, Anders, für so manches gemeinsame Feierabendbier und dafür dass Du mein MFD setup unter Deine Fittiche genommen hast. Philipp, der auch bei meinen abwägisten Themen noch immer bescheid weiß. Und auch vielen Dank an den Letzten aus dem Triumvirat aus Büro E1.064, Bässem, für ein technisches Verständnis, das absolut beeindruckend ist. Viola, nicht nur für etliche Getränkebestellungen, sondern auch für viele Gespräche zu wirklich interssanten Themen. Vielen Dank an die Mamas aus dem AK Bräuchle, Frauke und Meli, ihr habt einem gezeigt, dass es wichtigeres gibt, als die Forschung hier. Als letztes unter den Kollegen ist natürlich Moritz hervorzuheben: ich weiß gar nicht, wie ich ohne Deine Hilfe bei Anträgen, Reisekosten und Rechnungen hier durchgehalten hätte. Aber eigentlich muß ich Dir wirklich für die skurilsten Gesprächsthemen danken, ich wüßte nicht was ich ohne dieses Wissen tun würde.

Insgesamt muß ich den Arbeitskreisen Lamb, Bräuchle und Michaelis dafür danken, dass die Atmosphäre immer spitze war und ich jeden morgen gerne in die Arbeit gegangen bin.

Ich möchte meiner Familie ein wirklich herzliches und tief empfundenes Dankeschön sagen, weil ich mir nicht vorstellen kann, irgendwo anders mehr Unterstützung zu finden, als bei Euch.

Und zu Allerletzt möchte ich mich bei Dir, Franziska, bedanken, dafür dass Du ein Fixpunkt in meinem Leben bist, ohne den ich schon längst abgedriftet wäre und dafür dass Du mich schon immer so genommen hast, wie ich wirklich bin.